University of Strathclyde, Glasgow
Department of Naval Architecture, Ocean and Marine Engineering

Long Term Extreme Analysis of Moored FPSO with Emphasis on the Effect of Hydrodynamic Drag Coefficient

By
Aijun Wang

A thesis presented in fulfilment of the requirements for the degree of Doctor of Philosophy

2019

Declaration

This thesis is the result of the author‘s original research. It has been composed by the author and has not been previously submitted for examination which has led to the award of a degree.

Aijun Wang

Signature: Date:

Acknowledgement

First, I would like to express my sincere gratitude to Professor Nigel Barltrop for his supervision and advice for this work. I would like to show my gratitude to Professor Shan Huang, who had been my supervisor for the first two years before he moved to work in BP. He offered me the opportunity to start this research. He is one of the most important people that change my life.

I would like to thank the help and discussion with Dr Graham Stewart, Mr. Michael Dickin from Lloyd's Register and Dr Yingmin Low from National University of Singapore. I benefit a lot from the discussion with them. I acknowledge with gratitude to the stipend support from Lloyd's Register Energy.

I am grateful to Ms Thelma Will and Ms Susan Pawson for their support and help. Also, I would like to thank all the PhD students in the Research Center, who gave me help and made my life full of fun.

I would like to express my appreciation to my family for their continuous support and inspiration throughout my life. Lastly, I would like to express heartfelt thanks to my wife, Na Feng, for her patience, support and encouragement during my study.

Table of Contents

List of Figures

List of Tables

Nomenclature

General symbols

A	Cross-sectional area; Projected area
C_e	Equivalent linear coefficient
C_D	Drag coefficient
C_D^n	Normal drag coefficient
C_D^n	Tangential drag coefficient
C_m^n	Normal inertia coefficient
C_m^τ	Tangential inertia coefficient
C_w	Shape coefficient
$\mathbf{C}$	Damping matrix
CI	Confidence interval
D	Draught Chain bar diameter
$\mathbf{e}_{i+1/2}$	Unit direction vector of segment between i-th and (i+1)-th node
E	Elastic module
$f(\boldsymbol{u})$	Joint probability density function of uncertainty variables
f_{Bi}	Buoyancy at the i-th node
$f_{H_sT_p}(h_s,t_p)$	Joint probability density function of H_s and T_p
$f_{H_s}(h_s)$	Marginal distribution of H_s

$f_{T_p\|H_s}(t_p\|h_s)$	Conditional distribution of T_p for given H_s
$\boldsymbol{f}_{-}^{(2)}(\omega_i,\omega_j)$	Difference frequency QTF
$\boldsymbol{f}_{+}^{(2)}(\omega_i,\omega_j)$	Sum frequency QTF
$\boldsymbol{f}_d(\omega_i)$	Mean wave drift force terms
$\mathbf{F}^{(2)}(t)$	Wave drift force
$\mathbf{F}_c$	Current force
$\mathbf{F}_D$	Drag force matrix
$\mathbf{F}_{Di}$	Drag force at the *i*-th node
$\mathbf{F}_i$	Force concentrated at the node
$\mathbf{F}_I$	Inertia force matrix
$\mathbf{F}_{Ii}$	Inertia force at the *i*-th node
$\mathbf{F}_m$	Equivalent constant force
$\mathbf{F}_s$	Force on the lines of the seabed contaction
$\mathbf{F}_w$	Wind force on the vessel
$\mathrm{F}_X(x\|\boldsymbol{u})$	Conditional distribution of long term extreme given uncertainty variables
$F_{X_{3h}}(x)$	Long term distribution of 3-hour extreme
$F_{X_{3h}\|H_sT_p}(x\|h_s,t_p)$	Conditional distribution of the 3-hour extreme for short term condition given H_s and T_p
$\mathbf{G}^{(1)}$	First order load transfer function
$\mathrm{G}(\mathbf{x})$	Regression model
H_s	Significant wave height

$\mathbf{H}(\omega)$	Displacement transfer function or Displacement RAO
k	Number of simulation
$k(h_s, t_p)$	Number of peak values during a short term condition
$\mathbf{K}$	Stiffness matrix
$l_{i+1/2}$	Original length of segment between *i*-th and (*i*+1)-th node
$\tilde{l}_{i+1/2}$	Length of segment between *i*-th node and (*i*+1)-th node
L	Length between perpendiculars
m_k	*k*-th spectrum moment of the response
$\mathbf{m}_{a,i}$	Added mass on the *i*-th node
$\mathbf{m}_i$	Mass of *i*-th node
$\mathbf{M}$	**M**ass matrix
$\mathbf{M}_i$	Mass of *i*-th node include added mass
$\mathbf{M}_V$	Mass matrix of floating structure
$\mathbf{N}_{i+1/2}$	Transform matrix
$p(\boldsymbol{V}^n)$	Probability density function of $\boldsymbol{V}^n$
q	Probability of being exceeded per year
$\dot{\boldsymbol{r}}^n$	Normal line's velocity
$\boldsymbol{r}_i$	Position of *i*-th nodes
$\dot{\boldsymbol{r}}_i$	Velocity of *i*-th node
$\ddot{\boldsymbol{r}}_i$	Acceleration of *i*-th node
$R(\theta, \mathbf{x}_i, \mathbf{x}_j)$	correlation function
R^2	R-square analysis
R_{ij}	Covariance matrix of relative velocities

$\mathbf{R}$	Correlation model
$\hat{s}_k(x)$	Sample standard deviation
$S_\eta(\omega)$	Wave spectral density
$S_{\eta\eta}(\omega)$	Response Spectral of displacement
$S_T(\omega)$	Response Spectral of top tension
T_p	Spectral peak period
$\mathbf{T}_i$	Tension at the *i*-th node
$\boldsymbol{u}$	Uncertainty variables
$\boldsymbol{u}_i$	Wave particle velocity at node *i*
$\boldsymbol{u}^n$	Normal wave water particle velocity
$\boldsymbol{u}^n_{i,i+1/2}$	Normal wave particle velocity across the half of upper segment that connecting the *i*-th node
$\dot{\boldsymbol{u}}^n_{i,i+1/2}$	Normal wave particle acceleration across the half of upper segment that connecting the *i*-th node
$\boldsymbol{u}^\tau_{i,i+1/2}$	Tangential wave particle velocity across the half of upper segment that connecting the *i*-th node
$\dot{\boldsymbol{u}}^\tau_{i,i+1/2}$	Tangential wave particle acceleration across the half of upper segment that connecting the *i*-th node
$v^+(x)$	Mean rate of *x*-upcrossing of $X(t)$
$\boldsymbol{V}^n$	Normal relative velocity, $\boldsymbol{V}^n = \boldsymbol{u}^n - \dot{\boldsymbol{r}}^n$
$\boldsymbol{V}_c^n$	Normal current velocity
$\boldsymbol{V}_{ri}$	Relative velocity at *i*-th node
$\boldsymbol{V}^n_{ri,i+1/2}$	Normal relative velocity across the half of upper segment

	that connecting the *i*-th node
$\boldsymbol{V}_{ri,i+1/2}^{\tau}$	Tangential relative velocity across the half of upper segment that connecting the *i*-th node
$V_X^+(0 \mid h_s, t_p)$	Average zero-upcrossing rate given H_s and T_p
$\bar{V}_X^+(0)$	Long term average zero-upcrossing rate
w_j	Weight factor
x_c	Threshold
$X(t)$	Stationary response process
X_p	Peak value of response process $X(t)$
Z(**x**)	Gaussian process

Greek Characters

$\alpha(h_s, t_p)$	Location parameter of Gumbel distribution
$\alpha_{kj}(x)$	Exceedance probability conditional on $(k-1)$ previous non-exceedances
β	Reliability index
$\beta(h_s, t_p)$	Scale parameter of Gumbel distribution
θ	Unknown parameter
σ	Standard deviation
σ_r^2	Mean Square Response of displacement
$\sigma_{\dot{r}}^2$	Mean Square Response of velocity
$\varepsilon_k(x)$	Average conditional exceedance rate (ACER) function

$\hat{\varepsilon}_k(x)$	Estimation of the ACER function
$\tilde{\varepsilon}_k(x)$	Modified ACER function
ϕ_0	Incident wave potential
ϕ_7	Diffraction wave potential
ϕ_j	Radiation potential (j=1-6)
Φ	Standard Gaussian distribution function
η	Wave surface elevation; transition parameter
λ	Mean of lnH_s
ζ^2	Variance of lnH_s
γ	Shape parameter of Weibull distribution
ρ	Density of seawater;
	Scale parameter of Weibull distribution
ρ_m	Density of mooring lines
ρ_A	Density of air
$\boldsymbol{\tau}_{i+1/2}$	Transform matrix
Δ	Roughness number
Δt	Time step

Abbreviations

API	American Petroleum Institute
cdf	Cumulative distribution function
COV	Coefficient of variance
DNV	Det Norske Veritas

DOE	Design of Experiment
FORM	First order reliability method
FPSO	Floating production storage and offloading
KC	Keulegan-Carpenter number
HF	High frequency
IFORM	Inverse first order reliability method
LF	Low frequency
LHS	Latin Hypercube Sampling
MCS	Monte Carlo simulation
MPM	Most probable maximum
QTFs	Quadratic transfer functions
RAO	Response amplitude operator
Re	Reynolds number,
TLP	Tension leg platform
WF	Wave frequency

Abstract

One of the key coupling mechanisms between the FPSO and the mooring/riser, which remains to be a challenging topic, is the damping contribution from the mooring lines. The mooring line damping especially from hydrodynamic drag forces is of vital importance to FPSO's low frequency motion in deep water and its associated maximum mooring line tension and the maximum offset. The coupled analysis can take the mooring line damping into account automatically, but it suffers from the extremely high computational cost. Some methods use a linear damping coefficient to represent the damping effect but that estimate may not be accurate due to the line damping depending on several factors such as the wave frequencies, the response and offset position. An efficient and accurate analysis method is required to balance accuracy and efficiency. Morison's equation with a drag coefficient is often employed to calculate the hydrodynamic drag loads of mooring lines. The drag coefficient is not easily determined, particularly for chain, with its complex shape. The variation of hydrodynamic drag coefficient would alter the level of line damping. That means the drag coefficient is important to the damping and the ensuing extreme offset and maximum line tension. Therefore, it is worthwhile to investigate the effects of the hydrodynamic drag coefficient on the damping contribution to the extreme low frequency FPSO motion and the maximum mooring line tension.

To begin with, a hybrid time and frequency domain method is developed for dynamic analysis of moored FPSO. The time domain simulation with a large time step is performed for low frequency motion of the FPSO, whilst the wave frequency response of the mooring lines at a given mean offset position will be conducted in the frequency domain. The frequency domain analysis will be based upon a specific linearization approach where the damping to the low frequency FPSO motion from the wave frequency response of the mooring line can be accounted for in the form of an

increased mean tension. Comparison is made of the tension/motion results with that of the dynamically coupled time-domain analysis, as well as the computational efficiency.

Next, the methodologies for the long term extreme analysis are validated. The all sea state method for the long term extreme analysis is performed by use of Kriging metamodel (Simpson et al., 1998; Wang and Shan, 2006). The Monte Carlo simulation is applied for the long term probability integral based on the Kriging metamodel. The improved method based on the environmental contour method and accurate distribution tail extrapolation method is proposed. The contour line method assumes that the short term variability could be accounted for separately. This method evaluates the extreme response based on limited sea states along a well-defined environmental contour line with a given return period. Then the short term variability is considered by selecting a high fractile. The distribution of the response is evaluated by the average conditional exceedance rates (ACER) method. The ACER method, which can accurately capture the effect of statistical dependence for the extreme value prediction problem, is less restrictive and more flexible than the one based on asymptotic theory.

Finally, the reliability analysis for the extreme response considering the uncertainty influence of the drag coefficient is performed. The conditional distribution for the long term extreme response with given the drag coefficient is estimated by contour line method and ACER method. The perturbation method based on 4^{th}-order expansion is developed. The asymptotic approximation method based on the Laplace's method is also employed for the approximation of probability integral. The asymptotic evaluation is based on the assertion that the greatest contribution to an integral derives from the locations where the integrand is a maximum point.

1 Introduction

1.1 Background

As offshore oilfield developments have been moving toward deeper water, Floating Production Storage and Offloading unit (FPSO) are commonly used for processing and storage of oil and gas prior to offloading it to a tanker that can eliminate the need for costly long-distance pipelines to an onshore terminal. It is particularly effective in remote or deep water locations where seabed pipeline are not cost effective. In addition, FPSO can be relocated that can offer an alternative in short life oil fields. Due to these advantages, the demand to FPSOs increased dramatically during the last decade. Figure 1.1 presents the worldwide distribution of FPSO vessels. There are total 151 FPSOs until August 2014, which 67% are conversions and others are new builds (Barton, 2018).

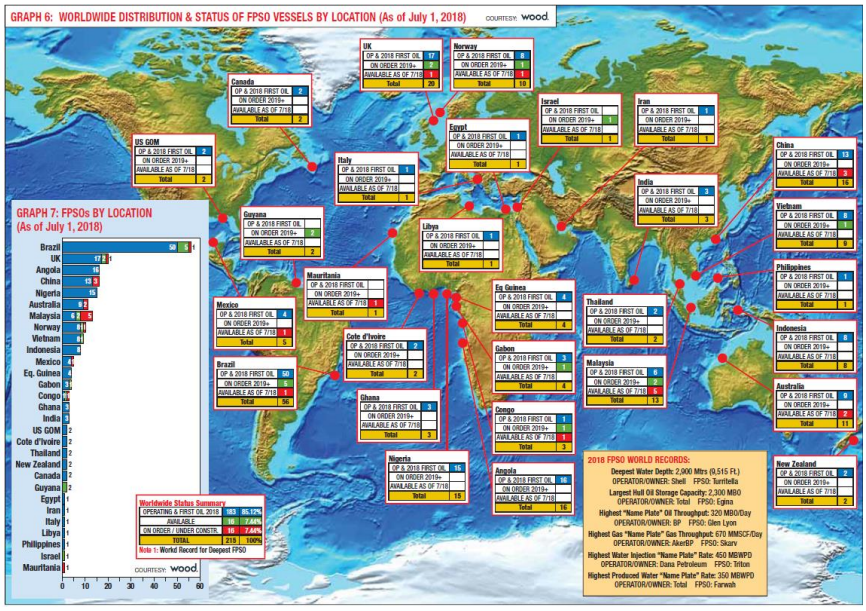

Figure 1.1 Worldwide distribution of FPSO vessels (Barton, 2018)

Under environmental loads such as wind, waves and current, the FPSO exhibits offsets different from the desired point for normal operations. The mooring systems are utilized to maintain it on a station within a specified tolerance which is typically based on an offset limit determined from the configuration of the risers. If the mooring lines fail, it will cause the operation interruption, oil-spill, even casualty and environmental issues. In the past decade, the relatively high failure rate of permanent mooring systems, more than 20 incidents, is raising a concern in the offshore industry (Ma et al., 2013). The incidents with single line breakage often have additional lines that sustained damage or failed prematurely. For the latter case, it would cause the vessel to drift a short distance, riser ruptures, production shutdown and small amount of hydrocarbon release. Some were of substantial consequence, with the need to repair or replace damaged lines.

Table 1.1 North Sea mooring line failure data, 1980 to 2001 (HSE Report, 2003)

Type of Unit	Number of Operating Years per Failure
Drilling Semi-submersible	4.7
Production Semi-submersible	9.0
FPSO	8.8

The failure statistics for North Sea operations for different floating units between 1980 and 2001 are shown in Table 1.1. It can be seen that the probability of line failure per operating year for an FPSO is relatively high (in comparison for example with the probability of structural failure). The cost of mooring line failure is significant when considering the expense of anchor handling tugs, ROV and dive support vessels, replacement parts and lost production. These total costs have been

estimated at a minimum of £2 million for a 50,000 bpd FPSO in the North Sea according to the JIP FPS mooring integrity Report (Noble Denton, 2006). For example, the four mooring lines of Gryphon Alpha FPSO (in the UK North Sea in February 2011) failed when subjected to high environmental forces. The subsequent loss of position resulted in significant damage to the subsea infrastructure and then operations were forced to shut down. It was estimated that the cost is in excess of $1 billion and still counting from the incident. Fortunately, there was no loss of hydrocarbons, and no one was injured. Therefore, it is crucial to ensure the integrity of mooring systems for successful marine operations and safety.

Mooring lines are often subjected to the environmental loads such as wave and current, and the motions of FPSO. The wave forces on the FPSO include first order forces at wave frequency (WF) and second order forces which comprise mean wave drift forces, forces at sum frequencies (HF) and forces at difference frequencies (LF). The first order wave forces are the dominant dynamic loads, orders of magnitude larger than any other dynamic loads. For the frequency of low frequency slow drift motion is usually near to the natural frequency of moored system, which means resonant motion could be excited. Once it occurs, large low frequency motion can yield quite high mooring load.

To the response of floating structure and mooring/ riser system, the traditional method first analyze the motions of floating structure where load effects from the moorings/ risers are modeled as non-linear position dependent forces (stiffness), and apply the responses of floating structure to the top of mooring lines as the boundary conditions, then calculate the response of mooring lines. This uncoupled method neglects or simplifies the hydrodynamic damping contribution from mooring lines. Huse (1986) had found out that the hydrodynamic damping of lines has an important effect on the low frequency motions of floating structure. As shown in Figure 1.2, the mean offset and low frequency motion increase considerably with increasing water depth. And in

2000 m water, offset related to mean offset and low frequency motion constitutes approximately 95% of total offset (Ormberg and Larsen, 1998). In order to obtain a more accurate estimate of the low frequency motion and improved estimates of dynamic loads in the moorings, coupled analysis should be performed, particularly in deep water.

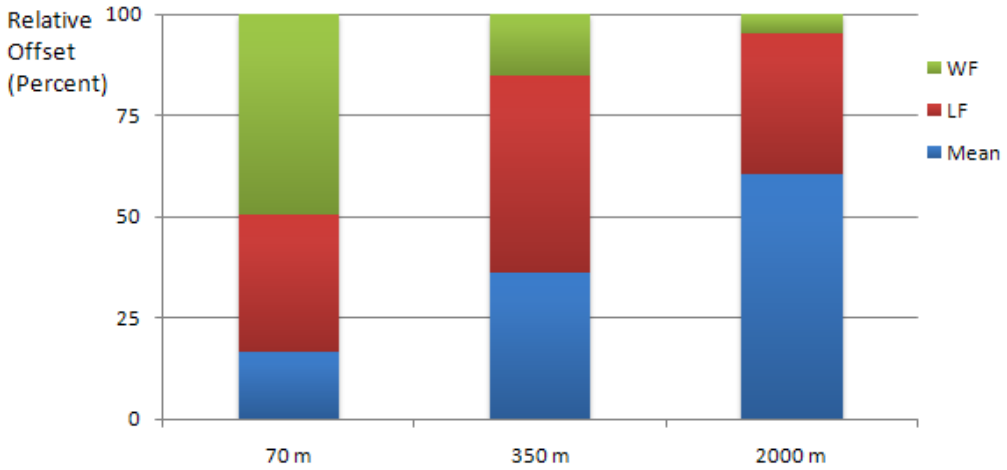

Figure 1.2 Typical characteristics of motion response for a catenary moored ship at different depths
(Ormberg and Larsen, 1998)

In fully coupled time-domain analysis, the dynamic motions of the moored FPSO are simulated together at every time step, which is prohibitively time consuming, and may be quite unnecessary, particularly for tanker-shaped FPSOs. Here the vessel's motions are calculated with the impulsive response function for the fully coupled analysis (proper fully coupled analysis need to obtain the vessel motion by Rankin source method in time domain). Under the assumption that FPSO's wave frequency motion/loading is unaffected by the mooring/riser due to its much greater mass, the fully coupled analysis can be simplified to some extent, e.g. mooring/riser dynamically coupled to the FPSO low frequency motion. However, such an approach, when simulated in time domain, will still be very expensive as the mooring/riser dynamic response needs to be computed at every time step, and moreover the time step has to be very small for the mooring/riser. Typically, it may take several hours to

complete a 3-hour sea sate time-domain simulation on the computer and mooring design will involve a large number of cases when taking into account of the combination of environmental parameters (e.g. wind, wave, current) and combination of direction of environmental parameters. So it is significant to develop a fast method for dynamic analysis of FPSO/mooring/riser.

For the FPSO/mooring/riser system, one of the key coupling mechanisms between the floater and the mooring/riser, which remains to be a challenging topic, is the damping effects of the latter and its impact on FPSO's low-frequency motion and its associated maximum mooring line tension and the maximum offset which is important for riser design. On this critical issue of the mooring design, the current industry practice is still largely empirical. A linear damping coefficient is often used to represent the effects, and the low-frequency vessel motion is then simulated on the horizontal water surface in extreme sea states. Maximum line tensions are calculated by including the FPSO's wave-frequency response in the extreme sea states. The input value of the damping needs to be calibrated against model test results. In the absence of model test results, it relies upon experience to select an appropriate damping level. The dynamically coupled analysis is also used in the industry, but it suffers from the aforementioned computational cost. It should be noted that other damping mechanisms also need to be considered, e.g. hull friction, wave drift damping, but typically these do not require extensive computation.

Hydrodynamic loads on mooring lines are usually calculated using Morrison's equation. Changes in hydrodynamic drag coefficients alter the level of line damping. There have been studies showing that the line hydrodynamic coefficients are important to the damping and the ensuing maximum line tension (Brown and Mavrakos, 1999). Given that, it is rather surprising that, for example, BS EN ISO 19901-7:2005 does not stipulate the values of hydrodynamic coefficients for mooring line analysis. Instead, it suggests that one should consult with relevant RCS (reorganised

classification society) rules. Similarly, API RP 2SK (2005) does not provide any guidance either. DNV-OS-E301 (2010) does give provide some information but it is extremely brief. In comparison, DNV-RP-F205 (2010) is an improvement of this rather unsatisfactory situation. It is however apparent that this is far from sufficient either, partly because of the wide range of coefficient values, and partly because the values were obtained mainly from towing tests, i.e. in steady flow conditions. It is also noted that these recommended values differ from the "normal values" used by some mooring line design houses. They are also different from the figures used in some technical publications.

Predicting the extreme response of the mooring line is one of the key problems for the mooring system design and selecting proper diameter and grade of mooring line. API RP 2SK (2005) recommend that the mooring systems should be designed to withstand the extreme load caused by the maximum design condition which is combination of wind, wave and current. However, we also should pay more attention to large ship-shaped FPSOs, which are dominated by low frequency motions. The maximum design condition, i.e. 100-year waves, may not yield most severe mooring loads since low frequency motions increase with decreasing wave periods. Lower waves with shorter periods could yield larger low frequency motions and thus higher mooring loads (API RP 2SK, 2005).

1.2 Literature Review

1.2.1 Mooring Line Damping

The slow oscillatory drift motions at resonant frequencies, which excited by second order wave forces, are a characteristic feature of moored floating structure. The resonant slow drift motion is normally much larger than the first order motions occurring at wave frequencies. They are correspondingly important to the maximum

offsets of the floating structure and the maximum tension in the mooring lines, riser design requirements, etc.

The slow drift motion amplitude of moored structure is controlled primarily by the level of damping. Thus, it is essential to accurately estimate the damping for reliable prediction of slow LF motion and tension. The contributions to the damping arise mainly from drag and friction on the vessel, wave drift damping and mooring line damping (hydrodynamic drag force). The first two terms have been treated by many researchers theoretically as well as experimentally. Early studies often assumed that the damping effects from the mooring system can be neglected and only consider the effect of stiffness when predicting the surge and sway motions of moored structures. However, Huse's work indicated that the effect of mooring line damping should be taken into account (Huse, 1986; Huse and Matsumoto, 1989). It can lead to obvious reduction in surge amplitudes, which will have a very significant effect on maximum tensions in the mooring lines and riser system performance. They found out the mooring line damping contribution to LF surge damping can provide over 80% of total damping, as shown in

Table 1.2. They also indicated that superimposing the wave frequency motions of the moored structure with the low frequency motion led to a dramatic increase in the low frequency surge damping. Matsumoto (1991) attempted to quantify the level of mooring line damping relative to other contributions. Results as given in Figure 1.3 show that the dominant effect is caused by mooring line damping, particularly for sea conditions corresponding to intermediate and high significant wave heights.

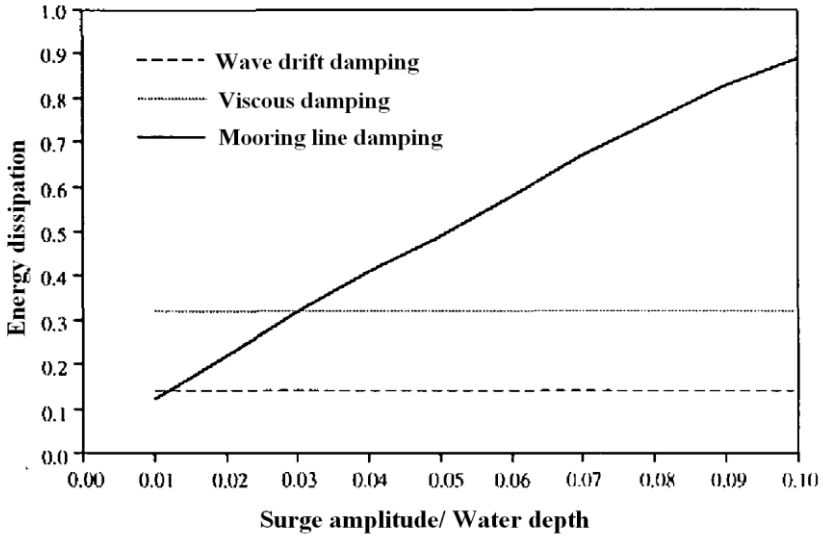

Figure 1.3 Relative energy dissipation caused by surge damping contributions (Matsumoto, 1991)

Table 1.2 Relative importance of different surge damping contributions (Huse and Matsumoto, 1989)

Hs (m)	Tp (s)	Damping contribution %		
		Mooring	Wave Drift	Viscous
8.64	12.7	81	15	4
16.29	16.9	84	22	4

Generally, the mooring line damping includes hydrodynamic drag damping, damping caused by seabed interaction, line structural damping. It is usually considered that the dominating line damping component is caused by hydrodynamic drag force (In this work, the mooring line damping only considers the hydrodynamic drag damping), which depends on the water depth, line pretension, weight and azimuth angle and the top end motions etc. Webster (1995) performed a comprehensive parametric study about the influence of line pretension, oscillation amplitude and frequency, scope, stiffness, drag coefficient and current on the line damping. Brown and Mavrakos (1999) summarized a comparative study to evaluate the level of uncertainty in

predicting the mooring line damping, where analytical results were provided by 15 contributions based on time or frequency domain methods. The influences of variations in line oscillation amplitude and frequency on line damping were discussed.

Huse and Matsumoto (1988) and Huse (1991) presented a model and an improved model to evaluate the mooring line damping, which was based on estimates of energy dissipation from drag on the mooring line due to an imposed motion at the top of the line. Liu and Bergdahl (1998) also have proposed an improvement to this method. They concluded that the quasi-static models of energy dissipation have compared favorably with results obtained using nonlinear time domain simulation of the mooring line response to imposed motion. These methods appear to be an easy way to estimate mooring line damping, but the fairlead motion as input should be provided in advance. An iterative process is really required because the vessel motion and the mooring damping are coupled. These methods may have limitations for practical application. Fan (2017) proposed an improved quasi-static model for predicting mooring line damping for designing truncated mooring system.

1.2.2 Integrated Dynamic Analysis of Moored Floating Structure

A deep water floating system is an integrated dynamic system of a floater, moorings and risers responding to wind, wave and current loadings in a complex way. The floater motions may contain the following components: mean response due to steady current, mean wave drift and mean wind load; wave frequency response due to first order wave force; low frequency response due to wave drift, wind and viscous force; high frequency response (TLP). These response components will consequently be present in the mooring line and riser response. Due to the importance of the effect of mooring line damping, coupled analysis should be performed for moored floating

structure to obtain a more accurate estimate of the LF motion and improved estimate of the tension in mooring lines. This method yields dynamic equilibrium between the force acting on the floater and mooring line response at each time step, which automatically includes the damping contribution from mooring lines. A number of coupled analyses for floating structure have been introduced (Garrett, 2005; Kim et al., 2005; Low and Langley, 2006; Ran et al., 1999; Tahar and Kim, 2003).

For the coupled analysis of a moored floating structure, the dynamic analysis of lines and the wave frequency analysis need a small time step. In addition, enough length of simulation should be performed (often 3 hours) to get the adequate statistical representation of dynamic response. These will lead to excessively high computational costs for the application of coupled analysis. Several strategies have been proposed to achieve computational efficiency.

1) Linear damping coefficient method

These strategies have in common that the floater motion and mooring line analyses are carried out separately. The floater motions are evaluated firstly and the damping contribution from mooring lines are taken into account by a prior estimation of damping coefficient. The damping can be estimated by various methods:

Ormberg and Larsen (1998) developed an improved method, i.e. “State-of-the-Art” method (SoA), to evaluate the motions of floating structures using a linear mooring line damping coefficient. The linear damping coefficient was estimated based on fitting a polynomial to the energy dissipation from mooring lines and risers. The mooring lines, which using a finite element model, are subjected to the prescribed top end motions including irregular wave frequency floater motions and sinusoidal low frequency floater motions corresponding to several low frequency oscillations.

The low frequency motion amplitude applied is equal to twice the standard deviation of the actual low frequency motion that estimated by a frequency domain method. Then, the damping coefficients are used in an uncoupled time domain motion analysis of the floater, leading to the floater motions. The current forces on the lines, as calculated by static analysis, are added to the forces on the floater. The responses of lines are estimated by applying the floater motions to the top end of the mooring lines. Since the floater motion and the mooring damping are coupled, an iterative process is really required for estimating the damping. Garrett et al. (2002) concluded that SoA method would produce as much as 30% too large a motion, for the example of a West Africa FPSO, even though the input was the best possible.

Ormberg et al. (1998) proposed a method similar to the SoA method where the linear damping estimated by short coupled analysis (20-25 LF motion cycles) with lines by coarse meshing. Then the floater motions including wave and low frequency motions are applied to top end of refined mooring lines to obtain the mooring line response. Alternatively, the low frequency motions may be accounted for by an additional static offset. They also proposed another method to perform the coupled analysis of moored structure where the lines using coarse mesh.

This coarse mesh for lines would be adequate to represent the global nonlinear behavior of the lines and their interaction with the vessel in terms of stiffness, damping and mass, but maybe not sufficiently refined for a localized assessment of the structural behavior. Furthermore, long simulation times are still needed for the adequate statistical representation of the response of floater and mooring lines.

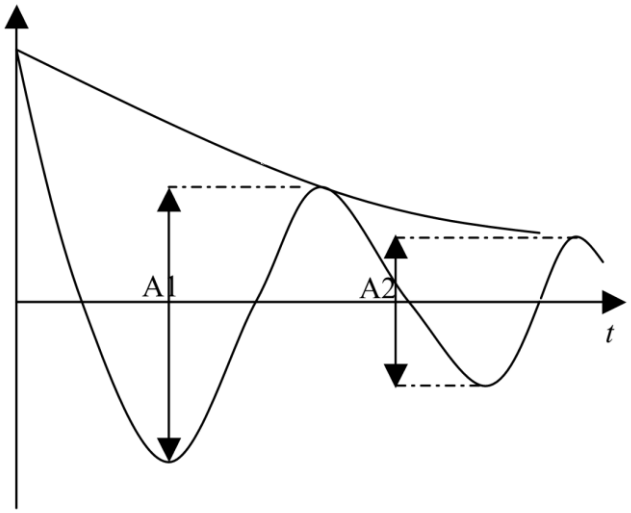

Figure 1.4 Numerical decay test

Connaire et al. (1999) and Correa et al. (2002) introduced a numerical decay test method to estimate the damping coefficient, where the moored floater is given an initial displacement and then released to oscillate freely. The decay test can be performed using the coupled model of floater and lines to obtain the damping estimate for the whole system. Then floater damping should be turned off in the uncoupled motion analysis to prevent superimposing the damping effects. It is not the best approach, since it introduces unnecessary simplifications in the floater damping. Another method is to perform a second set of decay tests with an uncoupled model of the floater. The difference between the first and the second set of tests gives the damping coefficients of the mooring and riser system. The direct approach however is to perform the decay test with the finite element model of mooring lines only. The estimation of the damping coefficient for a given motion component assumes that the decay is expressed as logarithmic decrement $e^{-\xi\omega t}$ as given in Figure 1.4, where ξ is the damping ratio, ω is the frequency of the response, and t is the elapsed time. A_i is the motion amplitude of i-th oscillation.

This method disregards the line damping behavior dependent on the initial

displacement due to changes in line geometry. They suggested estimating a series of damping coefficients by performing the decay test over a range of static positions. Given that the wave frequency motions and the environment excitation (wave height, period, current etc.) have influence on the line damping, this method still has some limitations to accurately estimate the damping.

2) Frequency domain method

Another method for dynamic analysis is in frequency domain，which is based on linear system assumptions. The nonlinear terms in the dynamic analysis should be linearized. Efficiency is the significant advantage of this method. Some researchers have performed the coupled analysis in frequency domain (Garrett, 2005; Lang et al., 2005; Le Cunff et al., 2008; Low and Langley, 2006; Ran et al., 1999).

Ran et al. (1999) compared the coupled frequency domain analysis with the coupled time domain analysis for a moored Spar. The first order wave forces, added mass and radiation damping, and the second order mean and difference frequency forces were computed for the time-domain or frequency-domain analysis. The two-term Volterra series model was adopted for the generation of the time series or spectra of first and second order wave loads for irregular waves. The mean position was first estimated based on the static loads, such as current and second order mean drift force. Then the dynamic analysis was performed with respect to the mean position. The nonlinear drag forces of lines were stochastically linearized by an iterative procedure. The results show that the time domain results generally give greater low frequency amplitudes than the frequency domain results, which implies that the viscous damping is likely to be overestimated by stochastic linearization.

Garrett (2005) performed the coupled analysis of a moored semi-submersible in the

frequency domain. The stiffness coefficient was calculated at the mean position and the hydrodynamic drag forces were linearized by a stochastic linearization method. An under-relaxation was employed to ensure convergence of the linearization. The results demonstrated an excellent match of the low frequency motions with time domain results. Garrett also found that the frequency domain and time domain results do not match as well for all cases, e.g. for the 100 year hurricane load case. The limitation of the frequency domain methods is a result of neglecting the nonlinear effects.

Low and Langley (2006) carried out the frequency domain coupled analyses for moored FPSO. The first and second order wave force transfer functions were calculated by diffraction analysis. The second order force spectrum was estimated from the cross-spectra matrix of the second order force. The frequency dependent added mass and radiation damping matrices of the vessel were obtained from a radiation analysis. The lines were modeled using a lumped mass method. Two nonlinear terms, geometric nonlinearity arising from large deflections of the lines and the nonlinear drag forces, were linearized. They concluded that that the frequency domain approach is likely to be robust and accurate when geometric nonlinearity is not prevalent. The nonlinear drag force was computed independently in two orthogonal directions which are each perpendicular to the line and linearized by formula for a one-dimensional drag force in a random sea with current. However, this approach is not strictly frame invariant (Hamilton, 1980).

1.2.3 Dynamics Analysis of Mooring Line

1) Lumped mass method

The mooring line is discretized into a number of point masses (nodes) that are joined

together by massless elements of finite lengths. All the forces are concentrated at the nodes. The governing equations, which lead to a set of ordinary differential equations, can be derived directly according to Newton's law of motion. The lumped mass method has the following advantages:

- Straightforwardness - The modelling and mathematical formulation has clear physical interpretation.
- Economy - The moderate amount of computation time.
- Versatility - A simple method can solve many different types of problems, including those of nonlinearity, unsteady state, non-uniform cable and oscillatory current.

Walton and Polachek (1960) were the first authors to apply this method to the dynamic analysis of a mooring line. The model was available for two dimensional and large displacements. The forces acting on the nodes were the drag force, inertia force, weight and buoyancy. The material elasticity was neglected. The finite difference method was used to solve the motion equations. Nakajima et al. (1982) modified this method for two-dimensional dynamic analysis of multi-component mooring lines under the excitation caused by the motion of platform. The elastic deformation of the mooring line was considered in his model. The time histories of dynamic tension calculated by this method have excellent agreement with the experimental results.

Huang (1994) extended this method to three-dimensional dynamic analyses of marine cables. The finite difference method was employed and the stability of the numerical scheme was discussed. Huang and Vassalos (1993) also applied the lumped mass method for predicting the snap loading of marine cables. A bi-linear axial stiffness was used for the calculation of operations in alternating taut-slack conditions. The results were validated and had a good agreement with the model

tests.

2) Finite element method

The finite element method (FEM) has been very popular for structure dynamic analysis. It divides the continuous structure into a number of elements that are connected by nodes. The forces are distributed along the element. Each element employs an interpolation function or shape function to describe the behavior of a given variable internal to the element in terms of the displacements of the nodes. For the nodal values of forces and displacements, it is intended to preserve the energy balance of stored and expended energy between the finite element model and the continuum model. This balance yields a set of coupled differential equations.

The finite element method for the dynamic analysis of mooring lines has been presented by many researchers. Garrett (1982) developed the three-dimensional finite element model of an inextensible elastic rod with equal principal stiffness for dynamic analysis of mooring lines. The rod is linearly elastic and torque free. This method permits large deflections and finite rotations. It also can consider the tension variation along the length. The governing equations, which are partial differential equations, are reduced to a system of ordinary differential equations by the Galerkin method. Mavrakos et al. (1996) studied the dynamics of mooring lines with attached submerged buoys using the FEM model based on rod theory in time and frequency domains. They presented that numerical predictions correlated very well with the experimental results.

Numerical efficiency and simplicity are the main advantages of the lumped mass method. The FEM requires higher computational cost. FEM is probably a closer approximation to the continuum than the lumped mass method. It is not easy to

establish which one is better. According to the study of Chen (2001), the lumped mass method and FEM both can evaluate well the dynamic response of mooring lines and agree well with experimental data.

1.2.4 Drag coefficient of Mooring Line Chain

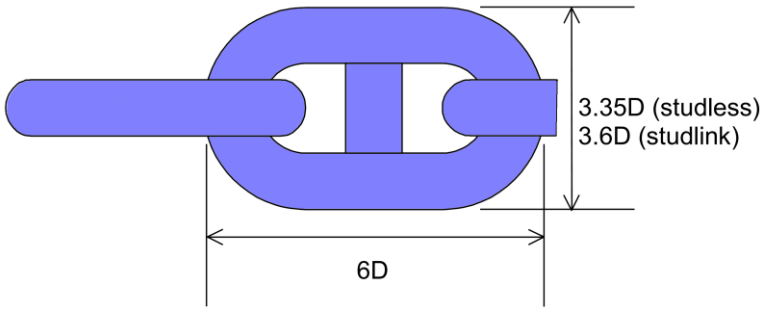

Figure 1.5 Geometry of chain (D is bar diameter of chain)

For a specified body shape, the drag coefficients depend on the following parameters: Reynolds number Re, Keulegan-Carpenter number KC and roughness number Δ. The drag coefficient is generally a function of these parameters. Mooring lines for deep water floating structures generally comprise different components, such as studless or studlink chain, unsheathed or sheathed wire or polyester rope. For the chain, its shape is complex, as shown in Figure 1.5.

1) Experiment of chain drag coefficient

Numerous investigations of hydrodynamic forces acting on slender bodies have been conducted. A limited number of model tests have been performed for evaluation of drag coefficient of chain. Occasionally, the manufacturers provide the drag coefficients for their own chain obtained from simple towing tests. Hwang (1986) performed the towing tests to estimate the drag coefficients of chain for steady state

flow conditions. He proposed the function of drag coefficient as Reynolds number as given in Figure 1.6. Figure 1.7 presents the drag coefficient from towing tests by Marintek (FPS2000, 1992). The drag coefficients of chains are normally defined with respect to their nominal diameters. These results only consider the effect of Reynolds number.

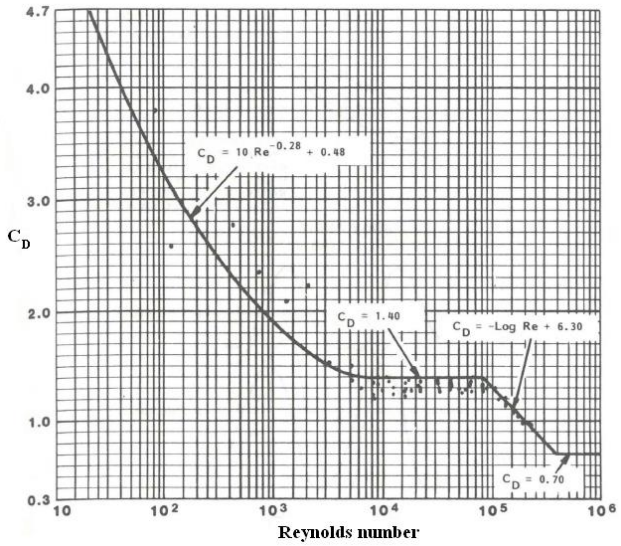

Figure 1.6 The function of drag coefficient as Reynolds number (Hwang, 1986)

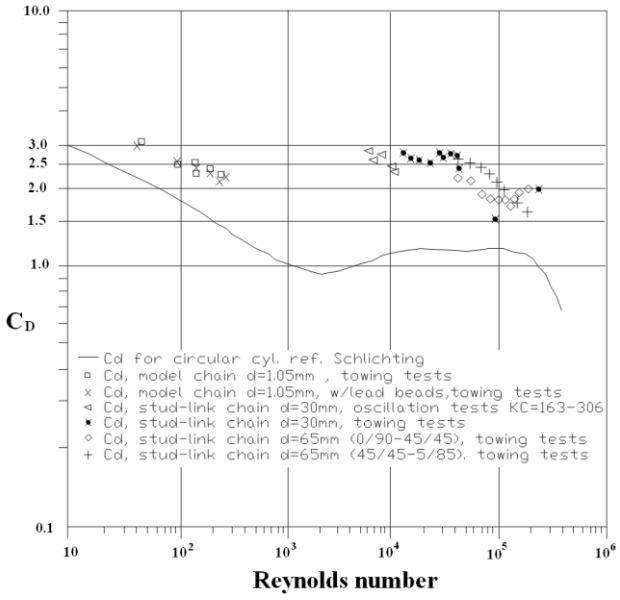

Figure 1.7 Drag coefficient of chain (FPS2000, 1992)

Lyons et al. (1997) performed drag coefficient tests with bi-harmonic oscillations in

order to consider the interaction between the low frequency and wave frequency flows. The large scale model test was employed to ensure that the Reynolds number flow regime was as close as possible to that encountered at full scale. A chain line segment was tested at various amplitudes and frequencies. The drag coefficients of chain, on which superimposed wave frequency motion was applied, would increase compared to the drag coefficients under low frequency oscillations only. But the drag coefficient has some reduction with higher WF amplitude. In particular, the drag coefficient for lines oscillated at wave frequencies in the transverse direction of mooring line can be up to 30% higher than those for in-line harmonic oscillation.

As computational fluid dynamics (CFD) has become more popular, some researchers have attempted to determine the drag coefficients of mooring line using this method. Xu and Huang (2014) evaluated the drag coefficients of a fixed studless chain under steady flows using the large eddy simulation (LES) model. They found that the drag coefficients for different, normal to the chain axis, flow directions are similar. The drag coefficients are 2.42, 2.36 and 2.41 under the 0, 45 and 90 degree flow at the Reynolds number of 6×10^4, respectively. The effect of the predicted Reynolds number was also discussed. As shown in Figure 1.8, the drag coefficients decrease with the increase of the Reynolds numbers. The range of the estimated values is in quite good agreement with DNV recommended range. The effect of Reynolds number on the drag coefficient of the smooth chain is not as important as for a smooth circular cylinder.

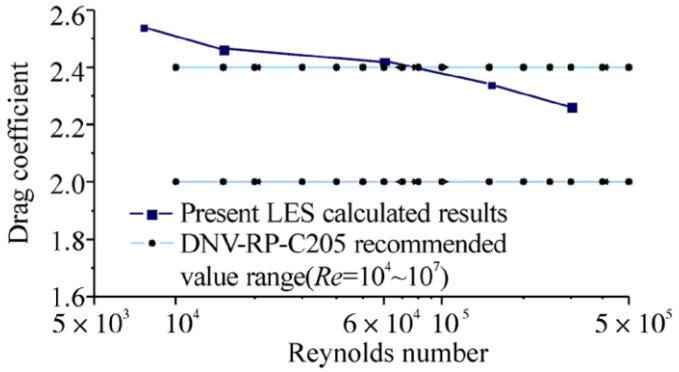

Figure 1.8 Predicted drag coefficient of stud-less chain as function of Reynolds number (Xu and Huang, 2014)

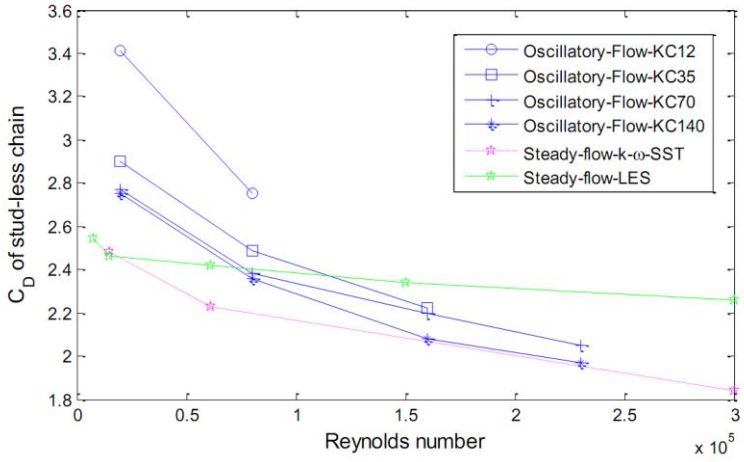

Figure 1.9 Drag coefficients of stud-less chain under different Re and KC numbers (Xu, 2014)

Xu (2014) evaluated the effect of KC on the drag coefficients of the chain, as given in Figure 1.9, by simulating a smooth chain segment oscillating in water using unsteady Reynolds-Averaged Navier-Stokes URANS model. The results show that the effect of KC number on drag coefficient is significant for the flows with lower Reynolds number.

2) Effect of drag coefficient

Ideally, the chain drag coefficient of dependence on Re, KC and roughness number should be implemented by choosing coefficients from tables and curves during the coupled analysis. However, present state of the art within coupled analyses usually does not make use of this option. It is difficult to come up with simple recommendations for which drag coefficients to use and (DNV-RP-F205, 2010) recommends a range of drag coefficients (relative to chain diameter) as listed in Table 1.3.

Table 1.3 Typical two-dimensional drag coefficients, C_D for Re = 10^4 - 10^7.

Type	C_D Range
Stud chain	2.2 - 2.6
Studless chain	2.0 - 2.4

The variation of drag coefficient will alter the level of damping, which is important to the vessel low frequency motion and the associated line tension. Some researchers have studied the importance of damping effect on motions of floaters by changing the drag coefficients of moorings. Wichers and Devlin (2001) concluded that the effect of variations on motions of floaters and line tension are significant for the loop-current condition. The damping of moorings could be very important in reducing amplitudes of LF motions. The existing conclusions on the effects of the hydrodynamic coefficients on damping and line tension have typically been derived from and quantified by analyses in simplified environmental conditions, e.g. prescribed motion of the fairlead, regular waves or extreme sea-states with given vessel mean positions (Brown and Mavrakos, 1999). However, these conclusions should be treated with caution. For example, an increase in the line drag coefficient will increase the mean offset as well as typically the dynamic tension, but reduce low frequency dynamic offset. The net impact on LF motions and the maximum line tension may not be obvious. This will depend on the contributions of these two

components (Luo and Baudic, 2003).

1.2.5 Extreme Response Estimation

One of the important aspects for offshore structure design is to accurately predict the extreme responses in a random environment. The maximum vessel excursions and mooring line/riser tensions are of interest for floating production systems. One of the following approaches is usually employed to evaluate the extreme response of offshore structure (Larsen and Olufsen, 1992):

- Design wave method.
- The short term stochastic method.
- The long term stochastic method.

1) Design wave method

This method is often used for linear system, e.g. fixed offshore platform, with the analysis based on a deterministic wave description (Barltrop and Adams, 1991). The wave height and period are determined according to the wave statistics. The response estimation by this method is simple due to the character of the load that periodic load produces periodic response at the same frequency. This method could be used to obtain structural action effects in certain circumstances (NORSOK N-003, 2007). It has been common practice to carry out the design check for a so-called 100-year wave, which means a wave with wave height H_{100} being exceeded on the average only once every 100 year or being exceeded with a probability of 10^{-2} during one year. This method will become questionable for nonlinear system and it would not be applicable to the moored floater motion analysis (Lim, 2018).

2) The short term stochastic method

API RP 2SK (2005) recommend that the mooring system analyses should be performed for combination of wave, current and wind conditions causing the extreme load, which is noted as the maximum design condition. Different combinations of wave, current and wind yielding the same return period for the combined environmental condition are typically applied. The stochastic wave is descripted in one specific sea state defined by its wave spectrum. The extreme responses are then identified as the expected or most probable maximum response for a specific duration (e.g. 3 hours) of this environmental condition. The main challenge is to select an adequate probabilistic distribution model for the peaks of response process. For the linear system, the peak of response process, which is a Gaussian process, follows a Rayleigh distribution. For a nonlinear system such as a moored floating structure, the peaks of the non-Gaussian response process can be modelled by a Weibull distribution. The extreme value distribution will approach a Gumbel distribution for increasing number of peaks (DNV-OS-E301, 2010). Another approach to evaluate the statistical distribution of extreme response based on time-series is by use of the upcrossing rates (Naess et al., 2013; Naess and Gaidai, 2008). The upcrossing events are assumed to be independent that is, the so-called Poisson assumption is adopted. They proposed a more robust technique for extreme response prediction by fitting the tail of the crossing rates to a natural exponential function.

For the coupled analysis of moored floating structure in frequency domain, the extreme response may be evaluated by empirical combination or upcrossing rates. For the former method, extreme responses are predicted from a combination of wave frequency and low frequency components of vessel motions and line tensions statistics. Turkstra's rule has been implemented in API RP 2SK (2005). Liu and Bergdahl (1999) compared different combination formulae and suggested a formula

considering WF and LF correlation effects where the correlation factor estimated from the cross-correlation information between the LF process and the WF envelope process. Grime and Langley (2003) compared various methods for prediction of crossing rates and estimated the extremes from the derived statistics of combined WF and LF motions using narrow band random vibration theory. The upcrossing rates were computed using the Rice formula that needs the joint probability density function for the displacement and velocity of combined WF and LF motion.

The design wave method and short term method are based on the environmental statistics. The shortcoming of them is basically that the largest response is assumed to be a result of the largest load. This may not be the case for dynamically responding systems such as moored floating structure (Farnes and Moan, 1993, Lim, 2018). The true return period or long term probability of the estimated extreme response remains unknown and this will in general lead to an inconsistent safety level.

3) The long term stochastic method

The most consistent way for estimating the extreme response is to establish a probabilistic description of the response from the long term environmental action. The most obvious and direct approach to evaluate the long term statistics of response is to work through all the sea states. The dynamic analysis is performed for each interval. Probability distributions are generated for the short term variability and the long term variability in the severity of sea states. Convolution of the two produces a probability distribution for the long term for the extreme response of interest. Baar et al. (2000) performed the long term response analysis of turret moored tankers in the deep water Gulf of Mexico based on the hurricane hindcast database. The short term distribution for each sea state was generated, where the motion responses calculated

in frequency domain were fitted to a Rayleigh distribution and line tension was fitted to an exponential distribution.

An alternative method for estimating the long term extreme response is the random storms method which was proposed by Jahns and Wheeler (1972), Haring and Heideman (1978) and Tromans (1995). In their approach, the focus is on storm events which considered as independent, similar to the peaks-over-threshold analysis. The hindcast time series of environmental variables is broken into storms by identifying the sea states whose significant wave height is higher than a threshold. Each storm consists of several steps that duration of each step is 3 hours. The dynamic analysis is performed to calculate statistics of extreme response for each step. It is assumed that the distribution of the storm extreme response value can be approximated by a Gumbel extreme value distribution conditional on the most probable extreme response for that storm. The distribution of the most probable extreme value itself is assumed to follow a generalized Pareto distribution. These are combined to produce a probability distribution of the extreme response for each storm. Then these probability distributions for each storm can be combined to produce a complete probability distribution for long term response. Leong (2018) proposed a subset simulation for long term extreme response prediction which dividing burdensome low probability problems into simpler ones of intermediate conditional probabilities.

The all sea states method is inefficient due to it involving the response analysis for a large number of sea states. The random storm method doesn’t need the joint statistics of the environmental variables and environmental variables can be included without additional difficulty. It reduced the number of sea states by selecting a proper threshold. However, it still requires the analysis of a lot of sea states that may be too time consuming to apply to the complex analysis such as moored floating structure.

1.3 The Issues

The integrity of mooring system is of importance for the safety operation of FPSO. The mooring line should have enough strength to withstand the extreme loads. It will be conservative using uncoupled dynamic analysis method to predict the extreme loads of mooring line system due to the effect of mooring lines/risers damping. Coupled analysis considering the damping effect of mooring lines/risers is necessary for precise evaluation of the FPSO/mooring line extreme response. The chain drag coefficient is not easily determined due to the influence of several factors such as Reynolds number, Keulegan-Carpenter number and roughness number. The variation of drag coefficient will alter the level of mooring line damping. As discussed above, this work will attempt to address the following issues.

1) An efficient approach for coupled analysis of moored FPSO

   The coupled dynamic analysis is time consuming. It requires a more computationally efficient method, other than the fully coupled time domain analysis, for analyzing moored tanker-shaped FPSOs that is capable of including automatically the damping effects of mooring/riser.

2) Prediction of the extreme response by probabilistic method

   The traditional design approach based upon extreme load case analysis may not necessarily produce safe designs in deep water. Probabilistic design provides a more rational basis. However, it is understood that a probabilistic analysis approach is much more computationally expensive. For example, to perform a response based analysis of the mooring line tension, its long term probability distributions of extreme responses are required. A large number of sea states, in

the order of hundreds/thousands, need to be analyzed. To this end, we again need an efficient, as well as accurate, analysis method.

3) The effect of uncertainty of drag coefficient on extreme response

Since the low frequency drift motion of the vessel is at or close to the resonant frequency of the mooring system, the low frequency drift motion amplitude and corresponding line tension is controlled primarily by the level of damping. Thus, accurate estimation of damping is essential for accurate motion prediction. This in turn relies on appropriate selection of the drag coefficient. The estimation of drag coefficient involves several factors, the effects of which are difficult to evaluate. There are no specific rules for selecting these coefficients. Therefore, it is worthwhile to study the effect of hydrodynamic coefficients on extreme response of FPSO/mooring line by a probabilistic analysis approach.

1.4 Objectives

Based on the issues discussed above, the main objectives of this work can be summarized as follows.

1) To develop a computationally efficient method for predicting the response of FPSO and mooring lines. It should take the damping contributions from the mooring lines into account.

2) To propose an improved method for the extreme response. It should be based on a probabilistic approach.

3) To ascertain the effects of the hydrodynamic coefficients on the damping contribution to the low frequency FPSO motion and the maximum mooring line tension based upon a probabilistic approach.

1.5 Outline of The Thesis

The thesis is organized in 3 main parts and each part is introduced as follows.

1) Hybrid time and frequency domain analysis method: In order to establish probability distributions of the extremes, fast and repeated simulations are required for different environmental conditions. The low frequency motion of the FPSO will be computed in the time domain, whilst the wave frequency response of the FPSO/mooring/riser at a given mean offset position will be conducted in the frequency domain. Relatively large time steps can be used for the time domain simulation. The frequency domain analysis will be based upon a specific linearization approach where the damping to the low frequency FPSO motion from the wave frequency response of the mooring/riser will be accounted for in the form of an increased mean tension. Comparison of the tension/motion results with a dynamically coupled time-domain analysis will be made, and the computational efficiency of the proposed approach demonstrated.

2) Probability distribution of extremes: The methodologies for the long term extreme analysis are validated. The all sea state method for the long term extreme analysis is performed by use of a Kriging metamodel. The Monte Carlo simulation is applied for the long term probability integral based on the Kriging metamodel. The improved method based on the environmental contour method and accurate distribution tail extrapolation method is proposed. The contour line method assumes that the short term variability could be accounted for separately, i.e. decoupling the environmental problem and the response problem. This method evaluates the extreme response based on limited sea states along a well-defined environmental contour line with a given return period. Then the short term variability is considered by selecting a high fractile. The distribution of the response is evaluated by the average conditional exceedance rates (ACER)

method (Naess et al., 2007; Naess and Gaidai, 2008). The ACER method, which can accurately capture the effect of statistical dependence for the extreme value prediction problem, is less restrictive and more flexible than the one based on asymptotic theory.

3) Effect of hydrodynamic drag coefficient on long term extreme response. The reliability analyses for the extreme response considering the uncertainty influence of drag coefficient are performed by a perturbation method and asymptotic approximation method. The perturbation method is based on a Taylor expansion. The 2^{nd}-order and 4^{th}-order expansion have been derived. The asymptotic approximation is a method based on the Laplace's method for asymptotic approximation of the probability integral. The asymptotic evaluation is based on the assertion that the greatest contribution to an integral derives from the locations where the integrand is a maximum point. The conditional long term distributions of responses are estimated by the contour line and ACER methods.

The flowchart of the research strategy of the thesis is illustrated in Figure 1.10.

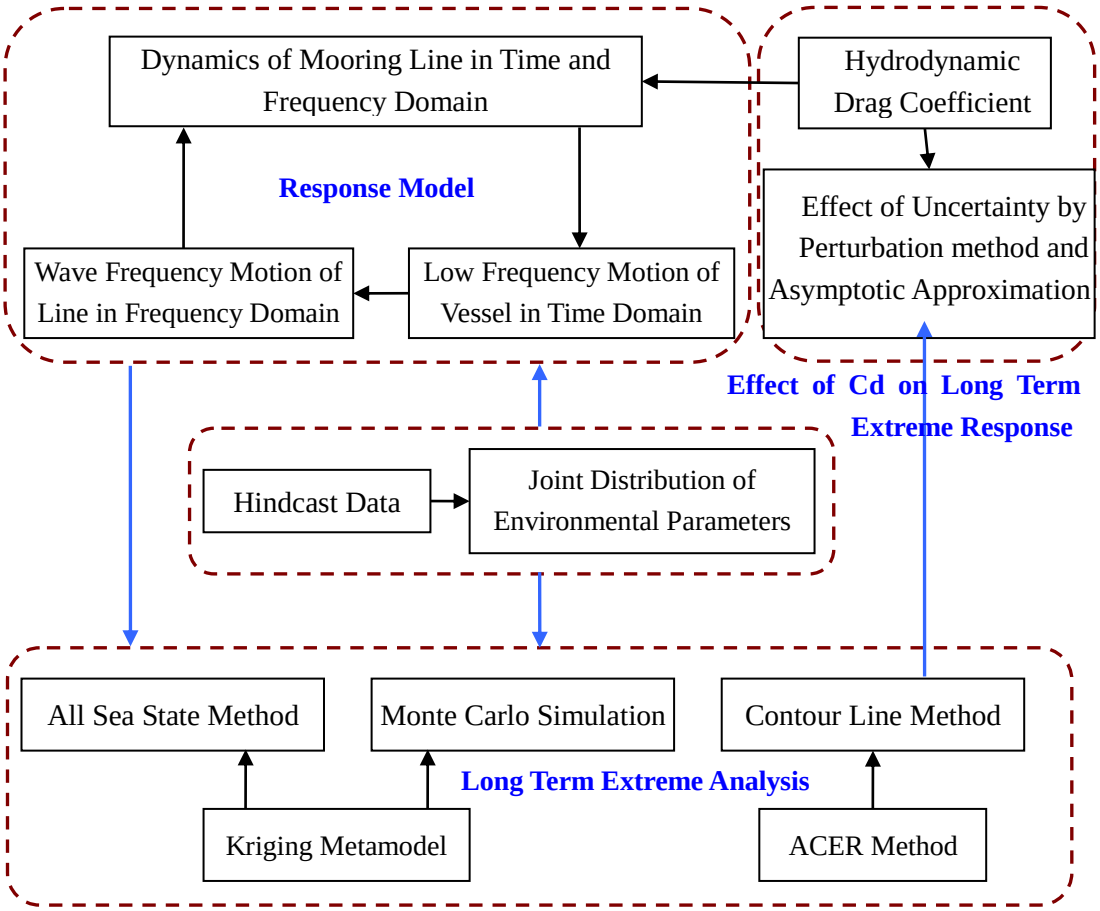

Figure 1.10 Research strategy of the thesis

2 Dynamic Analysis of Mooring Line

2.1 Introduction

In order to predict extreme responses such as line tensions, anchor loads, and vessel offsets under the design environment a mooring analysis is performed. The responses are then checked against allowable values to ensure adequate strength of the system against overloading and sufficient clearance to avoid interference with other structures. The quasi-static analysis method is usually used for mooring line design in shallow water. In deep water application, this method is not accurate and dynamic analysis should be performed. Dynamic analysis accounts for the time varying effects due to mass, damping, and fluid acceleration. Two methods, frequency domain and time domain analyses, can be used for predicting dynamic mooring loads. In the time domain method, all nonlinear effects including line geometry, hydrodynamic loading, and sea bottom effects can be modeled. The frequency domain method, on the other hand, needs linearization as the linear principle of superposition is used. This chapter derives the dynamical equations of mooring lines in time domain and frequency domain respectively and develops the program for dynamic analysis of mooring lines.

2.2 Mooring Line Model and Forces

The mooring line is discretized using lumped mass method for dynamic analysis. The lumped mass method divides the mooring line into segments and it is modeled as a series of lumped mass node and massless elastic segments (as shown in Figure 2.1). There are N nodes and (N-1) segments. The lumped mass model assumes that strains are small but large deflections are allowed.

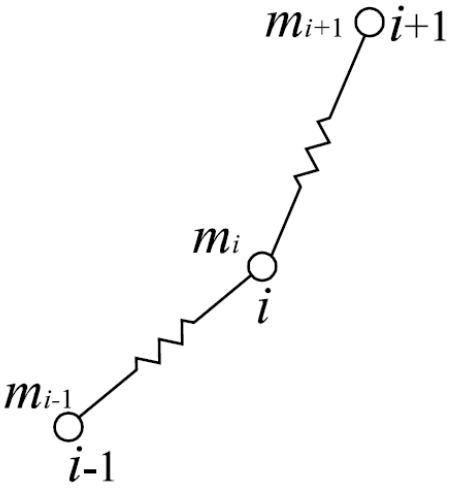

Figure 2.1 Discretized with lumped mass method

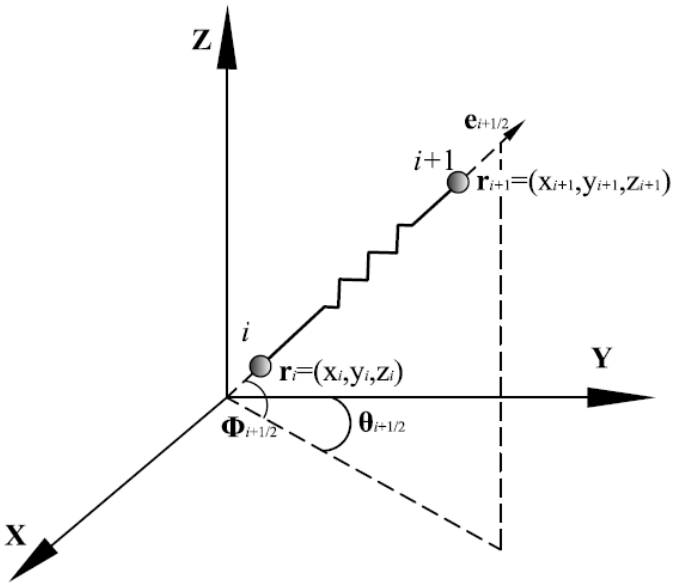

Figure 2.2 Mooring lines in global coordinate

A mooring line element in the global coordinate is shown in Figure 2.2. The *i*-th node's position is $\mathbf{r}_i = \begin{bmatrix} x_i & y_i & z_i \end{bmatrix}^{\mathrm{T}}$. $\mathbf{e}_{i+1/2}$ is the unit vector parallel to the centerline of the segment between *i*-th node and (*i*+1)-th node.

$$\mathbf{e}_{i+1/2} = (e_{x,i+1/2}, e_{y,i+1/2}, e_{z,i+1/2}) \tag{2.1}$$

where $e_{x,i+1/2} = \cos\phi_{i+1/2} \sin\theta_{i+1/2}$, $e_{y,i+1/2} = \cos\phi_{i+1/2} \cos\theta_{i+1/2}$, $e_{z,i+1/2} = \sin\phi_{i+1/2}$.

$$\cos\phi_{i+1/2} = \frac{\sqrt{(x_{i+1} - x_i)^2 + (y_{i+1} - y_i)^2}}{\tilde{l}_{i+1/2}}$$

$$\sin\phi_{i+1/2} = \frac{z_{i+1} - z_i}{\tilde{l}_{i+1/2}}$$

$$\cos\theta_{i+1/2} = \frac{y_{i+1} - y_i}{\sqrt{(x_{i+1} - x_i)^2 + (y_{i+1} - y_i)^2}}$$

$$\sin\theta_{i+1/2} = \frac{x_{i+1} - x_i}{\sqrt{(x_{i+1} - x_i)^2 + (y_{i+1} - y_i)^2}}$$

$\tilde{l}_{i+1/2}$ is the length of segment between *i*-th node and (*i*+1)-th node,

$$\tilde{l}_{i+1/2} = \sqrt{(x_{i+1} - x_i)^2 + (y_{i+1} - y_i)^2 + (z_{i+1} - z_i)^2} \tag{2.2}$$

Then we can rewrite the equation (2.1) as follows

$$\mathbf{e}_{i+1/2} = \frac{1}{\tilde{l}_{i+1/2}} (x_{i+1} - x_i, y_{i+1} - y_i, z_{i+1} - z_i) \tag{2.3}$$

All forces along the mooring lines are assumed to be concentrated at the node. The equation of motion of *i*-th node is:

$$\mathbf{M}_i \ddot{\boldsymbol{r}}_i = \mathbf{F}_i \tag{2.4}$$

where $\mathbf{M}_i$ is the mass of *i*-th node from the mass of adjacent segments and added mass, $\ddot{\boldsymbol{r}}_i = \begin{bmatrix} \ddot{x}_i & \ddot{y}_i & \ddot{z}_i \end{bmatrix}^{\mathrm{T}}$ is the acceleration of *i*-th node, $\mathbf{F}_i$ is the force concentrated at

the node including tension forces, inertia force, drag force, buoyancy and weight in the two segments.

The expression of forces is as follows.

$$\mathbf{F}_i = \mathbf{T}_i + \mathbf{F}_{Ii} + \mathbf{F}_{Di} + \mathbf{W}_i \tag{2.5}$$

where $\mathbf{T}_i, \mathbf{F}_{Ii}, \mathbf{F}_{Di}$ is the tension, inertia force and the drag force at the *i*-th node, $\mathbf{W}_i$ is other force such as gravity and buoyancy. In the following sections, these force components are detailed.

2.2.1 Tension

Tension forces at the *i*-th node including the tension forces in the lines segments on either side of the node *i* which respectively indicated as $T_{i+1/2}$ and $T_{i\text{-}1/2}$. The tension force at node *i* is as follows.

$$\mathbf{T}_i = \begin{bmatrix} T_{ix} \\ T_{iy} \\ T_{iz} \end{bmatrix} = \begin{bmatrix} T_{i+1/2}e_{x,i+1/2} - T_{i-1/2}e_{x,i-1/2} \\ T_{i+1/2}e_{y,i+1/2} - T_{i-1/2}e_{y,i-1/2} \\ T_{i+1/2}e_{z,i+1/2} - T_{i-1/2}e_{z,i-1/2} \end{bmatrix} \tag{2.6}$$

And

$$T_{i+1/2} = EA\left(\frac{\tilde{l}_{i+1/2}}{l_{i+1/2}} - 1\right) \tag{2.7}$$

$$T_{i-1/2} = EA\left(\frac{\tilde{l}_{i-1/2}}{l_{i-1/2}} - 1\right) \tag{2.8}$$

where E is the elastic modulus; A is cross-sectional area; $l_{i+1/2}$ is the original length of segment between *i*-th node and (*i*+1)-th node ; $l_{i\text{-}1/2}$ is the original length of segment between *i*-th node and (*i*-1)-th node.

Considering the equation (2.3), then the tension at *i*-th node is

$$\mathbf{T}_i = EA\begin{bmatrix} \left(\frac{x_{i+1}-x_i}{l_{i+1/2}} - \frac{x_{i+1}-x_i}{\tilde{l}_{i+1/2}}\right) - \left(\frac{x_i-x_{i-1}}{l_{i-1/2}} - \frac{x_i-x_{i-1}}{\tilde{l}_{i-1/2}}\right) \\ \left(\frac{y_{i+1}-y_i}{l_{i+1/2}} - \frac{y_{i+1}-y_i}{\tilde{l}_{i+1/2}}\right) - \left(\frac{y_i-y_{i-1}}{l_{i-1/2}} - \frac{y_i-y_{i-1}}{\tilde{l}_{i-1/2}}\right) \\ \left(\frac{z_{i+1}-z_i}{l_{i+1/2}} - \frac{z_{i+1}-z_i}{\tilde{l}_{i+1/2}}\right) - \left(\frac{z_i-z_{i-1}}{l_{i-1/2}} - \frac{z_i-z_{i-1}}{\tilde{l}_{i-1/2}}\right) \end{bmatrix} \tag{2.9}$$

The tension force in the segment between *i*-th node and (*i*+1)-th node is:

$$\mathbf{T}_{i+1/2} = EA\begin{bmatrix} \frac{x_{i+1}-x_i}{l_{i+1/2}} - \frac{x_{i+1}-x_i}{\tilde{l}_{i+1/2}} \\ \frac{y_{i+1}-y_i}{l_{i+1/2}} - \frac{y_{i+1}-y_i}{\tilde{l}_{i+1/2}} \\ \frac{z_{i+1}-z_i}{l_{i+1/2}} - \frac{z_{i+1}-z_i}{\tilde{l}_{i+1/2}} \end{bmatrix} \tag{2.10}$$

2.2.2 Inertia Force

Wave forces on the mooring line are computed using Morison equation which assumes the force to be composed of inertia and drag forces linearly added together. The wave particle velocity at node i is $\boldsymbol{u}_i = (u_{x,i}, u_{y,i}, u_{z,i})$. The normal wave particle velocity $\boldsymbol{u}^n_{i,i+1/2}$ across the half of upper segment that connecting the *i*-th node is:

$$\begin{aligned} \boldsymbol{u}^n_{i,i+1/2} &= \boldsymbol{u}_i - \left(\boldsymbol{u}_i \cdot \boldsymbol{e}_{i+1/2}\right)\boldsymbol{e}_{i+1/2} \\ &= \mathrm{N}_{i+1/2}\boldsymbol{u}_i \end{aligned} \tag{2.11}$$

$$\mathbf{N}_{i+1/2} = \begin{bmatrix} 1-e^2_{x,i+1/2} & -e_{x,i+1/2}e_{y,i+1/2} & -e_{x,i+1/2}e_{z,i+1/2} \\ -e_{y,i+1/2}e_{x,i+1/2} & 1-e^2_{y,i+1/2} & -e_{y,i+1/2}e_{z,i+1/2} \\ -e_{z,i+1/2}e_{x,i+1/2} & -e_{z,i+1/2}e_{y,i+1/2} & 1-e^2_{z,i+1/2} \end{bmatrix} \tag{2.12}$$

Similarly, the normal wave particle acceleration across the half of upper segment that connecting the *i*-th node is:

$$\dot{\boldsymbol{u}}^{n}_{i,i+1/2} = \mathrm{N}_{i+1/2}\dot{\boldsymbol{u}}_i \tag{2.13}$$

The tangential wave particle velocity $\boldsymbol{u}^{\tau}_{i,i+1/2}$ across the half of upper segment that connecting the *i*-th node is:

$$\begin{aligned}\boldsymbol{u}^{\tau}_{i,i+1/2} &= \left(\boldsymbol{u}_i \cdot \boldsymbol{e}_{i+1/2}\right)\boldsymbol{e}_{i+1/2} \\ &= \tau_{i+1/2}\boldsymbol{u}_i\end{aligned} \tag{2.14}$$

where

$$\tau_{\mathrm{i+1/2}} = \begin{bmatrix} e^2_{x,i+1/2} & e_{x,i+1/2}e_{y,i+1/2} & e_{x,i+1/2}e_{z,i+1/2} \\ e_{y,i+1/2}e_{x,i+1/2} & e^2_{y,i+1/2} & e_{y,i+1/2}e_{z,i+1/2} \\ e_{z,i+1/2}e_{x,i+1/2} & e_{z,i+1/2}e_{y,i+1/2} & e^2_{z,i+1/2} \end{bmatrix} \tag{2.15}$$

and the tangential wave particle acceleration across the half of upper segment that connecting the *i*-th node is

$$\dot{\boldsymbol{u}}^{\tau}_{i,i+1/2} = \tau_{i+1/2}\dot{\boldsymbol{u}}_i \tag{2.16}$$

The inertia or drag forces are usually computed separately for directions normal and tangent to the lines. The inertia force on the upper half segment on the side of node *i* is:

$$\begin{aligned}\mathrm{F}_{Ii,i+1/2} &= \mathrm{F}^{n}_{Ii,i+1/2} + \mathrm{F}^{\tau}_{Ii,i+1/2} \\ &= \frac{1}{4}\pi\rho D^2 C^{n}_{m}\frac{l_{i+1/2}}{2}\dot{\boldsymbol{u}}^{n}_{i,i+1/2} + \frac{1}{4}\pi\rho D^2 C^{\tau}_{m}\frac{l_{i+1/2}}{2}\dot{\boldsymbol{u}}^{\tau}_{i,i+1/2} \\ &= \frac{1}{8}\pi\rho D^2 C^{n}_{m} l_{i+1/2}\dot{\boldsymbol{u}}^{n}_{i,i+1/2} + \frac{1}{8}\pi\rho D^2 C^{\tau}_{m} l_{i+1/2}\dot{\boldsymbol{u}}^{\tau}_{i,i+1/2}\end{aligned} \tag{2.17}$$

where C^{n}_{m} and C^{τ}_{m} is normal and tangential inertia coefficient.

As the tangential component is usually small it is assumed that it can be neglected, i.e.

it is assumed that tangential inertia coefficient $C_m^t = 0$. Then the inertia forces on node *i* including two lines segments on either side of the node are:

$$\begin{aligned} \mathrm{F}_{Ii} &= \mathrm{F}_{Ii,i+1/2} + \mathrm{F}_{Ii,i-1/2} \\ &= \frac{1}{8}\pi\rho D^2 C_m^n l_{i+1/2}\dot{\boldsymbol{u}}_{i,i+1/2}^n + \frac{1}{8}\pi\rho D^2 C_m^n l_{i-1/2}\dot{\boldsymbol{u}}_{i,i-1/2}^n \\ &= \left(DI_{i+1/2}\mathrm{N}_{i+1/2} + DI_{i-1/2}\mathrm{N}_{i-1/2}\right)\dot{\boldsymbol{u}}_i \end{aligned} \tag{2.18}$$

where $DI_{i\pm1/2} = \frac{1}{8}\pi\rho D^2 C_m^n l_{i\pm1/2}$, here the normal inertia coefficient C_m^n=2.

2.2.3 Mass and Added Mass

The structural acceleration is not included in the inertia forces and it is usually accounted for by the inclusion of an added mass term of mass matrix in the equation of motion.

$$\begin{aligned} \mathrm{F}_{Ai} &= \mathrm{F}_{Ai,i+1/2} + \mathrm{F}_{Ai,i-1/2} \\ &= \left(\frac{1}{4}\pi\rho D^2 C_a^n \frac{l_{i+1/2}}{2}\dot{\boldsymbol{r}}_{i,i+1/2}^n + \frac{1}{4}\pi\rho D^2 C_a^n \frac{l_{i-1/2}}{2}\dot{\boldsymbol{r}}_{i,i-1/2}^n\right) \\ &= \left(\frac{1}{8}\pi\rho D^2 C_a^n l_{i+1/2}\mathrm{N}_{i+1/2} + \frac{1}{8}\pi\rho D^2 C_a^n l_{i-1/2}\mathrm{N}_{i-1/2}\right)\dot{\boldsymbol{r}}_i \\ &= \left(DA_{i+1/2}\mathrm{N}_{i+1/2} + DA_{i-1/2}\mathrm{N}_{i-1/2}\right)\dot{\boldsymbol{r}}_i \end{aligned} \tag{2.19}$$

where $DA_{i\pm1/2} = \frac{1}{8}\pi\rho D^2 C_a^n l_{i\pm1/2}$, The normal added mass coefficient $C_a^n = C_m^n - 1$.

The added mass on the node *i* is:

$$\mathbf{m}_{a,i} = DA_{i+1/2}\mathbf{N}_{i+1/2} + DA_{i-1/2}\mathbf{N}_{i-1/2} \tag{2.20}$$

The mass including added mass matrix is:

$$\mathbf{M}_i = \mathbf{m}_i + \mathbf{m}_{a,i} \tag{2.21}$$

where $\mathbf{m}_i$ represents the mass of two mooring line segments on each side of *i*-th node,

$$\mathbf{m}_i = \begin{bmatrix} m_i & & \\ & m_i & \\ & & m_i \end{bmatrix} \tag{2.22}$$

where $m_i = \frac{1}{2}\rho_m A(l_{i+1/2} + l_{i-1/2})$,and ρ_m is the density of mooring lines.

And the weight and buoyancy force is

$$\mathbf{W}_i = \begin{bmatrix} 0 \\ 0 \\ -m_i g + f_{Bi} \end{bmatrix} \tag{2.23}$$

where f_{Bi} is the buoyancy $f_{Bi} = \frac{1}{2}\rho A(l_{i+1/2} + l_{i-1/2})$ and ρ is the density of seawater.

2.2.4 Drag Force

Using the Morrison's equation, the drag force on the upper half segment on the side of node *i* is:

$$\begin{aligned} \mathrm{F}_{Di,i+1/2} &= \mathrm{F}^n_{Di,i+1/2} + \mathrm{F}^\tau_{Di,i+1/2} \\ &= \frac{1}{2}\rho C_D^n D \frac{l_{i+1/2}}{2} \left|\boldsymbol{V}^n_{ri,i+1/2}\right| \boldsymbol{V}^n_{ri,i+1/2} + \frac{1}{2}\rho C_D^\tau D \frac{l_{i+1/2}}{2} \left|\boldsymbol{V}^n_{ri,i+1/2}\right| \boldsymbol{V}^\tau_{ri,i+1/2} \\ &= \frac{1}{4}\rho C_D^n D l_{i+1/2} \left|\boldsymbol{V}^n_{ri,i+1/2}\right| \boldsymbol{V}^n_{ri,i+1/2} + \frac{1}{4}\rho C_D^\tau D l_{i+1/2} \left|\boldsymbol{V}^\tau_{ri,i+1/2}\right| \boldsymbol{V}^\tau_{ri,i+1/2} \end{aligned} \tag{2.24}$$

where $\boldsymbol{V}_{ri}$ is relative velocity (between the water particle velocity from wave $\boldsymbol{u}_i$ and current $\boldsymbol{V}_{ci}$ at node *i* and the velocity of node $\dot{\boldsymbol{r}}_i$):

$$\boldsymbol{V}_{ri} = \boldsymbol{u}_i - \dot{\boldsymbol{r}}_i + \boldsymbol{V}_{ci} \tag{2.25}$$

And $\boldsymbol{V}_{ri,i+1/2}^{n}$ and $\boldsymbol{V}_{ri,i+1/2}^{\tau}$ are the normal and tangential relative velocity to the upper segment connected with node *i* respectively.

$$\boldsymbol{V}_{ri,i+1/2}^{n} = \mathbf{N}_{i+1/2}\boldsymbol{V}_{ri} \tag{2.26}$$

$$\boldsymbol{V}_{ri,i+1/2}^{\tau} = \boldsymbol{\tau}_{i+1/2}\boldsymbol{V}_{ri} \tag{2.27}$$

C_D^n and C_D^τ is the normal and tangential drag coefficient.

The tangential drag is assumed to be neglected as it is usually small. The drag forces on the *i*-th node including two lines segments on either side of the node are:

$$\begin{aligned} \mathrm{F}_{Di} &= \mathrm{F}_{Di,i+1/2} + \mathrm{F}_{Di,i-1/2} \\ &= \frac{1}{4}\rho C_D^n Dl_{i+1/2}\left|\boldsymbol{V}_{ri,i+1/2}^{n}\right|\boldsymbol{V}_{ri,i+1/2}^{n} + \frac{1}{4}\rho C_D^n Dl_{i-1/2}\left|\boldsymbol{V}_{ri,i-1/2}^{n}\right|\boldsymbol{V}_{ri,i-1/2}^{n} \\ &= DT_{i+1/2}\left|\boldsymbol{V}_{ri,i+1/2}^{n}\right|\boldsymbol{V}_{ri,i+1/2}^{n} + DT_{i-1/2}\left|\boldsymbol{V}_{ri,i-1/2}^{n}\right|\boldsymbol{V}_{ri,i-1/2}^{n} \end{aligned} \tag{2.28}$$

where $DT_{i\pm1/2} = \frac{1}{4}\rho C_D^n Dl_{i\pm1/2}$.

2.3 Line Dynamics in Time Domain

2.3.1 Equations of Line Dynamics in Time Domain

According to previous derivation about node, we summarize the equation of motion of mooring line as follows:

$$\mathbf{M}\ddot{\boldsymbol{r}} = \mathbf{T} + \mathbf{F}_I + \mathbf{F}_D + \mathbf{W} \tag{2.29}$$

where mass matrix, $\mathbf{M} = \begin{bmatrix} \mathbf{M}_1 & & & \\ & \mathbf{M}_2 & & \\ & & \ddots & \\ & & & \mathbf{M}_N \end{bmatrix}$, $\mathbf{M}_i = \mathbf{m}_i + \mathbf{m}_{a,i}$;

The displacement matrix are $\boldsymbol{r} = \begin{bmatrix} \boldsymbol{r}_1 & \boldsymbol{r}_2 & \cdots & \boldsymbol{r}_N \end{bmatrix}^{\mathrm{T}}$; the acceleration matrix are $\ddot{\boldsymbol{r}} = \begin{bmatrix} \ddot{r}_1 & \ddot{r}_2 & \cdots & \ddot{r}_N \end{bmatrix}^{\mathrm{T}}$; tension matrix are $\mathbf{T} = \begin{bmatrix} \mathbf{T}_1 & \mathbf{T}_2 & \cdots & \mathbf{T}_N \end{bmatrix}^{\mathrm{T}}$; Inertia force matrix are $\mathbf{F}_I = \begin{bmatrix} \mathbf{F}_{I1} & \mathbf{F}_{I2} & \cdots & \mathbf{F}_{IN} \end{bmatrix}^{\mathrm{T}}$; $\mathbf{F}_D = \begin{bmatrix} \mathbf{F}_{D1} & \mathbf{F}_{D2} & \cdots & \mathbf{F}_{DN} \end{bmatrix}^{\mathrm{T}}$ are the drag force matrix; the weight and buoyance force matrix are $\mathbf{W} = \begin{bmatrix} \mathbf{W}_1 & \mathbf{W}_2 & \cdots & \mathbf{W}_N \end{bmatrix}^{\mathrm{T}}$.

And for the end of lines, there is only one segment attached. So the relative equations are different.

Bottom end:

Mass $\mathbf{M}_1 = \mathbf{m}_1 + \mathbf{m}_{a,1}$

where $\mathbf{m}_1 = \begin{bmatrix} m_1 & & \\ & m_1 & \\ & & m_1 \end{bmatrix}$, $m_1 = \frac{1}{2}\rho_m A l_{1+1/2}$ and $\mathbf{m}_{a,1} = DA_{1+1/2}\mathbf{N}_{1+1/2}$;

Tension $\mathbf{T}_1 = \mathbf{T}_{1+1/2}$; Inertia force $\mathbf{F}_{I1} = \mathbf{F}_{I,1+1/2} = DI_{1+1/2}\mathbf{N}_{1+1/2}\dot{\boldsymbol{u}}_1$

Drag force $\mathrm{F}_{D1} = \mathrm{F}_{D,1+1/2} = DT_{1+1/2}\left|\boldsymbol{V}^n_{r1,1+1/2}\right|\boldsymbol{V}^n_{r1,1+1/2}$

Top end:

Mass $\mathbf{M}_N = \mathbf{m}_N + \mathbf{m}_{a,N}$

where $\mathbf{m}_N = \begin{bmatrix} m_N & & \\ & m_N & \\ & & m_N \end{bmatrix}$, $m_N = \frac{1}{2}\rho_m A l_{N-1/2}$ and $\mathbf{m}_{a,N} = DA_{N-1/2}\mathbf{N}_{N-1/2}$;

Tension $\mathbf{T}_N = \mathbf{T}_{N-1/2}$; Inertia force $\mathbf{F}_{IN} = \mathbf{F}_{I,N-1/2} = DI_{N-1/2}\mathbf{N}_{N-1/2}\dot{\boldsymbol{u}}_{\mathrm{N}}$;

Drag force $\mathrm{F}_{DN} = \mathrm{F}_{D,N-1/2} = DT_{N-1/2}\left|\boldsymbol{V}^n_{rN,N\text{-}1/2}\right|\boldsymbol{V}^n_{rN,N\text{-}1/2}$

2.3.2 Boundary Conditions

The upper end connects with vessel, so the motion is the same as the vessel.

$$\mathbf{r}_N = \begin{bmatrix} x_N(t) \\ y_N(t) \\ z_N(t) \end{bmatrix} = \begin{bmatrix} x_V(t) \\ y_V(t) \\ z_V(t) \end{bmatrix} \tag{2.30}$$

where $x_V(t)$, $y_V(t)$ and $z_V(t)$ are the motions of vessel in surge, sway and heave.

The bottom end is considered as a fixed point:

$$\mathbf{r}_1 = \begin{bmatrix} 0 \\ 0 \\ 0 \end{bmatrix} \tag{2.31}$$

2.3.3 Initial Conditions

The initial positions and initial velocities for the second order ordinary differential equations:

$$\mathbf{r}_i(0) = \begin{bmatrix} x_i(0) \\ y_i(0) \\ z_i(0) \end{bmatrix} = \begin{bmatrix} x_i^0 \\ y_i^0 \\ z_i^0 \end{bmatrix} \tag{2.32}$$

$$\dot{\mathbf{r}}_i(0) = \begin{bmatrix} \dot{x}_i(0) \\ \dot{y}_i(0) \\ \dot{z}_i(0) \end{bmatrix} = \begin{bmatrix} \dot{x}_i^0 \\ \dot{y}_i^0 \\ \dot{z}_i^0 \end{bmatrix} \quad i=1,\ldots, \text{N} \tag{2.33}$$

2.3.4 Solving the Equation of Motion by Modified Euler Method

The equation of motion of mooring lines can be solved using numerical integration schemes. Here a modified Euler method (Hahn, 1991; Huang and Vassalos, 1993) is used to solve the equation of motion.

$$\mathbf{M}_i\ddot{\boldsymbol{r}}_i = \mathbf{T}_i + \mathbf{F}_{Ii} + \mathbf{F}_{Di} + \mathbf{W}_i \tag{2.34}$$

$\boldsymbol{r}_i^j$ and $\dot{\boldsymbol{r}}_i^j$ are the known displacement and velocity of the *i*-th node, respectively, at time $t_j = j\Delta t$. The displacement and velocity of the *i*-th node, $\boldsymbol{r}_i^{j+1}$ and $\dot{\boldsymbol{r}}_i^{j+1}$, at time are evaluated as follows.

$$\ddot{\boldsymbol{r}}_i^j = \mathbf{M}_i^{j-1}\left[\mathbf{T}_i^j + \mathbf{F}_{Ii}^j + \mathbf{F}_{Di}^j + \mathbf{W}_i^j\right] \tag{2.35}$$

$$\dot{\boldsymbol{r}}_i^{j+1} = \dot{\boldsymbol{r}}_i^j + \ddot{\boldsymbol{r}}_i^j \Delta t \quad \text{or} \quad \begin{bmatrix} \dot{x}_i^{j+1} \\ \dot{y}_i^{j+1} \\ \dot{z}_i^{j+1} \end{bmatrix} = \begin{bmatrix} \dot{x}_i^j \\ \dot{y}_i^j \\ \dot{z}_i^j \end{bmatrix} + \begin{bmatrix} \ddot{x}_i^j \\ \ddot{y}_i^j \\ \ddot{z}_i^j \end{bmatrix} \Delta t \tag{2.36}$$

$$\boldsymbol{r}_i^{j+1} = \boldsymbol{r}_i^j + \dot{\boldsymbol{r}}_i^{j+1} \Delta t \quad \text{or} \quad \begin{bmatrix} x_i^{j+1} \\ y_i^{j+1} \\ z_i^{j+1} \end{bmatrix} = \begin{bmatrix} x_i^j \\ y_i^j \\ z_i^j \end{bmatrix} + \begin{bmatrix} \dot{x}_i^{j+1} \\ \dot{y}_i^{j+1} \\ \dot{z}_i^{j+1} \end{bmatrix} \Delta t \tag{2.37}$$

where Δt is the time step, The new displacements, velocities and accelerations of all the nodes can be evaluated easily using this method.

It can be seen that the modified Euler method is very simple and can lead to accurate

response evaluations (Hahn, 1991). It is explicit and forward different from the Newmark beta method which needs iteration for each step. This method is conditionally stable, time step should satisfy the condition of stability as follows.

$$\Delta t < \frac{T_n}{\pi} \tag{2.38}$$

where T_n is shortest natural period of vibration of the system.

2.4 Dynamic Analysis of Mooring Line in Frequency Domain

The dynamic analysis in frequency domain is based on the linear system. There are nonlinear effects that can have an important influence on mooring line behavior. One is geometric nonlinearity, which is associated with large changes in shape of the mooring line. The other is fluid loading, the Morrison equation is most frequently used to represent fluid loading effects on mooring lines. The drag force on the line is proportional to the square of the relative velocity (between the water particle velocity from wave and current and the line's velocity), hence is nonlinear. In addition, the contact with line with seabed also is nonlinear. These nonlinearities have to be linearized.

2.4.1 Linearization

1) Linearization for Stiffness

Frequency analysis is inherently linear, so the nonlinearities in the mooring dynamical equations must be linearized. One of the nonlinear effects inherent in the dynamic analysis of mooring is the geometric nonlinearity. It is assumed that dynamic deflections around the static equilibrium position are small. Thus, it is assumed that the stiffness matrices do not change during the analysis.

The tangent stiffness matrix for node *i* is

$$k_i = \frac{\partial \mathbf{T}_{i+1/2}}{\partial \mathbf{r}_i}$$

$$= EA\begin{bmatrix} (\frac{1}{l_{i+1/2}} - \frac{1}{\tilde{l}_{i+1/2}}) + \frac{(x_{i+1} - x_i)^2}{\tilde{l}_{i+1/2}^3} & \frac{(x_{i+1} - x_i)(y_{i+1} - y_i)}{\tilde{l}_{i+1/2}^3} & \frac{(x_{i+1} - x_i)(z_{i+1} - z_i)}{\tilde{l}_{i+1/2}^3} \\ \frac{(y_{i+1} - y_i)(x_{i+1} - x_i)}{\tilde{l}_{i+1/2}^3} & (\frac{1}{l_{i+1/2}} - \frac{1}{\tilde{l}_{i+1/2}}) + \frac{(y_{i+1} - y_i)^2}{\tilde{l}_{i+1/2}^3} & \frac{(y_{i+1} - y_i)(z_{i+1} - z_i)}{\tilde{l}_{i+1/2}^3} \\ \frac{(z_{i+1} - z_i)(x_{i+1} - x_i)}{\tilde{l}_{i+1/2}^3} & \frac{(z_{i+1} - z_i)(y_{i+1} - y_i)}{\tilde{l}_{i+1/2}^3} & (\frac{1}{l_{i+1/2}} - \frac{1}{\tilde{l}_{i+1/2}}) + \frac{(z_{i+1} - z_i)^2}{\tilde{l}_{i+1/2}^3} \end{bmatrix} \tag{2.39}$$

The stiffness matrix for segment between *i*-th node and (*i*+1)-th node is:

$$K_{i+1/2} = \begin{bmatrix} k_i & -k_i \\ -k_i & k_i \end{bmatrix} \tag{2.40}$$

where:

$$k_i = EA\begin{bmatrix} (\frac{1}{l_{i+1/2}} - \frac{1}{\bar{l}_{i+1/2}}) + \frac{(\bar{x}_{i+1} - \bar{x}_i)^2}{\bar{l}_{i+1/2}^3} & \frac{(\bar{x}_{i+1} - \bar{x}_i)(\bar{y}_{i+1} - \bar{y}_i)}{\bar{l}_{i+1/2}^3} & \frac{(\bar{x}_{i+1} - \bar{x}_i)(\bar{z}_{i+1} - \bar{z}_i)}{\bar{l}_{i+1/2}^3} \\ \frac{(\bar{y}_{i+1} - \bar{y}_i)(\bar{x}_{i+1} - \bar{x}_i)}{\bar{l}_{i+1/2}^3} & (\frac{1}{l_{i+1/2}} - \frac{1}{\bar{l}_{i+1/2}}) + \frac{(\bar{y}_{i+1} - \bar{y}_i)^2}{\bar{l}_{i+1/2}^3} & \frac{(\bar{y}_{i+1} - \bar{y}_i)(\bar{z}_{i+1} - \bar{z}_i)}{\bar{l}_{i+1/2}^3} \\ \frac{(\bar{z}_{i+1} - \bar{z}_i)(\bar{x}_{i+1} - \bar{x}_i)}{\bar{l}_{i+1/2}^3} & \frac{(\bar{z}_{i+1} - \bar{z}_i)(\bar{y}_{i+1} - \bar{y}_i)}{\bar{l}_{i+1/2}^3} & (\frac{1}{l_{i+1/2}} - \frac{1}{\bar{l}_{i+1/2}}) + \frac{(\bar{z}_{i+1} - \bar{z}_i)^2}{\bar{l}_{i+1/2}^3} \end{bmatrix} \tag{2.41}$$

And $\mathbf{r}_i = \begin{bmatrix} \bar{x}_i & \bar{y}_i & \bar{z}_i \end{bmatrix}^T$ is the static equilibrium position of node *i*, $\bar{l}_{i+1/2}$ is the length of segment between *i*-th node and (*i*+1)-th node at its static equilibrium position.

Then we can obtain the global linearized stiffness matrix:

$$\mathbf{K} = \begin{bmatrix} k_1 & -k_1 & & & & \\ -k_1 & k_1+k_2 & -k_2 & & & \\ & -k_2 & k_2+k_3 & -k_3 & & \\ & & & \ddots & & \\ & & & -k_{N-2} & k_{N-2}+k_{N-1} & -k_{N-1} \\ & & & & -k_{N-1} & k_{N-1} \end{bmatrix} \tag{2.42}$$

2) Linearization for Drag Force

The drag force is often calculated using Morison's equation as follows.

$$\begin{aligned} \boldsymbol{F}_D &= \frac{1}{2}\rho C_D L \boldsymbol{V}_r^n \left|\boldsymbol{V}_r^n\right| \\ &= \frac{1}{2}\rho C_D L (\boldsymbol{V}^n + \boldsymbol{V}_c^n)\left|\boldsymbol{V}^n + \boldsymbol{V}_c^n\right| \end{aligned} \tag{2.43}$$

where $\boldsymbol{V}_r^n = \boldsymbol{V}^n + \boldsymbol{V}_c^n$

$\boldsymbol{V}^n = \boldsymbol{u}^n - \dot{\boldsymbol{r}}^n$

$\boldsymbol{V}_r^n$ is the relative velocity between the normal water particle velocity from wave $\boldsymbol{u}^n$ and current $\boldsymbol{V}_c^n$ and the normal line's velocity $\dot{\boldsymbol{r}}^n$ to the axis of lines. $\boldsymbol{V}^n$ is the relative velocity between the normal water particle velocity from wave $\boldsymbol{u}^n$ and the normal line's velocity $\dot{\boldsymbol{r}}^n$.

The drag force is nonlinear and should be linearized for frequency domain dynamic analysis which is based on a linear system. There are several linearization methods for the drag force. The linear form of drag force in regular wave can be obtained by the equivalent energy method (Chakrabarti and Cotter, 1979). In random wave, the statistical linearization is often used (Atalik and Utku, 1976; Krolikowski and Gay, 1980; Spanos et al., 2005). It is based on minimization of the expected square error between the nonlinear drag force and linearized drag force. Wu (1976) derived the

equivalent linear form for a one-dimensional drag force in a random sea with current. And the one-dimension linearization is extended to the three-dimension case by linearizing each component with this equivalent linear form. Hamilton (1980) pointed out this approach is not strictly frame invariant, i.e. it depends upon the choice of reference axes. Langley (1984) found that this linearization method can lead to a significant underestimate of the drag force, since coupling between perpendicular flows directions is neglected. Langley formulated a frame invariant linearization method for random waves with current that is more rigorous. This method is used here.

The nonlinear term in drag force is replaced by the linear form:

$$\left(\boldsymbol{V}^n + \boldsymbol{V}_c^n\right)\left|\boldsymbol{V}^n + \boldsymbol{V}_c^n\right| = C_e \boldsymbol{V}^n + \mathrm{F}_m \tag{2.44}$$

where C_e is the equivalent linear coefficient and $\mathbf{F}_m$ is a constant force vector. The normal water particle velocity from wave $\boldsymbol{u}^n$ is a Gaussian random process, the corresponding structure's velocity $\dot{\boldsymbol{r}}^n$ and the relative velocity $\boldsymbol{V}^n = \boldsymbol{u}^n - \dot{\boldsymbol{r}}^n$ is also a Gaussian random process. The C_e and $\mathbf{F}_m$ can estimated from minimizing the expected square error between the nonlinear and linearized form.

The expected square error is:

$$E[\left\{\left(\boldsymbol{V}^n + \boldsymbol{V}_c^n\right)\left|\boldsymbol{V}^n + \boldsymbol{V}_c^n\right| - \left(C_e \boldsymbol{V}^n + \mathrm{F}_m\right)\right\}^2] \tag{2.45}$$

Minimization of the error with respect to C_e and $\mathbf{F}_m$ leads to the following:

$$C_e = \frac{E\left[\boldsymbol{V}^n \cdot \left(\boldsymbol{V}^n + \boldsymbol{V}_c^n\right)\left|\boldsymbol{V}^n + \boldsymbol{V}_c^n\right|\right]}{E\left[\boldsymbol{V}^n \cdot \boldsymbol{V}^n\right]} \tag{2.46}$$

$$\mathrm{F}_m = E\left[\left(\boldsymbol{V}^n + \boldsymbol{V}_c^n\right)\left|\boldsymbol{V}^n + \boldsymbol{V}_c^n\right|\right] \tag{2.47}$$

Since the relative velocity $\boldsymbol{V}^n$ is normal to the centerline of the line, it has only two nonzero components in a coordinate system that has the tangent to the centerline as a basis vector. If the two components are uncorrelated, evaluation of the expected values in the above equations can be simplified. We can choose the coordinate based on the principal directions of the relative velocity covariance matrix: one base vector, denoted as axis 1, is in the direction of the maximum velocity variance and the other, denoted as axis 2, is in the direction of the minimum velocity variance. In this coordinate system, the two components of the relative velocity $\boldsymbol{V}^n = [v_1, v_2]$ are un-correlated, or the covariance of v_1 and v_2 is zero. The current velocity is $\boldsymbol{V}_c^n = [V_{c1}, V_{c2}]$ in this coordinate system. The transformation about the local coordinate from global coordinate can be found in Appendix A.

Therefore the above equations can be rewritten as:

$$\begin{aligned} C_e &= \frac{E[\boldsymbol{V}^n \cdot (\boldsymbol{V}^n + \boldsymbol{V}_c^n)|\boldsymbol{V}^n + \boldsymbol{V}_c^n|]}{E[\boldsymbol{V}^n \cdot \boldsymbol{V}^n]} \\ &= \frac{\int_{-\infty}^{\infty}\int_{-\infty}^{\infty} \boldsymbol{V}^n \cdot (\boldsymbol{V}^n + \boldsymbol{V}_c^n)|\boldsymbol{V}^n + \boldsymbol{V}_c^n| \, p(\boldsymbol{V}^n) dv_1 dv_2}{\int_{-\infty}^{\infty}\int_{-\infty}^{\infty} (\boldsymbol{V}^n \cdot \boldsymbol{V}^n) \, p(\boldsymbol{V}^n) dv_1 dv_2} \\ &= \frac{I_1}{\sigma_1^2 + \sigma_2^2} \end{aligned} \tag{2.48}$$

$$\begin{aligned} \mathrm{F}_m &= E[(\boldsymbol{V}^n + \boldsymbol{V}_c^n)|\boldsymbol{V}^n + \boldsymbol{V}_c^n|] \\ &= \int_{-\infty}^{\infty}\int_{-\infty}^{\infty} (\boldsymbol{V}^n + \boldsymbol{V}_c^n)|\boldsymbol{V}^n + \boldsymbol{V}_c^n| \, p(\boldsymbol{V}^n) dv_1 dv_2 \\ &= \begin{bmatrix} \int_{-\infty}^{\infty}\int_{-\infty}^{\infty} (v_1 + V_{c1})|\boldsymbol{V}^n + \boldsymbol{V}_c^n| \, p(\boldsymbol{V}^n) dv_1 dv_2 \\ \int_{-\infty}^{\infty}\int_{-\infty}^{\infty} (v_2 + V_{c2})|\boldsymbol{V}^n + \boldsymbol{V}_c^n| \, p(\boldsymbol{V}^n) dv_1 dv_2 \end{bmatrix} \\ &= \begin{bmatrix} I_2 \\ I_3 \end{bmatrix} = \begin{bmatrix} F_1^m \\ F_2^m \end{bmatrix} \end{aligned} \tag{2.49}$$

where:

$$I_1 = \int_{-\infty}^{\infty}\int_{-\infty}^{\infty} \boldsymbol{V}^n \cdot \left(\boldsymbol{V}^n + \boldsymbol{V}_c^n\right)\left|\boldsymbol{V}^n + \boldsymbol{V}_c^n\right| p(\boldsymbol{V}^n) dv_1 dv_2 \tag{2.50}$$

$$I_2 = \int_{-\infty}^{\infty}\int_{-\infty}^{\infty} \left(v_1 + V_{c1}\right)\left|\boldsymbol{V}^n + \boldsymbol{V}_c\right| p(\boldsymbol{V}^n) dv_1 dv_2 \tag{2.51}$$

$$I_3 = \int_{-\infty}^{\infty}\int_{-\infty}^{\infty} \left(v_2 + V_{c2}\right)\left|\boldsymbol{V}^n + \boldsymbol{V}_c\right| p(\boldsymbol{V}^n) dv_1 dv_2 \tag{2.52}$$

$p(\boldsymbol{V}^n)$ is the probability density function of $\boldsymbol{V}^n$. Considering $\boldsymbol{V}^n$ is a Gaussian random process and v_1 and v_2 are un-correlated, the probability density function is:

$$p(\boldsymbol{V}^n) = \frac{1}{2\pi\sigma_1\sigma_2} e^{-\frac{1}{2}\left[\left(\frac{v_1}{\sigma_1}\right)^2 + \left(\frac{v_2}{\sigma_2}\right)^2\right]} \tag{2.53}$$

The linearization needs the integration of double infinite integrals. Only a few special cases have the closed form of the integration. For the one-dimensional drag force, the linearization results are:

$$C_e = \sqrt{\frac{8}{\pi}}\left\{\sigma e^{-\frac{1}{2}\left(\frac{Vc}{\sigma}\right)^2} + \sqrt{2\pi} V_c erf\left(\frac{V_c}{\sigma}\right)\right\} \tag{2.54}$$

$$F_m = \sqrt{\frac{2}{\pi}}\sigma V_c e^{-\frac{1}{2}\left(\frac{Vc}{\sigma}\right)^2} + 2(V_c^2 + \sigma^2) erf\left(\frac{V_c}{\sigma}\right) \tag{2.55}$$

where $erf(x) = \frac{1}{\sqrt{2\pi}}\int_0^x e^{-\frac{1}{2}t^2} dt$.

If there is no current, then the linearization coefficient for one-dimension drag force is:

$$C_e = \sqrt{\frac{8}{\pi}}\sigma \tag{2.56}$$

Because the drag force is three dimensional, the integrals require numerical method. Rodenbusch et al. (1986) simplified the infinite integral required in the linearization of drag force. The infinite integrals are transformed into finite integrals by trigonometric functions. Then the finite integrals are evaluated by trapezoidal rule. The detail about this method can be found in Appendix B.

Using the above linearization method, we can obtain the linearized drag force at node *i* is as follows.

$$\begin{aligned}\mathbf{F}_{Di} &= \frac{1}{4}\rho C_D Dl_{i+1/2}\mathbf{P}^{\mathrm{T}}_{i+1/2}\left(C_{e,i+1/2}\mathbf{P}_{i+1/2}\mathbf{N}_{i+1/2}\left(\boldsymbol{u}_i-\dot{\boldsymbol{r}}_i\right)+\mathbf{F}_{m,i+1/2}\right)\\ &\quad+\frac{1}{4}\rho C_D Dl_{i-1/2}\mathbf{P}^{\mathrm{T}}_{i-1/2}\left(C_{e,i-1/2}\mathbf{P}_{i-1/2}\mathbf{N}_{i-1/2}\left(\boldsymbol{u}_i-\dot{\boldsymbol{r}}\right)+\mathbf{F}_{m,i-1/2}\right)\\ &= DT_{i+1/2}\mathbf{P}^{\mathrm{T}}_{i+1/2}C_{e,i+1/2}\mathbf{P}_{i+1/2}\mathbf{N}_{i+1/2}\left(\boldsymbol{u}_i-\dot{\boldsymbol{r}}\right)+DT_{i+1/2}\mathbf{P}^{\mathrm{T}}_{i+1/2}\mathbf{F}_{m,i+1/2}\\ &\quad+DT_{i-1/2}\mathbf{P}^{\mathrm{T}}_{i+1/2}C_{e,i-1/2}\mathbf{P}_{i-1/2}\mathbf{N}_{i-1/2}\left(\boldsymbol{u}_i-\dot{\boldsymbol{r}}\right)+DT_{i-1/2}\mathbf{P}^{\mathrm{T}}_{i-1/2}\mathbf{F}_{m,i-1/2}\\ &= (\mathbf{Q}_{i+1/2}+\mathbf{Q}_{i-1/2})\left(\boldsymbol{u}_i-\dot{\boldsymbol{r}}\right)+\mathbf{F}_{mi}\end{aligned} \tag{2.57}$$

where $\mathbf{P}^{T}_{i\pm1/2}$ is the orthogonal transformation from the local principal coordinate system to the global coordinate system as described in Appendix A.

$$DT_{i\pm1/2}=\frac{1}{4}\rho C_D Dl_{i\pm1/2}\ ;$$

$$\mathbf{Q}_{i\pm1/2}=DT_{i\pm1/2}\mathbf{P}^{T}_{i\pm1/2}C_e\mathbf{P}_{i\pm1/2}\mathbf{N}_{i\pm1/2}\,;$$

$$\mathbf{F}_{mi}=DT_{i+1/2}\mathbf{P}^{\mathrm{T}}_{i+1/2}\mathbf{F}_{m,i+1/2}+DT_{i-1/2}\mathbf{P}^{\mathrm{T}}_{i-1/2}\mathbf{F}_{m,i-1/2}\,.$$

The drag force matrix can be written as:

$$\mathbf{F}_D=\mathbf{Q}(\boldsymbol{u}-\dot{\mathbf{r}})+\overline{\mathbf{F}} \tag{2.58}$$

where:

$$\mathbf{Q} = \begin{bmatrix} \mathbf{Q}_{1+1/2} & & & & \\ & \mathbf{Q}_{2-1/2} + \mathbf{Q}_{2+1/2} & & & \\ & & \mathbf{Q}_{3-1/2} + \mathbf{Q}_{3+1/2} & & \\ & & & \ddots & \\ & & & & \mathbf{Q}_{(N-1)-1/2} + \mathbf{Q}_{(N-1)+1/2} \\ & & & & & \mathbf{Q}_{N-1/2} \end{bmatrix}$$

$$\overline{\mathbf{F}} = \begin{bmatrix} \mathbf{F}_{m1} & \mathbf{F}_{m2} & \cdots & \mathbf{F}_{mN} \end{bmatrix}^T$$

3) Linearization for Line-Seabed Contact

Another nonlinearity that should be treated for the frequency domain analysis is the line-soil contact. During the dynamic analysis, the TDP changes as the floating unit moves. To remove that nonlinear effect in this model, the static TDP is replaced by a pinned support (based on the static TDP?) and only the suspended part of the mooring line is dynamically analyzed.

2.4.2 Equations of Line Dynamics in Frequency Domain

After linearization, substituting the Eq.(2.42) and Eq.(2.58) into the motion equation. And then it is transformed into frequency domain. The equation of motion of mooring lines in frequency domain has the form as follows.

$$-\omega^2 \mathbf{M}\mathbf{r}(\omega) = -\mathbf{K}\mathbf{r}(\omega) + \mathbf{M}_I \dot{u}(\omega) + \mathbf{Q}(u(\omega) - \dot{\mathbf{r}}(\omega)) \tag{2.59}$$

It can be written as:

$$(-\omega^2 \mathbf{M} + i\omega \mathbf{Q} + \mathbf{K})\mathbf{r}(\omega) = \mathbf{M}_I \dot{\boldsymbol{u}}(\omega) + \mathbf{Q}\boldsymbol{u}(\omega) \tag{2.60}$$

The wave kinematics is calculated using airy wave theory. The wave particle velocity and acceleration are

$$\boldsymbol{u}(\omega) = \begin{bmatrix} \omega e^{kz} \\ 0 \\ i\omega e^{kz} \end{bmatrix} \eta(\omega) = \mathbf{H}_u(\omega)\eta(\omega) \tag{2.61}$$

$$\dot{\boldsymbol{u}}(\omega) = \begin{bmatrix} i\omega^2 e^{kz} \\ 0 \\ -\omega^2 e^{kz} \end{bmatrix} \eta(\omega) = \mathbf{H}_a(\omega)\eta(\omega) \tag{2.62}$$

where real parts are implied.

Then the equation of motion can be rewritten as follows:

$$\begin{aligned} (-\omega^2\mathbf{M} + i\omega\mathbf{Q} + \mathbf{K})\mathbf{r}(\omega) &= \mathbf{M}_I\mathbf{H}_a(\omega)\eta(\omega) + \mathbf{Q}\mathbf{H}_u(\omega)\eta(\omega) \\ &= \left[\mathbf{M}_I\mathbf{H}_a(\omega) + \mathbf{Q}\mathbf{H}_u(\omega)\right]\eta(\omega) \\ &= \mathbf{G}(\omega)\eta(\omega) \end{aligned} \tag{2.63}$$

2.4.3 Boundary Conditions

The top end is connected to the floating structure, so its response is equal to the response of floating structure. For the bottom fixed end, its response is zero. For the boundary conditions, we can use the method of multiplying the stiffness by a large number or substituting the zero response of the support points into the equation to eliminate the related row and column.

2.4.4 Solving the Equation of Motion

After applied the boundary conditions, the displacement responses can be obtained as

$$\begin{aligned} \mathbf{r}(\omega) &= (-\omega^2\mathbf{M} + i\omega\mathbf{Q} + \mathbf{K})^{-1}\mathbf{G}(\omega)\eta(\omega) \\ &= \mathbf{T}(\omega)\mathbf{G}(\omega)\eta(\omega) \\ &= \mathbf{H}(\omega)\eta(\omega) \end{aligned} \tag{2.64}$$

where $\mathbf{H}(\omega)$ is the transfer function.

$$\mathbf{T}(\omega) = (-\omega^2\mathbf{M} + i\omega\mathbf{Q} + \mathbf{K})^{-1}, \quad \mathbf{H}(\omega) = \mathbf{T}(\omega)\mathbf{G}(\omega)$$

And velocity of lines：

$$\dot{\mathbf{r}}(\omega) = i\omega\mathbf{r}(\omega) \tag{2.65}$$

Relative velocity response between water particle velocity and lines' velocity：

$$\begin{aligned}\mathbf{V}(\omega) &= \boldsymbol{u}(\omega) - \dot{\mathbf{r}}(\omega) \\ &= \boldsymbol{u}(\omega) - i\omega\mathbf{r}(\omega) \\ &= \left[\mathbf{H}_u(\omega) - i\omega\mathbf{H}(\omega)\right]\eta(\omega) \\ &= \mathbf{H}_v(\omega)\eta(\omega)\end{aligned} \tag{2.66}$$

Top Tension can be obtained as:

$$\mathbf{T}(\omega) = k_{N-1}\left[\mathbf{r}_N(\omega) - \mathbf{r}_{N-1}(\omega)\right] \tag{2.67}$$

The Response Spectra of displacement and top tension are:

$$S_{rr}(\omega) = \left|\mathbf{H}(\omega)\right|^2 S_{\eta\eta}(\omega) \tag{2.68}$$

$$S_T(\omega) = \left|\mathbf{H}_T(\omega)\right|^2 S_{\eta\eta}(\omega) \tag{2.69}$$

Mean square response of displacement and velocity are：

$$\sigma_r^2 = \int_0^\infty S_{rr}(\omega)d\omega \tag{2.70}$$

$$\sigma_{\dot{r}}^2 = \int_0^\infty \omega^2 S_{rr}(\omega)d\omega \tag{2.71}$$

The statistics of the response can be easily obtained from response at each frequency by a discretized approach. The variance and *k*-th spectrum moment of the response in *i*-th degree of freedom can be simply computed as

$$\sigma_i^2 = \sum_{j=1}^{N} \frac{1}{2}\left[r_i(\omega_j)\right]^2 \tag{2.72}$$

$$m_k = \sum_{j=1}^{N} \frac{1}{2}\left[r_i(\omega_j)\right]^2 \omega_j^k \tag{2.73}$$

And the covariance matrix of relative velocities:

$$R_{ij} = \mathrm{Re}\sum_{k=1}^{N} \frac{1}{2} V_{r,i}(\omega_k) V_{r,j}^*(\omega_k) \tag{2.74}$$

2.5 Numerical Case in Time Domain

Table 2.1 Properties of the mooring line

Type	Diameter (mm)	Axial Stiffness (kN)	Weight (kg/m)	
			Air	Water
R4 Chain	157	3350000	491	426
Spiral Strand wire	144	1893000	106	84

The codes for the dynamic analyses of mooring lines in time domain are programmed using Matlab. The numerical case analysis of single component and multi-component mooring lines are performed. To verify this program, the results are compared with the results from commercial software, Orcaflex. The detailed properties of the lines are listed in Table 2.1. The harmonic excitations are applied to the top end of the lines. The horizontal and vertical harmonic excitations represent the motions of wave frequency and low frequency of floating structure, respectively.

Three test cases are performed and compared with the results from Orcaflex. The first case is a single component mooring line only under harmonic excitation applied to its top end. There are no environmental loads and no seabed contact. In the second

case, the environmental loads, wave and current are applied to the line. The third case is about multi-components mooring lines. The lines are subjected to wave, current and harmonic top excitation. In addition, the contact with seabed is also taken into accounted.

2.5.1 Case for Single Component Mooring Line

1) Single Component Mooring Line under Harmonic Excitation

Dynamic response of a single component mooring line, R4 chain, is simulated. The mooring line is subjected to vertical, horizontal and combined vertical and horizontal harmonic excitations, respectively. The given harmonic excitations are as follows.

$$x_N(t) = 10\cos(0.02\pi t) \tag{2.75}$$

$$z_N(t) = 5\cos(0.2\pi t) \tag{2.76}$$

The environmental loads are not taken into account here. Water depth is 400m. The length of line is 400m. The top end is 10m under the water surface and bottom end is at 50m from water level. The configuration of the mooring line is shown in Figure 2.3 by static analysis. And the results of dynamic analysis are compared with Orcaflex's, which use the lumped mass method too and implicit method is used here to solve the dynamic problem. There are 20 segments. Figure 2.4 to Figure 2.6 give the dynamic response of single component mooring line under vertical, horizontal and combined vertical and horizontal harmonic excitations. From the results, the codes described above agree well with the outputs of Orcaflex, although the top tension range is 1% greater in Orcaflex.

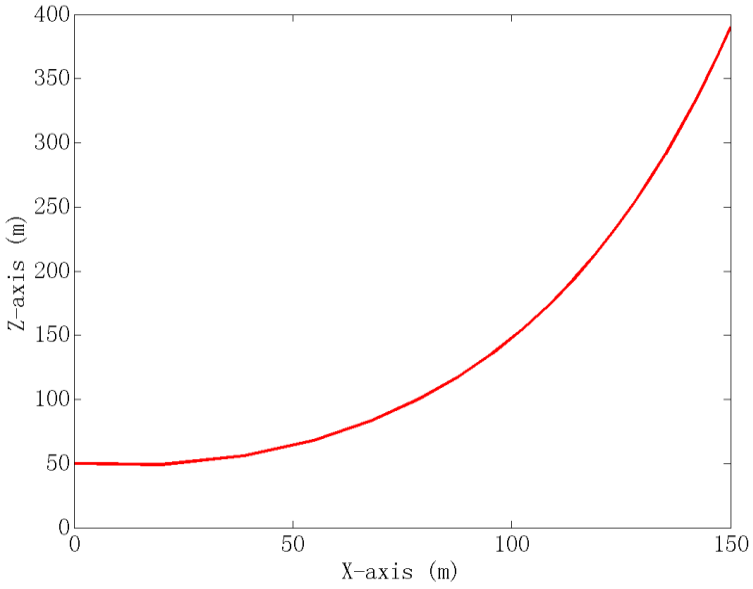

Figure 2.3 Configuration of single mooring line

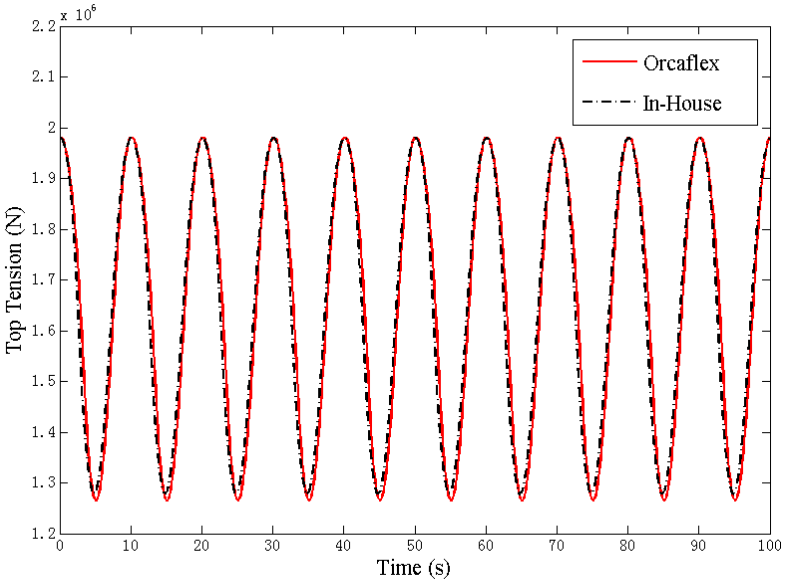

Figure 2.4 Single mooring line under the vertical harmonic excitation only

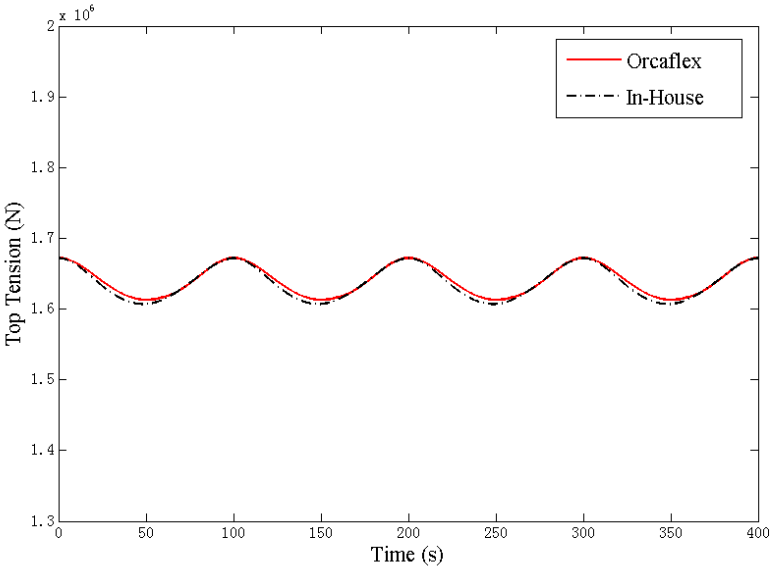

Figure 2.5 Single mooring line under the horizontal harmonic excitation only

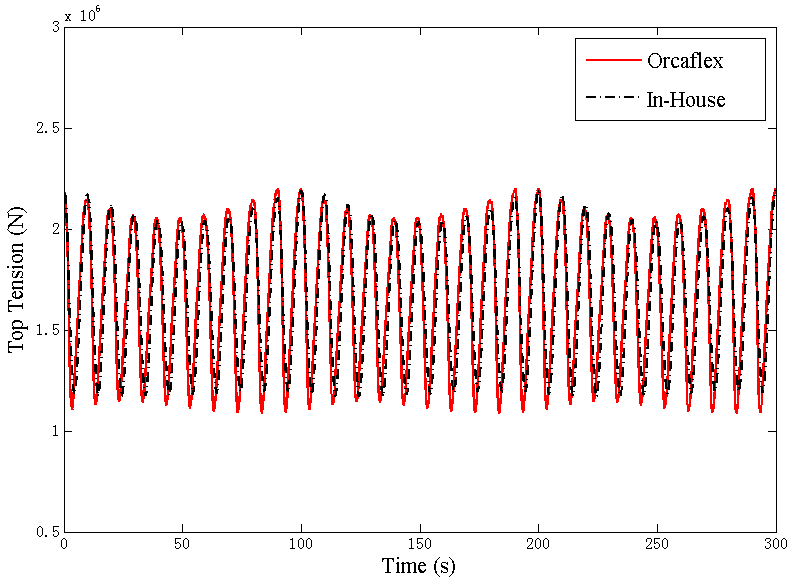

Figure 2.6 Single mooring line under the combined vertical and horizontal harmonic excitations

2) Single Component Mooring Line under Harmonic Excitation and Wave and Current

In this case, the environmental loads from wave and current are applied to the lines. The wave is an Airy wave that has wave height at 7.0m and the period of 8.0s. The

current is 1m/s in the x direction and linear decay along the depth until zero at seabed. And the mooring line is still subjected to three harmonic excitations (vertical, horizontal and combined vertical and horizontal harmonic excitations). Both the results of mooring line dynamic analysis by our code and Orcaflex are shown in Figure 2.7 to Figure 2.9. It can be seen that they agree well and the difference is within 1%.

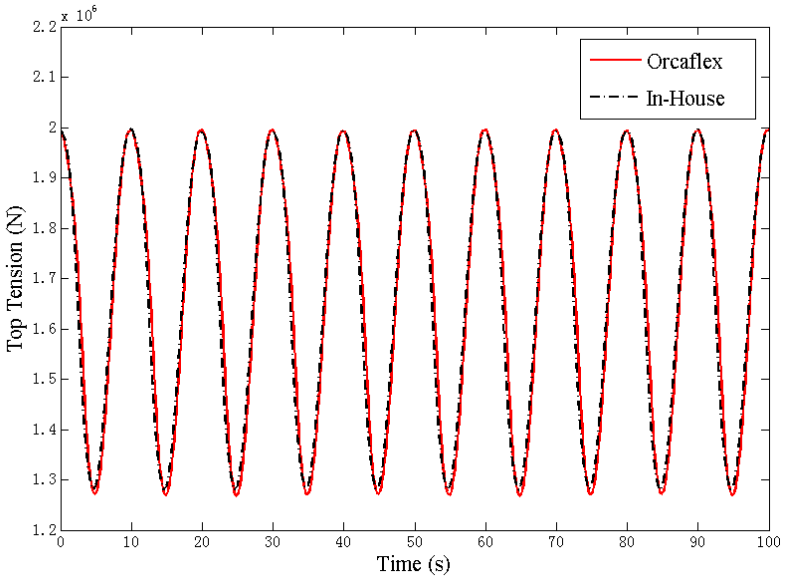

Figure 2.7 Single mooring line under vertical harmonic excitation with wave and current

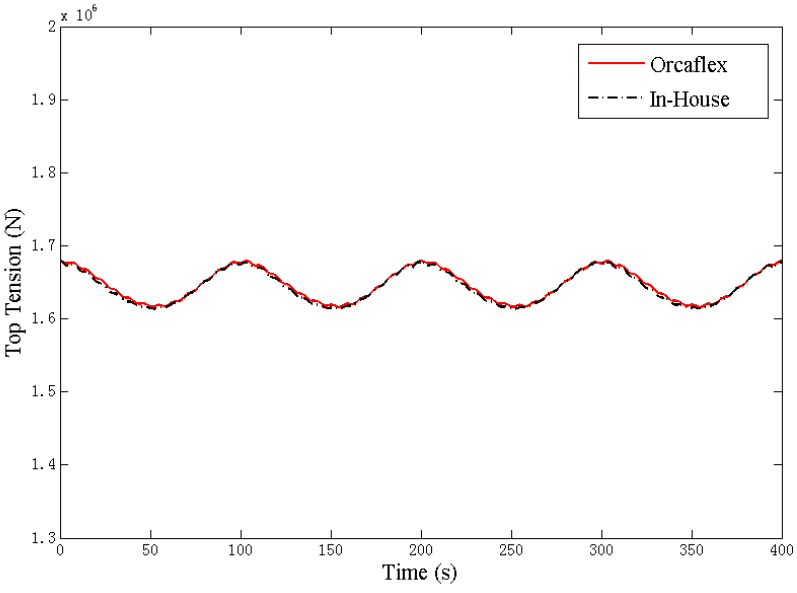

Figure 2.8 Single mooring line under horizontal harmonic excitation with wave and current

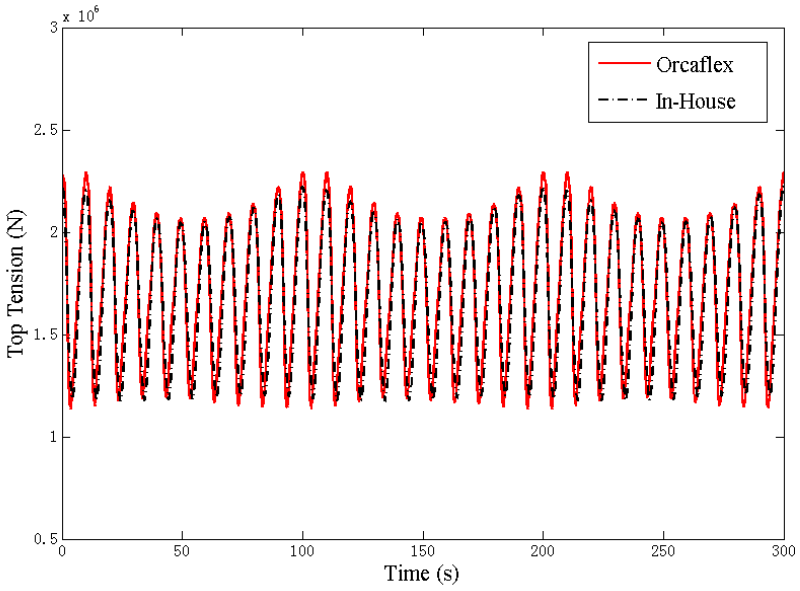

Figure 2.9 Single mooring line under combined vertical and horizontal harmonic excitation with wave and current

2.5.2 Case for Multi-Component Mooring Line

This code can also perform the dynamic analysis for multi-component mooring line. Here a test case of a multi-component mooring line (R4 chain - Spiral Strand wire - R4 chain) is simulated. The line length is 100, 400 and 1480 m, respectively. The static analysis for multi-component mooring line based on the Catenary equation is derived in Appendix A. The static analysis cases, given different offsets, are presented and the results are compared with Orcaflex's which show they agree well. Then the static analysis results as the initial configuration for dynamic analysis as presented in Figure 2.10. The first part of 100m R4 chain is divided into 5 segments and the second part of Spiral Strand wire is divided into 6 segments. The third part of R4 chain takes the seabed contact into account; parts on the touch down zone are meshed by 10m per segment (in total 58 segments) and other parts always on seabed are coarsely meshed by 100m per segment. The given harmonic excitations are as follows.

$$x_N(t) = 40\cos(0.02\pi t) \tag{2.77}$$

$$z_N(t) = 5\cos(0.2\pi t) \tag{2.78}$$

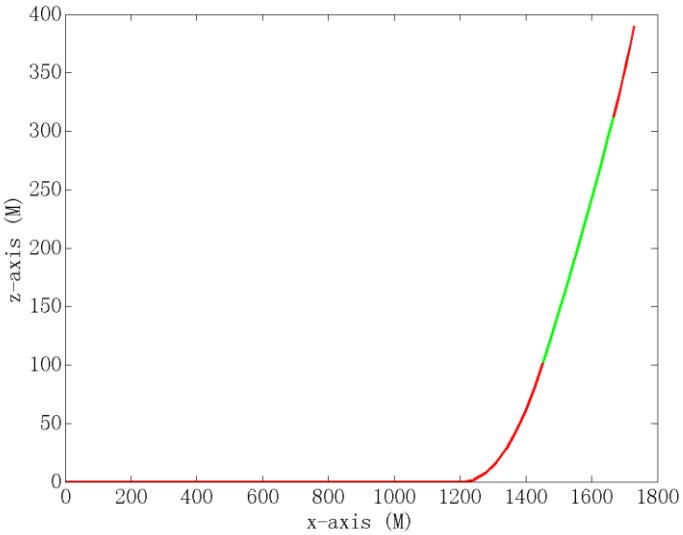

Figure 2.10 Configuration of multi-components mooring line

Wave and current are the same as used in the single component mooring line. In addition, seabed interaction is also considered. For mooring line resting on the seabed, a modified bilinear spring is used to model the vertical contact force on a node (Ghadimi, 1988), which has the form as follow. Friction effects are considered to be less significant for the system analyzed and are neglected. A gradual transition is proposed for numerical stability. The effects of wave and current are considered, using the same parameters in the single line case.

$$F_s = \frac{1}{2}a\left\{-z + \frac{1}{b}\ln[\cosh(bz+c)] + d\right\} \tag{2.79}$$

where *a*, *b*, *c*, and d are suitably chosen constants, which can be taken from Ghadimi, 1988. In particular, *d* should have a value such that F_s is close to 0 when z is a suitable distance away from the seabed.

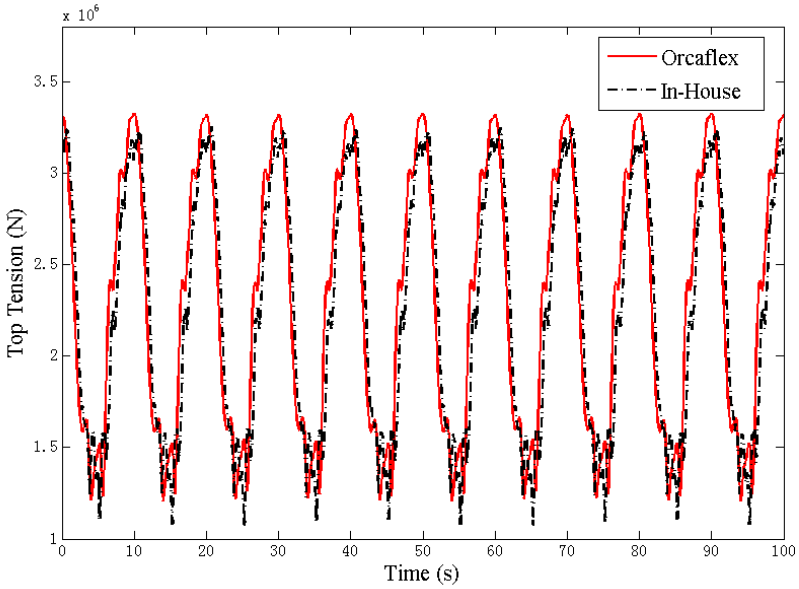

Figure 2.11 Multi-components mooring line under the vertical harmonic excitation

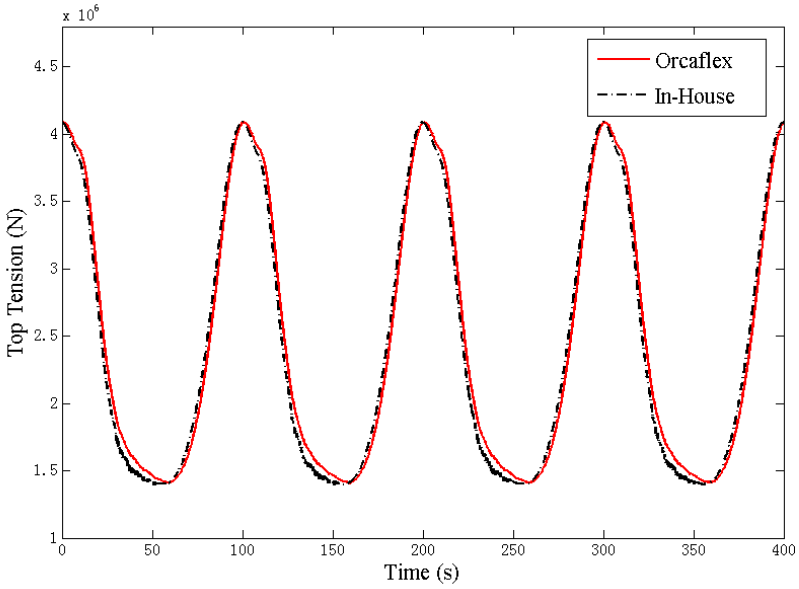

Figure 2.12 Multi-components mooring line under the horizontal harmonic excitation

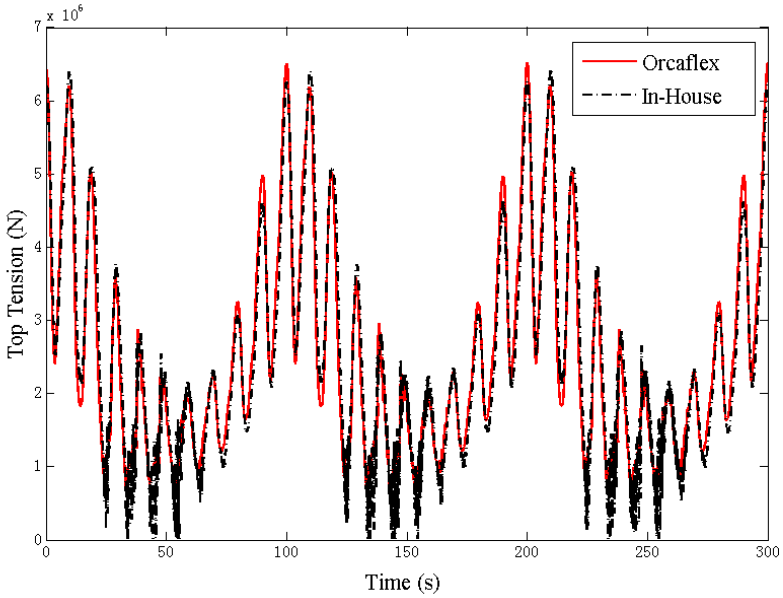

Figure 2.13 Multi-components mooring line under the combined vertical and horizontal harmonic excitation

Dynamic response of multi-components mooring line under vertical, horizontal and combined vertical and horizontal harmonic excitations are shown in Figure 2.11 - Figure 2.13. According to the results of the dynamic analysis in timed domain, it can be seen that this program can perform as well as the commercial software and the difference is within 3%.

2.6 Numerical Case in Frequency Domain

The code for the dynamic analysis of mooring lines in frequency domain are programmed and compared with the results from Orcaflex. Orcaflex can only perform the limited dynamic analysis in frequency domain, the dynamic responses in time domain are transformed to response in frequency domain using FFT. The nonlinearities in the mooring lines are linearized using aforementioned method. Two cases of single component and multi-component lines are performed.

2.6.1 Single Component Mooring Line

The configuration of the single component mooring line is shown in Figure 2.14. The length is 668.8m, water depth is 400m. Both top and bottom are pinned, top is at (366.89, 366.89, 390) and bottom is at origin point. The natural frquency can be calculated from the equation of $-\omega^2\mathbf{M}+\mathbf{K}=0$. The natural frequencies of lines from modal analysis are listed in Table 2.2 and also compared with results from Orcaflex.

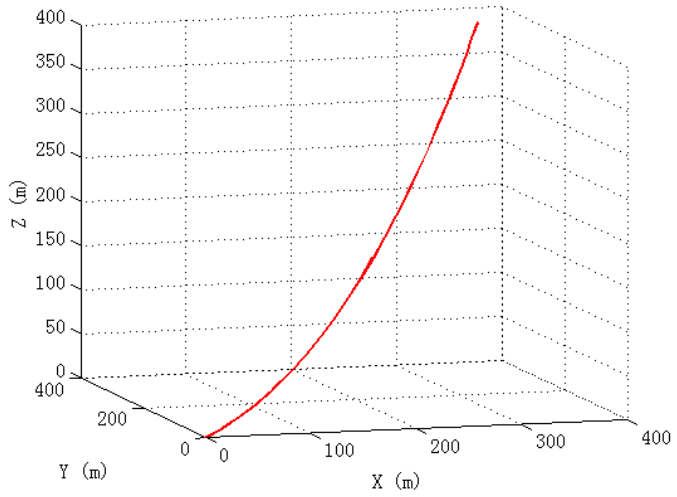

Figure 2.14 Configuration of single mooring line

Table 2.2 Natural frequency of single component mooring line (Hz)

Mode	In-House	Orcaflex
1	0.0518	0.0518
2	0.0961	0.0961
3	0.1027	0.1028
4	0.1439	0.144
5	0.1531	0.1532
6	0.1998	0.1998
7	0.2028	0.2029
8	0.2453	0.2454
9	0.251	0.2511
10	0.2963	0.2964

1) Harmonic excitation

The dynamic analyses of a single component mooring line, R4 chain, under different horizontal surge harmonic excitations are performed in frequency domain and time domain, respectively. The surge motion amplitudes of 1m, 5m and 10m with period of 10s are investigated.

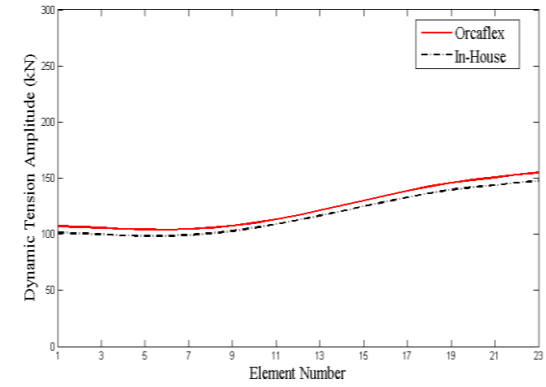

(a) Surge amplitude 1m

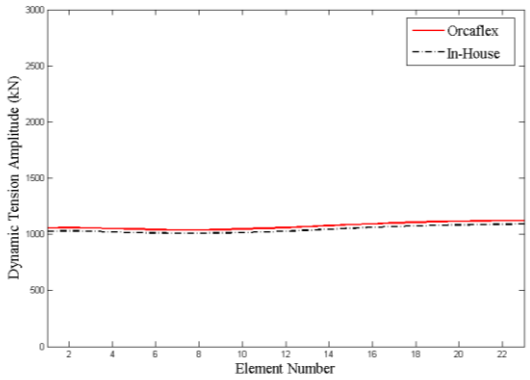

(b) Surge amplitude 5m

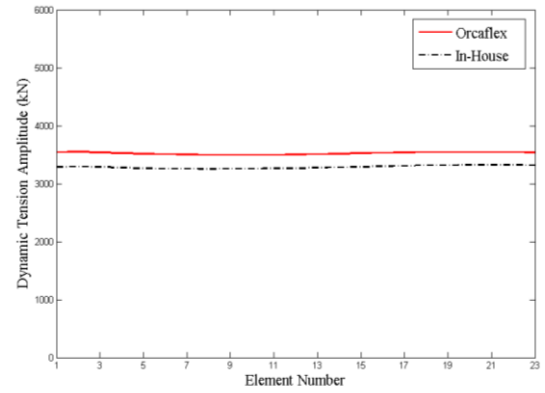

(c) Surge amplitude 10m

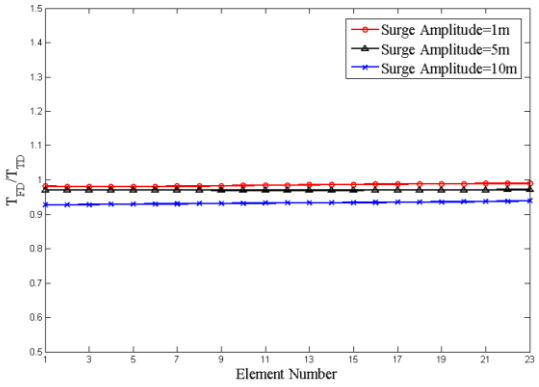

(d) Ratio between T_{FD} and T_{TD}

Figure 2.15 Comparison of dynamic tension amplitude of single component line in frequency and time domain under harmonic excitation

The dynamic tension amplitudes along the line under different surge amplitudes from analysis in frequency domain and time domain results from Orcaflex are presented in Figure 2.15. The difference here, particularly at low amplitude, may be due to the time

domain results were also slightly smaller than Orcaflex. The ratio of dynamic tension amplitude in frequency and time domain decreases with addition of surge amplitude.

2) Regular wave

The frequency domain simulations of single component mooring line under regular wave are performed. The wave height is 10m, 15m and 20m, respectively. The dynamic tension amplitudes under different wave heights are shown in Figure 2.16 and compared with the results from Orcaflex. The difference of dynamic tension amplitude between frequency domain and time domain widens with the increase of wave height.

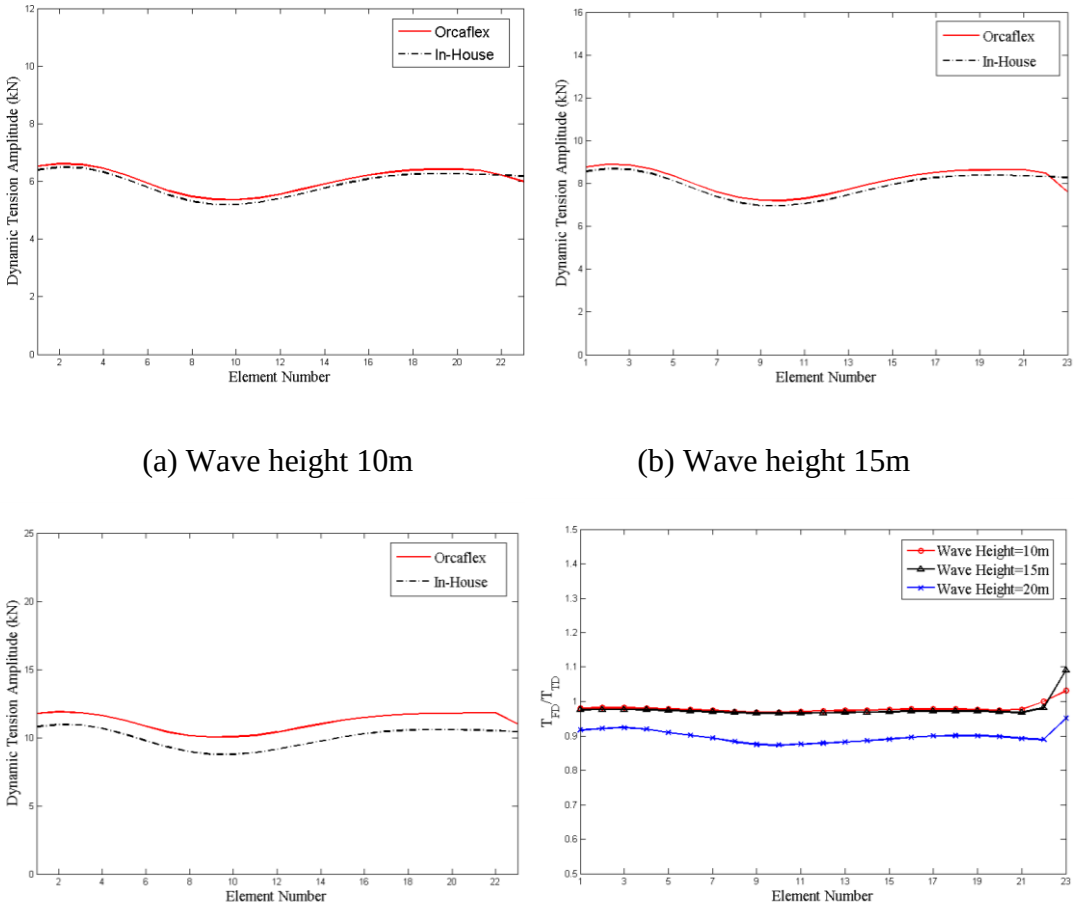

(a) Wave height 10m (b) Wave height 15m

(c) Wave height 20m (d) Ratio between T_{FD} and T_{TD}

Figure 2.16 Comparison of dynamic tension amplitude of single component line in frequency and time domain under regular wave

3) Random Wave with Current

The dynamic analysis in frequency domain for a single component mooring line, R4 chain, is simulated in random waves. The random wave is defined by an ISSC spectrum as shown as follows. The significant wave height is 7.8m and the peak period is 5.6s and the spectrum is shown in Figure 2.17. The current velocity is 1m/s in the x direction.

$$S_\eta(\omega) = \frac{5}{16} H_s^2 \omega^{-5} \omega_p{}^4 \exp\left[-\frac{5}{4}\left(\frac{\omega_p}{\omega}\right)^4\right] \tag{2.80}$$

After linearization and performing the frequency analysis, the spectral density of top tension is presented in Figure 2.19. The dynamic analysis in time domain is simulated for 3-hour using Orcaflex as shown in Figure 2.18 and the response then transformed to frequency domain. The standard variance of top tension is shown in Table 2.3. The difference between them is 13.41%.

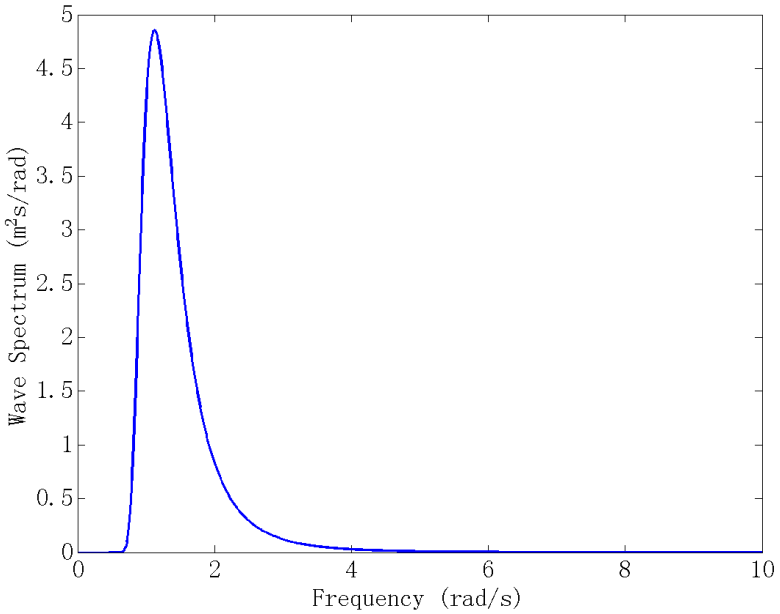

Figure 2.17 Wave spectrum

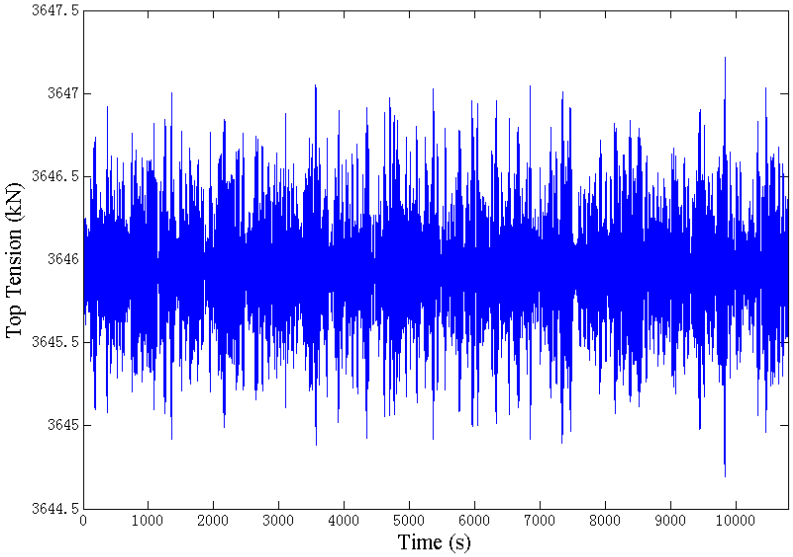

Figure 2.18 Top tension in time series (3 hours) of single component line

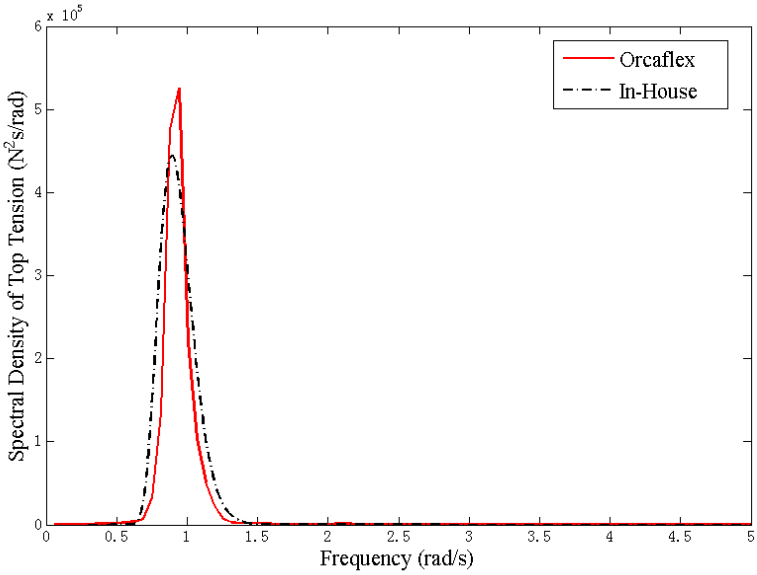

Figure 2.19 Spectral density of top tension single mooring line

Table 2.3 Standard variance of top tension

	In-House	Orcaflex
Standard variance of Top Tension (N)	368.3	318.9

2.6.2 Multi-Components Mooring Line

The frequency analysis for multi-components (R4 chain - Spiral Strand wire - R4 chain) mooring line is also performed. The line configuration is shown in Figure 2.20. The length is 100m, 300m and 268.8m, respectively. Both ends are pinned and positions are the same as single component line. The natural frequencies from modal analysis are compared with the results from Orcaflex in Table 2.4.

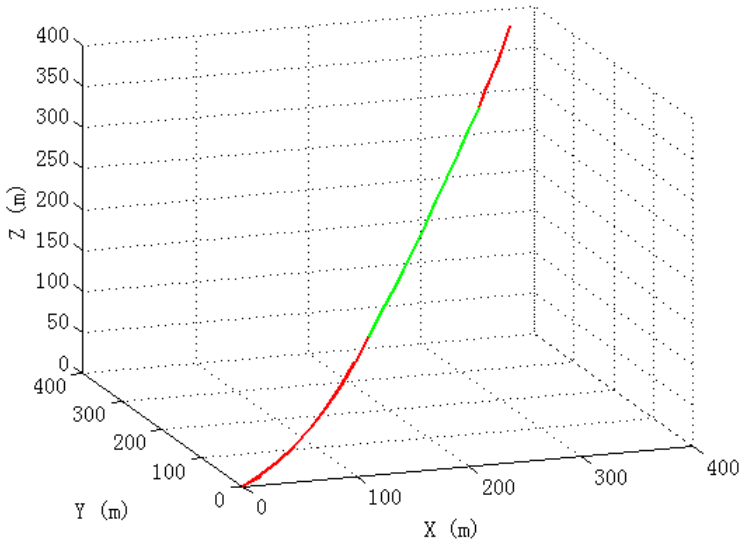

Figure 2.20 Configuration of multi-components mooring line

Table 2.4 Natural frequency of multi-components mooring line (Hz)

Mode	In-House	Orcaflex
1	0.0527	0.0528
2	0.1076	0.1076
3	0.1149	0.1149
4	0.1373	0.1374
5	0.1503	0.1504
6	0.2014	0.2013
7	0.2043	0.2043
8	0.2379	0.2379
9	0.2442	0.2442
10	0.2964	0.2964

1) Harmonic excitation

The dynamic analyses of multi-components mooring line under different surge harmonic excitations are also performed in frequency domain and time domain, respectively. Figure 2.21 gives dynamic tension amplitude along the line in frequency domain and time domain with the surge motion amplitudes of 1m, 5m and 10m. The ratios of dynamic tension amplitude in frequency domain and time domain under wave height of 10m, 15m and 20m are also presented. It can be seen that they agree well when surge amplitude is small.

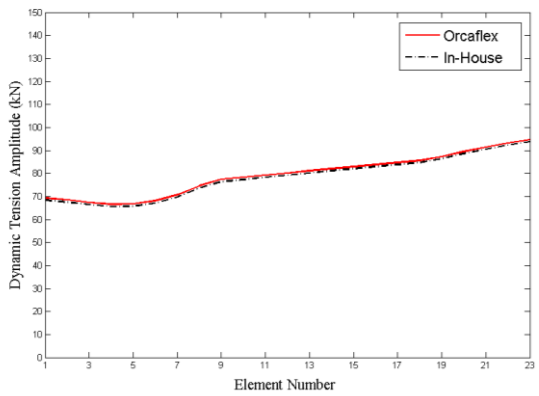

(a) Surge amplitude 1m

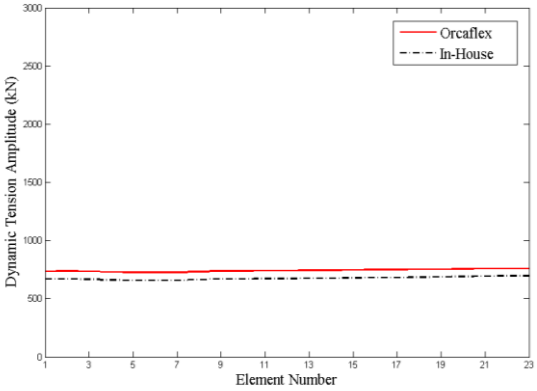

(b) Surge amplitude 5m

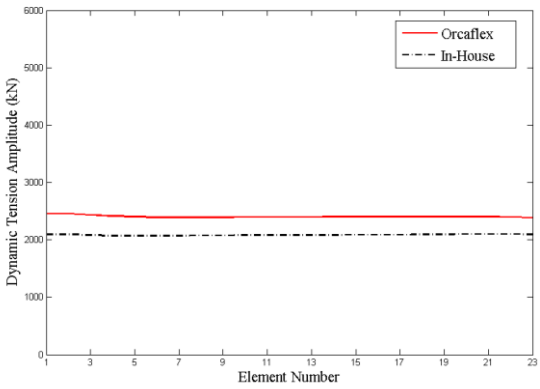

(c) Surge amplitude 10m

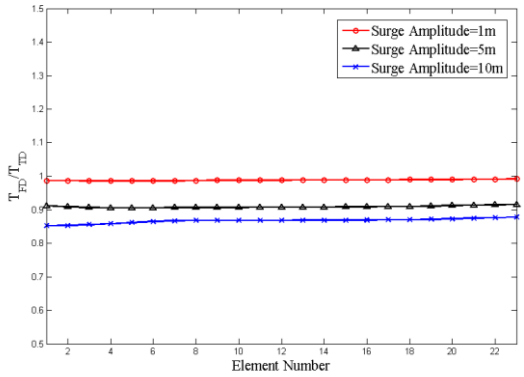

(d) Ratio between T_{FD} and T_{TD}

Figure 2.21 Comparison of dynamic tension amplitude of multi-component line in frequency and time domain under harmonic excitation

2) Regular wave

The frequency domain simulations of multi-components mooring line under regular wave are performed. The wave height is 10m, 15m and 20m, respectively. The dynamic tension amplitudes under different wave heights are shown in Figure 2.22 and compared with the results from Orcaflex. The difference of dynamic tension amplitude between frequency domain and time domain widens with the increase of wave height.

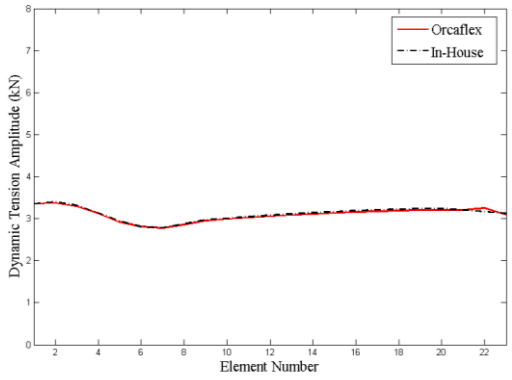

(a) Wave height 10m

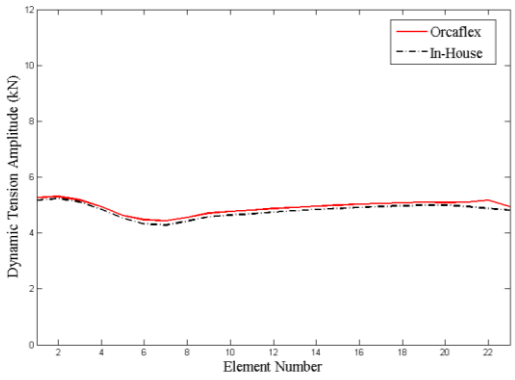

(b) Wave height 15m

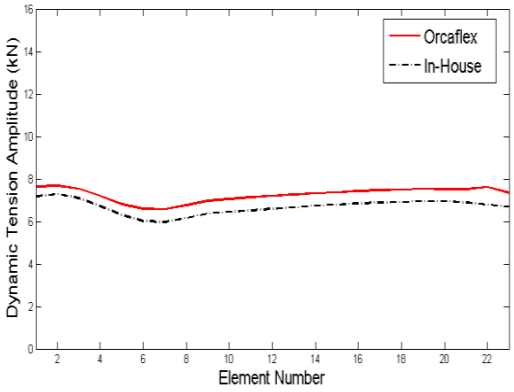

(c) Wave height 20m

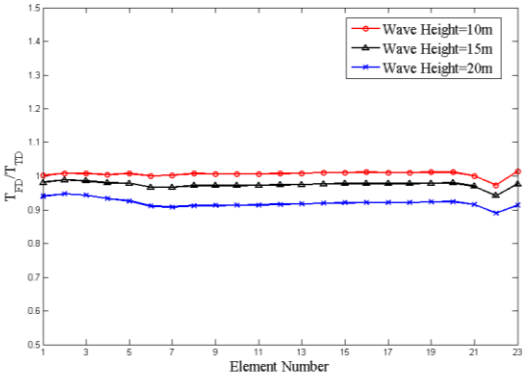

(d) Ratio of dynamic tension amplitude in frequency and time domain

Figure 2.22 Comparison of dynamic tension amplitude of multi-component line in frequency and time domain under regular wave

3) Random Wave with Current

The dynamic analysis in frequency domain for multi-components mooring line under random wave is simulated. The dynamic analysis in the time domain is simulated for 3-hours using Orcaflex as shown in Figure 2.23. Then the top tension response time series is transformed to frequency domain. The frequency analysis for multi-component line is performed to obtain the spectral density of top tension, which is presented in Figure 2.24. The standard variance of top tension is shown in Table 2.5. The difference between them is 5.81%.

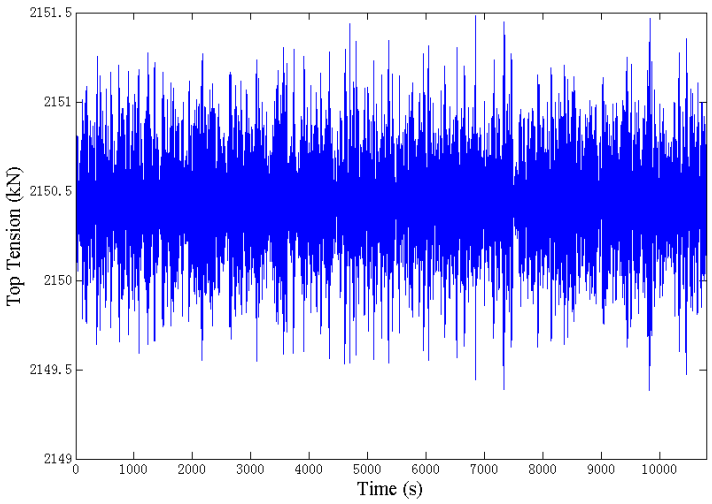

Figure 2.23 Top tension in time series (3 hours) of multi-components line

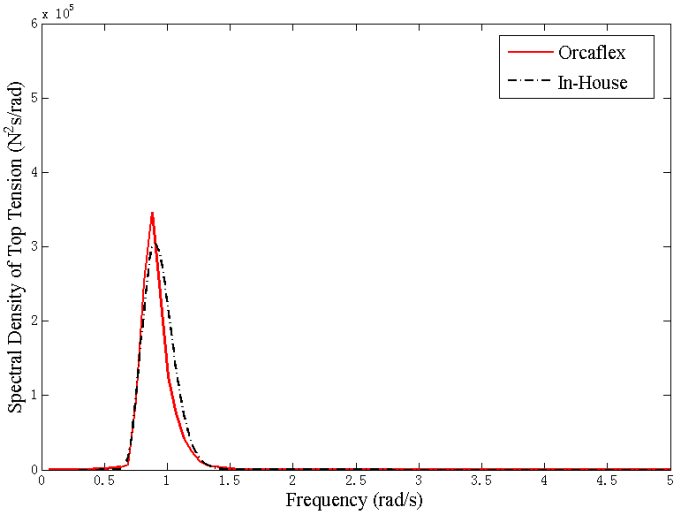

Figure 2.24 Spectral density of top tension single mooring line

Table 2.5 Standard variance of top tension

	In-House	Orcaflex
Standard variance of Top Tension (N)	298.0	280.7

2.7 Conclusion

The numerical procedures for dynamic analysis of mooring lines in time domain and frequency domain are developed in this chapter. The lumped mass method is used to model the mooring lines. In the time domain dynamic analysis, the modified Euler method is used to solve the motion equation of mooring lines. The dynamic analyses of mooring lines under horizontal, vertical harmonic excitations and combined are performed. The cases of single component and multi-component mooring lines under these excitations are studied. The case considering the seabed contact is also included. The program is validated by comparison with the results from commercial software, Orcaflex. For the frequency domain dynamic analysis, an improved frame invariant stochastic linearization method is applied to the nonlinear hydrodynamic drag term. The cases of single component and multi-component mooring lines are studied. The comparison of results shows that frequency domain results agree well with time domain results when the nonlinearity is not very strong (the forced surge amplitude is small) and difference between the standard variance of top tension is 5.81% for random wave. The code developed in this chapter has been applied in LR's mooring software.

3 Hybrid Time and Frequency Domain Method

3.1 Introduction

Coupled analysis should be performed for moored floating structure to obtain a more accurate estimate of the LF motion and improved estimate of the tension in mooring lines due to the importance of the effect of mooring line damping in deep water. In fully coupled time domain analysis, the dynamic motions of the moored FPSO are simulated together at every time step, which is prohibitively time consuming. Several methods considering the damping contribution from lines as a constant have been developed (Connaire et al., 1999; Correa et al., 2002; Ormberg et al., 1998; Ormberg and Larsen, 1998). However, the mooring line damping is nonlinear and thus dependent on the amplitude of the oscillation, which is unknown priori. It also dependent on the vessel offset due to changes in the line geometry and the associated dynamic behavior. In addition, WF motions are especially important for the mooring line damping.

Considering the large mass of an FPSO, it can be assumed that the FPSO's wave frequency motion/loading is unaffected by the mooring/riser, the coupled analysis can then be simplified to some extent, e.g. mooring/riser dynamically coupled to the FPSO low frequency motion. However, such an approach simulated in the time domain will still be very expensive as the mooring/riser dynamic response needs to be computed at every time step, and moreover the time step has to be very small for the mooring/riser. In this chapter, a computationally efficient method using a combined time and frequency domain analysis methodology is proposed where the time domain simulation is used for predicting the low frequency vessel motion and the frequency

domain analysis of the mooring/riser is employed for the wave frequency response. The wave frequency responses of mooring lines are performed for several fixed offsets within the range of the low frequency motion. The damping contributions from the mooring lines are calculated from the wave frequency responses of mooring lines and then updated and transferred to the time domain analysis of low frequency vessel motion.

3.2 Dynamics of Floating Structure

The diffraction of waves around the large-displacement floating structure is significant. The incident waves upon arriving at the structure undergo significant scattering or diffraction. Diffraction of waves from the surface of the structure has a most important effect on the wave loading for these structures. Diffraction analysis is usually used to account for this effect. The responses of the floating structure in a stationary environmental state often include three components: 1) Mean displacement due to mean environmental loads. 2) Wave frequency motions, where it oscillates in the frequency range of the incoming waves, due to first-order wave loads. Low frequency motion, in the frequency range of the natural periods of the moored structure in surge, sway and yaw modes of motion, due to second-order wave loads and low-frequency wind loads. The wave frequency motion of floating structure motion RAO (Response Amplitude Operator), is easily obtained from the linear diffraction analysis. And the low frequency motion in time domain can be calculated using QTFs (Quadratic Transfer Functions). Then the hybrid time/frequency domain method is used for coupled analysis of the FPSO/mooring lines.

3.2.1 Wave Frequency Motion of Floating Structure

The first order wave forces on floating structure are determined by linear (first order) diffraction analysis. The velocity potential a point in the fluid in the presence of a

moving structure in waves can be expressed as be the sum of the following components: the potential of the incident wave as described by linear wave theory; the potential of the diffracted waves when the structure is stationary; the radiated potentials caused by simple harmonic motion of structure in still water. The velocity potential can be written as follows:

$$\Phi^{(1)} = \phi_0 + \phi_7 + \sum_{j=1}^{6} X_j \phi_j \tag{3.1}$$

Where ϕ_0 and ϕ_7 are the incident wave and diffraction wave potential for a unit wave amplitude. X_j denotes the complex motion amplitude in the *j*-th rigid body mode. ϕ_j (j = 1,2,...,6) are radiation potentials caused by a unit amplitude motion in the *j*th mode that represent the fluid generated as a result of wave radiated out from the body as it undergoes pure harmonic motion in *j*-th rigid body mode.

To solve this velocity potential problem during the linear diffraction analysis, numerical methods such as boundary element method, also known as panel or source-sink method are often used. The panels are used to model the structure body surface and a source/sink, defined by a Green's function, is placed in each panel with a strength and phase calculated to meet the velocity potential boundary conditions on the surface of the FPSO hull. The dynamic pressures are computed using the linearized Bernoulli's equation from the calculated velocity potential. The forces acting on the structure, ***P***, are calculated by integrating the pressure over the wetted surface of structure. The total complex hydrodynamic force in a unit amplitude incident wave is:

$$\mathbf{F}_{unit}{}^{(1)} = \int_S \boldsymbol{P}\boldsymbol{n}dS = i\omega\rho \int_S (\phi_0 + \phi_7 + \sum_{j=1}^{6} X_j \phi_j)\boldsymbol{n}dS \tag{3.2}$$

The contribution from the incident potential is called the Froude-Krylov force, $\mathbf{F}_{\text{unit},0}$.

And the force from the diffraction potential is called diffraction force, $\mathbf{F}_{\text{unit},7}$. The sum of them is called wave excitation force. The forces from the radiation potentials are called the radiation forces and are normally expressed in terms of the added mass $\mathbf{M}_a$ and wave damping coefficients **C**, i.e. components in phase with the motion acceleration and velocity respectively.

Then the motion equation of floating structure is:

$$[-\omega^2\mathbf{M} + i\omega\mathbf{C} + \mathbf{K}]\mathbf{X}(\omega) = \mathbf{F}^{(1)}(\omega) \tag{3.3}$$

where $\mathbf{M}=\mathbf{M}_{\text{vessel}}+\mathbf{M}_a$ is the mass matrix, **C** is the damping matrix and **K** is stiffness matrix. $\mathbf{F}^{(1)}$ is the first order wave force vector on floating structure, which obtained from the vector of first order load transfer function $\mathbf{G}^{(1)}$ with wave surface elevation η, defined as

$$\mathbf{F}^{(1)}(\omega) = [\mathbf{F}_{unit,0}(\omega) + \mathbf{F}_{unit,7}(\omega)]\eta(\omega) = \mathbf{G}^{(1)}(\omega)\eta(\omega) \tag{3.4}$$

The displacement response of floating structure is

$$\begin{aligned}\mathbf{X}(\omega) &= (-\omega^2\mathbf{M} + i\omega\mathbf{C} + \mathbf{K})^{-1}\mathbf{F}(\omega) \\ &= (-\omega^2\mathbf{M} + i\omega\mathbf{C} + \mathbf{K})^{-1}\,\mathrm{G}(\omega)\eta(\omega) \\ &= \mathbf{H}(\omega)\eta(\omega)\end{aligned} \tag{3.5}$$

where $\mathbf{H}(\omega)$ is the displacement transfer function or RAO (Response Amplitude Operator).

3.2.2 Low Frequency Motion of Floating Structure

The linear diffraction analysis is only the first order approximation to the wave loads acting on a floating structure in waves. In linear analysis, forces and responses are

proportional to wave amplitude and response frequencies are at the wave frequency. Extension of the first order regular wave to an irregular wave is straightforward through the translation function or RAO. In a second order analysis, the basic case to solve is a bichromatic sea which includes two regular waves with amplitude a_i, a_j and frequencies ω_i, ω_j. The incident free surface elevation is to first order:

$$\eta^{(1)}(x,t) = a_i \cos(k_i x - \omega_i t) + a_j \cos(k_j x - \omega_j t) \tag{3.6}$$

Both components are assumed to in the x direction. First, the first order diffraction analyses for each wave component are performed to get the first order velocity potential and first order response. Then the second order loading can be computed using the pressure integration method, or 'near field' method, introduced by Pinkster (Pinkster, 1980) as below.

$$\begin{aligned}\mathbf{F}^{(2)} = &\int_{\Gamma_0} \frac{1}{2}\rho g\left(\eta^{(1)} - \zeta^{(1)}\right)^2 \mathbf{n}_0 d\Gamma + \mathbf{A}^{(1)} \times \iint_{Sc_0} -\rho \frac{\partial \Phi^{(1)}}{\partial t}\mathbf{n}_0 dS \\ &+ \iint_{Sc_0} -\rho\left(\frac{\partial \Phi^{(2)}}{\partial t} + \frac{1}{2}\nabla\Phi^{(1)2} + \mathbf{X}_p^{(1)} \cdot \nabla \frac{\partial \Phi^{(1)}}{\partial t}\right)\mathbf{n}_0 dS\end{aligned} \tag{3.7}$$

Where $\zeta^{(1)}$ denotes the vertical motion of a point linked to the waterline Γ, $\mathbf{A}^{(1)}$ is the angular motion, $\mathbf{X}_p^{(1)}$ is the motion of a point P linked to the hull. Subscripts 0 refer to the geometry at rest: Sc_0 is the wetted hull at rest and $\mathbf{n}_0$ is the inward normal vector.

The second order force can be written as the following form.

$$\begin{aligned}\mathbf{F}^{(2)}(t) = &a_i^2 \boldsymbol{f}_d(\omega_i) + a_j^2 \boldsymbol{f}_d(\omega_j) + \mathrm{Re}\left\{a_i^2 \boldsymbol{f}_+^{(2)}(\omega_i,\omega_i)e^{-2i\omega_i t} + a_j^2 \boldsymbol{f}_+^{(2)}(\omega_j,\omega_j)e^{-2i\omega_j t}\right. \\ &\left. + 2a_i a_j \boldsymbol{f}_-^{(2)}(\omega_i,\omega_j)e^{-i(\omega_i-\omega_j)t} + 2a_i a_j \boldsymbol{f}_+^{(2)}(\omega_i,\omega_j)e^{-i(\omega_i+\omega_j)t}\right\}\end{aligned} \tag{3.8}$$

where $\boldsymbol{f}_-^{(2)}(\omega_i,\omega_j)$ and $\boldsymbol{f}_+^{(2)}(\omega_i,\omega_j)$ are the difference and sum frequency QTF

(Quadratic Transfer Functions). $\boldsymbol{f}_d(\omega_i) = \boldsymbol{f}_-^{(2)}(\omega_i, \omega_i)$ is the mean wave drift force terms.

The second order analysis determines wave forces which are proportional to wave amplitude squared and oscillating with the sum ($\omega_i+\omega_j$) and difference ($\omega_i-\omega_j$) frequencies. The second order wave forces are made up of three components: a constant term called the mean wave drift force; difference frequency terms, which have frequencies given by the differences between combinations of different wave component frequencies; sum frequency terms, which have frequencies given by the sums of combinations of wave component frequencies. The constant and difference terms are known as the wave drift loads. The second order wave forces are much smaller than first-order ones and cover a much wider range of frequencies. The moored structure's natural frequencies in surge, sway and yaw are typically quite low and so the difference frequency second order forces can generate large slow drift excursions in these directions, while sum frequency forces can cause the springing response of TLPs. In this study for the second order forces on FPSO, only the former is accounted for.

The random wave can be represented by the summation of a large number of sine waves as fol1ows:

$$\eta(t) = \sum_{i=1}^{N} a_i \cos(\omega_i t + \theta_i) \tag{3.9}$$

Then the corresponding wave drift force in random wave is given by the double summation:

$$\mathbf{F}^{(2)}(t) = \sum_{i=1}^{N}\sum_{j=1}^{N} a_i a_j \boldsymbol{f}_-^{(2)}(\omega_i, \omega_j)\cos[(\omega_i - \omega_j)t + (\theta_i - \theta_j)] \tag{3.10}$$

For the difference frequency force, a large frequency difference ($\omega_i - \omega_j$) gives a smaller oscillation period which is further away from the resonance period of the structure. This means we can estimate the off-diagonal terms close to the leading diagonal using Newman proposed approximation:

$$\boldsymbol{f}_{-}^{(2)}(\omega_i, \omega_j) = \frac{1}{2}\left[\boldsymbol{f}_d(\omega_i) + \boldsymbol{f}_d(\omega_j)\right] \tag{3.11}$$

However, direct summation for wave drift force is still relatively time consuming. Newman (1974) proposed an approximate method for the double summation by the square of a single series. The wave drift force can be written as

$$\mathbf{F}^{(2)}(t) = 2\left(\sum_{j=1}^{N} a_j \sqrt{\boldsymbol{f}_d(\omega_j)}\cos(\omega_i t + \theta_j)\right)^2 \tag{3.12}$$

This method implies that only N terms should be added together at each step compared to N^2 terms by Eq.(3.10). The calculated wave drift damping can also account for encounter frequency using a method that modifies the ordinary QTFs (Molin, 1994).

The wind forces acting on a moored structure are calculated using the following equation (OCIMF, 1994):

$$\mathbf{F}_w = \frac{1}{2} C_w \rho_A \boldsymbol{V}_w |\boldsymbol{V}_w| A \tag{3.13}$$

where F_w is the wind force, C_w is shape coefficient and A is the projected area, ρ_A is the air density, V_w is the wind velocity measured at an elevation of 10 meters above the water surface. The wind is assumed to be steady and it supplies a mean force for floating structure.

The current force also uses the drag load formula, as for wind force.

$$\mathbf{F}_c = \frac{1}{2} C_c \rho \boldsymbol{V}_c |\boldsymbol{V}_c| LD \tag{3.14}$$

where C_c is coefficient, ρ is the seawater density, L is the length between perpendiculars and D is the draught.

The low frequency motion equation of floating structure in time domain is as follows.

$$\mathbf{M}_V \ddot{\mathbf{X}} = \mathbf{F}^{(2)}(t) + \mathbf{F}_w + \mathbf{F}_c \tag{3.15}$$

where $\mathbf{M}_V$ is mass matrix of floating structure, FPSO.

3.3 Hybrid Time and Frequency Domain Method

Coupled analysis in time domain should perform simulations of mean, low, and wave frequency vessel and mooring system responses together. Obviously this approach involves solving the general equations of motion for the combined mean, low, and wave frequency responses of the vessel, mooring lines/risers. This approach fully takes the coupling between the vessel and the mooring/riser system into account. The low frequency damping from the vessel, mooring lines/risers are internally generated in the simulation. However, this approach requires very high computer resources.

To solve this computer resource problem, an improved hybrid method will be developed, in which the low frequency motion of FPSO is simulated in the time domain while the wave frequency motion of mooring lines at a given mean offset position is solved in the frequency domain. This method is based on the assumption that the LF and WF motion have different time scales because the low frequency motion is slowly varying compared to the wave frequency motion. In this method, the mooring line damping to the low frequency motion is evaluated separately from wave frequency analysis in frequency domain and transformed back for low frequency

motion. A series of frequency domain analysis of the WF response is carried out at fixed intervals. The schematic diagram of this method is shown in Figure 3.1. The calculation step is as follow:

1. The vessel's wave frequency (WF) motion with mooring is calculated in the frequency domain at several locations (X_1, X_2,…X_i) along the LF motion range of vessel. The mooring analysis is performed with linearization of drag force.

2. At position X_i, the frequency domain analysis of the mooring, provides the mean top tension of mooring T_i.

3. LF motion is solved in time domain with second order force and the mean mooring top tension T_i between two locations (X_i, X_{i+1}).

4. At position X_{i+1}, the top tension of mooring T_{i+1} is updated from the frequency domain analysis of WF motion of vessel and mooring line.

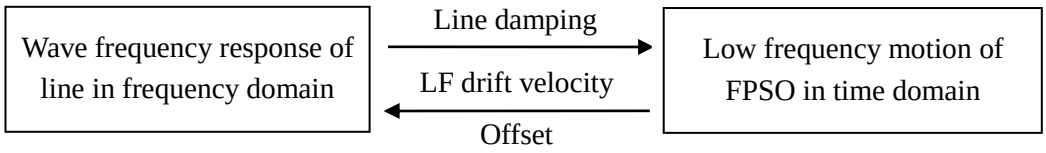

Figure 3.1 Illustration of Hybrid time and frequency method

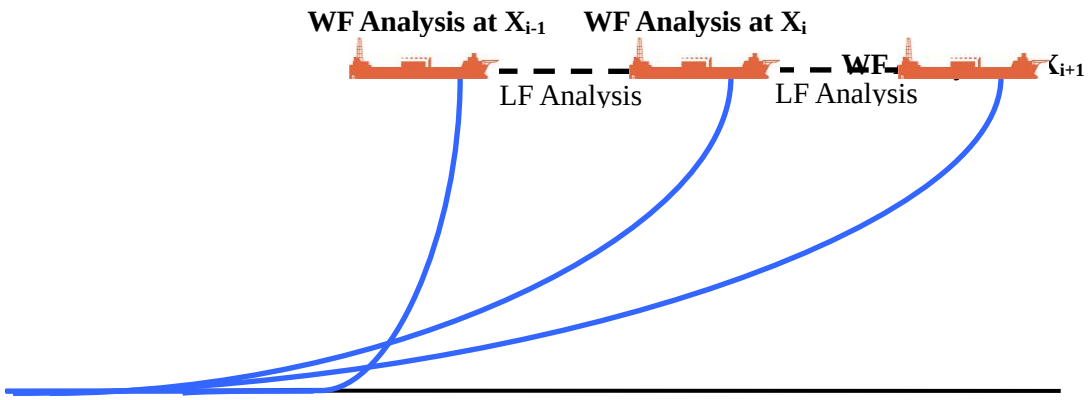

Figure 3.2 Wave frequency response of mooring line in frequency domain

Wave frequency motion equation:

$$(-\omega^2\mathbf{M} + i\omega\mathbf{Q} + \mathbf{K})\mathbf{r}(\omega) = \mathbf{M}_I\ddot{\boldsymbol{u}}(\omega) + \mathbf{Q}\boldsymbol{u}(\omega) \tag{3.16}$$

where $\mathbf{Q}$ is the linearized damping matrix, $\mathbf{K}$ is the stiffness matrix, $\mathbf{M}_I$ is the inertia force coefficient matrix. Assuming that the FPSO's wave frequency motion is unaffected by the mooring lines due to its much greater mass. The FPSO's wave frequency motion can be obtained with displacement RAO. As the low frequency drift velocity is slow and can be treated as a constant current. The wave frequency response of mooring lines in frequency domain can be obtained based on linearized approach. Then the tension of top end will be fed back into the low frequency motion as the damping contribution.

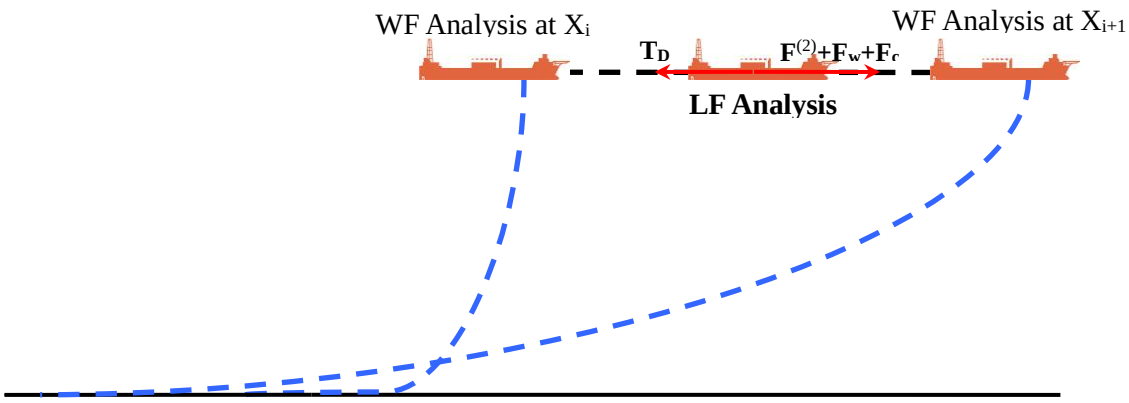

Figure 3.3 Low frequency motion of FPSO in time domain

Low frequency motion equation of FPSO:

$$\mathbf{M}_V \ddot{\mathbf{X}} = \mathbf{F}^{(2)} + \mathbf{F}_w + \mathbf{F}_c + \mathbf{T}_D \tag{3.17}$$

where $\mathbf{M}_V$ is mass matrix of FPSO. $\mathbf{T}_D$ is the damping to the low frequency FPSO motion from the wave frequency response of mooring lines. It can be accounted for in the form of the top tension from frequency domain analysis. As there are two different time scale for wave frequency motion and low frequency motion and latter is very slow, therefore the effect of mooring in wave frequency motion on very slow LF motion is taken into account the mean top tension at different position during the low frequency motion.

The total response of FPSO/mooring line can be combined wave frequency motions with response of the low frequency motions. The response of wave frequency motions in frequency domain is transformed to a time history, which is added to response of low frequency motions to arrive at the combined response. The seed values for generating wave frequency and low frequency time histories should be the same to yield consistent results.

3.4 Numerical Case

The irregular wave assumes it is a linear superposition of a number of airy waves. The irregular wave elevation is generated with ISSC spectrum. The significant wave height is 7m and wave period Tz is 8s. The generated wave is compared with Orcaflex's wave in Figure 3.4. Figure 3.5 and 3.6 present wave particle velocity at x=10 m varies along the water depth at t=0s and 15s. It matches well with Orcaflex's results.

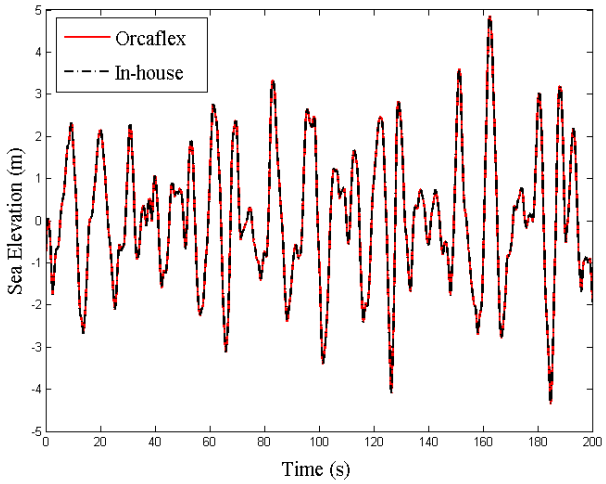

Figure 3.4 Wave elevation in time series

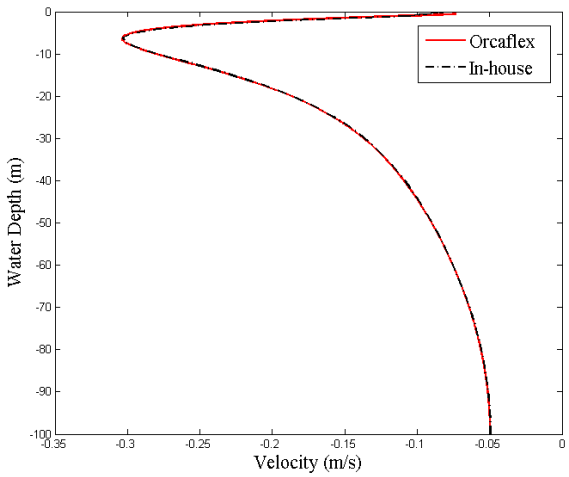

Figure 3.5 Wave particle velocity at x=10s and t=0s

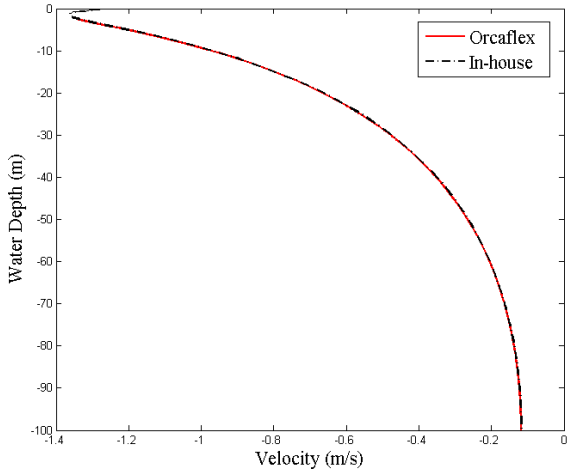

Figure 3.6 Wave particle velocity at x=10s and t=15s

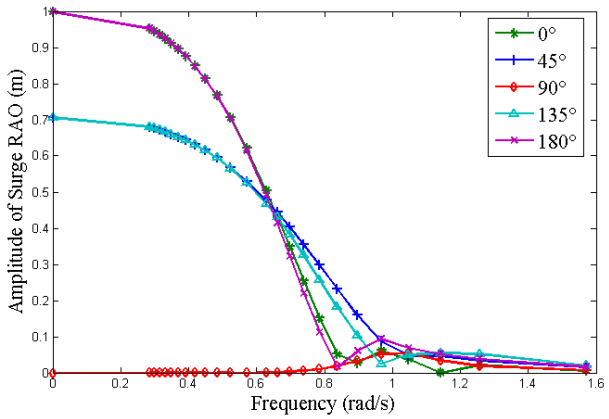

Figure 3.7 Amplitude of surge RAO

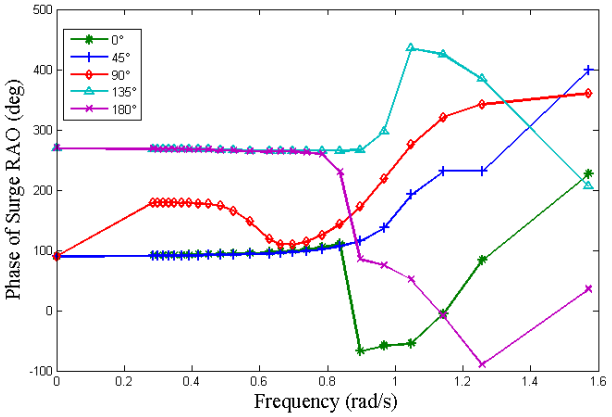

Figure 3.8 Phase of surge RAO

The prediction of wave frequency motion, from the motion RAO shown in Figure 3.7 and 3.8 with the wave elevation above, is presented in Figure 3.9. The hydrodynamic analysis was assessed by use of AQWA. The prediction of initial low frequency motions are calculated from the QTF in Figure 3.10. The LF surge motion shown in Figure 3.11 and 3.12 only consider the surge LF force applied on the vessel. Only head sea is taken into account for the numerical case.

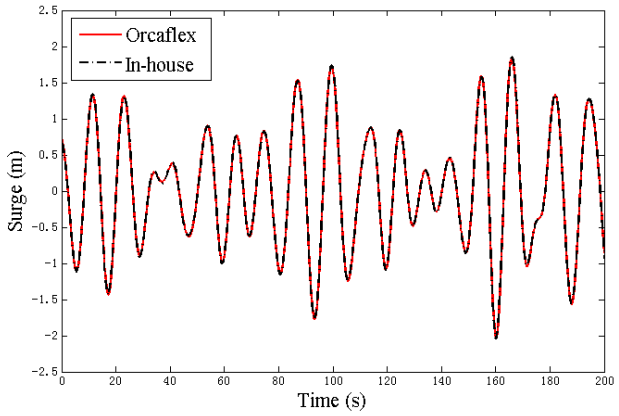

Figure 3.9 Surge motion under random wave

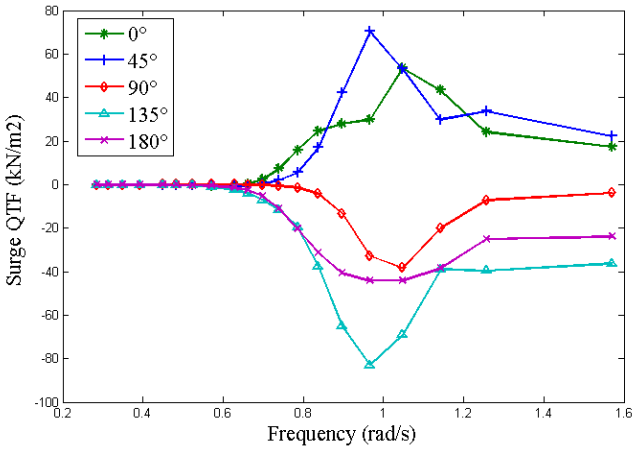

Figure 3.10 Surge QTF

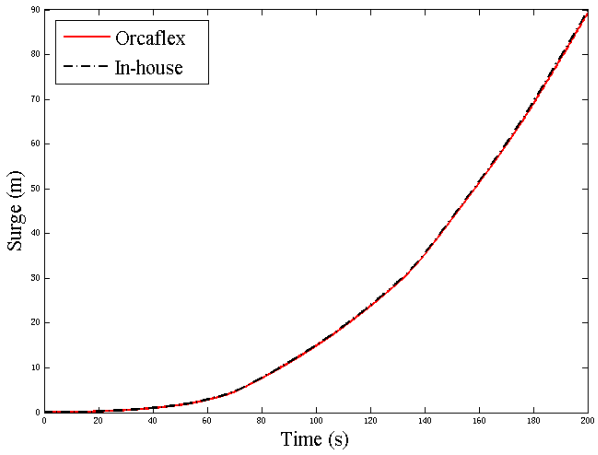

Figure 3.11 LF surge motion under irregular wave

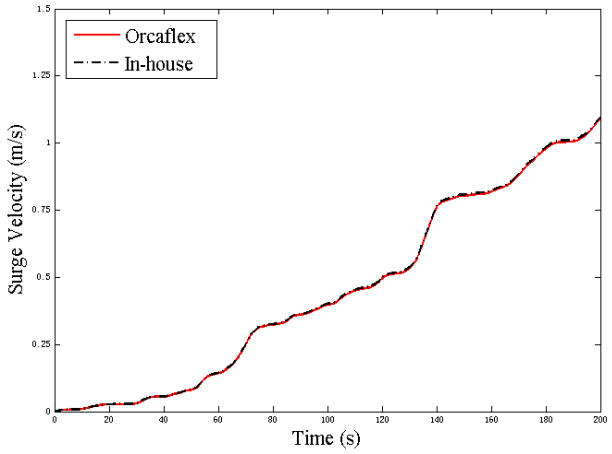

Figure 3.12 LF surge velocity under irregular wave

The configuration employed here is the same as in Figure 2.10, which is a multi-component mooring line (R4 chain - Spiral Strand wire - R4 chain). The line length is 100, 400 and 1480 m, respectively. Figure 3.8 presents the line tension and compared with the results from Orcaflex. The standard variance between them are 5.7%. And the cost for time can be reduced to one tenth of conventional coupled simulation.

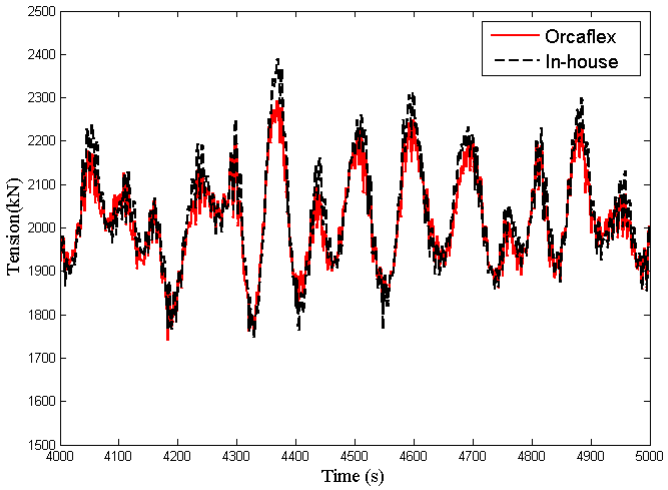

Figure 3.13 Line tension under irregular wave

3.5 Conclusion

This chapter proposed a combined time and frequency domain analysis methodology where the time domain simulation is used for predicting the low frequency motion of FPSO and the frequency domain analysis of the mooring/riser is employed for the wave frequency response separately. This method fully separated the analyses of FPSO and mooring line, meanwhile the position-dependent damping of mooring line was taken into account rather than just used a constant damping coefficient. This method could adopt a large time step for the low frequency motion of the FPSO.

4 Long Term Extreme Analysis by All Sea States Method

4.1 Introduction

Mooring systems are used for station keeping of offshore floating installations including, for example, FPSOs. Mooring lines are subjected to environmental loads such as wave and current, and the motions of floating structure. The floater motions are commonly split into LF, WF and HF motion components. The slow drift low frequency motion is usually near to the natural frequency of moored FPSO, which means resonant motion could be excited. Once it occurs, large low frequency motion can yield quite high mooring load (Barltrop, 1998). The low frequency drift motion amplitude is very dependent on the surge damping and Huse found the damping from mooring lines makes a significant contribution to the surge damping, especially in deepwater (Huse and Matsumoto, 1989). The traditional global response analyses of moored floating structures are calculated in a way known as de-coupled analysis. The damping of mooring lines is neglected or simplified by an equivalent linear damping in the conventional de-coupled analysis. These simplifications will become less accurate when the water depth increases (Garrett, 2005; Ormberg and Larsen, 1998). Therefore, coupled analysis should be performed in order to accurately predict the FPSO motions as well as the mooring and riser responses with due regard of the FPSO/mooring coupling effects. In the coupled analysis, the mooring lines are included in the model along with the FPSO and damping of the mooring lines is incorporated directly.

The mooring lines should have sufficient strength to withstand the load effects imposed by the metocean environment. In addition, the extreme response of FPSO offset has a great influence on riser design. Traditional design approach based upon

extreme load case analysis may not necessarily produce safe designs. Probabilistic design provides a more rational basis. Long term statistics of the response, which takes into account the contribution of every short term condition, is the most accurate method to determine extreme load effects. However, coupled dynamic analysis of a moored FPSO for every short term condition (often 3 hours) is time consuming because time domain simulation is required for taking into account the coupling effects between FPSO and lines (Ran et al., 1999) and the long term extreme analysis needs to establish short term probabilistic responses for a large number of sea states.

In this chapter, an approach for the long term extreme analysis of moored FPSO systems, based on the Kriging metamodel, is proposed. First, a test case is devised to illustrate the Kriging metamodel. Then it is applied to the long term extreme analysis of FPSO mooring systems. A series of short term probabilistic distributions of mooring line tension and FPSO offset under the selected sea states by design of experiment are established. Kriging metamodels, which represent the mapping between the sea states characteristics and short distribution parameters, are established with the training data from a small number of short term distributions parameters. The accuracy of metamodel is checked. Finally, the long term distribution of FPSO mooring systems based on all sea states can be established based on the metamodel.

4.2 Short Term Extreme Analysis

For the short term stochastic method, the extreme response can be estimated as the expected or most probable largest response peak for the specified duration of the design condition. For the narrow banded Gaussian response process, the distribution follows the Rayleigh distribution. For the moored floating structure, the response is non-Gaussian due to the nonlinear effect, which can be considered by the nonlinear

time simulation. Since the limitation of the computational costs, the duration of the simulation is often shorter than the specified duration of the design condition. Therefore, the extrapolation is required for the estimation of the extreme response.

4.2.1 Extreme Response Estimation Based on Peaks

For the narrow banded stationary response process $X(t)$, its peaks are the maxima between adjacent zero-upcrossing. The major challenge is related to selection of an adequate probabilistic distribution model for the individual peaks of the response process. Special attention should be paid to the upper tail of the distribution, which is of vital importance for the estimation of extreme values. For the linear system, the response process is a Gaussian process as the wave elevation is a Gaussian process. It can be well modelled by a Rayleigh distribution. For the nonlinear system, $X(t)$ is non-Gaussian and can be modelled by Weibull distribution. The selected model can be fitted to the simulated peak samples by an appropriate statistical estimation technique, e.g. method of moments, maximum likelihood method etc.

Let $X_e = \max\{X_1, X_2, ..., X_N\}$ and $X_1, X_2, ..., X_N$ are the peaks of process $X(t)$ during the period T. Assuming that the peaks are independent, and then the cumulative distribution function of the extreme value for a short term period T can be expressed as follows.

$$\begin{aligned} F_{X_e}(x) &= P\{X_e \le x\} \\ &= P\left\{X_1 \le x, X_2 \le x, \ldots, X_N \le x\right\} \\ &= P\left\{X_1 \le x\right\} \cdot P\left\{X_2 \le x\right\} \cdots\cdots P\left\{X_N \le x\right\} \\ &= \left[F_{X_p}(x)\right]^N \end{aligned} \tag{4.1}$$

The exact distribution of $F_{X_e}(x)$ can be accurately approximated by the Gumbel distribution for marine structures (Haver et al., 1998; Naess and Gaidai, 2009; Vázquez-hernández et al., 2011).

$$F_{X_e}(x) = \exp\left\{-\exp\left[-\left(\frac{x-\alpha}{\beta}\right)\right]\right\} \tag{4.2}$$

4.2.2 Extreme Response Estimation Based on Upcrossing Rate

Another statistical approach for predicting extreme values is based on the upcrossing rates. Assuming that the response $X(t)$ can be modeled as a stationary stochastic process. The *x*-upcrossing means that the level x is exceeded with positive slope. Figure 4.1 shows the example of process $X(t)$ with upcrossings and each upcrossing is marked with a circle.

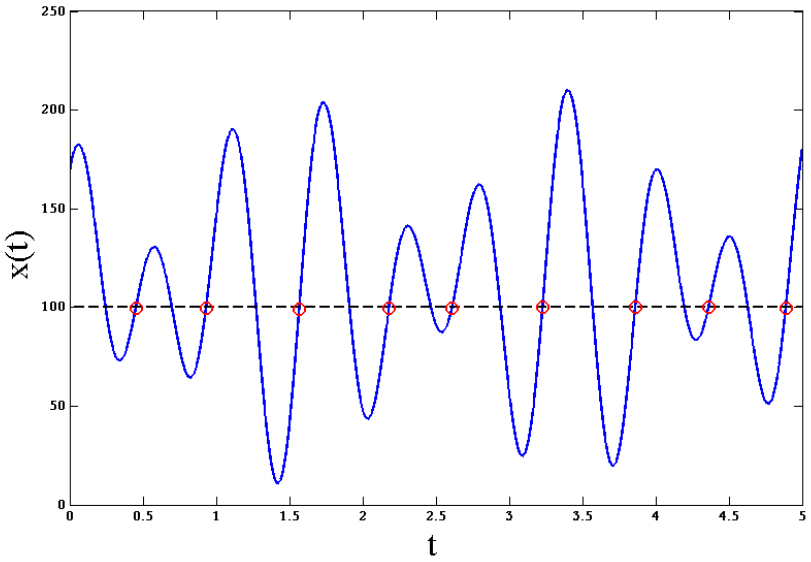

Figure 4.1 Upcrossing analysis of process *X*(t)

The random number of times that the process $X(t)$ upcrosses the level x during the time interval T is $N^+(x;\mathrm{T})$. It can be expressed by $\mathrm{E}[N^+(x;\mathrm{T})] = \mathrm{E}[v^+(x)]\mathrm{T}$

for stationary process, where $v^+(x)$ is the mean rate of *x*-upcrossing of $X(t)$. Under the assumption that the upcrossing rates are statistically independent such that they constitute a Poisson process, then the extreme value distribution can be expressed in terms of the average upcrossing rate by the following formula for a stationary short-term sea state.

$$\mathrm{F}_X(x) = \exp\{-v^+(x)\,\mathrm{T}\} \tag{4.3}$$

The mean upcrossing rate can be estimated from the ergodic mean value for the ergodic response process.

$$v^+(x) = \lim_{\mathrm{T}\to\infty} \frac{n^+(x;\mathrm{T})}{\mathrm{T}} \tag{4.4}$$

where $n^+(x;\mathrm{T})$ is a realization of $N^+(x;\mathrm{T})$. It denotes the counted number of upcrossings during time T. If M times responses of a suitable time interval T_0 are simulated, the appropriate mean value of $v^+(x)$ can be estimated by the formula given in Eq.(4.5), where the $n_j^+(x;\mathrm{T}_0)$ is the counted number of upcrossings of the level x for the no. j response.

$$\hat{v}^+(x) = \frac{1}{k\,\mathrm{T}_0} \sum_{j=1}^{k} n_j^+(x;\mathrm{T}_0) \tag{4.5}$$

The 95% confidence interval for the value $v^+(x)$ can be evaluated as follows.

$$\mathrm{CI}^{\pm}(x) = \hat{v}^+(x) \pm 1.96 \frac{\hat{s}(x)}{\sqrt{M}} \tag{4.6}$$

where $\hat{s}(x)$ is empirical standard deviation of $v^+(x)$ and

$$\hat{s}(x) = \frac{1}{M-1} \sum_{j=1}^{M} \left[\frac{n_j^+(x;\mathrm{T}_0)}{\mathrm{T}_0} - \hat{v}^+(x)\right]^2 \tag{4.7}$$

The mean upcrossing rate $v^+(x)$ as a function of the level x is in general highly regular in a particular manner. Naess and Gaidai (2008) proposed that the mean upcrossing rate tail behaves very closely like the exponential function $\exp\{-a(x-b)^c\}$ ($x \geq x^*$). The x^* is the tail marker that corresponds to the beginning of regular tail behavior. The mean upcrossing rate can be expressed as

$$v^+(x) = q(x)\exp\left\{-a(x-b)^c\right\}, \quad x \geq x^* \tag{4.8}$$

where a, b, c are suitable constants and the $q(x)$ varies slowly compared with the exponential function such that it can be considered as a constant. These parameters can be estimated by plotting $\ln\left|\ln(v^+(x)/q)\right|$ versus $\ln(x-b)$ or doing the optimization at the log level by minimizing the mean square error function, the detail will be discussed in Chapter 7.

4.3 All Sea States Method

The most accurate method for predicting extreme response is some sort of a stochastic long term response analysis if the response depends both on sea severity and on the period and on the previous history of the wave process (Naess and Moan, 2012). In order to obtain a consistent estimate for the q-probability response, the long term distribution of the response is needed. The long term variability can be described in various ways. One may consider the long term distribution of:

- The individual maxima or peaks of the response process.
- The d-hour (0.5-hour for Gulf of Mexico or 3-hour for North Sea) maximum of the response process.
- The annual extreme value of the response process.

The general approach for long term statistics of structural response is to work through all the sea states. Short term probabilistic distribution needs to be established for a large number of short term sea states (often 3 hours). Then long term distribution can be obtained based on all peak values by the following formula when the short term sea state is characterized by significant wave height H_S and spectral peak period T_p (Battjes, 1972).

$$F_{X_p}(x) = \frac{1}{\bar{V}_X^+(0)} \int_{h_s} \int_{t_p} V_X^+(0 \mid h_s, t_p) F_{X_p \mid H_s T_p}(x \mid h_s, t_p) f_{H_s T_p}(h_s, t_p) dt_p dh_s \tag{4.9}$$

X_p is the peak value of response process $X(t)$, defined as the maximum value of $X(t)$ between two consecutive zero upcrossings. $\bar{V}_X^+(0)$ denotes the long term average zero-upcrossing rate given by

$$\bar{V}_X^+(0) = \int_{h_s} \int_{t_p} V_X^+(0 \mid h_s, t_p) f_{H_s T_p}(h_s, t_p) dt_p dh_s \tag{4.10}$$

$V_X^+(0 \mid h_s, t_p)$ is the average zero-upcrossing rate for each short term condition given H_s and T_p. $f_{H_s T_p}(h_s, t_p)$ is the joint probability density function for the sea state characteristics, significant wave height H_s and spectral peak period T_p.

An extreme value distribution of the short term response can be applied to predict the long term response distribution instead of using the distribution of each peak. We can obtain the conditional distribution of the largest peak values during a short term (3 hours):

$$F_{X_{3h} \mid H_s T_p}(x \mid h_s, t_p) = \left(F_{X_p \mid H_s T_p}(x \mid h_s, t_p) \right)^{k(h_s, t_p)} \tag{4.11}$$

where $k(h_s, t_p) = \nu_X^+(0 \mid h_s, t_p) T$ is the number of peak values during a short term condition given H_s and T_p.

If the number is large enough, conditional distribution of the largest peak values can be accurately approximated by Gumbel distribution:

$$F_{X_{3h}|H_sT_p}(x\,|\,h_s,t_p)=\exp\left\{-\exp\left[-\frac{x-\alpha(h_s,t_p)}{\beta(h_s,t_p)}\right]\right\} \tag{4.12}$$

where $\alpha(h_s,t_p)$ and $\beta(h_s,t_p)$ are location and scale parameters.

Then the long term distribution of 3-hour extreme can be given as follows.

$$F_{X_{3h}}(x)=\int_{h_s}\int_{t_p}F_{X_{3h}|H_sT_p}(x\,|\,h_s,t_p)\,f_{H_sT_p}(h_s,t_p)dt_p dh_s \tag{4.13}$$

$F_{X_{3h}|H_sT_p}(x\,|\,h_s,t_p)$ is the conditional distribution of the 3-hour extreme for each short term condition given H_s and T_p. $f_{H_sT_p}(h_s,t_p)$ is the joint probability density function for the sea state significant wave height H_s and spectral peak period T_p. It consists of a marginal distribution of H_s and a conditional distribution of T_p for given H_s.

$$f_{H_sT_p}(h_s,t_p)=f_{H_s}(h_s)\cdot f_{T_p|H_s}(t_p\,|\,h_s) \tag{4.14}$$

Haver and Nyhus (1986) developed a hybrid lognormal and Weibull distribution for the marginal distribution of H_s. They used the transition parameter η to separate the lognormal distribution for smaller values of H_s from the Weibull distribution for larger values, as seen in Eq. (4.15), where λ and ζ^2 are the mean and variance of $\ln H_s$. γ and ρ are the shape and scale parameters in the Weibull distribution.

$$f_{H_s}(h_s)=\begin{cases}\dfrac{1}{\sqrt{2\pi}\zeta h_s}\exp\left\{-\dfrac{(\ln h_s-\lambda)^2}{2\zeta^2}\right\} & h_s\le\eta\\[2ex] \dfrac{\gamma}{\rho}\left(\dfrac{h_s}{\rho}\right)^{\gamma-1}\exp\left\{-\left(\dfrac{h_s}{\rho}\right)^{\gamma}\right\} & h_s>\eta\end{cases} \tag{4.15}$$

The conditional distribution of T_p for given H_s, can be modeled by a lognormal distribution in Eq. (4.16), where μ_{h_s} and $\sigma_{h_s}^2$ are the mean and variance of $\ln T_p$.

$$f_{T_p|H_s}(t_p|h_s) = \frac{1}{\sqrt{2\pi}\sigma_{h_s} t_p} \exp\left\{-\frac{(\ln t_p - \mu_{h_s})^2}{2\sigma_{h_s}^2}\right\} \tag{4.16}$$

Then the value x with return period T years or a probability q of being exceeded per year (q=1/T) can be found by

$$1 - F_{X_{3h}}(x) = \frac{1}{2920\mathrm{T}} \tag{4.17}$$

The long term distribution requires that the short-term response variability be available for all relevant sea states, which is quite time consuming to calculate for complex responses, especially when the coupled dynamic analysis needs to be performed. The challenge for the present problem is to establish a proper model for the conditional distribution of X_{3h} for all sea states. Here, a Kriging metamodel is applied and the detail is given in the section below.

4.4 Kriging Metamodel

Metamodeling techniques, which use statistical techniques to describe the functional relationship between a vector of inputs or variables and the corresponding vector of outputs or responses, have been developed from many different disciplines including statistics, mathematics, computer science, and various engineering disciplines (Simpson et al., 1998; Wang and Shan, 2006). Among these, the Kriging metamodel has recently been applied to the analysis of offshore structures. Yang and Wang (2012) performed the reliability based design optimization of bending stiffener

fatigue life by the use of metamodels in an attempt to reduce the computational time without sacrificing the model accuracy. Three metamodels were used in their study, i.e. response surface model (RSM), radial basis function model (RBF), and Kriging metamodel, and it was found that the accuracy of Kriging model is superior to the other two. He et al. (2013) also used different metamodels for uncertainty quantification of resistance, motions and slamming loads and found that the Kriging model was the most effective metamodel for predicting wave periods and heights and geometry parameters for uncertainty quantification.

The Kriging metamodel (Simpson et al., 1998) treats the deterministic response as a realization of a stochastic process, $y(\mathbf{x})$. It is a two-step process, as seen in Eq.(4.18), a regression model $G(\mathbf{x})$ is constructed based on the training data and a Gaussian process $Z(\mathbf{x})$ which is constructed through the residuals.

$$y(\mathbf{x}) = G(\mathbf{x}) + Z(\mathbf{x}) \tag{4.18}$$

Consider a set of normalized training data: sampled data $\boldsymbol{X} = (\mathbf{x}_1, \mathbf{x}_2, \ldots, \mathbf{x}_m)^T$ are a series of sea states, for variable $\mathbf{x}_i$ has two components, $\mathbf{x}_i = (x_i^{(1)}, x_i^{(2)})$ which represent significant wave height and spectral peak period, and responses $\boldsymbol{Y} = (y_1, y_2, \ldots, y_m)^T$ represent the short term extreme distribution parameters under different sea states. The distribution parameters can be treated as a realization of a stochastic process, $y(\mathbf{x})$, which consists of a regression model $G(\mathbf{x})$ and a Gaussian process $Z(\mathbf{x})$. The Gaussian process is assumed to be mean zero, and covariance is as follows.

$$\mathrm{Cov}(Z(\mathbf{x}_i), Z(\mathbf{x}_j)) = \sigma^2 R(\theta, \mathbf{x}_i, \mathbf{x}_j) \tag{4.19}$$

where σ^2 is the process variance and the correlation function $R(\theta, \mathbf{x}_i, \mathbf{x}_j)$ between each sea state, as seen in Eq.(4.20), is element of the correlation model $\mathbf{R}$ with parameters θ.

$$R(\theta, \mathbf{x}_i, \mathbf{x}_j) = \prod_{k=1}^{n} R_k(\theta, x_i^{(k)} - x_j^{(k)}) \tag{4.20}$$

The correlation function often can employ the form of linear, spline, exponent, or Gauss, as seen in Eq.(4.21)-Eq.(4.24). Figure 4.2 presents the four correlation functions for the one dimensional normalized training data, d is the distance between two arbitrary points. It can be seen that the correlation decreases with d increasing and it decreases faster for a larger theta. For the linear behavior near the origin, the linear or exponent correlation function usually perform well, and for the nonlinear behavior, the Gaussian or spline function would perform better (Isaaks and Srivastava, 1990). The Gaussian correlation function is used in this work.

Linear correlation function:

$$R_k(\theta, x_i^{(k)} - x_j^{(k)}) = \max\left\{0, 1 - \theta_k \left| x_i^{(k)} - x_j^{(k)} \right|\right\} \tag{4.21}$$

Spline correlation function:

$$R_k(\theta, x_i^{(k)} - x_j^{(k)}) = \begin{cases} 1 - 15\left(\theta_k \left| x_i^{(k)} - x_j^{(k)} \right|\right)^2 + 30\left(\theta_k \left| x_i^{(k)} - x_j^{(k)} \right|\right)^3 & 0 \le \theta_k \left| x_i^{(k)} - x_j^{(k)} \right| \le 0.2 \\ 1.25\left(1 - \theta_k \left| x_i^{(k)} - x_j^{(k)} \right|\right)^3 & 0.2 < \theta_k \left| x_i^{(k)} - x_j^{(k)} \right| < 1 \\ 0 & \theta_k \left| x_i^{(k)} - x_j^{(k)} \right| \ge 1 \end{cases} \tag{4.22}$$

Exponent correlation function:

$$R_k(\theta, x_i^{(k)} - x_j^{(k)}) = \exp(-\theta_k \left| x_i^{(k)} - x_j^{(k)} \right|) \tag{4.23}$$

Gaussian correlation function:

$$R_k(\theta, x_i^{(k)} - x_j^{(k)}) = \exp(-\theta_k \left| x_i^{(k)} - x_j^{(k)} \right|^2) \tag{4.24}$$

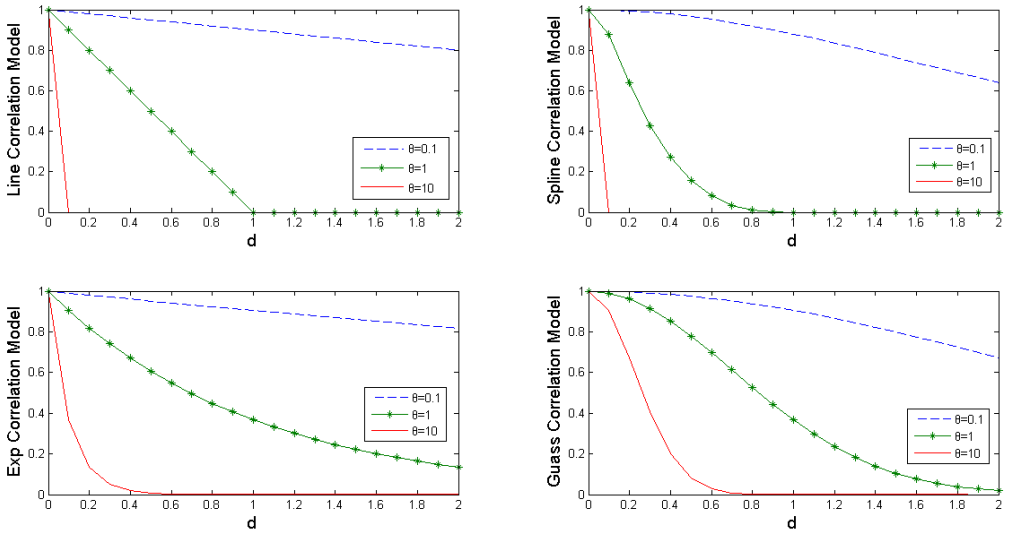

Figure 4.2 Linear, Spline, Exponent and Gaussian correlation function

The regression model G($\boldsymbol{X}$), can be a linear combination of basic function $\boldsymbol{F}$=($\boldsymbol{f}(\mathbf{x}_1)$, $\boldsymbol{f}(\mathbf{x}_2)$,…, $\boldsymbol{f}(\mathbf{x}_m)$)^T as follows.

$$G(\boldsymbol{X}) = \boldsymbol{F}\boldsymbol{\beta} \tag{4.25}$$

where $\boldsymbol{f}(\mathbf{x}_i)$ = ($f_1(\mathbf{x}_i)$, $f_2(\mathbf{x}_i)$,…, $f_t(\mathbf{x}_i)$) and coefficients $\boldsymbol{\beta}$ = (β_1, β_2,…, β_t)^T are regression parameters.

The regression model has the generalized least squares solution and corresponding variance estimate as in Eq.(4.26) and Eq.(4.27), respectively.

$$\boldsymbol{\beta} = (\boldsymbol{F}^T\mathbf{R}^{-1}\boldsymbol{F})^{-1}\boldsymbol{F}^T\mathbf{R}^{-1}\boldsymbol{Y} \tag{4.26}$$

$$\sigma^2 = \frac{1}{m}(\boldsymbol{Y} - \boldsymbol{F}\boldsymbol{\beta})^T\mathbf{R}^{-1}(\boldsymbol{Y} - \boldsymbol{F}\boldsymbol{\beta}) \tag{4.27}$$

The Kriging metamodel is a linear unbiased predictor. The distribution parameters can be obtained through minimizing the mean squared error (MSE) of the predictor, as seen in Eq.(4.28), where $\mathbf{r}(\mathbf{x})$ is the correlation matrix at predicted sea state $\mathbf{x}$, $\mathbf{r}(\mathbf{x})$=[R(θ,x,x_1), R(θ,x,x_2),…, R(θ,x,x_m)]^T.

$$\hat{\mathbf{y}}(\mathbf{x}) = \mathbf{f}(\mathbf{x})\boldsymbol{\beta} + \mathbf{r}(\mathbf{x})^{\mathrm{T}}\mathbf{R}^{-1}(\boldsymbol{Y} - \mathbf{F}\boldsymbol{\beta}) \tag{4.28}$$

It can be seen that the predicted line tension response or offset response depends on unknown parameter θ. The optimal parameter θ can be determined by maximum likelihood estimation or its equivalent minimization problem.

$$\text{Max} \quad -\frac{1}{2}(m\ln\sigma^2 + \ln|\mathbf{R}|) \tag{4.29}$$

Or

$$\text{Min} \quad \sigma(\theta)^2 + |\mathbf{R}(\theta)|^{\frac{1}{m}} \tag{4.30}$$

The optimization problem for parameter θ employs the pattern search method (Song et al., 2008). It is a direct search method that does not involve the gradient of the problem. The process of pattern search contains two moves, exploratory move and pattern move. The former finds out the probable directions and latter execute actual minimizing of the objective function. The detail flow chart for establishing the Kriging metamodel is shown in Figure 4.3. The Design of Experiment (DOE) method, usesa prescribed set of experiments or computer simulations, to obtain the training data as input for Kriging metamodel. DOE can decide how to select the inputs for the deterministic computer code in order to most efficiently control or reduce the statistical uncertainty of the computed prediction. Latin Hypercube Sampling (LHS) (Huntington and Lyrintzis, 1998), a kind of design of experiment is employed in this work. LHS can divide the parameter space into bins of equal probability, with the goal of attaining a more even distribution of sample points in the parameter space than typically occurs with pure Monte Carlo sampling.

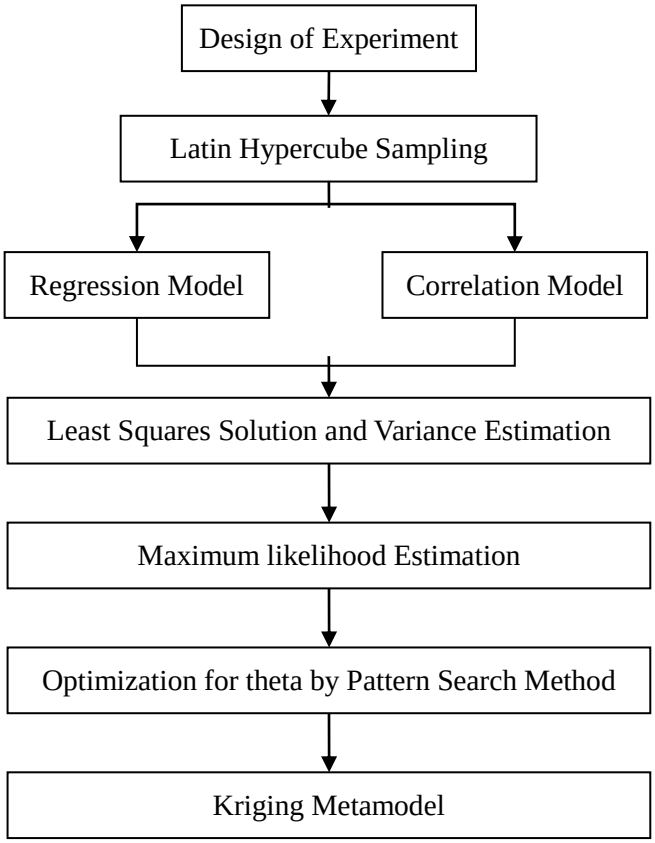

Figure 4.3 Flowchart of Kriging metamodel

4.5 Long Term Extreme Analysis with Kriging Metamodel

If k 3-hour short term simulations for all sea states are carried out, the Gumbel parameters, α and β, for each sea state can be obtained by point estimates. Then the long term extreme probability distribution or exceedance probability can be easily estimated through all sea states according to the Eq.(4.13). However, this is computationally time consuming, as discussed. Here, the Kriging metamodel is used to construct the metamodel of short term distribution by mapping the relations between the sea states characteristics and Gumbel distribution parameters, $\boldsymbol{\alpha}=\alpha(h_s,t_p)$ and $\boldsymbol{\beta}=\beta(h_s,t_p)$. The flowchart of long term extreme analysis based on Kriging metamodel is shown in Figure 4.4. Firstly, the Latin hypercube sampling is

performed to select the sampled sea states from all sea states. Then the short term probabilistic distributions of mooring line tension and FPSO offset for the selected sea states are established. For each selected sea state, the short term probabilistic distributions of the maximum line tension and FPSO offset are estimated by performing 20 3-hour coupled time domain simulations with random seeds for each 3-hour. Subsequently, the short term distribution of the 3-hour maximum line tension response and FPSO offset are fitted by Gumbel distribution. Then the Kriging metamodel is established through the training data of the Gumbel parameters. The accuracy of metamodel is checked to assure its predictive ability. Finally, the long term distribution or exceedance probability of FPSO mooring systems can be estimated based on all the sea states.

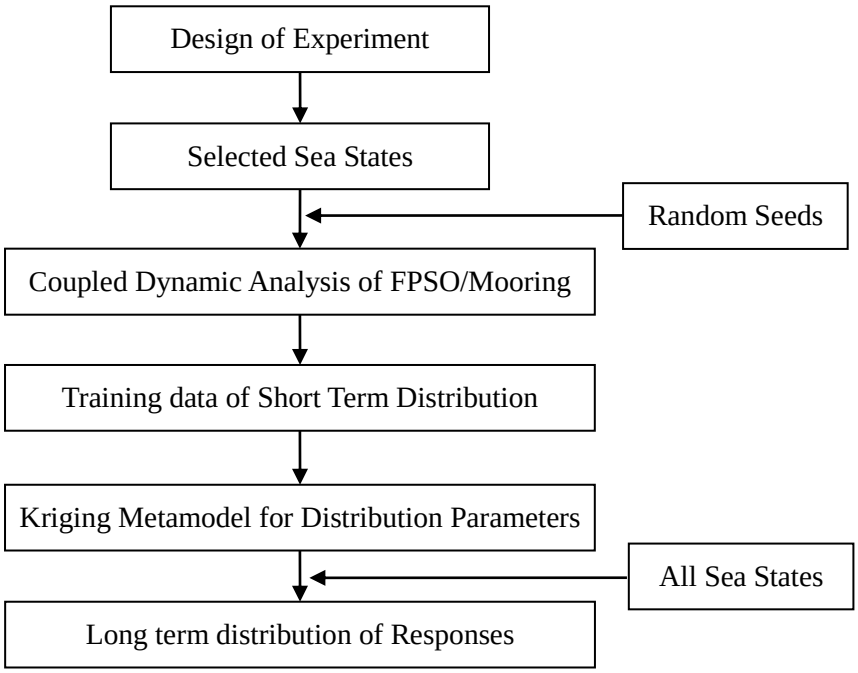

Figure 4.4 Long term extreme analysis of FPSO mooring system based on Kriging metamodel

4.6 Numerical Case

4.6.1 Case for Test Function

Here a mathematical function is used to illustrate and test the feasibility of Kriging metamodel. The test function is as follows and Figure 4.5 shows its plot.

$$z = \sin(x+3)\sin(2\,y+5) \quad x \in [0, 2\pi], y \in [0, \pi] \tag{4.31}$$

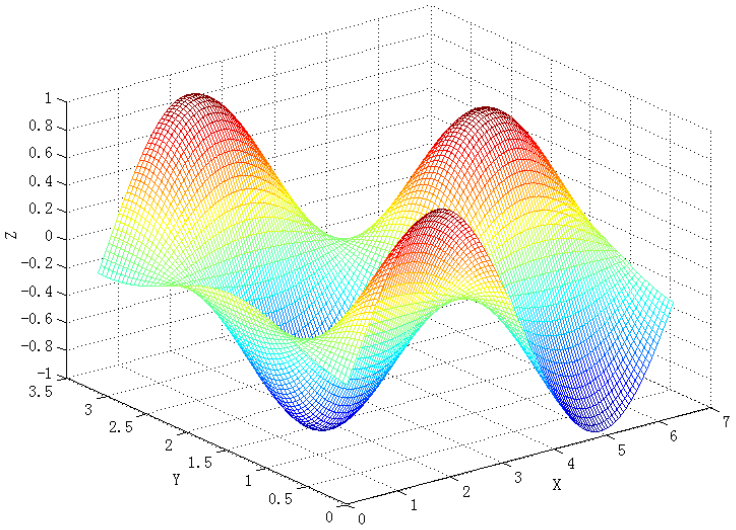

Figure 4.5 Test function

Latin hypercube sampling is performed to select the training data from the value range. Here 100 sampled points are selected by Latin hypercube sampling and shown in Figure 4.6 (black dot). Then the Kriging metamodel is established according to the process presented in Figure 4.3. The established Kriging metamodel is shown in Figure 4.6.

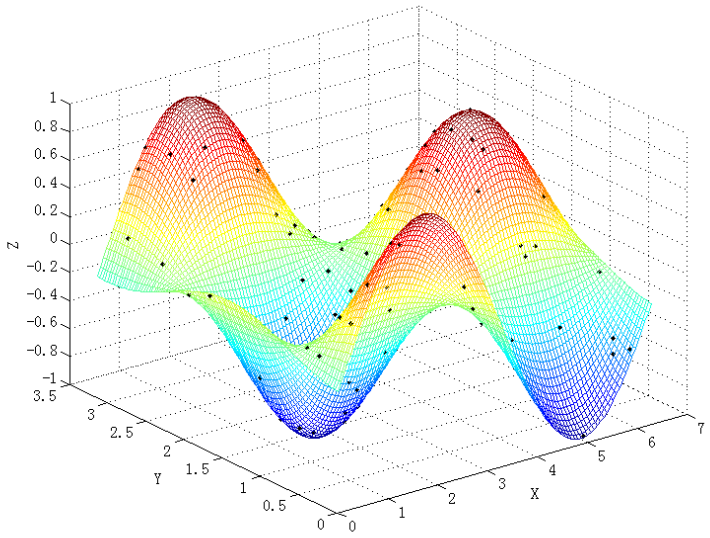

Figure 4.6 Kriging metamodel of test function

To assess the accuracy of the prediction, the R^2 analysis is used here, as given in Eq. (4.32) where y_i is the actual response, $\hat{y}_i$ is the predicted response, $\overline{y}_i$ is the mean of the actual responses.

$$R^2 = 1 - \frac{\sum_{i=1}^{n}(y_i - \hat{y}_i)^2}{\sum_{i=1}^{n}(y_i - \overline{y}_i)^2} \tag{4.32}$$

The maximum R^2 value of unity indicates that predicted values and actual values are identical. The greater the value of R^2, the more accurate the metamodel is. Here the R^2 analysis is performed with another 50 sampled points to check the accuracy of metamodel. These predicted and observed points, calculated from the Kriging metamodel and the original function respectively, are shown in Figure 4.7. The value of R^2 is 1.00 that shows the metamodel can nearly perfectly fit with the actual values. This test case demonstrates the Kriging metamodel can show the good mapping relationship only requiring a certain amount of training data based on the design of experiment method.

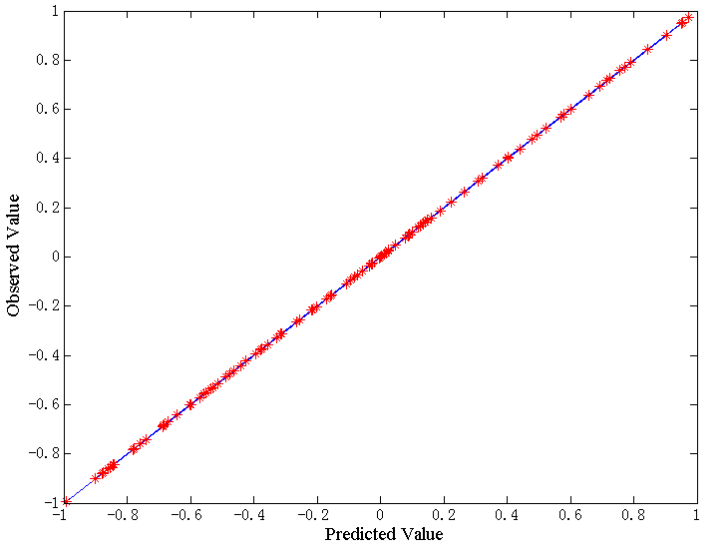

Figure 4.7 Accuracy check of Kriging metamodel of test function

4.6.2 Case for Long Term Extreme Analysis

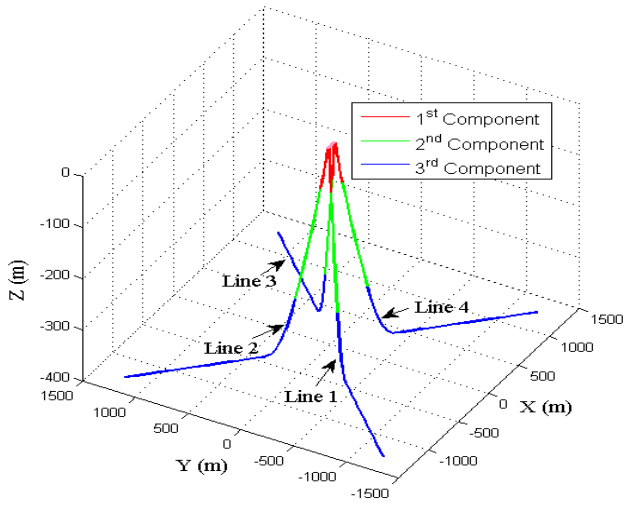

Figure 4.8 Configuration of FPSO mooring system

The model of FPSO mooring system is shown in Figure 4.8. The mooring lines are multi components (chain-wire-chain) and the properties of mooring lines are given in Table 4.1. The lumped mass method is used for dynamic analysis of mooring lines

using Orcaflex. The FPSO is modeled as a rigid body and the water depth is 400m. The wave force is considered as the main environmental force here. The marginal distribution of H_s and conditional distribution of T_p for given H_s are established from the data of Northern North Sea in literature according to the Eq. (4.14) - Eq. (4.16) (Haver and Nyhus, 1986). The joint probability density function of the sea state characteristics, H_s and T_p is shown in Figure 4.9. The wave is assumed to be unidirectional along the x direction as seen in Figure 4.8. The Line 1 and Line 2 are the most loaded lines and they are taken into account.

Table 4.1 Particulars of the mooring lines

Component	1st	2nd	3rd
Type	R4 Chain	Spiral Strand wire	R4 Chain
Diameter (mm)	157	144	157
Length (m)	100	300	1480
Axial Stiffness (kN)	3.35E6	1.893E6	3.35E6
Weight (kg/m)	491	106	491

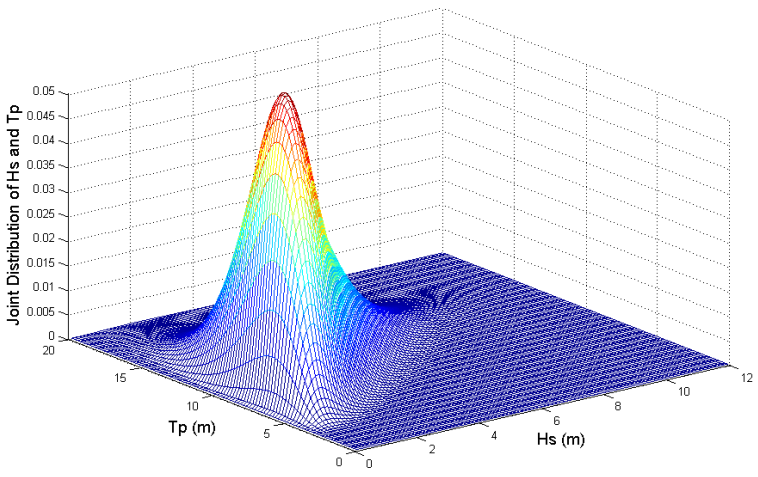

Figure 4.9 Joint probability density function of H_s and T_p

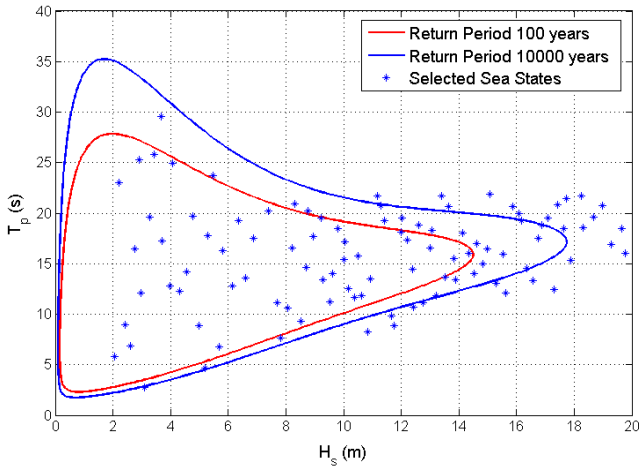

Figure 4.10 Selected sea states by Latin hypercube sampling

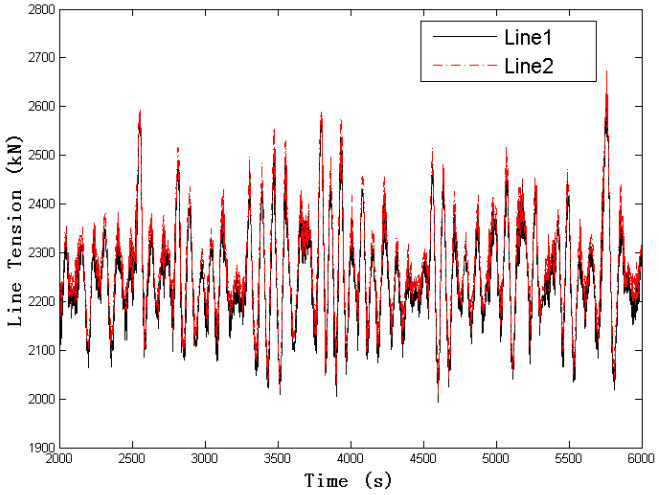

Figure 4.11 Top tension response of Line 1 and Line 2

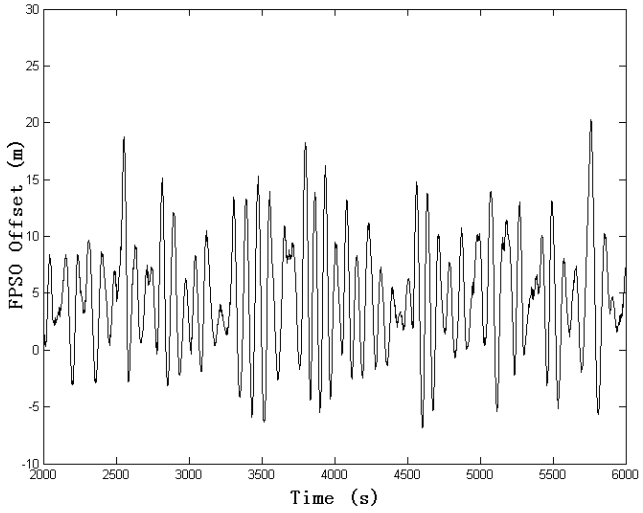

Figure 4.12 FPSO offset response

The Design of Experiment method is used to obtain the training data for constructing Kriging metamodel in advance. Firstly, Latin hypercube sampling is executed to select the 100 sampled sea states from all sea states as show in Figure 4.10. Then 20 3-hour coupled dynamic analysis of FPSO mooring system are simulated for each of the selected sea states. Figure 4.11 presents the dynamic response of Line 1 and Line 2 and Figure 4.12 gives the response of FPSO offset.

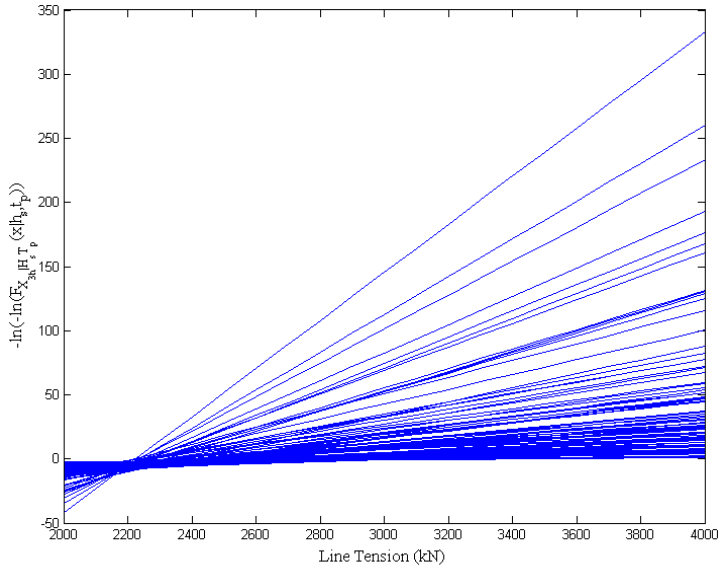

Figure 4.13 Short term distribution of Line 1 tension

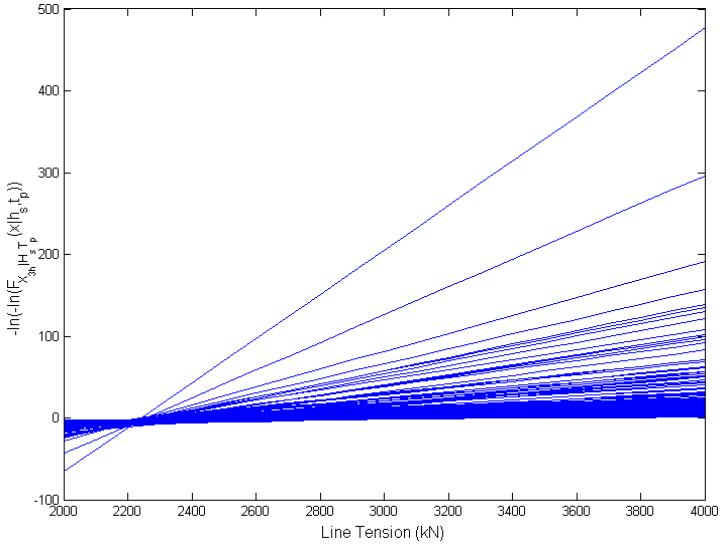

Figure 4.14 Short term distribution of Line 2 tension

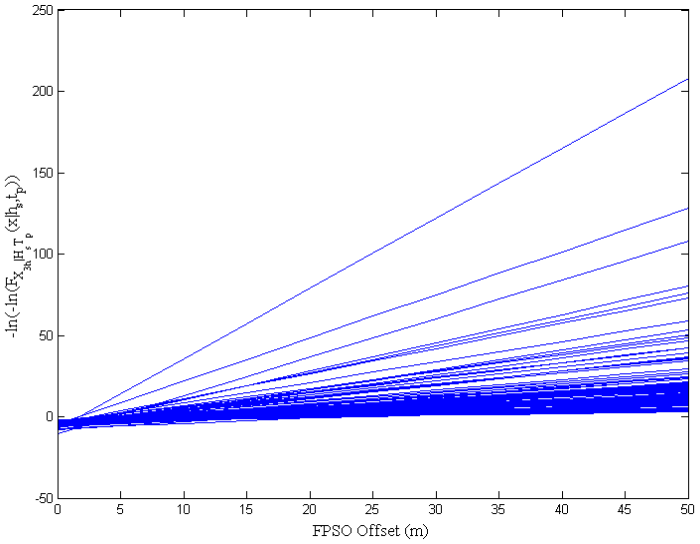

Figure 4.15 Short term distribution of FPSO offset

Based on the generated response time series, Gumbel distribution parameters are fitted to the maxima response samples for each sea state and the results are shown in Figure 4.13 - Figure 4.15. Then the Gumbel distribution parameters for the short term extremes are obtained for all sampled sea states, $\alpha_1(h_s,t_p)$ and $\beta_1(h_s,t_p)$ for top tension response of Line 1, $\alpha_2(h_s,t_p)$ and $\beta_2(h_s,t_p)$ for top tension response of Line 2 and $\alpha_3(h_s,t_p)$ and $\beta_3(h_s,t_p)$ for FPSO offset. These location and scale parameters are used as the training data to construct the Kriging metamodel according to the process described in Figure 4.3. The established Kriging metamodels for the distribution parameters of line tension and offset are shown in Figure 4.16-Figure 4.18, respectively.

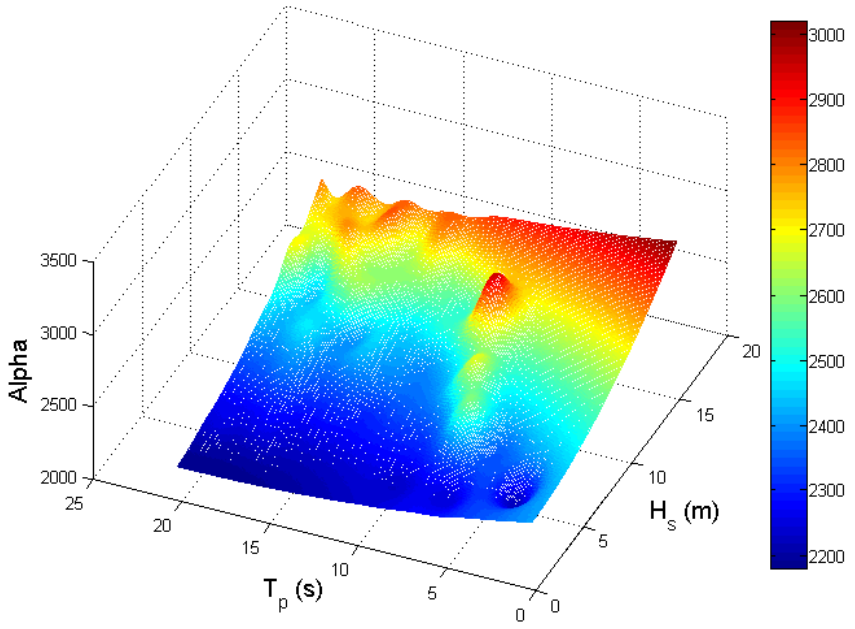

(a) Location parameter

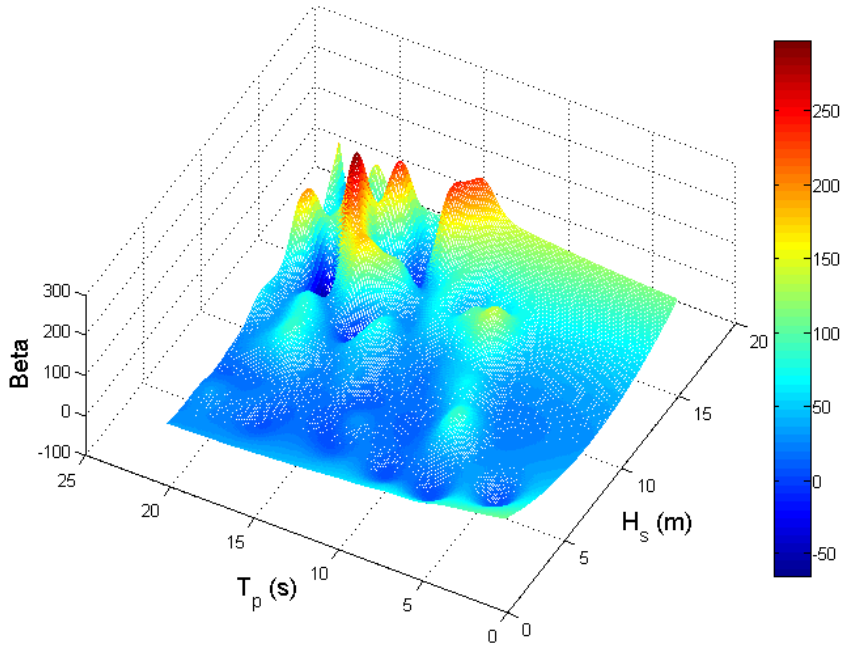

(b) Scale parameter

Figure 4.16 Kriging metamodel for distribution parameters of Line 1 Tension

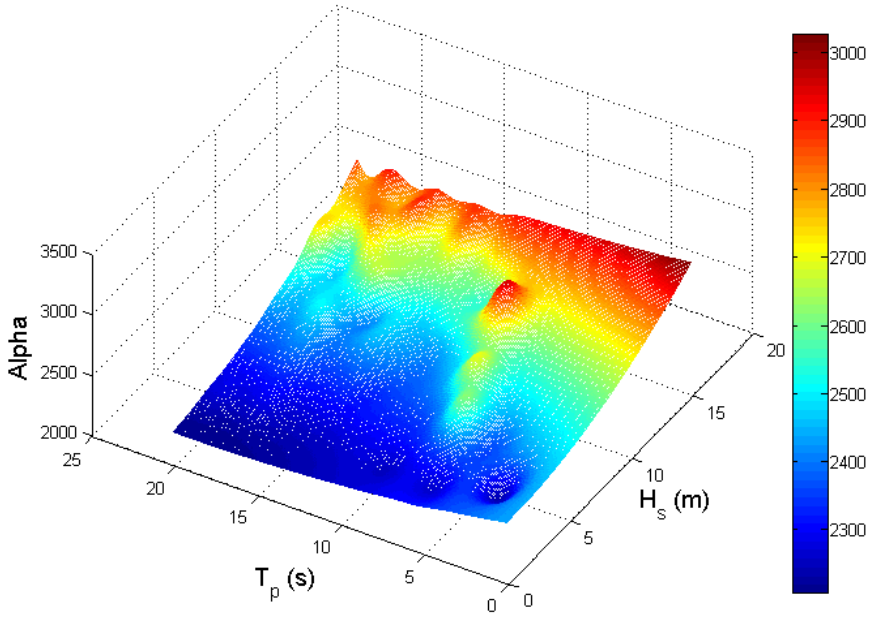

(a) Location parameter

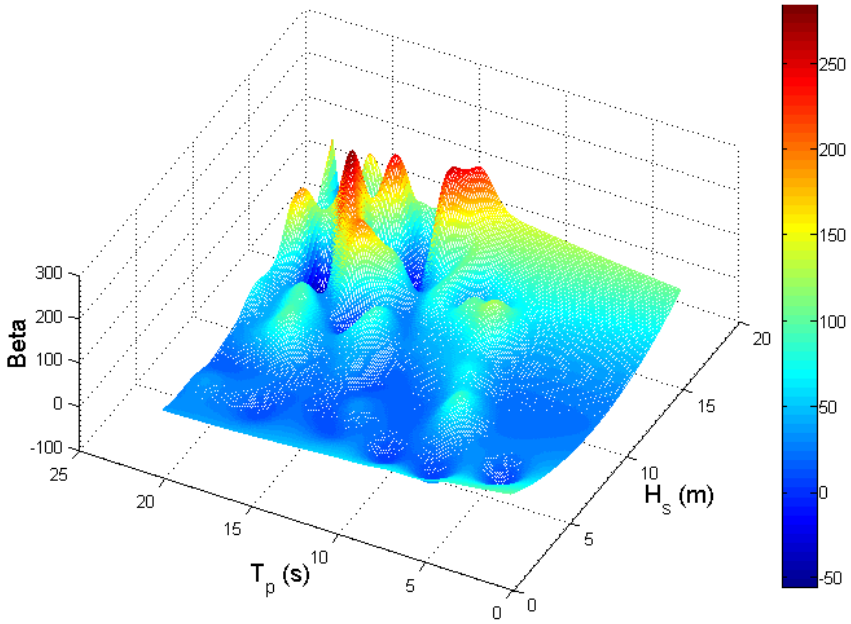

(b) Scale parameter

Figure 4.17 Kriging metamodel for distribution parameters of Line 2 Tension

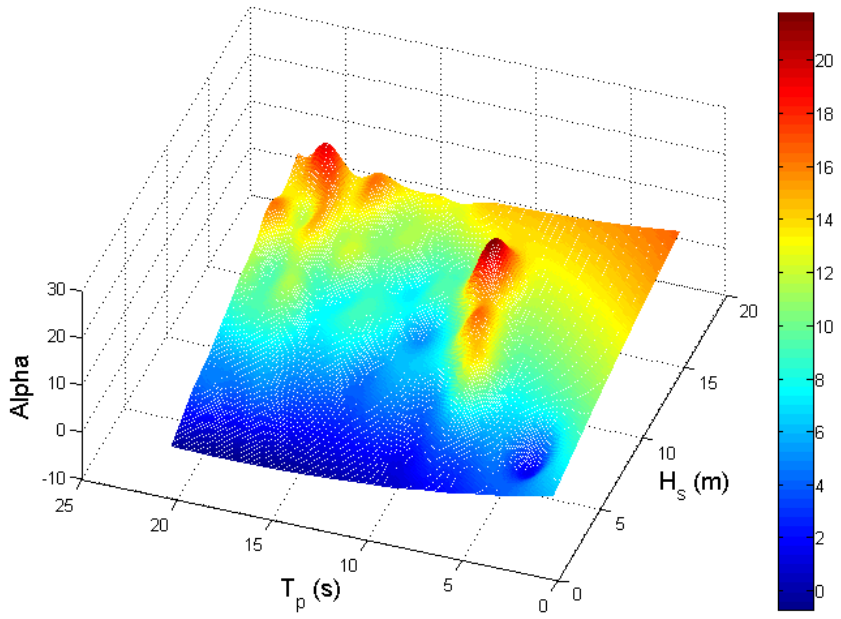

(a) Location parameter

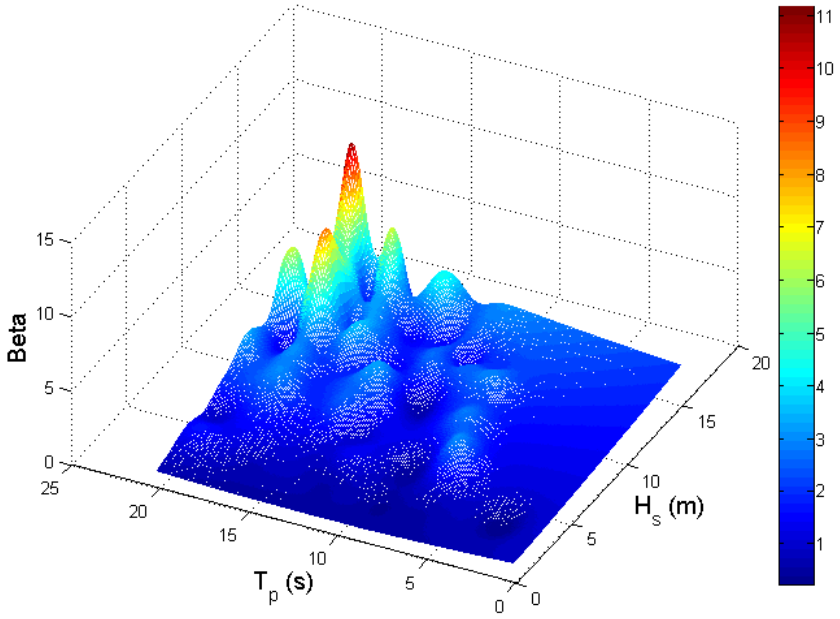

(b) Scale parameter

Figure 4.18 Kriging metamodel for distribution parameters of FPSO offset

A different sub-set of the sea states are further sampled to check the accuracy of the metamodel. For this sub-set of sea states, the Gumbel distribution parameters are estimated from the coupled dynamic response as well as from the Kriging metamodel. The R^2 analysis is used to quantify the prediction accuracy and the results are shown in Figure 4.19. It can be seen that the Kriging metamodel can predict the response very well.

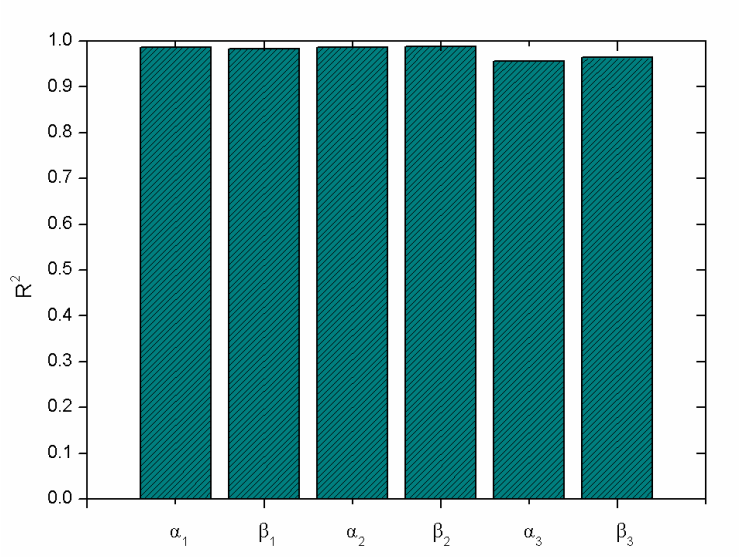

Figure 4.19 Accuracy quantification of Kriging metamodels for the distribution parameters by R^2 analysis

The long-term probabilities of exceedance for the tensions of Line 1 and Line 2 are estimated through integral over all the sea states probability and their corresponding short term distribution based on the Kriging metamodel. Figure 4.20 and Figure 4.21 give the exceedance probability distribution of Line 1 and Line 2 top tensions and the FPSO offset, respectively. Table 4.2 presents the top tension and FPSO offset under different exceedance probabilities. Mooring design analyses are usually performed by a simplified design wave approach which given the environmental conditions with a certain return period. Here the characteristic tension (most probable maximum response) in a 100-year sea state (Hs=14.5m, Tp=15.9s) are estimated. Figure 4.22 gives the comparison of characteristic tension with probabilistic extreme tension from long term distribution.

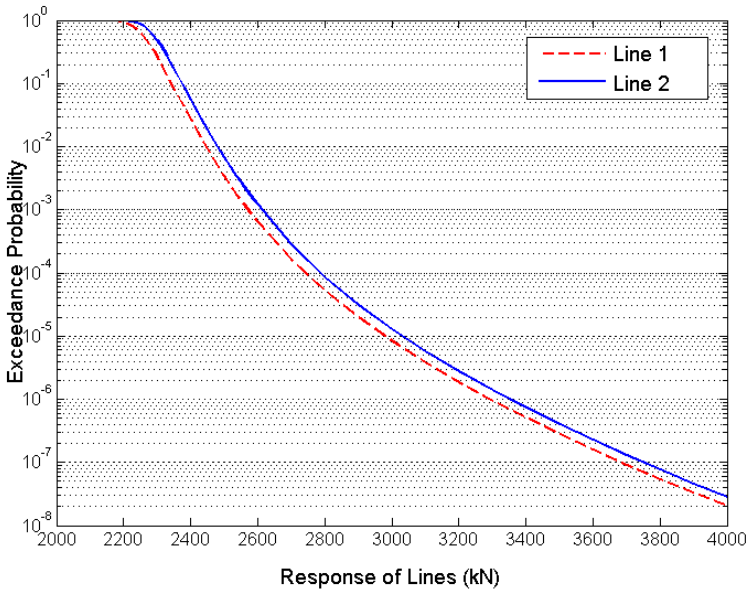

Figure 4.20 Exceedance probability distribution of Line 1 and Line 2's top tension

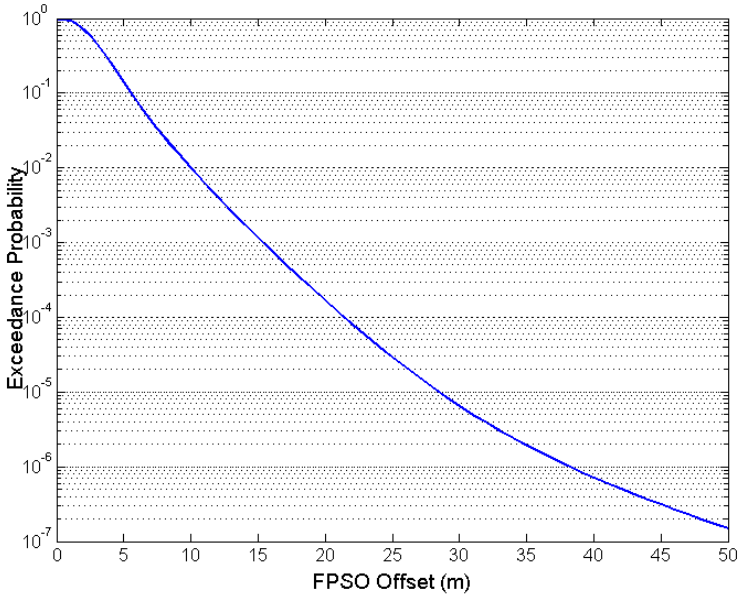

Figure 4.21 Exceedance probability distribution of offset

Table 4.2 Responses under different exceedance probabilities

Exceedance Probability	10^{-2}	10^{-3}	10^{-4}	10^{-5}	10^{-6}
Tension of Line 1 (kN)	2446	2571	2757	2986	3295
Tension of Line 2 (kN)	2480	2621	2792	3039	3361
FPSO Offset (m)	10.0	15.4	21.4	28.5	38.2

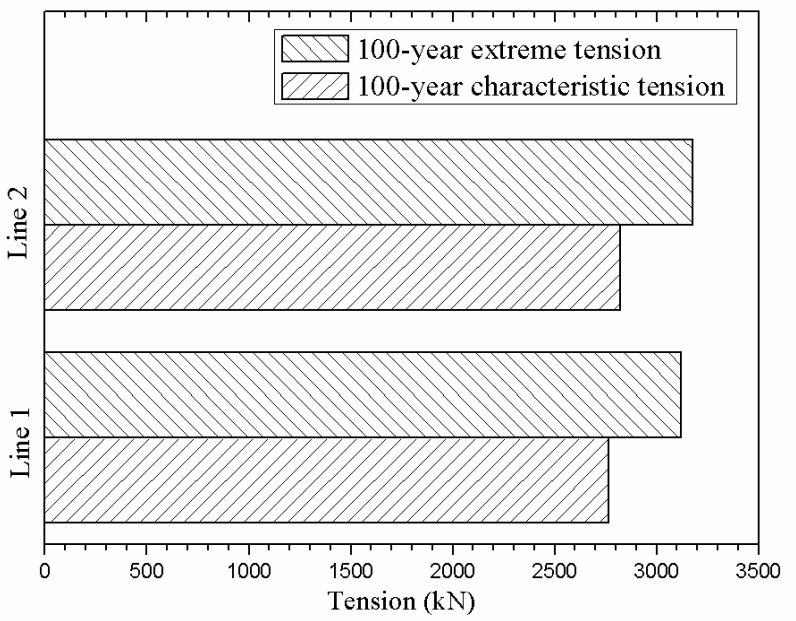

Figure 4.22 Characteristic tension in 100-year sea state and long term extreme tension (return period 100 years)

4.7 Conclusion

Calculating the long term distribution of 3-hour maximum response, X_{3h}, usually involves response calculations for all sea states and the corresponding short term probabilistic distribution for each sea state. The process for long term extreme analysis is extremely time-consuming for complex nonlinear response problems such as coupled analysis of FPSO/ mooring lines. A computational efficient methodology for the long term analysis of FPSO mooring systems by the use of Kriging metamodel has been proposed in the present work. The results indicate that long term extreme analysis with Kriging metamodel avoids the short term extreme analysis over all sea states and this method can improve the efficiency of the long term extreme analysis due to it only involves the sea states selected by applying the design of experiment method. The Kriging metamodel is good alternative approach for the long term analysis which involve in large number of cases but the sampling is crucial to the accuracy of Kriging metamodel.

5 Long Term Extreme Analysis by Monte Carlo Simulation

5.1 Introduction

The traditional and accurate method to estimate the long term extreme needs to solve the integral given by Eq. (4.13) which accounts for the contribution of all short term conditions to the long term response. It is a very time-consuming process, mainly when nonlinear time domain simulations are employed to obtain the response. How to solve this integral efficiently seems to be the most challenging problem associated with long term response analysis.

Monte Carlo simulation is a good and simple method for generation of samples from a probability distribution to estimate their probability distribution (Rubinstein and Kroese, 2007). Here, long term extreme response is estimated by Monte Carlo simulation that avoids the integration. An approach for long term extreme analysis of a moored FPSO using Monte Carlo simulation based on a Kriging metamodel is proposed. Exceedance probability of line tension and FPSO offset are estimated from the samples obtained by Monte Carlo simulation using inverse transform sampling. The Kriging metamodel which represent the mapping between the sea states characteristics and short distribution parameters, is established with the training data from a series of short term distributions. The effects of sample size for Monte Carlo simulation are discussed. The exceedance probabilities of line tension and FPSO offset are compared with the results obtained from full long term analysis that integral over all sea states.

5.2 Monte Carlo Simulation Method

Inverse transform sampling (also known as inverse probability integral transform) is a method for generating sample numbers at random from probability distribution given its cumulative distribution function (cdf) (Angus, 1994; Devroye, 1986). In this sampling method, it generates a random variable u from the standard uniform distribution between 0 and 1 and then the random variable $x=F^{-1}(u)$ is transformed from the distribution F, as seen in Figure 5.1. The details of long term extreme analysis by Monte Carlo simulation are illustrated as follows.

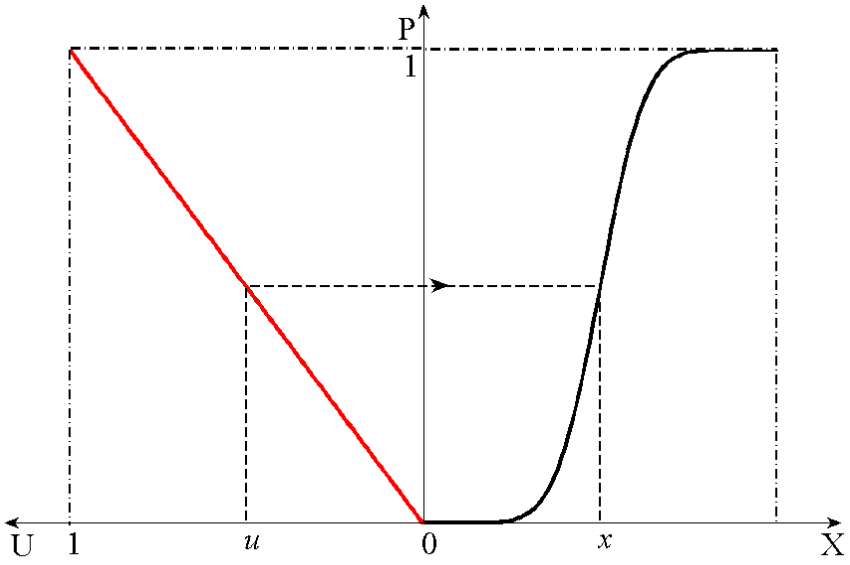

Figure 5.1 Inverse sampling method

Firstly, a random numbers u_1 is generated from a variable being uniformly distributed between 0 and 1. The significant wave height H_s, which its probability is u_1, can be obtained from the transformation in Eq. (5.1).

$$h_s = F_{H_s}^{-1}(u_1) \tag{5.1}$$

Then, a random number u_2 is generated from uniform distribution between 0 and 1. The spectral peak period T_p given significant wave height $H_s=h_s$ can be transformed as follows.

$$t_p = F^{-1}_{T_p|H_s}(u_2|h_s) \tag{5.2}$$

Given that the short term extreme distribution parameters for different sea states are obtained, the short term response of any required sea state can be calculated with the transformation method. A random number u_3, being uniformly distributed between 0 and 1, is generated. The short term extreme response in a sea state given by h_s and t_p can be calculated by:

$$x = \alpha(h_s, t_p) - \beta(h_s, t_p)\ln\left[-\ln(u_3)\right] \tag{5.3}$$

A series of short term extreme responses are obtained from Monte Carlo simulation by repeating the aforementioned steps N times. Finally, we can estimate exceedance probabilities of long term response from these simulated samples as seen in Eq.(5.4), where m is the number of response larger than x_0.

$$\mathrm{P}(\mathrm{X} > \mathrm{x}_0) = \frac{m}{N} \tag{5.4}$$

Using Monte Carlo simulation, we can obtain a large number of observations of extreme response. The long term extreme distribution can be estimated directly from these observations. This method requires that the short-term response variability should be available for all relevant sea states, which is quite time consuming for coupled dynamic analysis of moored FPSO. Kriging is applied to establish a proper model for the conditional distribution of X_{3h} for all sea states in order to solve the challenge for the present problem. The flowchart of the proposed method is presented in Figure 5.2.

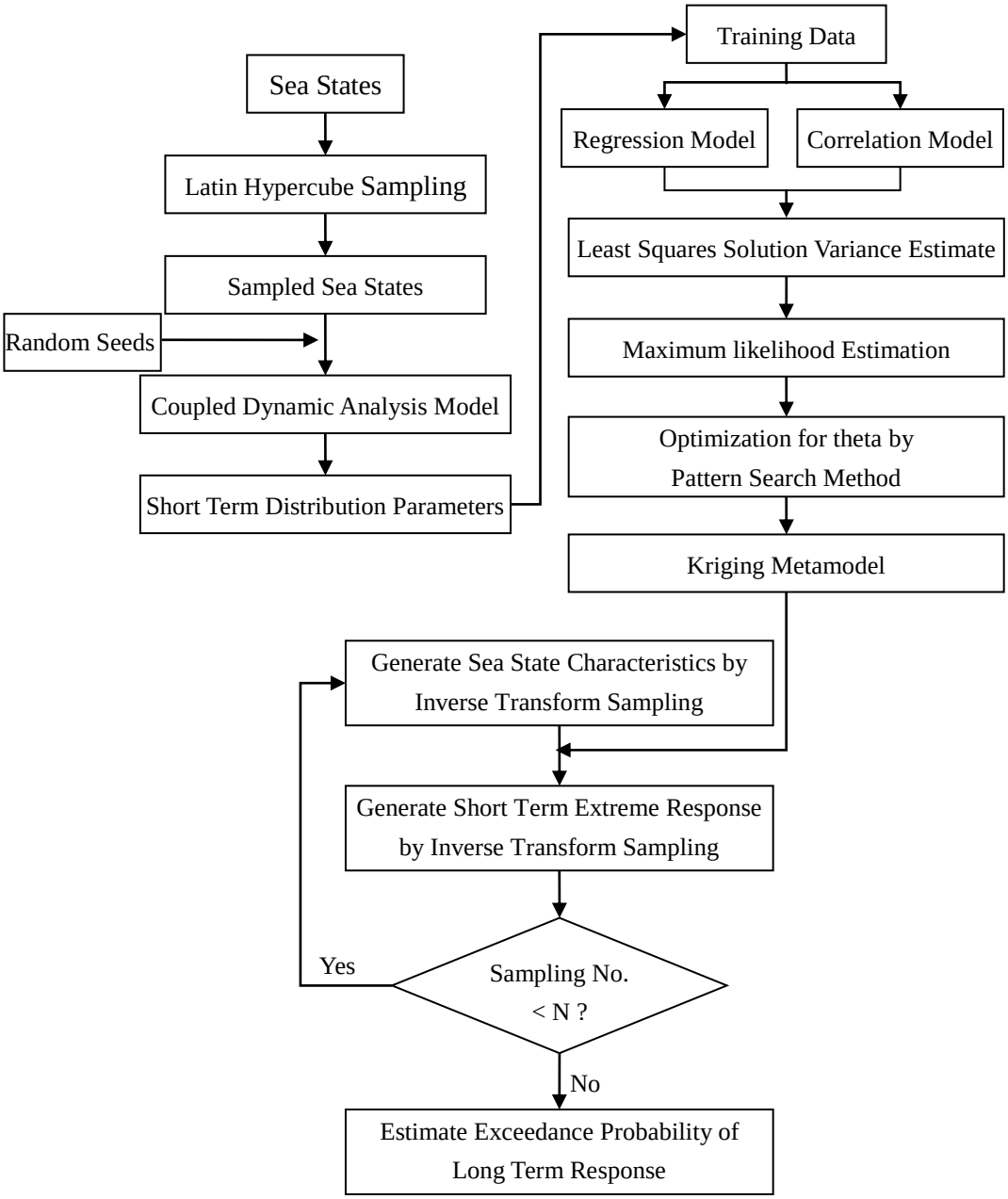

Figure 5.2 Probabilistic analysis of moored FPSO using Monte Carlo simulation with Kriging metamodel

5.3 Numerical Case

The model and data used in this case are taken from the chapter 4. The marginal distribution of H_s and conditional distribution of T_p for given H_s are established from the data of Northern North Sea as given in previous chapter. The marginal distribution of H_s and conditional distribution of T_p for given H_s are shown in Figure 5.3 and Figure 5.4.

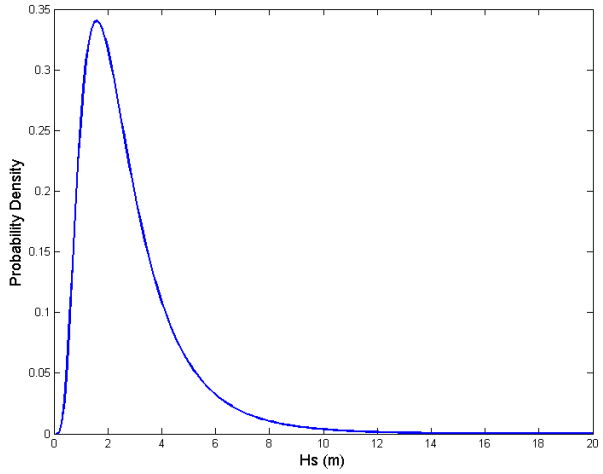

Figure 5.3 Marginal distribution of H_s

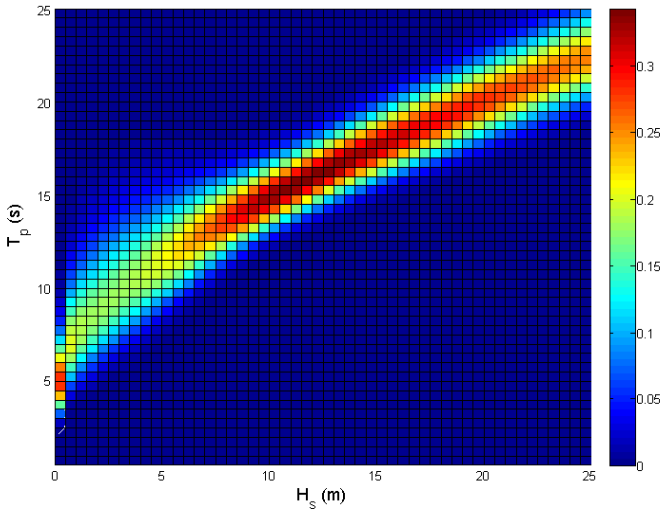

Figure 5.4 Conditional distribution of T_p for given H_s

The Kriging metamodels for the Gumbel distribution parameters, location and scale parameters including $\alpha_1(h_s, t_p)$ and $\beta_1(h_s, t_p)$ for top tension response of Line 1, $\alpha_2(h_s, t_p)$ and $\beta_2(h_s, t_p)$ for top tension response of Line 2 and $\alpha_3(h_s, t_p)$ and $\beta_3(h_s, t_p)$ for FPSO offset, have been established in Section 4.5.

The long-term probabilities of exceedance for the line tension and FPSO offset are evaluated by Monte Carlo simulation with Kriging metamodels. Random sea state characteristics are generated by inverse transform sampling. The short term extreme response for random sea state characteristics are estimated based on Kriging metamodel. The long term probability distribution or exceedance probability is assessed from sampled response. Monte Carlo simulations with different sample sizes ($N=10^5$, 10^6,10^7 and 10^8) are performed to study the effects of amount of sample data on the tail distribution.

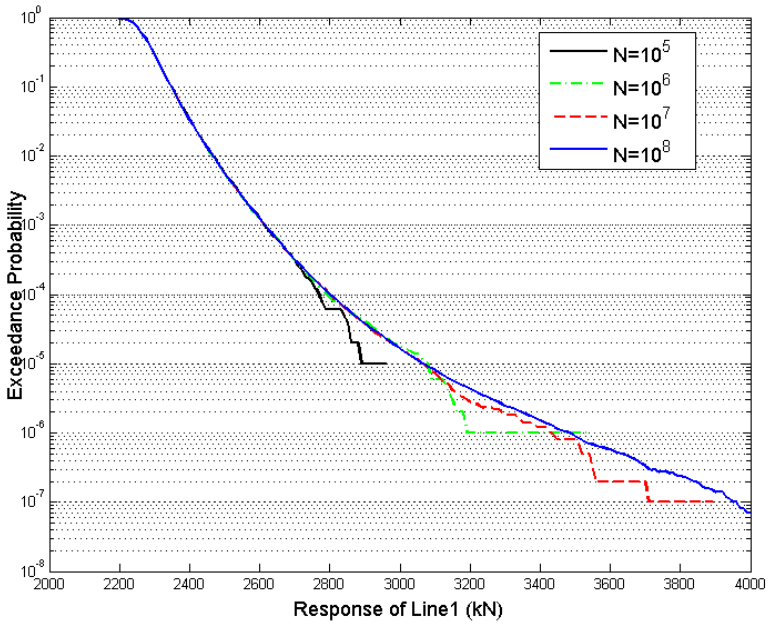

Figure 5.5 Exceedance probability distribution of Line 1 tension by Monte Carlo simulation with different sample sizes

Figure 5.5 and Figure 5.6 give the exceedance probability distributions of Line 1 and Line 2 top tensions for different numbers of sample points. The exceedance probability distributions of FPSO offset for different samples are shown in Figure 5.7. It can be seen that the accuracy of tail distribution by use of 10^5 and 10^6 sample sizes can reach the exceedance probability of 10^{-4} and 10^{-5}, respectively. If the response with probability level of 10^{-6} needs to be evaluated, at least 10^7 sample size is used for the simulation. Using Mont Carlo simulation with the Kriging metamodel results in a very fast calculation.

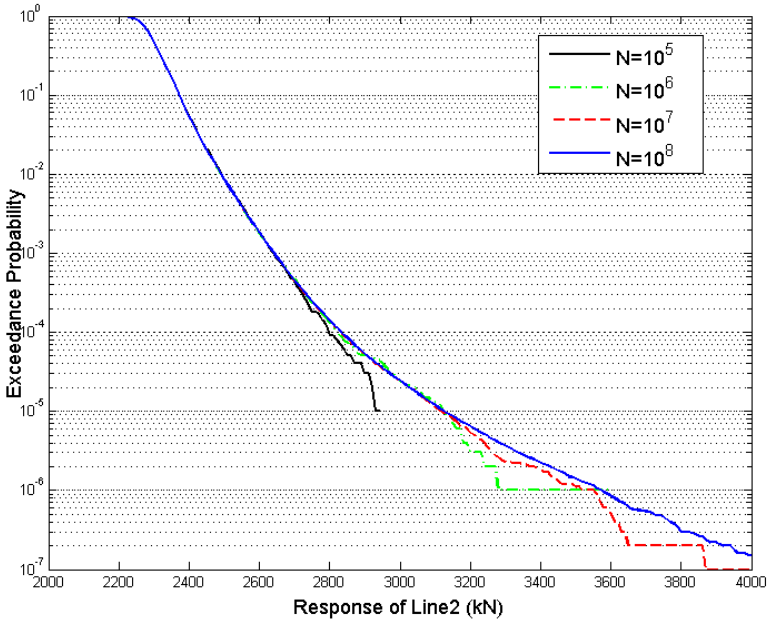

Figure 5.6 Exceedance probability distribution of Line 2 tension by Monte Carlo simulation with different sample sizes

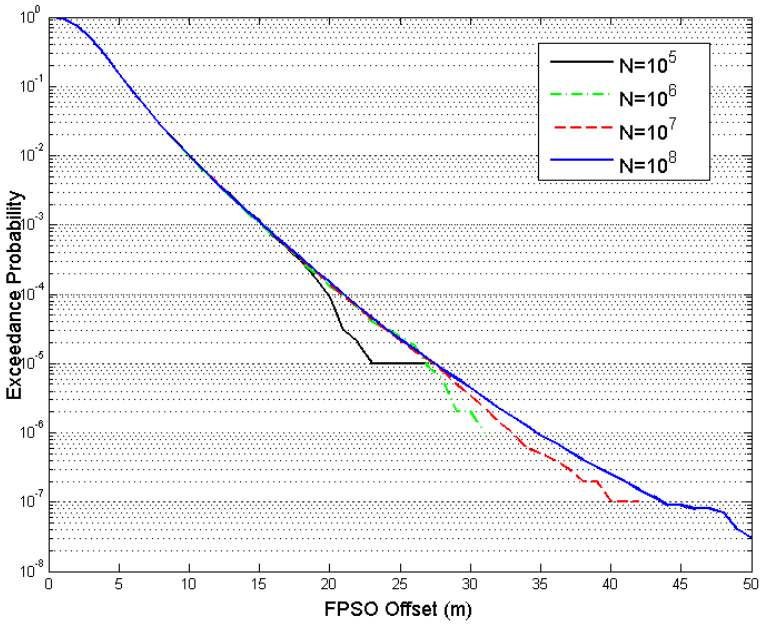

Figure 5.7 Exceedance probability distribution of FPSO offset by Monte Carlo simulation with different sample sizes

Table 5.1 Long term extreme responses estimated by Monte Carlo simulation (MCS) and all sea states

Exceedance Probability		10^{-2}	10^{-3}	10^{-4}	10^{-5}	10^{-6}
Line 1 Tension	MCS	2466	2615	2801	3066	3485
	All Sea States	2446	2571	2757	2986	3295
	Error (%)	0.82	1.71	1.60	2.68	5.77
Line 2 Tension	MCS	2491	2642	2833	3125	3573
	All Sea States	2480	2621	2792	3039	3361
	Error (%)	0.44	0.80	1.47	2.83	6.31
FPSO Offset	MCS	10.0	15.2	21.0	27.5	34.7
	All Sea States	10.0	15.4	21.4	28.5	38.2
	Error (%)	0	1.30	1.87	3.51	9.16

The long term extreme responses evaluated by Monte Carlo simulation with 10^8 sample size are compared with extreme responses estimated by use of long term analysis that integral over all the sea states and their corresponding short term distribution, namely all sea states method. The exceedance probability of Line 1, Line 2 tension and FPSO offset estimated by the two methods are presented in Table 5.1. The comparison of the calculation results show that Monte Carlo simulation method can predict the extreme responses very well.

5.4 Conclusions

Traditional long term extreme analysis, which should compute through all sea states, is a challenge for the design and analysis of mooring. A methodology for probabilistic analysis of FPSO mooring systems using Monte Carlo simulation with a Kriging metamodel has been proposed in this chapter for long term analysis. The effect of sample size for Monte Carlo simulation on the tail distribution was discussed. The exceedance probability distributions estimated by Monte Carlo simulation and all sea states, respectively, were compared. The results demonstrate that long term extreme analysis with a Kriging metamodel avoids the short term extreme analysis over all sea states and this method can improve the efficiency of the long term extreme analysis due to it only involving the sea states selected by applying the design of experiment method.

6 Long Term Extreme Analysis by Contour Line Method

6.1 Introduction

One of the design criteria for mooring systems is the ultimate limit state, which ensures that the individual mooring lines have adequate strength to withstand the load effects imposed by extreme environmental actions (API RP 2SK, 2005; DNV-OS-E301, 2010). The general method for the extreme analysis of the mooring line is a fully long term response analysis accounting for the contribution of every short term condition, i.e., an all sea states method. There are two inherent randomness during the long term extreme analysis. One is the long term variability for the slowly varying environmental characteristics and the other is the short term variability for the short term response given sea states.

The long term extreme analysis by all sea states method requires that the short term response variability should be available for all relevant sea states and it is quite time consuming for complex responses, especially when time domain simulations for coupled mooring lines have to be performed to get correct response characteristics. A more practical and computationally cheaper method to estimate the long term extreme response without having to carry out the full long term analysis can employ the contour line method (Haver et al., 1998; Winterstein et al., 1993). The environmental contour line (or surface), which has a combinations of environmental parameters with identical return period, is determined on the basis of the inverse first order reliability method (IFORM). This method assumes that we could account for short term variability separately, i.e. decoupling the environmental problem and the response problem. The contour line method can be used to predict the extreme response based on limited short term analyses along a well-defined environmental

contour line with a given return period. Baarholm and Moan (2001) used the contour line method to estimate the extreme ship hull loads considering operational restrictions. They found out the contour line method is useful to estimate extreme values for ships with and without forward speed.

The long term extreme analysis of coupled mooring lines is estimated by the contour line method in this paper. The extreme response corresponding to different return periods are calculated. A high fractile value is selected to account for the short-term variability. The results are validated by comparing with the results from the all sea states method. The coefficient of variation (COV) of extreme response is also calculated by the bootstrap method.

6.2 Reliability Method for Extreme Response Estimation

In connection with extreme value predictions, we will primarily be interested in an accurate prediction of the very upper tail of the long term distribution of the 3-hour maximum. The exceedance probability corresponding to a given high threshold, x_c, can be estimated by a method from structural reliability analysis. The limit state function is defined as follows.

$$g = x_c - X_{3h}(h_s, t_p) \tag{6.1}$$

where g=0 is the limit state surface, which separates the failure domain (g<0) from the safe domain (g>0). The failure probability is determined by the following integral:

$$P_f(x_c) = \iiint_{g<0} f_{X_{3h}|H_s T_p}(x \mid h_s, t_p)\, f_{HsTp}(h_s, t_p)\, dx dh_s dt_p \tag{6.2}$$

The failure probability can be predicted by first order reliability method (FORM) and the above integral should be transformed over to the space of standard Gaussian

variables by Rosenblatt transformation (Madsen et al., 1986), as seen in Eqs.(6.3)-(6.5), where Φ is the standard Gaussian distribution function. The transformation is one-to-one correspondence between the point in standard Gaussian space, i.e. U-space, and the point in physical parameter space as the corresponding functions are monotonic.

$$F_{H_s}(h_s) = \Phi(u_1) \tag{6.3}$$

$$F_{T_p|H_s}(t_p \mid h_s) = \Phi(u_2) \tag{6.4}$$

$$F_{X_{3h}|H_sT_p}(x_{3h} \mid h_s, t_p) = \Phi(u_3) \tag{6.5}$$

The limit state surface in the U-space can be determined by the transformation. In the first order reliability method (FORM), the limit state surface in the U-space is approximated by a tangent plane at the design point, $(\hat{u}_1, \hat{u}_2, \hat{u}_3)$, which is the point on the limit state surface closest to the origin in the U-space as shown in Figure 6.1. The distance between design point and origin is calculated as seen in Eq. (6.6). It is the reliability index in structural reliability analysis, which uniquely related to the exceedance probability P_f, as seen in Eq. (6.7). The points of constant probability density are located on a sphere (or a circle for two variables) in the U-space.

$$\beta = \sqrt{\sum_{i=1}^{3} \hat{u}_i^2} \tag{6.6}$$

$$P_f(x_c) = \Phi(-\beta) \tag{6.7}$$

The upper tail of the extreme value distribution can be estimated by repeating the reliability analysis for different values of x_c.

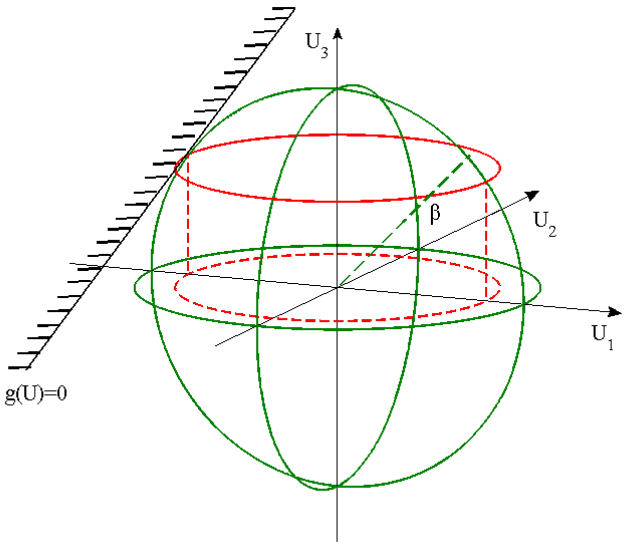

Figure 6.1 The limit state surface in the U-space

6.3 Inverse FORM Contour Line Method

We can estimate the response value corresponding to a given annual exceedance probability by inverting the above procedure, i.e. the inverse first order reliability method (IFORM) (Haver et al., 1998; Winterstein et al., 1993).

The relative importance of the randomness of a variable is reflected by its value at the design point. The more important the randomness of one variable, U_i, the value of U_i is larger. The variable U_i can be replaced by its mean value which is equal to the median for u-space variables if the randomness around the mean does not affect the failure probability. For the long term extreme problem, we assume that the short term probability density function of X_{3h} given H_s and T_p is extremely narrow (approaching a Dirac delta function). It means that the variability of the 3-hour maximum response is not important regarding the failure probability. The randomness of U_3 can be neglected and replace it by $u_3 = 0$. Then the design point will locate on a circle with radius β in the U_1-U_2 plane as shown in Figure 6.2 and the radius β can be calculated by given the probability as follows.

$$\beta = -\Phi^{-1}(P_f) \tag{6.8}$$

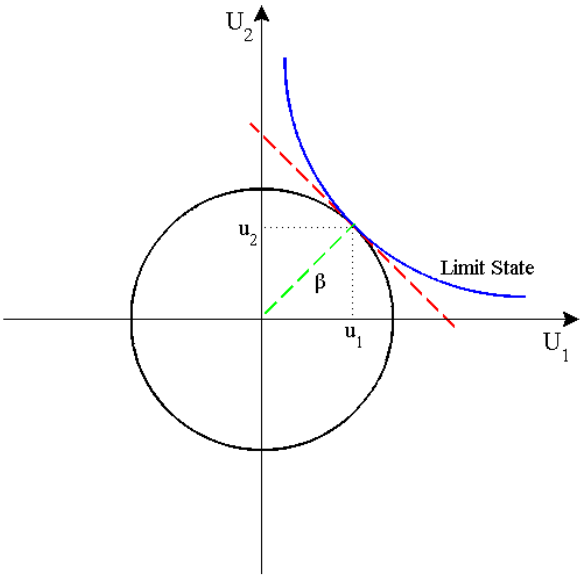

Figure 6.2 The limit state in the U_1-U_2 plane

Then all points on this circle in the U-space can be transformed back to the physical parameter space by Rosenblatt transformation and contour lines which contain all combinations of h_s and t_p along the T-year return period (or annual exceedance probability q) are obtained as seen in Figure 6.3. We use the median values for short term extreme response X_d for all combinations along the constant probability contour as neglecting the randomness of U_3. The median value is used as the characteristic short term response because the transformation conserves cumulative probability. The response corresponding to T-year return period is estimated by the maximum value of these median values. The extreme response given return period or probability of exceedance can be found along the contour line.

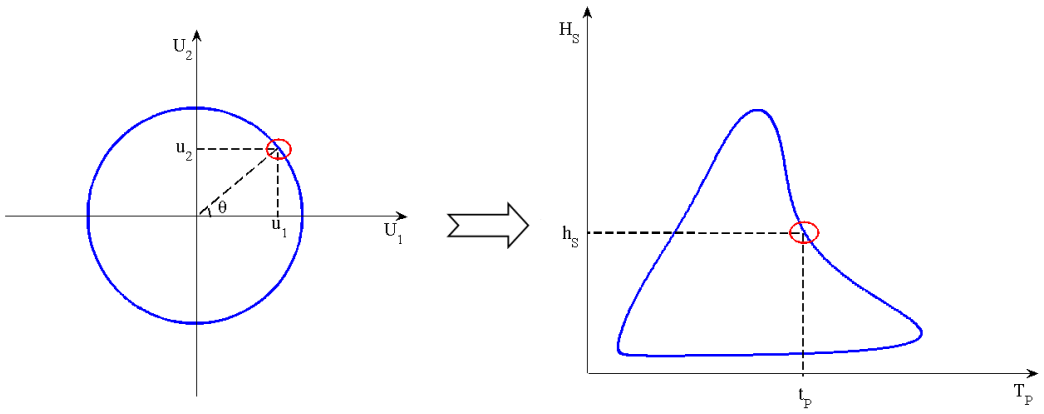

Figure 6.3 Transformation of contour line from U-space

However, this method will tend to underestimate extreme response levels because it neglects the response variability due to different short term sea state realizations. Short term variability can be accounted for by selecting a high fractile value of short term extreme value distribution as shown in Figure 6.4. To obtain the action effect corresponding to an annual exceedance probability of 10^{-2}, the fractile should be 85 % to 95 % (NORSOK N-003, 2007).

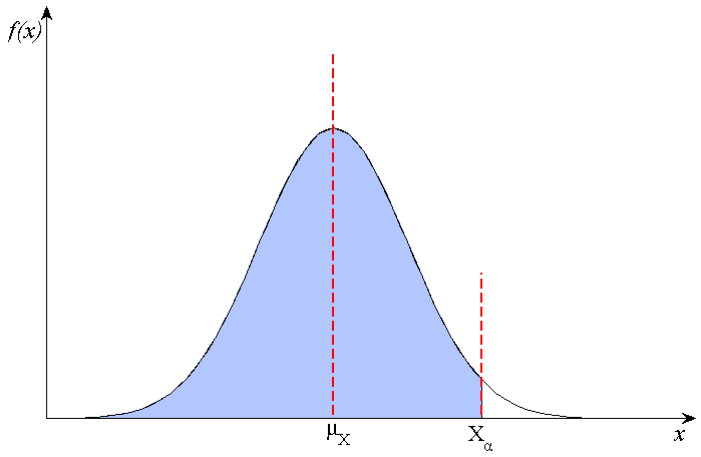

Figure 6.4 Selecting a fractile value of short term extreme value distribution

The contour line method is used to predict consistent estimates of extremes corresponding to given annual probability of being exceeded or return period. For full

long term analysis with all sea states, the short term probabilistic response needs to be established for a large number of short term sea states. This is difficult for complicated response problems requiring expensive time domain simulations in order to establish proper distributions of short term extremes. The contour line approach could eliminate the short term distribution and account for this source of randomness separately, i.e. decoupling the environmental problem and the response problem. We can estimate long term extremes without carrying out a full long term analysis for complicated response problems.

6.4 Numerical Case

The model of the FPSO mooring system is shown in Figure 4.8. The mooring lines are multi components (chain-wire-chain) and the properties of mooring lines are given in Table 4.1. The lumped mass method is used for dynamic analysis of mooring lines. The FPSO is modeled as a rigid body and the water depth is 400m. The wave force is considered as the main environmental force here. The wave is assumed to be unidirectional along the x direction. The most loaded lines, Line 1 and Line 2, are considered in the work.

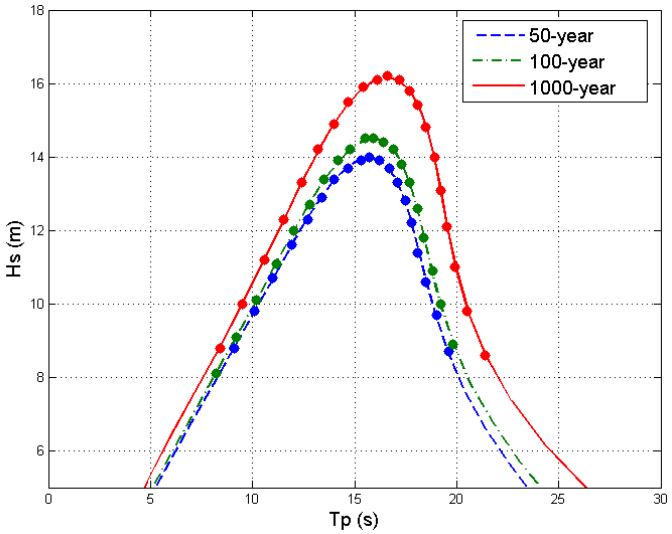

Figure 6.5 Contour lines of 50, 100 and 1000-year return period

Table 6.1 Selected sea states from contour lines

Sea states	50 year		100 year		1000 year	
No.	T_p (s)	H_s (m)	T_p (s)	H_s (m)	T_p (s)	H_s (m)
1	9.1	8.8	8.2	8.1	8.4	8.8
2	10.1	9.8	9.2	9.1	9.5	10.0
3	11.0	10.7	10.2	10.1	10.6	11.2
4	11.9	11.6	11.2	11.1	11.5	12.3
5	12.7	12.3	12.0	12.0	12.4	13.3
6	13.4	12.9	12.8	12.7	13.2	14.2
7	14.0	13.4	13.5	13.4	14.0	14.9
8	14.7	13.7	14.2	13.9	14.7	15.5
9	15.3	13.9	14.8	14.2	15.4	15.9
10	15.7	14.0	15.5	14.5	16.1	16.1
11	16.2	13.9	15.9	14.5	16.6	16.2
12	16.7	13.7	16.4	14.4	17.2	16.1
13	17.1	13.3	16.9	14.2	17.7	15.8
14	17.5	12.8	17.3	13.8	18.1	15.4
15	17.8	12.2	17.7	13.3	18.5	14.8
16	18.1	11.4	18.1	12.6	18.9	14.0
17	18.5	10.6	18.4	11.8	19.2	13.1
18	19.0	9.7	18.8	10.9	19.5	12.1
19	19.6	8.7	19.2	10.0	19.9	11.0
20	--	--	19.8	8.9	20.5	9.8
21	--	--	--	--	21.4	8.6

The contour lines of 50, 100 and 1000-year return period (or 1/50, 10^{-2} and 10^{-3} annual exceedance probability) are transformed from the points on the circles with

radius β=4.35, 4.50 and 4.97 respectively in the U-space. The contour lines are shown in Figure 6.5. The sea states along the contour lines are selected as shown in Figure 6.5 (marked by circle dot) and the details are presented in Table 6.1.

Then 20 3-hour time domain simulations for these selected sea states are performed and the short term extreme distributions are fitted by Gumbel distribution. The characteristic values of the short term line tension distribution are calculated for different return period, as seen in Figure 6.6-Figure 6.8. The critical sea state corresponding to the maxima response is found from these selected sea states. Figure 6.6 - Figure 6.8 give the maxima line characteristic tensions for different return periods and the worst sea states are also marked in the Table 6.1, Hs=14.7 m and Tp=13.7 s for contour line of 50-year return period; Hs=16.9 m and Tp=14.2 s for contour line of 100-year return period; and Hs=18.1 m and Tp=15.4 s for contour line of 1000-year return period.

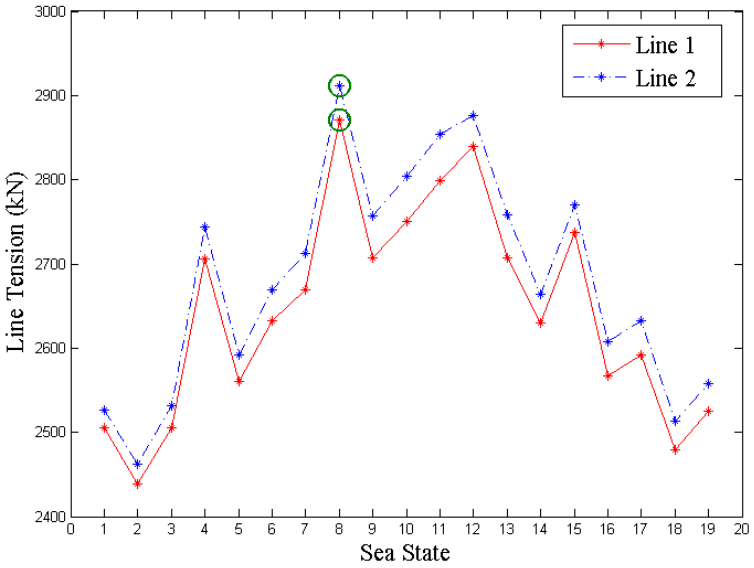

Figure 6.6 The line tension response for selected sea states from contour line of 50-year return period (circle denotes the maxima line characteristic tension)

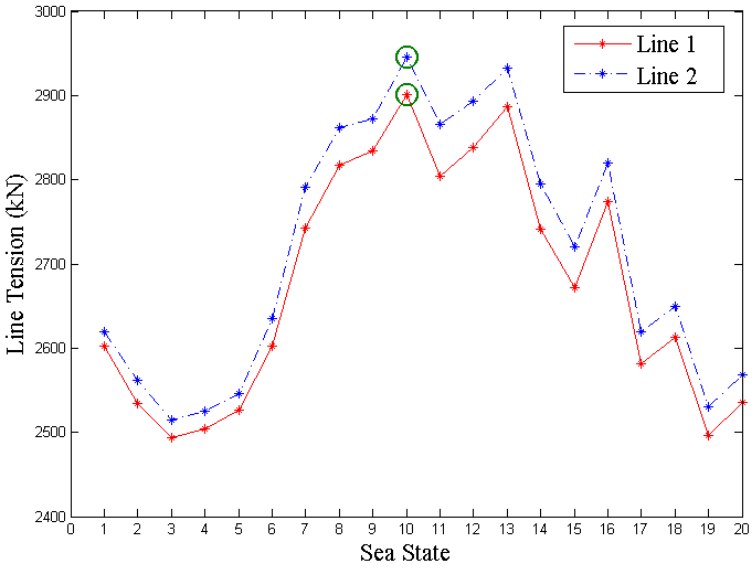

Figure 6.7 The line tension response for selected sea states from contour line of 100-year return period (circle denotes the maxima line characteristic tension)

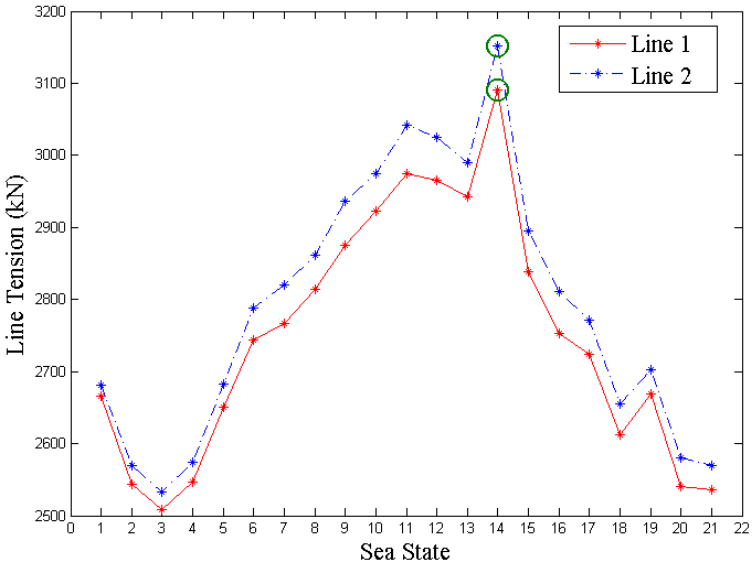

Figure 6.8 The line tension response for selected sea states from contour line of 1000-year return period (circle denotes the maxima line characteristic tension)

The critical sea states along the contour lines have been identified. Then the short term distributions of X_{3h}, for these critical sea states are established according to largest responses of 600 3-hour time domain coupled dynamic analysis. The long term extreme responses corresponding to 50, 100 and 1000-year return period can be estimated by the short term distribution of maxima line tension under the critical sea

states. However, these estimated extreme responses neglect the randomness of short term extreme response. The omitted variability can be accounted for by selecting a higher fractile response instead of the median response as the short term characteristic. The estimated long term extreme responses by selecting different fractiles are shown in Figure 6.9 - Figure 6.11.

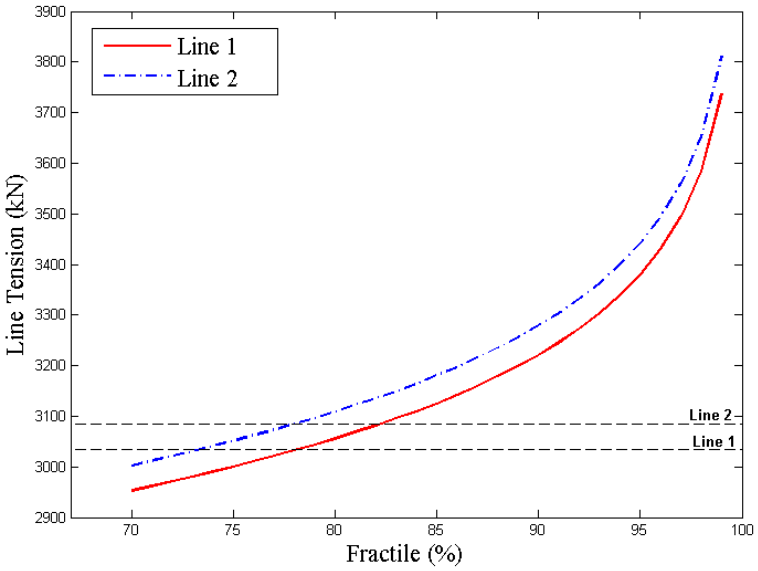

Figure 6.9 Long term extreme response of 50-year return period with different fractiles (dash line is the long term extreme response of 50-year return period by all sea states method)

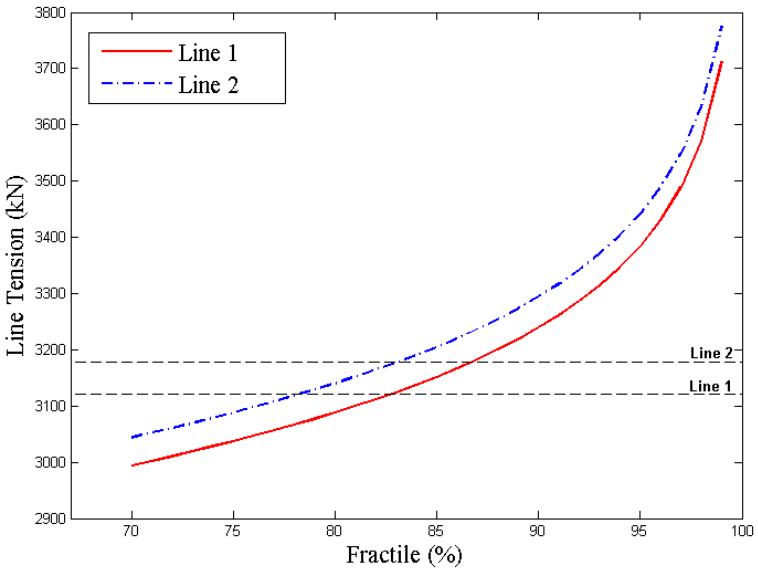

Figure 6.10 Long term extreme response of 100-year return period with different fractiles (dash line is the long term extreme response of 100-year return period by all

sea states method)

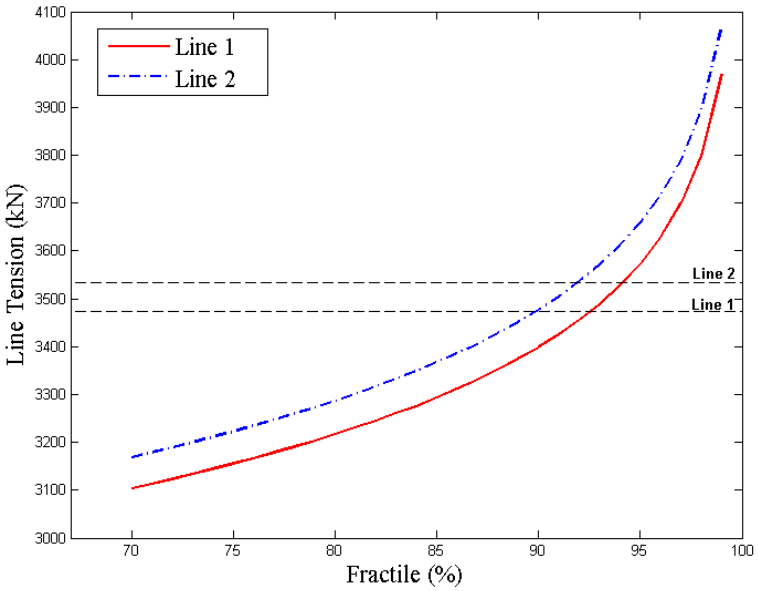

Figure 6.11 Long term extreme response of 1000-year return period with different fractiles (dash line is the extreme response of 1000-year return period by all sea states method)

Table 6.2 Long term extreme responses by all sea states method and contour line method

Return Period (years)	All sea states		Contour line Method		
	Line 1 (kN)	Line 2 (kN)	Line 1 (kN)	Line 2 (kN)	Fractile
50	3033	3084	3032	3085	78%
100	3121	3178	3124	3177	83%
1000	3473	3534	3455	3536	92%

The selected fractiles for the contour line method are verified by a full long term analysis using all sea states method from previous work. The results of the comparison between the two methods are listed in Table 6.2. The selected fractiles are 78%, 83% and 92% for 50, 100, and 1000-year return period, respectively. The fractile can be selected as about 80% for the 50-year return period and 90% for the 1000-year return period. Line 1 and Line 2 tension are 3056 kN and 3109 kN for

80% fractile for the 50-year return period respectively. The errors are 0.75% and 0.81% respectively by comparing them with the results from all sea states method. For 90% fractile for the 1000-year return period, the line 1 and line 2 tensions are 3399 kN and 3477 kN and the errors are 2.1% and 1.6% respectively.

The uncertainty in the extreme estimates can be assessed by the bootstrap approach (Efron and Tibshirani, 1993). The variance and confidence interval are evaluated based on the resampling from a distribution determined by the available sample of data. Figure 6.12 - Figure 6.14 present coefficient of variance (COV) for the 78%, 83%, 92% fractile of the extreme response distribution corresponding to different numbers of 3-hour time domain simulation at the critical sea state for different return periods, respectively. The COVs decrease with the increase of number of simulation. When the number increases above 100, the rate of reduction of the COV becomes small and the COV itself is very small (close to or less than 1%). The 95% confidence intervals of extreme response of line 1 and 2, by selecting relevant fractiles, are shown in Figure 6.15 and Figure 6.16, respectively. It can be seen that the uncertainty in the extreme response analysis by contour line method is rather small.

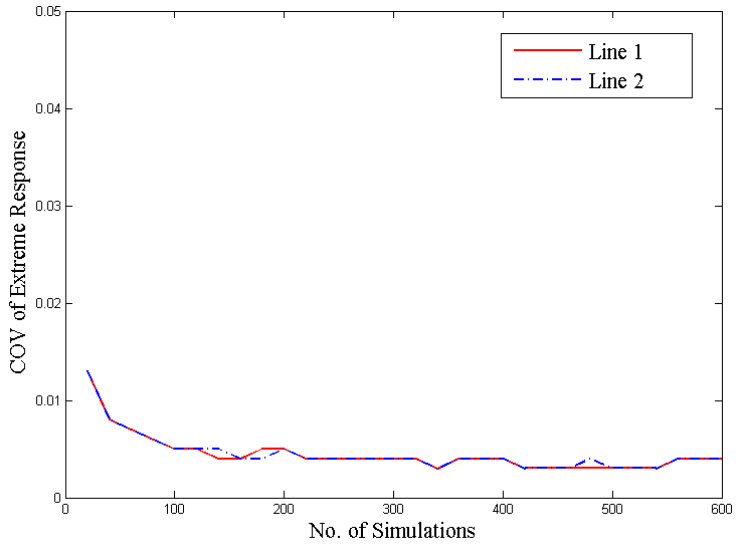

Figure 6.12 COV of extreme response for 50-year return period

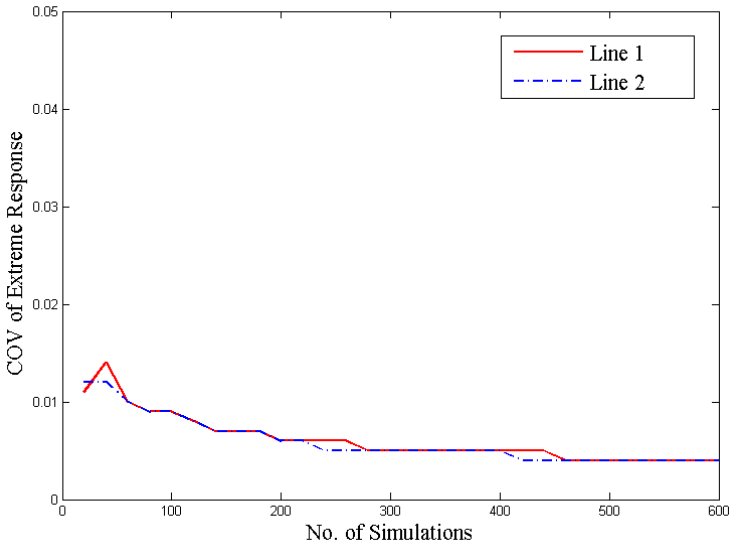

Figure 6.13 COV of extreme response for 100-year return period

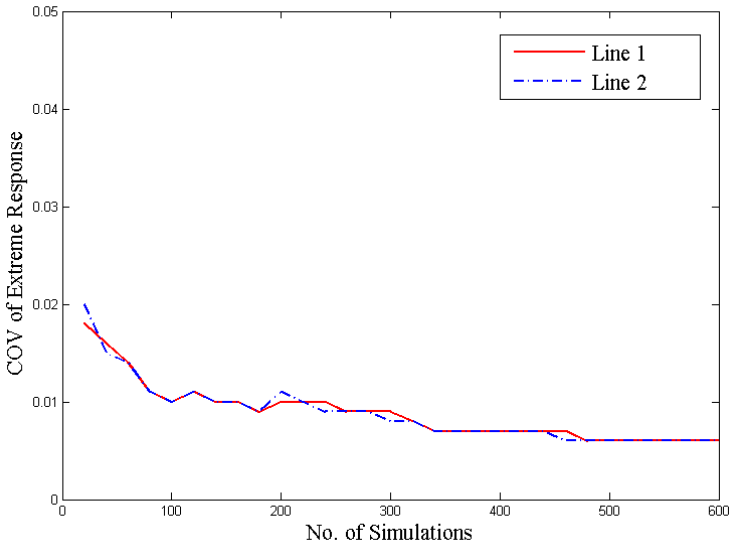

Figure 6.14 COV of extreme response for 1000-year return period

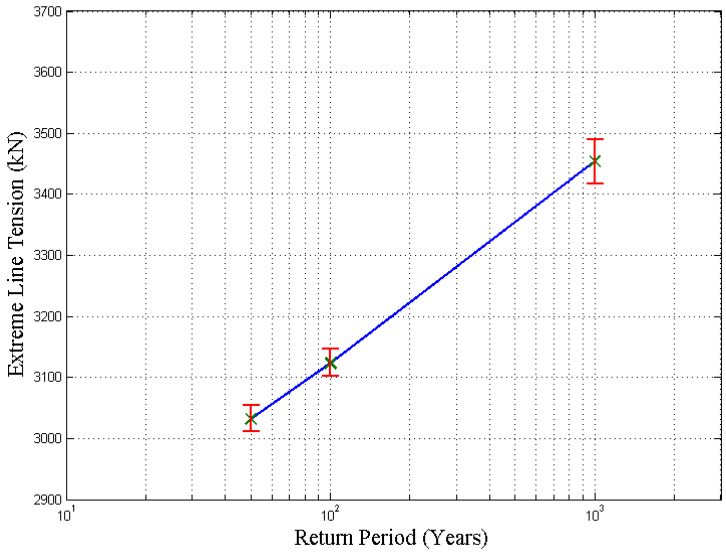

Figure 6.15 95% confidence intervals of extreme response of line 1 for different return periods

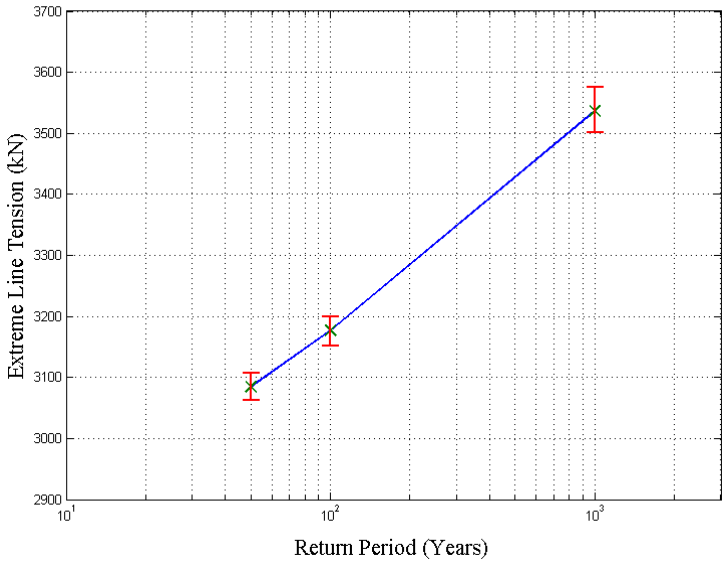

Figure 6.16 95% confidence intervals of extreme response of line 2 for different return periods

6.5 Conclusions

The contour line method which considers the environmental loads independently of the structural response is very useful for predicting the extreme response

corresponding to a given return period or annual exceedance probability for complicated coupled mooring line response problem. The environmental contour line can be established by inverse first order reliability method (IFORM). Time-consuming coupled dynamic analysis are only needed for a limited set of selected sea states along the contour line and critical sea state can be identified from them. The estimated long term extreme response corresponding to n-year return period is nonconservative as it neglects the randomness of short term extreme response. The randomness is accounted for by selecting a high fractile value of short term extreme distribution. The results were compared with the fully long term extreme analysis with all sea states. The fractile values about 78%, 83% and 92%, for 50, 100, 1000-year return period respectively, were adopted in this paper. The uncertainty qualification analysis was performed by the bootstrap method to evaluate the coefficient of variance and confidence interval of extreme response. The results of a numerical case demonstrated the feasibility of the contour line method for the extreme response of a mooring line.

7 Improved Method for Long Term Extreme Analysis

7.1 Introduction

Extreme value analysis is generally based on asymptotic results. It often employs the generalized asymptotic extreme value distribution with unknown parameters to be estimated with the observed data. Or it is assumed that the exceedances above high thresholds follow a generalized asymptotic Pareto distribution with parameters that can be estimated from the data. However, the asymptotic extreme value theory itself cannot be used in practice to decide to what extent it is applicable for the observed data. It is significant to develop an approach for the extreme value prediction problem that is less restrictive and more flexible than the ones based on asymptotic theory.

Naess and Gaidai (2009) developed the average conditional exceedance rates (ACER) method for the extreme value prediction problem that is less restrictive and more flexible than the ones based on asymptotic theory. It has the capability to accurately capture the effect of statistical dependence in the data and it could also incorporate, to a certain extent, the sub-asymptotic part of the data into the extreme value prediction, which is of some importance for accurate prediction.

In this chapter, an improved method for long term analysis is proposed, which based on the ACER method and contour line method. The hybrid response method developed in Chapter 3 is employed for the dynamic analysis and critical sea states are identified by contour line method. The long term extreme responses are obtained by ACER method.

7.2 Average Conditional Exceedance Rate (ACER) Method

Considering a stochastic process of $X(t)$ during a time interval, i.e. 3-hours, $X_1,...,X_N$ is a sample of peaks of $X(t)$ (Naess et al., 2007; Naess and Gaidai, 2008). Then the extreme value distribution follows that

$$\begin{aligned} F_{X_e}(x) &= P\{X_1 \le x, X_2 \le x, \ldots, X_N \le x\} \\ &= P\{X_N \le x | X_1 \le x, \ldots, X_{N-1} \le x\} \cdot P\{X_1 \le x, \ldots, X_{N-1} \le x\} \\ &= \prod_{j=2}^{N} P\{X_j \le x | X_1 \le x, \ldots, X_{j-1} \le x\} \cdot P\{X_1 \le x\} \end{aligned} \tag{7.1}$$

If assume that all the X_j are statistically independent, which leads to the classical approximation as follows.

$$F_{X_e}(x) \approx \prod_{j=2}^{N} P\{X_j \le x\} \tag{7.2}$$

In general, the variables X_j are not statistically independent, the following one-step memory approximation will to a certain extent account for the dependence between the X_j's,

$$P\{X_j \le x | X_1 \le x, \ldots, X_{j-1} \le x\} \approx P\{X_j \le x | X_{j-1} \le x\}, \quad 2 \le j \le N \tag{7.3}$$

If considering the two-step memory approximation,

$$P\{X_j \le x | X_1 \le x, \ldots, X_{j-1} \le x\} \approx P\{X_j \le x | X_{j-2} \le x, X_{j-1} \le x\}, \; 3 \le j \le N \tag{7.4}$$

If considering the (k-1)-step memory approximation,

$$P\{X_j \le x | X_1 \le x, \ldots, X_{j-1} \le x\} \approx P\{X_j \le x | X_{j-(k-1)} \le x, \ldots, X_{j-1} \le x\}, \; k \le j \le N \tag{7.5}$$

This approximation can capture the effect of statistical dependence between

neighboring data in the time series with increasing accuracy. For the distribution with the independence assumption, it can be rewritten as

$$F_{X_e}(x) \approx \prod_{j=1}^{N} p_{1j}(x) = \prod_{j=1}^{N} (1-\alpha_{1j}(x)) \tag{7.6}$$

where $p_{kj}(x) = P\left\{X_{j-(k-1)} \le x, \ldots, X_j \le x\right\}$ for $j \ge k$

$$\alpha_{1j}(x) = P\left\{X_j > x\right\} = 1 - p_{1j}(x)$$

Then

$$F_{X_e}(x) \approx P_1(x) = \exp(-\sum_{j=1}^{N} \alpha_{1j}(x)) \tag{7.7}$$

The extreme value distribution with the one-step approximation, the following relation is obtained.

$$\begin{aligned} F_{X_e}(x) &\approx \prod_{j=2}^{N} P\left\{X_j \le x \middle| X_{j-1} \le x\right\} P\left\{X_1 \le x\right\} \\ &= \prod_{j=2}^{N} \frac{P\left\{X_{j-1} \le x, X_j \le x\right\}}{P\left\{X_{j-1} \le x\right\}} P\left\{X_1 \le x\right\} \\ &= \prod_{j=2}^{N} \frac{p_{2j}(x)}{p_{1,j-1}(x)} p_{11}(x) \\ &= \prod_{j=2}^{N} (1-\alpha_{2j}(x)) p_{11}(x) \end{aligned} \tag{7.8}$$

where $\alpha_{kj}(x)$ denotes the exceedance probability conditional on $(k-1)$ previous non-exceedances

$$\begin{aligned} \alpha_{kj}(x) &= P\left\{X_j > x \middle| X_{j-(k-1)} \le x, \ldots, X_{j-1} \le x\right\} \\ &= 1 - \frac{p_{kj}(x)}{p_{k-1,j-1}(x)} \end{aligned} \tag{7.9}$$

Considering that $p_{11}(x) \approx \exp(-\alpha_{11}(x))$, the extreme value distribution can be obtained in the form that

$$F_{X_e}(x) \approx P_2(x) = \exp(-\sum_{j=2}^{N} \alpha_{2j}(x) - \alpha_{11}(x)) \tag{7.10}$$

Similarly, conditioning on the two previous observations X_{j-2}, X_{j-1} preceding X_j or with the two-step memory approximation, The extreme value distribution can be expressed as

$$F_{X_e}(x) \approx P_3(x) = \exp(-\sum_{j=3}^{N} \alpha_{3j}(x) - \alpha_{22}(x) - \alpha_{11}(x)) \tag{7.11}$$

The distribution can be extended to general form when consider the $(k-1)$-step memory approximation.

$$F_{X_e}(x) \approx P_k(x) = \exp(-\sum_{j=k}^{N} \alpha_{kj}(x) - \sum_{j=1}^{k-1} \alpha_{jj}(x)) \tag{7.12}$$

The extreme value prediction by the conditioning approach reduces to estimation of the $\alpha_{kj}(x)$ functions. For most practical applications N >> k, $\sum_{j=1}^{k-1} \alpha_{jj}(x)$ is small compared to $\sum_{j=k}^{k} \alpha_{kj}(x)$ and it can be neglected. Then the extreme value distribution can be obtained as follow.

$$F_{X_{3h}}(x) \approx \exp(-\sum_{j=k}^{N} \alpha_{kj}(x)) \tag{7.13}$$

7.2.1 Empirical Estimation of the ACER Function

The distribution that considers the $(k-1)$-step memory approximation can be rewritten in the form as follows.

$$F_{X_e}(x) \approx \exp(-\varepsilon_k(x)(N-k+1) - \sum_{j=1}^{k-1} \varepsilon_j(x)) \approx \exp(-\varepsilon_k(x)(N-k+1)) \tag{7.14}$$

where $\varepsilon_k(x)$ can be expressed as follows.

$$\varepsilon_k(x) = \frac{1}{N-k+1} \sum_{j=k}^{N} \alpha_{kj}(x) \tag{7.15}$$

$\varepsilon_k(x)$ is the average conditional exceedance rate (ACER) function. Extreme value prediction by the cascade of conditioning approach described above then reduces to estimation of average conditional exceedance rate (ACER) function, $\varepsilon_k(x)$.

The numerical estimation of $\varepsilon_k(x)$, k=2,3,…, is based on the following random functions,

$$A_{kj}(x) = \mathbf{1}\{X_j > x, X_{j-1} \le x, \ldots, X_{j-k+1} \le x\} \tag{7.16}$$

$$B_{kj}(x) = \mathbf{1}\{X_{j-1} \le x, \ldots, X_{j-k+1} \le x\} \tag{7.17}$$

For $k \ge 2, j = k, ..., N$, where $\mathbf{1}\{Q\}$ denotes the indicator function of some random event Q and $\mathrm{E}[\mathbf{1}\{Q\}] = P(Q)$. Then the function $\alpha_{kj}(x)$ can be expressed as

$$\alpha_{kj}(x) = \frac{\mathbb{E}[A_{kj}(x)]}{\mathbb{E}[B_{kj}(x)]}, \quad k \ge 2, j = k, ..., N \tag{7.18}$$

where $\mathbb{E}[\cdot]$ denotes the expectation operator. Under the assumption that the process $X(\mathrm{t})$ is ergodic, obviously that $\varepsilon_k(x) = \alpha_{kk}(x) = ... = \alpha_{kN}(x)$. Then by replacing ensemble means with corresponding time averages, it has the form as follows.

$$\varepsilon_k(x) = \lim_{N \to \infty} \frac{\sum_{j=k}^{N} a_{kj}(x)}{\sum_{j=k}^{N} b_{kj}(x)} \tag{7.19}$$

where $a_{kj}(x)$ and $b_{kj}(x)$ are the realizations of the random functions $A_{kj}(x)$ and

$B_{kj}(x)$, respectively, for the observed time series. $\sum_{j=k}^{N} a_{kj}(x)$ is the number of time points j when the event $\left\{X_j > x, X_{j-1} \le x, \ldots, X_{j-k+1} \le x\right\}$ occurs for $k \le j \le N$ and $\sum_{j=k}^{N} b_{kj}(x)$ is the number of time points j when the event $\left\{X_{j-1} \le x, \ldots, X_{j-k+1} \le x\right\}$ occurs for $k \le j \le N$.

Then the estimate $\hat{\varepsilon}_k(x)$ of the ACER function $\varepsilon_k(x)$ can be expressed as:

$$\hat{\varepsilon}_k(x) = \frac{\sum_{j=k}^{N} a_{kj}(x)}{\sum_{j=k}^{N} b_{kj}(x)} \tag{7.20}$$

Considering that $\lim_{x\to\infty} \mathbb{E}[B_{kj}(x)] = 1$, we can obtain the following modified ACER function.

$$\begin{aligned} \tilde{\varepsilon}_k(x) &= \frac{1}{N-k+1} \sum_{j=k}^{N} \alpha_{kj}(x) \\ &= \frac{1}{N-k+1} \sum_{j=k}^{N} \frac{\mathbb{E}[A_{kj}(x)]}{\mathbb{E}[B_{kj}(x)]} \\ &= \frac{\sum_{j=k}^{N} \mathbb{E}[A_{kj}(x)]}{N-k+1} \end{aligned} \tag{7.21}$$

for which the following holds: $\lim_{x\to\infty} \tilde{\varepsilon}_k(x) / \varepsilon_k(x) = 1$. It turns out that the modified ACER function $\tilde{\varepsilon}_k(x)$ for $k \ge 2$ is easier to use for non-stationary or long-term statistics than $\varepsilon_k(x)$.

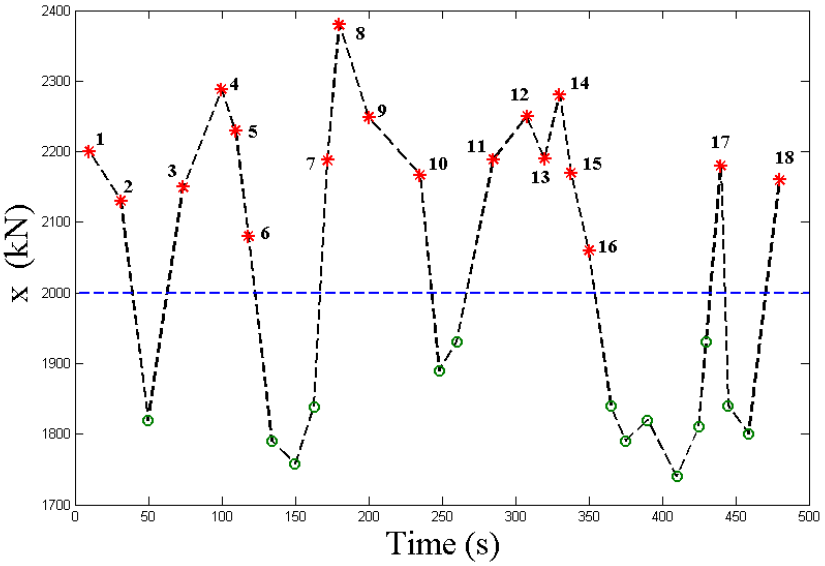

Figure 7.1 Illustration of the exceedance estimation

The process for the exceedances counting is explained by an example shown in Figure 7.1. Considering that the level $x = 2000\,\text{kN}$, the points (green circle) under the level indicates the corresponding non-exceedances, which are used to taken into account for $b_{kj}(x)$. The points (red star) above the level are unconditional exceedances considered for $a_{1j}(x)$. The points are considered for $a_{kj}(x)$, $k = 2\text{-}5$ summarized in the table, which "1" shows the point should be considered and "0" means the point will not be considered, seen in the Table 7.1. We can have a look at what events are actually counted for the estimation of the various $\varepsilon_k(x)$, $\text{k} \geq 2$. For $k = 2$, $\varepsilon_2(x)(N-1)$ is the expected number of exceedances above the level x provided by conditioning on one immediately preceding non-exceedance. And $\varepsilon_2(x)(N-1)$ also equals the average number of clumps of exceedances above x for the realizations considered, where a clump of exceedances is defined as a maximum number of consecutive exceedances above x. In general, $\varepsilon_k(x)(N-k+1)$ then equals the average number of clumps of exceedances above x separated by at least $(k-1)$ non-exceedances.

Table 7.1 Statistical result for the exceedance

No. of point	$a_{1j}(x)$	$a_{2j}(x)$	$a_{3j}(x)$	$a_{4j}(x)$	$a_{5j}(x)$
1	**1**	**0**	**0**	**0**	**0**
2	**1**	**0**	**0**	**0**	**0**
3	**1**	**1**	**0**	**0**	**0**
4	**1**	**0**	**0**	**0**	**0**
5	**1**	**0**	**0**	**0**	**0**
6	**1**	**0**	**0**	**0**	**0**
7	**1**	**1**	**1**	**1**	**0**
8	**1**	**0**	**0**	**0**	**0**
9	**1**	**0**	**0**	**0**	**0**
10	**1**	**0**	**0**	**0**	**0**
11	**1**	**1**	**1**	**0**	**0**
12	**1**	**0**	**0**	**0**	**0**
13	**1**	**0**	**0**	**0**	**0**
14	**1**	**0**	**0**	**0**	**0**
15	**1**	**0**	**0**	**0**	**0**
16	**1**	**0**	**0**	**0**	**0**
17	**1**	**1**	**1**	**1**	**1**
18	**1**	**1**	**1**	**0**	**0**

Estimation of confidence interval

To measure the reliability of an estimate of the $\varepsilon_k(x)$, we should estimate the confidence interval (CI) for $\varepsilon_k(x)$, assuming a stationary time series. In case several

realizations of the time series $X(t)$ are provided, the sample estimate of $\varepsilon_k(x)$ would be:

$$\hat{\varepsilon}_k(x) = \frac{1}{M}\sum_{m=1}^{M}\hat{\varepsilon}_k^{(m)}(x) \tag{7.22}$$

where M is the number of realizations, m is the index of sample no. m and the $\hat{\varepsilon}_k^{(m)}$ can be estimated by using either the result from Eq. (7.23) for the stationary process.

$$\hat{\varepsilon}_k^{(m)}(x) = \frac{\sum_{j=k}^{N_m} a_{kj}^{(m)}(x)}{\sum_{j=k}^{N_m} b_{kj}^{(m)}(x)} \tag{7.23}$$

Or in case the considered stochastic process is non-stationary using the Eq. (7.24),

$$\hat{\varepsilon}_k^{(m)}(x) = \frac{\sum_{j=k}^{N_m} a_{kj}^{(m)}(x)}{N_m - k + 1} \tag{7.24}$$

The sample standard deviation $\hat{s}_k(x)$ can be estimated by the standard formula,

$$\hat{s}_k(x)^2 = \frac{1}{M-1}\sum_{m=1}^{M}(\hat{\varepsilon}_k^{(\mathrm{m})}(x) - \hat{\varepsilon}_k(x))^2 \tag{7.25}$$

Then the confidence interval CI can be evaluated by the form as follows.

$$\mathrm{CI}^{\pm}(x) = \hat{\varepsilon}_k(x) \pm \tau\frac{\hat{s}_k(x)}{\sqrt{M}} \tag{7.26}$$

where τ is the corresponding quantile of the Student's t-distribution.

For the non-stationary case, it is consistent with the adopted approach to assume that the stream of conditional exceedances over a threshold x constitute a Poisson process. The $\mathrm{Var}[\sum_{j=k}^{N} A_{kj}(x)] = \mathbb{E}[\sum_{j=k}^{N} A_{kj}(x)]$.

Then, the limits of the confidence interval of $\tilde{\varepsilon}_k(x)$ for high levels x can be estimated as:

$$\mathrm{CI}^{\pm}(x) = \hat{\varepsilon}_k(x)\left(1 \pm \frac{\tau}{\sqrt{(N-k+1)\hat{\varepsilon}_k(x)}}\right) \tag{7.27}$$

where τ is the corresponding quantile of the normal distribution.

7.2.2 Prediction of the ACER Function

Based on the sampled time series only, possible sub-asymptotic functional forms of $\varepsilon_k(x)$ cannot easily be obtained. Naess and Gaidai (2009) proposed that the asymptotic extreme value distribution is of Gumbel type can be used as a guide. Using the asymptotic form as a guide, it is assumed that the behavior of the mean exceedance rate in the tail is dominated by a function of the form $\exp\left\{-a(x-b)^c\right\}$, $x \geq x^* > b$, where a, b, c are suitable constants and x^* is the chosen tail maker that corresponds to the beginning of regular tail behavior of the ACER function. This method has been applied for mean up-crossing rate estimation for extreme value analysis of the response processes related to different dynamic systems (Naess et al., 2007; Naess and Gaidai, 2008). Then the ACER functions can be expressed in the tail as follows

$$\varepsilon_k(x) = q_k(x)\exp\left\{-a_k(x-b_k)^{c_k}\right\}, \quad x \geq x^* \tag{7.28}$$

where $q_k(x)$ is slowly varying compared with the exponential function, and a_k, b_k, c_k are suitable constants. When $c_k = q_k = 1$, it corresponds to the asymptotic Gumbel form.

The equation can be rewritten to the form as follows,

$$-\ln\left|\ln\left(\frac{\varepsilon_k(x)}{q_k(x)}\right)\right| = -c_k(x)\ln(x-b_k) - \ln(a_k) \tag{7.29}$$

It can be seen that a plot of $\ln\left|\ln(\varepsilon_k(x)/q_k(x))\right|$ versus $\ln(x-b_k)$ reveals the linear behavior in the tail. Considering that the variation of $q_k(x)$ in the tail region is sufficiently slow and it can be replaced by a constant q_k, possibly by adjusting the tail marker x^*. The tail marker x^* can be identified from the log plot $(x, \ln\varepsilon_k(x))$ where the value of x corresponds to the start of the regular tail behavior. If the initial values estimates for parameters b_k and q_k are calculated by linearizing the tail on the transformed scale. Then the initial value of the parameters a_k and c_k can be determined from the fitted straight line to the data tail.

This representation of the ACER function can capture to a certain extent sub-asymptotic behavior of any extreme value distribution that is asymptotically Gumbel and this parametric function agree with a wide range of known special cases (Naess et al., 2013). We also should cut from consideration the very tail of the data, where uncertainty is too high according to the following criterion; Naess suggest a practical procedure to neglect data points, where the relative confidence band width is greater than some constant δ, whose value is dependent on the accuracy of the data tail and it could typically in the interval (0.5,1]. It is expressed in the form as follows.

$$\frac{1.96\hat{s}_k(x)/\sqrt{M}}{\varepsilon_k(x)} > \delta \tag{7.30}$$

Instead of obtaining the parameters directly from the loglog-plot, the Levenberg-Marquardt least squares optimization method can be employed to optimize the fit on the log level with respect to all four parameters a_k, b_k, c_k, q_k and the optimal estimation of the four parameters are obtained by minimizing the mean square error function.

$$F(a_k, b_k, c_k, q_k) = \sum_{j=1}^{L} w_j \left| \ln \varepsilon_k(x_j) - \ln q_k + a_k (x_j - b_k)^{c_k} \right|^2 \tag{7.31}$$

where x_j , $j = 1, ..., L$ are the levels where the ACER functions have been empirically estimated. w_j denotes a weight factor and $w_j = [\ln C^+(x_j) - \ln C^-(x_j)]^{-\theta}$, θ=1 or 2, combined with the Levenberg-Marquardt least squares optimization method (Gill et al., 1981). The summation has to stop at the high level x_j at which $C^-(x_j)$ becomes negative.

Naess and Gaidai (2009) developed a more direct and transparent method for the optimization problem using Levenberg-Marquardt method. It is assumed that b_k and c_k are fixed, then the optimal values of a and log q can be estimated by the closed form weighted linear regression formulas, which is shown as follows.

$$a_k^*(b_k, c_k) = -\frac{\sum_{j=1}^{L} w_j (m_j - \bar{m})(y_j - \bar{y})}{\sum_{j=1}^{L} w_j (m_j - \bar{m})^2} \tag{7.32}$$

$$q_k^*(b_k, c_k) = \exp(\bar{y} + a_k^*(b_k, c_k) m) \tag{7.33}$$

where $m_j = (x_j - b_k)^{c_k}$, $y_j = \ln \varepsilon_k(x_j)$, $\bar{m} = \frac{\sum_{j=1}^{L} w_j x_j}{\sum_{j=1}^{L} w_j}$ and $\bar{y} = \frac{\sum_{j=1}^{L} w_j y_j}{\sum_{j=1}^{L} w_j}$.

Then the function $F(a_k^*(b_k, c_k), b_k, c_k, q_k^*(b_k, c_k))$ involves two parameters and it can employ the Levenberg-Marquardt to evaluate the optimal value b_k^* and c_k^* and then the corresponding a_k^* and q_k^* can be estimated.

Now the deep tail extreme value can be predicted by the ACER function with the fitted parametric curve. Then it is significant to estimate the confidence interval of the deep tail extreme value. Naess and Gaidai (2009) proposed a method to evaluate the confidence interval of the extreme value predicted using the parametric ACER function. The empirical confidence band is reanchored to the optimally fitted curve by centering the individual confidence intervals $\mathrm{CI}^{\pm}(x_j)$ for the point estimates of the ACER function on the fitted curve, as shown in Eq. (7.34). Naess et al. (2013) proposed that the corresponding parametric curves can be fitted to the given set of points $(x_j, \mathrm{CI}^{+}(x_j))$ and $(x_j, \mathrm{CI}^{-}(x_j))$ of the re-anchored confidence band. The same fitting procedure for ACER function can be used here.

$$\mathrm{CI}^{\pm}(x_j) = \varepsilon_k(x_j) \pm \tau \frac{\hat{s}_k(x_j)}{\sqrt{M}}, \quad j = 1, 2, ..., L \tag{7.34}$$

7.3 Improved Method for Long Term Extreme Analysis by Contour Line Method with Hybrid Method

As the advantage of the average conditional exceedance rates (ACER) method for the extreme value prediction problem, it is less restrictive and more flexible than the ones based on asymptotic theory. Here, the assessment for long term extreme analysis of mooring lines can be done by the ACER method with the contour line method which discussed in Chapter 6. The detail for the proposed method is shown in Figure 7.2. Firstly, the contour line (surface) is constructed based on the joint distributions of environmental parameters. Then, the critical sea state is identified from the selected sea states along the contour line. Long term extreme analysis is performed by using of ACER method.

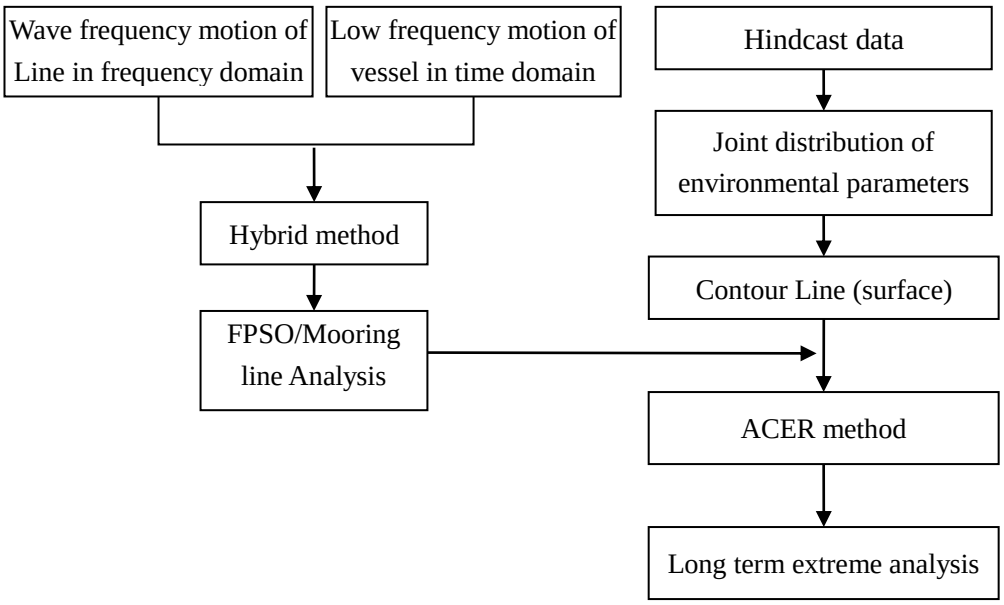

Figure 7. 2 Flowchart of improved method for long term extreme analysis

7.4 Numerical Case

The case used in Chapter 6 is used here. The model of FPSO mooring system is shown in Figure 4.8. The mooring lines are multi components (chain-wire-chain) and the properties of mooring lines are given in Table 4.1. The most loaded lines, Line 1 and Line 2, are considered here.

The ACER method can take the $(k-1)$-step memory approximation into account. The different memory step approximations are calculated in Figure 7.3. It can be seen that when k=3 the ACER function has convergerged. Figure 7.4 presents the prediction of extreme line tension for Line1 corresponding to the probability level of 10^{-6}. The blue dot dash line gives the 95% CI.

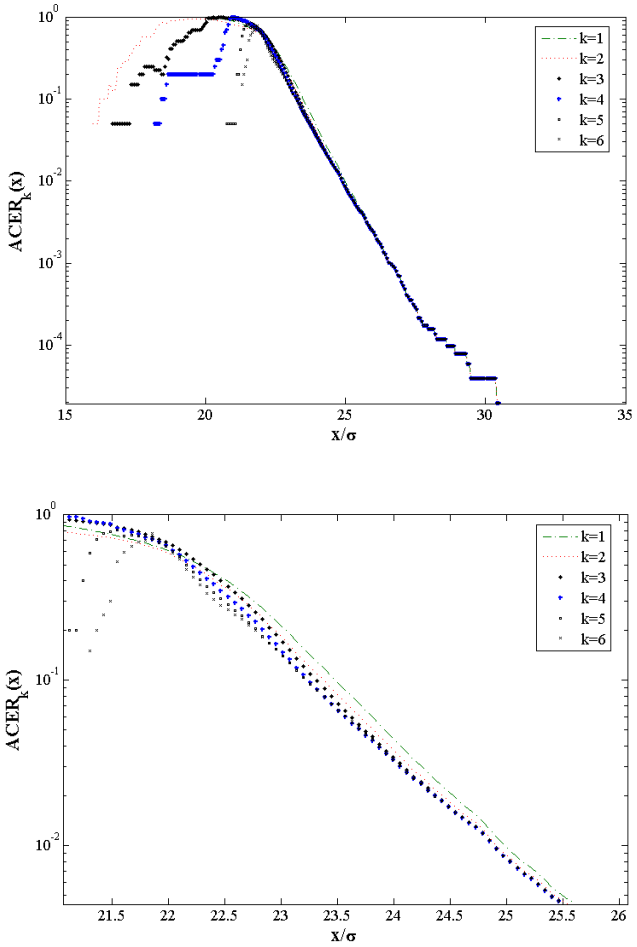

Figure 7.3 ACER function convergence for Line1

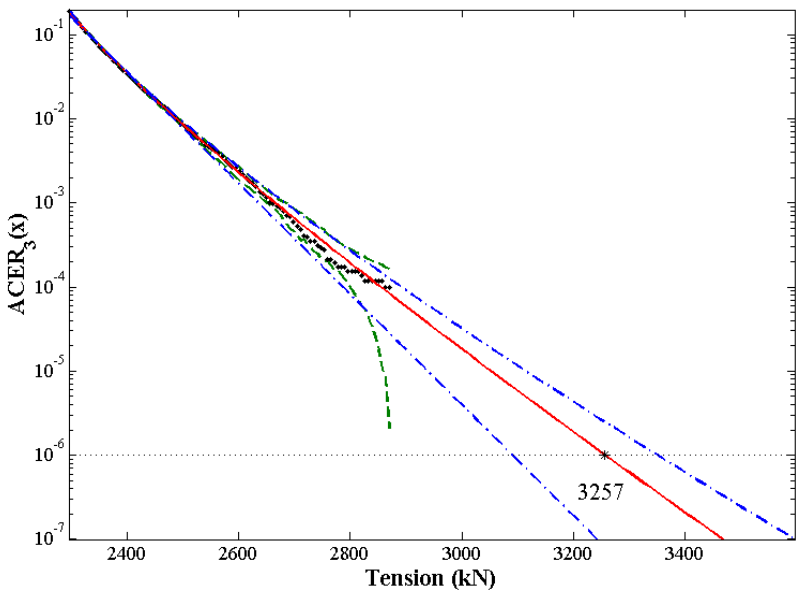

Figure 7.4 ACER extrapolation toward probability level of 10^{-6} for Line1(blue dot dash - 95% CI, green dash - empirical 95% CI, red line - extreme line tension)

Figure 7.5 presents the different steps memory approximations and it can be seen that the ACER function has convergerged when k is 3. The prediction of extreme line tension for Line2 corresponding to the probability level of 10^{-6}, with blue dot dash line indicating the 95% CI, is presented in Figure 7.6.

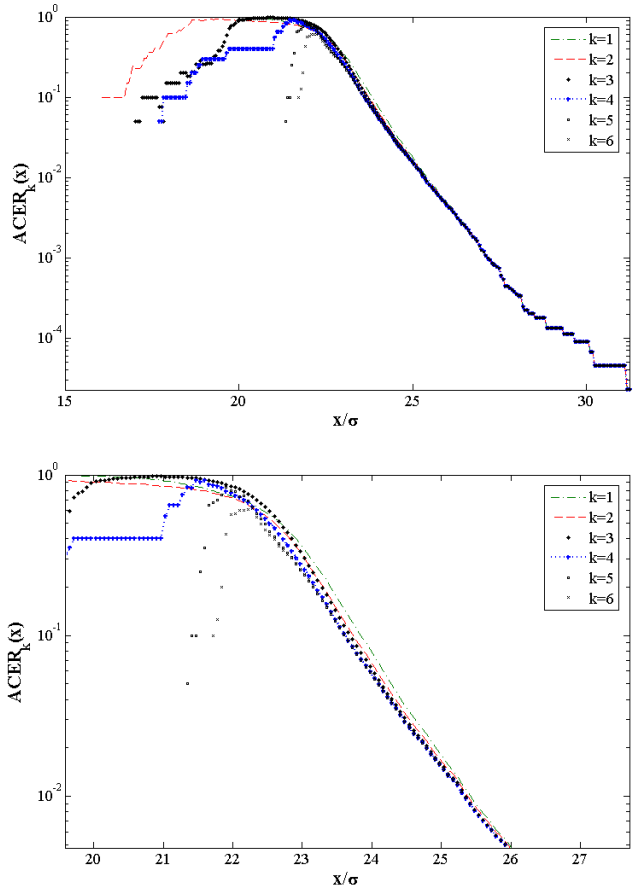

Figure 7.5 ACER function convergence for Line2

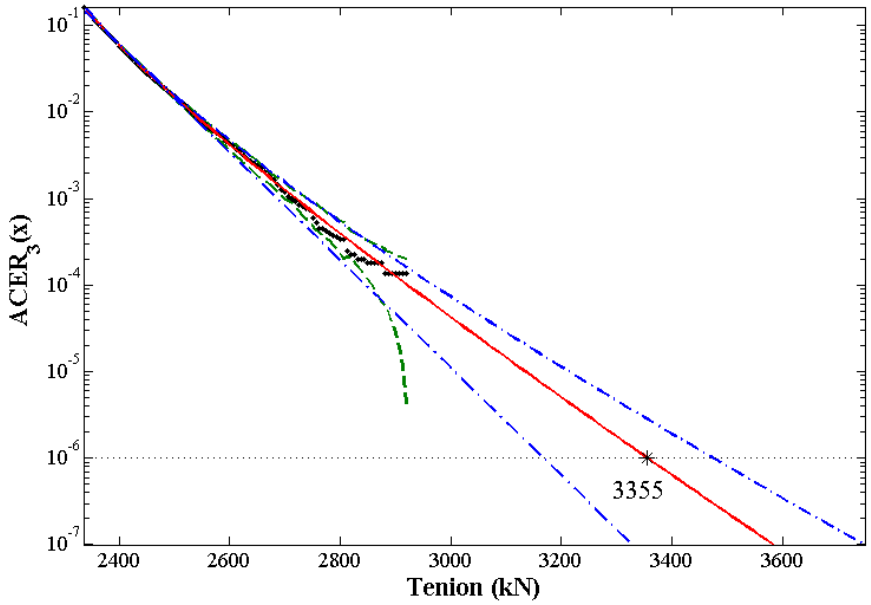

Figure 7.6 ACER extrapolation toward probability level of 10^{-6} for Line2 (blue dot dash - 95% CI, green dash - empirical 95% CI, red line - extreme line tension)

The improved method for assessing long term extreme response are verified by a full long term analysis using all sea states method from previous work. The results of the comparison between the two methods are listed in Table 7.2. The prediction of Line 1 and Line 2 tension with ACER method are 3257 kN and 3355 kN, corresponding to probability level of 10^{-6}. The errors are 1.15% and 0.18% respectively by comparing them with the results from all sea states method. The numerical case demonstrate the proposed method can be good at prediction of the long term extreme responses of mooring lines.

Table 7.2 Long term extreme responses by all sea states method and ACER method

Exceedance Probability 10^{-6}	Line 1 Tension (kN)	Line 2 Tension (kN)
ACER	3257	3355
All Sea States	3295	3361
Error (%)	1.15	0.18

7.5 Conclusions

The improved method which employs the average conditional exceedance rates (ACER) method for the extreme value prediction problem was demonstrated in this chapter. The ACER method has the capability to accurately capture the effect of statistical dependence in the data and it could incorporate to a certain extent also the sub-asymptotic part of the data into the extreme value prediction. With the assumption of the tail behaving very closely like an exponential function, this method enables extrapolation up to the probability level of 10^{-6}. The estimated long term extreme responses of mooring line were compared with the fully long term extreme analysis with all sea states. The results of numerical case demonstrated the feasibility of the ACER method for extreme response of mooring line.

8 Effect of Hydrodynamic Drag Coefficient on Long Term Extreme Response

8.1 Introduction

For a specified body shape, the drag coefficients depend on the following factors: Reynolds number, Keulegan-Carpenter number and roughness number. For mooring lines in deep water it is crucial to apply proper drag coefficients for calculating line damping contributions. The drag coefficient depends on the three factors in the free-surface zone with both waves and current actions. In steady current flow, the KC number is not of relevance and the drag coefficient depends on the Reynolds number and the roughness number. Ideally, the coefficient dependence on Re, KC and roughness number should be implemented by choosing coefficients from tables and curves when performing a coupled analysis. However, present state of the art within coupled analyses usually does not make use of this option (DNV-RP-F205, 2010) and it is difficult to introduce simple recommendations on which drag coefficients to be used.

The mooring line damping is very important for the estimation of the maximum offset of FPSO and corresponding maximum line tension. Morrison equation using the drag coefficient is employed to evaluate the hydrodynamic force on the mooring lines. The variation of drag coefficient will alter the level of damping, which is important to extreme response of the vessel low frequency motion and the associated line tension. It is useful to study the effect of drag coefficient on the long term extreme response.

The general approach for investigating the effect of uncertainty on long term extreme value estimation is proposed. The perturbation method, which aexpanded to 2nd order and 4th order, is proposed for the study. The asymptotic approximation of the probability integral is utilized and validation the the effect of the uncertainty. Then, the proposed approach is applied to investigate the effect of drag coefficient on the long term extreme response.

8.2 Effect of Uncertainty on Long Term Extreme Value Estimation

Uncertainty parameters or randomness have effect on extreme response estimation of structures, which should take in into account. The uncertainty parameters are described by random variables $\boldsymbol{u} = (u_1, u_2, ..., u_n)$ with a joint probability density function $f(\boldsymbol{u})$ or parameters such as mean values, standard deviation, etc. Then the extreme response can be evaluated using the form as follows.

$$\mathrm{F}_X(x) = \int \mathrm{F}_X(x|\boldsymbol{u}) f(\boldsymbol{u}) d\boldsymbol{u} \tag{8.1}$$

It is impractical to employ the direct numerical integration for this probability integral. Monte Carlo simulation can provide the accurate results for the extreme response considering the effect of uncertainty. The samples $\boldsymbol{u}_i$ (i=1,2,..,N) of $\boldsymbol{u}$ can be sampled according to its underlying distribution. Then the estimated extreme value is given as

$$\mathrm{F}_X(x) \approx \frac{1}{N} \sum_{i=1}^{N} \mathrm{F}_X(x|\boldsymbol{u}_i) \tag{8.2}$$

However, this method is crude that it requires a large number of simulations. An improved method, importance sampling, is by choosing a distribution $g(\boldsymbol{u})$ to simulate more samples, which give more contribution to the evaluation of the probability integral.

$$\mathrm{F}_X(x) = \int \frac{\mathrm{F}_X(x|\boldsymbol{u})\, f(\boldsymbol{u})}{g(\boldsymbol{u})}\, g(\boldsymbol{u}) d\boldsymbol{u} \tag{8.3}$$

$$\mathrm{F}_X(x) \approx \frac{1}{N} \sum_{i=1}^{N} \frac{\mathrm{F}_X(x|\boldsymbol{u}_i)\, f(\boldsymbol{u}_i)}{g(\boldsymbol{u}_i)} \tag{8.4}$$

8.2.1 Perturbation Method

The perturbation method is based on expanding the $\mathrm{F}_X(x|\boldsymbol{u})$ into a Taylor series about the mean $\bar{\boldsymbol{u}}$ of $\boldsymbol{u}$. The second-order Taylor expansion yields

$$\mathrm{F}_X(x|\boldsymbol{u}) = \mathrm{F}_X(x|\bar{\boldsymbol{u}}) + \mathrm{F}'_X(x|\bar{\boldsymbol{u}})(\boldsymbol{u}-\bar{\boldsymbol{u}}) + \frac{\mathrm{F}''_X(x|\bar{\boldsymbol{u}})}{2}(\boldsymbol{u}-\bar{\boldsymbol{u}})^2 \tag{8.5}$$

Then submit it into Eq.(8.1), we can obtain that

$$\begin{aligned} \mathrm{F}_X(x) &= \int \mathrm{F}_X(x|\boldsymbol{u}) f(\boldsymbol{u}) d\boldsymbol{u} \\ &= \int \left\{ \mathrm{F}_X(x|\bar{\boldsymbol{u}}) + \mathrm{F}'_X(x|\bar{\boldsymbol{u}})(\boldsymbol{u}-\bar{\boldsymbol{u}}) + \frac{1}{2}\mathrm{F}''_X(x|\bar{\boldsymbol{u}})(\boldsymbol{u}-\bar{\boldsymbol{u}})^2 \right\} f(\boldsymbol{u}) d\boldsymbol{u} \\ &= \mathrm{F}_X(x|\bar{\boldsymbol{u}}) + \frac{1}{2}\mathrm{F}''_X(x|\bar{\boldsymbol{u}})\,\mathrm{Var}(\boldsymbol{u}) \end{aligned} \tag{8.6}$$

where $\mathrm{Var}(\boldsymbol{u})$ is the variance of $\boldsymbol{u}$ under the probability distribution $f(\boldsymbol{u})$.

The second-derivative $\mathrm{F}''_X(x|\bar{\boldsymbol{u}})$ can be evaluated numerically by use of employing a central difference scheme.

$$\mathrm{F}''_X(x|\bar{\boldsymbol{u}}) = \frac{\mathrm{F}_X(x|\bar{\boldsymbol{u}}+\Delta\boldsymbol{u}) + \mathrm{F}_X(x|\bar{\boldsymbol{u}}-\Delta\boldsymbol{u}) - 2\,\mathrm{F}_X(x|\bar{\boldsymbol{u}})}{(\Delta\boldsymbol{u})^2} \tag{8.7}$$

The perturbation method is computational least expensive method and it works well only for limited cases and for relatively small levels of uncertainties (Koyluoglu, 1995).

We can see that the 2nd-order expansion of $\mathrm{F}_X(x|\boldsymbol{u})$ just includes the variance of $\boldsymbol{u}$. If it is expanded to higher order series, the more information about the distribution will been given. The following 4th-order expansion is derived. The 4th-order expansion includes the skewness and kurtosis of $\boldsymbol{u}$.

$$\begin{aligned}\mathrm{F}_X(x) &= \int \mathrm{F}_X(x|\boldsymbol{u}) f(\boldsymbol{u}) d\boldsymbol{u} \\ &= \int \left\{ \mathrm{F}_X(x|\bar{\boldsymbol{u}}) + \mathrm{F}'_X(x|\bar{\boldsymbol{u}})(\boldsymbol{u}-\bar{\boldsymbol{u}}) + \frac{1}{2}\mathrm{F}''_X(x|\bar{\boldsymbol{u}})(\boldsymbol{u}-\bar{\boldsymbol{u}})^2 + \frac{1}{6}\mathrm{F}'''_X(x|\bar{\boldsymbol{u}})(\boldsymbol{u}-\bar{\boldsymbol{u}})^3 + \frac{1}{24}\mathrm{F}^{(4)}_X(x|\bar{\boldsymbol{u}})(\boldsymbol{u}-\bar{\boldsymbol{u}})^4 \right\} f(\boldsymbol{u}) d\boldsymbol{u} \\ &= \mathrm{F}_X(x|\bar{\boldsymbol{u}}) + \frac{1}{2}\mathrm{F}''_X(x|\bar{\boldsymbol{u}})\,\mathrm{Var}(\boldsymbol{u}) + \frac{1}{6}\mathrm{F}'''_X(x|\bar{\boldsymbol{u}})\mathrm{E}[(\boldsymbol{u}-\bar{\boldsymbol{u}})^3] + \frac{1}{24}\mathrm{F}^{(4)}_X(x|\bar{\boldsymbol{u}})\mathrm{E}[(\boldsymbol{u}-\bar{\boldsymbol{u}})^4]\end{aligned} \tag{8.8}$$

8.2.2 Asymptotic Approximation

The asymptotic approximation is a method based on Laplace's method for the asymptotic approximation of probability integral. The asymptotic evaluation is based on the assertion that the greatest contribution to an integral derives from the locations where the integrand is a maximum point.

Let $\mathrm{T}(\boldsymbol{u}) = \ln[\mathrm{F}_X(x|\boldsymbol{u}) f(\boldsymbol{u})]$. The Eq.(8.1) can be evaluated by this asymptotic approximation method, introduced in Appendix F, as a multivariate case where $\boldsymbol{u}$ is a n-dimensional vector.

$$\mathrm{F}_X(x) = \int \exp[\mathrm{T}(\boldsymbol{u})] d\boldsymbol{u} \tag{8.9}$$

Then expanding $\mathrm{T}(\boldsymbol{u})$ around its maximum point $\boldsymbol{u}^*$ by Taylor expansion series and considering that the derivatives are zero at $\boldsymbol{u}^*$, we can obtain that

$$\mathrm{T}(\boldsymbol{u}) \approx \mathrm{T}(\boldsymbol{u}^*) - \frac{1}{2}(\boldsymbol{u}-\boldsymbol{u}^*)^T H(\boldsymbol{u}^*)(\boldsymbol{u}-\boldsymbol{u}^*) \tag{8.10}$$

where $H(\boldsymbol{u}^*)$ is the Hessian matrix of $\mathrm{V}(\boldsymbol{u}) = -\mathrm{T}(\boldsymbol{u})$ that evaluated at the maximum point $\boldsymbol{u}^*$. The Hessian matrix is a square matrix of second-order partial derivate of $\mathrm{V}(\boldsymbol{u})$.

The asymptotic approximation result for the probability integral can be obtained as follows.

$$\mathrm{F}_X(x) \approx \mathrm{F}_X(x|\boldsymbol{u}^*) f(\boldsymbol{u}^*) \frac{(2\pi)^{n/2}}{\sqrt{\det[H(\boldsymbol{u}^*)]}} \tag{8.11}$$

where $\det[\cdot]$ denotes the matrix determinant. This approximation is asymptotically correct as λ tends towards infinitude and here λ is the minimum eigenvalue of the Hessian matrix $H(\boldsymbol{u}^*)$.

In the case where there are multiple local maximum points, it can be evaluated by summing the asymptotic contribution from each maximum point $\boldsymbol{u}_i^*$.

$$\mathrm{F}_X(x) \approx \sum_{i=1}^{m} \mathrm{F}_X(x|\boldsymbol{u}_i^*) f(\boldsymbol{u}_i^*) \frac{(2\pi)^{n/2}}{\sqrt{\det[H(\boldsymbol{u}_i^*)]}} \tag{8.12}$$

8.3 Effect of Drag Coefficient on Long Term Extreme Response

The mooring line's drag coefficient is very important to the damping and the ensuing maximum line tension. Furthermore, there are no specific selecting rules for it because the mooring line's drag coefficient is not easily determined by test. It is significant to ascertain the effect of the drag coefficients on the long term extreme response. Firstly, the effect of uncertainty on the extreme response can be evaluated by the pertrbation method. The 2nd-order expansion and 4th-order expansion will be used to estimate the extreme response, which formulas are listed below. Here random

variable u indicates the drag coefficient.

$$\mathrm{F}_X(x) = \mathrm{F}_X(x|\bar{u}) + \frac{1}{2}\mathrm{F}''_X(x|\bar{u})\,\mathrm{Var}(u) \tag{8.13}$$

$$\mathrm{F}_X(x) = \mathrm{F}_X(x|\bar{u}) + \frac{1}{2}\mathrm{F}''_X(x|\bar{u})\,\mathrm{Var}(u) + \frac{1}{6}\mathrm{F}'''_X(x|\bar{u})\mathrm{E}[(u-\bar{u})^3] + \frac{1}{24}\mathrm{F}^{(4)}_X(x|\bar{u})\mathrm{E}[(u-\bar{u})^4] \tag{8.14}$$

The second-derivative, 3rd-derivative and 4th-derivative derived from the above formulas can be evaluated numerically by use of a central difference scheme.

$$\mathrm{F}''_X(x|\bar{u}) = \frac{\mathrm{F}_X(x|\bar{u}+\Delta u) + \mathrm{F}_X(x|\bar{u}-\Delta u) - 2\,\mathrm{F}_X(x|\bar{u})}{(\Delta u)^2}$$

$$\mathrm{F}'''_X(x|\bar{u}) = \frac{\mathrm{F}_X(x|\bar{u}+2\Delta u) - 2\,\mathrm{F}_X(x|\bar{u}+\Delta u) + 2\,\mathrm{F}_X(x|\bar{u}-\Delta u) - \mathrm{F}_X(x|\bar{u}-2\Delta u)}{2(\Delta u)^3}$$

$$\mathrm{F}^{(4)}_X(x|\bar{u}) = \frac{\mathrm{F}''_X(x|\bar{u}+\Delta u) + \mathrm{F}''_X(x|\bar{u}-\Delta u) - 2\,\mathrm{F}''_X(x|\bar{u})}{(\Delta u)^2}$$

The extreme response can be evaluated using the asymptotic approximation method discussed as above.

$$\mathrm{F}_X(x) \approx \mathrm{F}_X(x|u^*)\,f(u^*)\frac{\sqrt{2\pi}}{\sqrt{|\mathrm{V}''(u^*)|}} \tag{8.15}$$

Searching for the maxima point u^* of $\mathrm{T}(u)$ is equivalent to finding the minimum point u^* of $\mathrm{V}(u)$, which it can be evaluated using Newton's method.

$$u^*_{k+1} = u^*_k - \frac{\mathrm{V}'(u^*_k)}{\mathrm{V}''(u^*_k)} \tag{8.16}$$

Where:

$$V'(u^*) = -\left\{\frac{F'_X(x|u^*)}{F_X(x|u^*)} + \frac{f'(u^*)}{f(u^*)}\right\} \tag{8.17}$$

$$V''(u^*) = -\left\{\frac{F''_X(x|u^*)F_X(x|u^*) - [F'_X(x|u^*)]^2}{[F_X(x|u^*)]^2} + \frac{f''(u^*)f(u^*) - [f'(u^*)]^2}{[f(u^*)]^2}\right\} \tag{8.18}$$

And the corresponding derivatives can be evaluated by employing the central difference method.

$$F'_X(x|u^*) = \frac{F_X(x|u^* + \Delta u) - F_X(x|u^* - \Delta u)}{2\Delta u} \tag{8.19}$$

$$F''_X(x|u^*) = \frac{F_X(x|u^* + \Delta u) + F_X(x|u^* - \Delta u) - 2F_X(x|u^*)}{(\Delta u)^2} \tag{8.20}$$

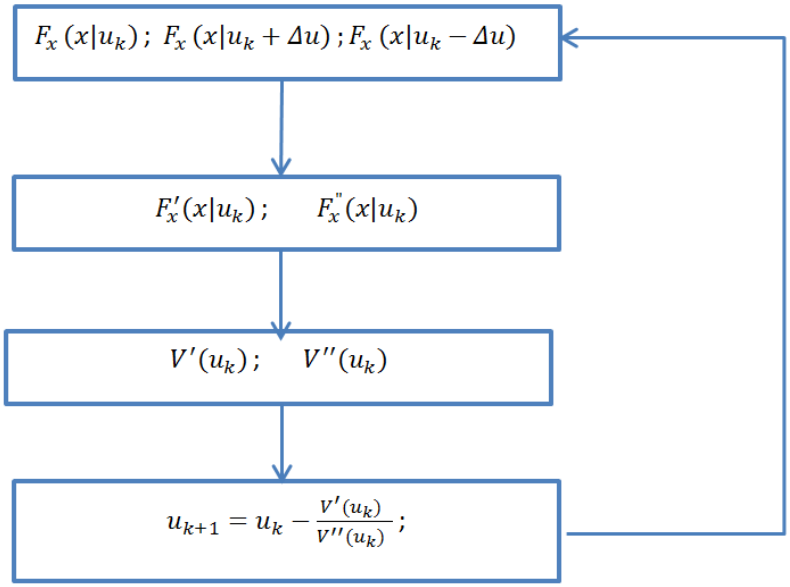

Figure 8.1 Flowchart of asymptotic approximation method

8.4 Numerical Case

To ascertain the effect of the drag coefficients on the long term extreme response, the model of FPSO mooring system shown in Figure 4.8 is used here. It assumes that the drag coefficients obey the normal distribution which has a mean value and coefficient of variance (COV). The previously proposed ACER method is used to

predict the extreme response of mooring line tension.

Figure 8.2 and 8.3 present the up-crossing rate or ACER function for the line tension with different mean values of drag coefficient and then predicted the extreme values at the probability level of 10^{-6}. The estimated extreme responses are 3637kN, 3247kN and 3775kN with respect to the mean value of drag coefficient 2.2, 2.4 and 2.6, respectively. An increase in the line drag coefficient will increase the mean offset as well as typically the dynamic tension, but reduce low frequency dynamic offset. From the results, we can see that the line tension will depend on the contributions of these two components.

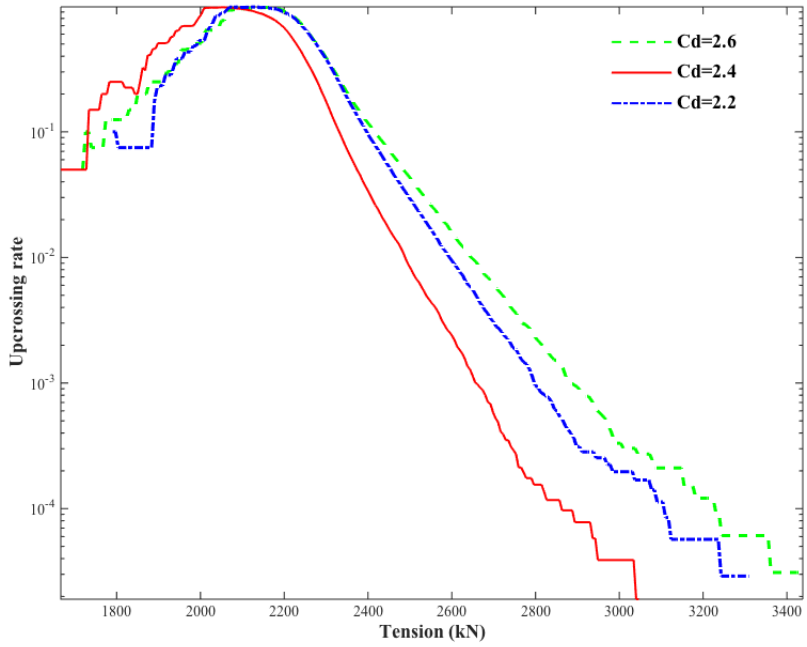

Figure 8.2 Upcrossing rate by ACER method (k=3) for different mean values

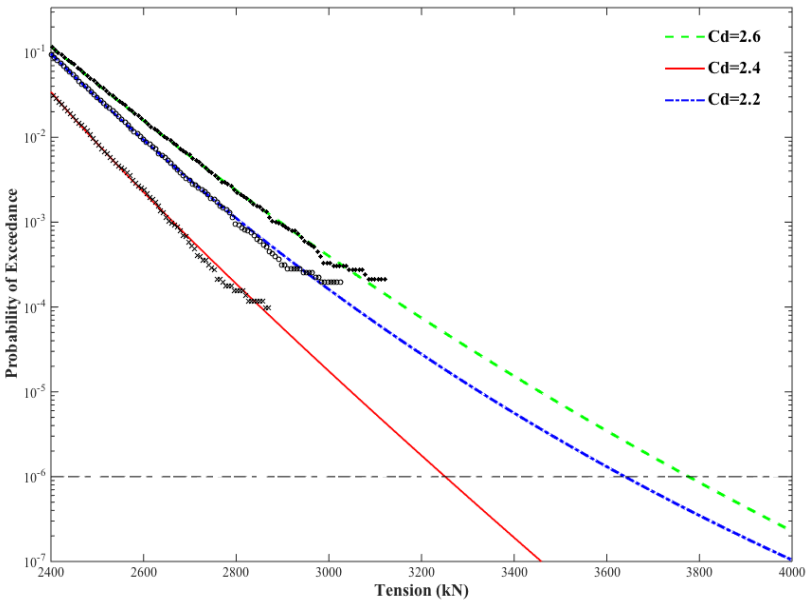

Figure 8.3 Prediction of extreme response by ACER method (k=3) for different mean values

To study the variation of drag coefficient impact on the extreme response of mooring line, the perturbation method is firstly employed here. The mean value of drag coefficient is 2.4. For the case of COV equals 0.02, shown in Figure 8.4, the extreme responses of mooring line tension, corresponding to probability level of 10^{-6}, are 3499kN for 2^{nd}-order expansion and 3525kN for 4^{th}-order expansion. The difference between the extreme responses based on different expansions for low coefficient of variance is small. Figure 8.5 presents the case of COV equal to 0.04. The extreme responses, corresponding to a probability level of 10^{-6}, are 3601kN for 2^{nd}-order expansion and 3707kN for 4^{th}-order expansion. It can be seen that the predicted extreme responses by different expansion method will different for high coefficient of variance. It means that the accuracy of 2^{nd} -order expansion may be not enough for predicting the response. Compared with 2^{nd}-order expansion, the 4^{th}-order expansion can have more information about distribution that not only includes the variance but also includes the skewness and kurtosis of distribution.

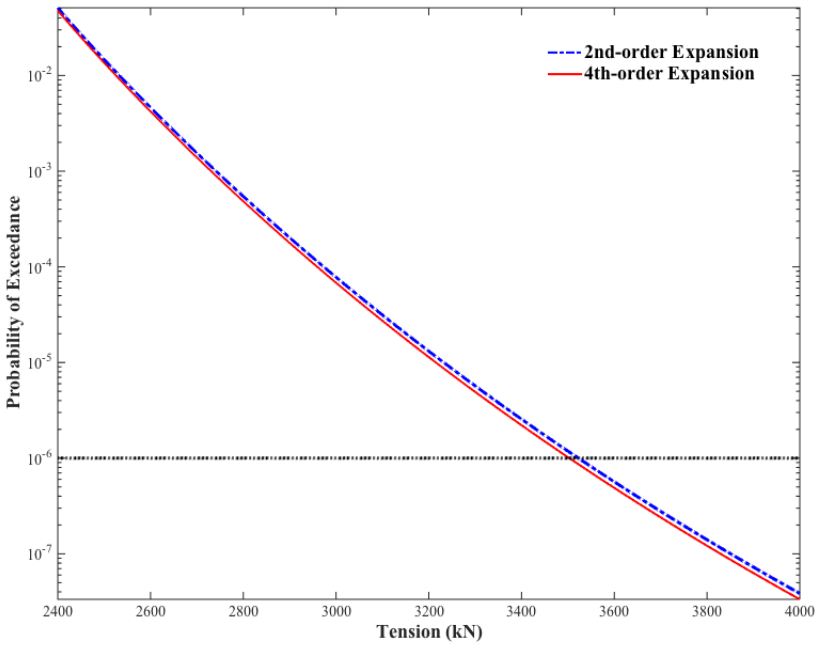

Figure 8.4 Extreme response by perturbation method for COV=0.02

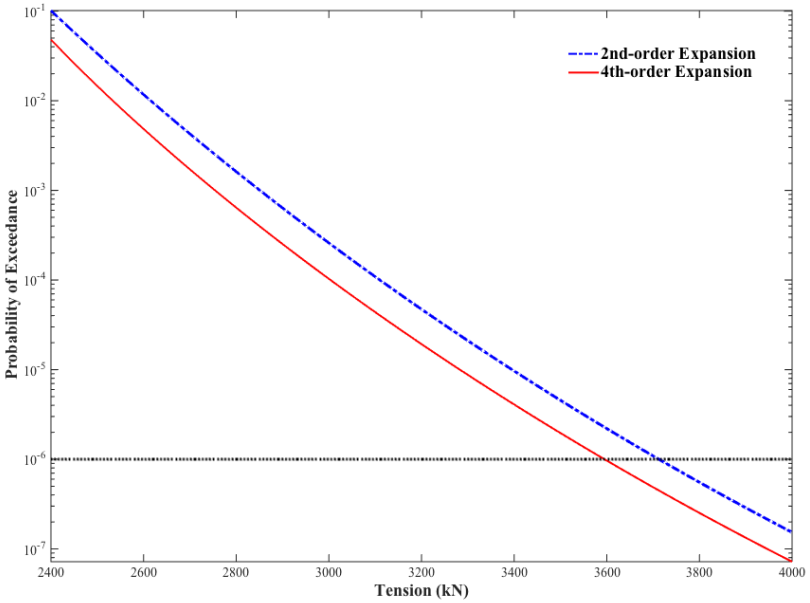

Figure 8.5 Extreme response by perturbation method for COV=0.04

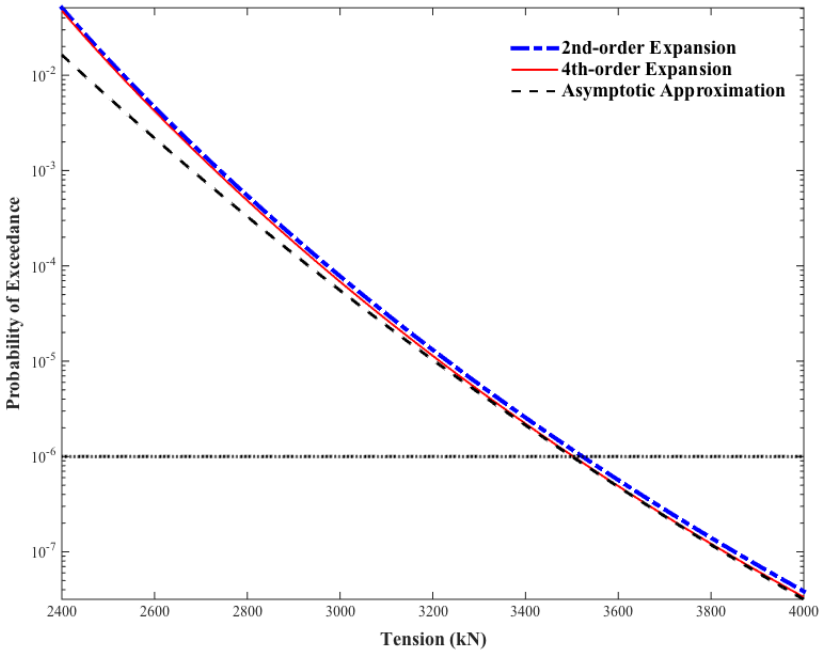

Figure 8.6 Extreme response by asymptotic approximation method for COV=0.02

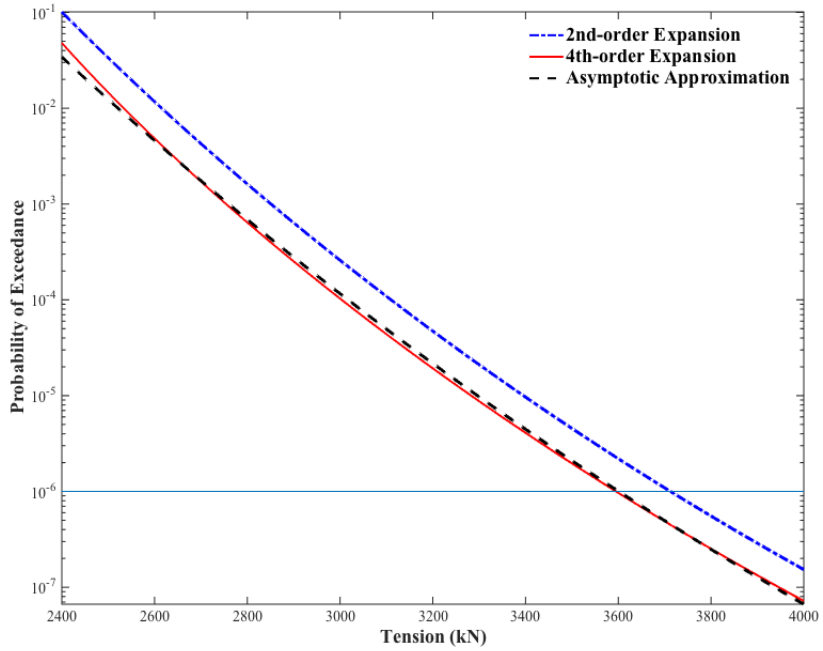

Figure 8.7 Extreme response by asymptotic approximation method for COV=0.04

The asymptotic approximation assessment which based on the Laplace's method

applies to the assessment of the effect of the variation of drag coefficient on the extreme response of mooring line. Newton's method is employed to find the point which has the greatest contribution to the integral. The predictions of extreme responses by the asymptotic approximation method for different coefficient of variation cases are presented in Figure 8.6 and 8.7. The results are compared with the results from the perturbation method. It can be seen that the asymptotic approximation method has a good match with the results when expanded to 4^{th}-order.

8.5 Conclusion

The drag coefficient of a mooring line depends on several parameters, Reynolds number, Keulegan-Carpenter number and roughness number. The variation of drag coefficient will alter the level of damping, which is important for the extreme response of the vessel low frequency motion and the associated line tension. In this chapter the perturbation method and asymptotic approximation method are employed to study the effect of drag coefficient on the extreme response of a mooring line. The perturbation method expanded to 4^{th}-order has a better prediction than to 2^{nd}-order, especially for the case with high coefficient of variance. The method of asymptotic approximation of the probability integral has as good accuracy as the perturbation method expanded to 4^{th}-order. The case with different mean values of drag coefficient was evaluated. It demonstrated that an increase in the line drag coefficient will increase the mean offset as well as typically the dynamic tension, but reduce low frequency dynamic offset. The line tension will depend on the contributions of these two components.

9 Summary and Further Work

This research work mainly focused on the development of a computationally efficient method for the dynamic analysis and probabilistic analysis of moored FPSO system and the identification of the effect of the hydrodynamic drag coefficient on the damping contribution to the low frequency FPSO motion and the maximum mooring line tension, based upon a probabilistic approach. This chapter will summarize this work and discuss the main contributions. Then further work is recommended.

9.1 Summary and Conclusion

The mooring line damping, especially from hydrodynamic drag forces, is of vital importance to FPSO's low frequency motion in deep water and its associated maximum mooring line tension and the maximum offset. Morison's equation with a drag coefficient is often employed to calculate the hydrodynamic drag loads of mooring lines. The drag coefficient is not easily determined, particularly for the chain with complex shape. The variation of hydrodynamic drag coefficient would alter the level of line damping. That means the drag coefficient is important to the damping and the ensuing extreme offset and maximum line tension. Therefore, it was worthwhile to investigate the effects of the hydrodynamic drag coefficients on the damping contribution to the extreme low frequency FPSO motion and the maximum mooring line tension.

As the exploitation of oil and gas continues in deep water, the global dynamic response of a floating production system needs to be predicted with coupled analysis

methods to ensure accuracy and reliability. Fully coupled time-domain analysis, whereby the dynamic motions of the FPSO/mooring/riser are simulated together at every time step, is prohibitively time consuming. Under the assumption that the FPSO's wave frequency motion/loading is unaffected by the mooring/riser due to its much greater mass, the fully coupled analysis can be simplified to some extent. However, such an approach, simulated in the time domain, will still be very expensive. Some methods use a linear damping coefficient to represent this damping's effect, that estimated in prior may not be accurately due to the line damping depending on several factors such as wave frequency response and offset position. An efficient methodology for the dynamic analysis of a moored FPSO system should be appreciated with a view to balancing accuracy and efficiency.

Firstly, the numerical procedures for dynamic analysis of mooring lines in time domain and frequency domain were developed. The mooring lines were modeled based on the lumped mass method where the mooring lines were divided into a series of lumped mass node and massless elastic segments. All the forces on the segments including the tension, inertia force and drag force etc. were concentrated onto the nodes. The equations for dynamic analysis of mooring lines in the time and frequency domain were derived separately. The cases of single component and multi-component mooring lines under different excitations were studied and validated by comparison with the results from commercial software, Orcaflex. The results demonstrated that they could predict the dynamic response of mooring lines in time and frequency domain quite well.

Next, this work attempted to develop a computationally efficient method using a combined time and frequency domain analysis methodology. The time domain simulation with a large time step was performed for low frequency motion of the FPSO, whilst the wave frequency responses of the mooring lines at a given mean

offset position was conducted separately in the frequency domain. The damping contributions from mooring lines was evaluated and added to the calculation of low frequency motions of FPSO. Comparison of the tension/motion results as well as the computational efficiency was made of the proposed method and the dynamically coupled time-domain analysis, .

Then, the methodologies for the long term extreme analysis were validated and an improved method for the long term extreme analysis was proposed. The all sea state method for the long term extreme analysis was performed by use of a Kriging metamodel. The Monte Carlo simulation was applied for the long term probability integral based on the Kriging metamodel. The improved method based on the environmental contour method and accurate distribution tail extrapolation method was proposed. The contour line method assumes that the short term variability could be accounted for separately, i.e. decoupling the environmental problem and the response problem. This method evaluates the extreme response based on limited sea states along a well-defined environmental contour line with a given return period. Then the short term variability is considered by selecting a high fractile. The distribution of the response is evaluated by the average conditional exceedance rates (ACER) method. The ACER method, which can accurately capture the effect of statistical dependence for the extreme value prediction problem, is less restrictive and more flexible than the one based on asymptotic theory.

Finally, the effects of the hydrodynamic coefficient on the damping contribution to the low frequency FPSO motion and the maximum mooring line tension were investigated based upon a probabilistic approach. The probabilistic analyses for the extreme response considering the uncertainty influence of drag coefficient were performed by the perturbation method and the asymptotic approximation method. The conditional long term distributions of responses were estimated by contour line

method and ACER method. The perturbation method expanded to 4^{th}-order had been derived. The asymptotic evaluation is based on the assertion that the greatest contribution to an integral derives from the locations where the integrand is a maximum point.

9.2 Contributions and Major Findings

In summary, on the basis of the work carried out during this research, the main contributions and major findings can be drawn as follows:

1) The modified Euler method is adopted for the dynamic analysis of mooring lines in time domain. This method is straightforward and simple. An improved frame invariant stochastic linearization method was employed to linearize the nonlinear hydrodynamic drag term for the frequency domain dynamic analysis, assuming that dynamic deflections around the static equilibrium position are small. The code has been expanded and integrated by LR for the mooring analysis software.

2) A hybrid time and frequency domain method is developed. The wave frequency response of the FPSO/mooring/riser at a given mean offset position is conducted in the frequency domain, whilst the low frequency motion of the FPSO is computed in the time domain. In this method, the dynamic analyses for FPSO and mooring lines can be separated and the coupling effect still can be taken into account. The time domain simulation for the low frequency FPSO motion can employ large time steps due to separating the wave frequency motion and dynamic analysis of mooring lines. The frequency domain analysis is based upon a specific linearization approach where the damping to the low frequency FPSO motion from the wave frequency response of the mooring/riser can be accounted for in the form of top tension from frequency domain analysis. This method

effectively improves the efficiency. The contribution to this approach is the wave frequency motion and low frequency motion is solved separately and the mooring line is taken into account during the wave frequency motion and its damping as input for low frequency motion.

3) Improved long term extreme analysis strategy based on the contour line method with the ACER method is proposed. The environmental contour line with a given return period is constructed by employing the inverse FORM method (IFORM). The critical sea state is compared and selected from limited sea states along the contour line. Then the extreme response is evaluated based on the critical sea state. The contour line method decouples the environmental problem and the response problem by assuming that the short term variability could be accounted for separately. The distribution of the response is evaluated by the average conditional exceedance rates (ACER) method. The ACER method, which can accurately capture the effect of statistical dependence for the extreme value prediction problem, is less restrictive and more flexible than the one based on asymptotic theory. Then the short term variability is taken into account by selecting a high fractile response. The contribution to this approach is combing the ACER method and contour line approach with hybrid response model first time.

4) Apply a Kriging metamodel of the mooring system for long term extreme analysis. The all sea state method for the long term extreme analysis is performed by use of a Kriging metamodel. The Kriging metamodel is a metamodeling technique which uses statistical techniques to describe the functional relationship between a vector of inputs or variables and the corresponding vector of outputs or responses. It is used to represent the mapping between the sea states characteristics and short distribution parameters. The

results indicate that long term extreme analysis with Kriging metamodel avoids the short term extreme analysis over all sea states and this method can improve the efficiency of the long term extreme analysis because it only involves the sea states selected by applying the sampling approach of design of experiment method. Exceedance probability of line tension and FPSO offset are also estimated from the samples that obtained by Monte Carlo simulation using inverse transform sampling. The uncertainty in the extreme estimates can be assessed by the bootstrap approach. The contribution to this approach is to apply the Kriging model for the assessment of long term extreme response.

5) The effects of the drag coefficient on the long term extreme response of FPSO offset and line tensions has been investigated by the perturbation method and by an asymptotic approximation method. The maximum point is estimated by Newton's method and in the perturbation method with expansion to 4^{th}-order has a better prediction than expansion to 2^{nd}-order, especially for the case with high coefficient of variance. The asymptotic approximation method which, uses asymptotic approximation of the probability integral, has as good an accuracy as the perturbation method with expansion to 4^{th}-order. The case with different mean values of drag coefficient was evaluated. It demonstrated that an increase in the line drag coefficient will increase the mean offset as well as typically increasing the dynamic tension, but it will reduce low frequency dynamic offset. The line tension will depend on the contributions of these two components. The contribution to this part is apply the two methods, perturbation and asymptotic approximation for investigating the effect of the drag coefficient on the mooring long term extreme response. The perturbation expanded to the 4-th order was proposed.

9.3 Recommendations for Future Work

The present work was concerned with the efficient dynamic analysis and probabilistic analysis for a moored FPSO system with emphasis on the effect of drag coefficients. There are still some other issues required to be identified and deserved further investigation in the future.

1) Improved model for hybrid analysis method: In this work, the hybrid time and frequency domain analysis model was mainly developed to study the maximum FPSO offset and line tension and the effect of the line damping. The model for the vessel focused on the surge motion. Therefore, the other motion such as yaw, roll and pitch should be included for general application. The developed model also needs to be validated against full time history simulation and model tests. In addition, the model for the riser should be included.

2) During the extreme analysis, more environmental parameters may be taken into account in order to simulate real environmental conditions: It is a challenge to fit the joint probabilistic distributions to more variables. The random storm method with hybrid time and frequency analysis may provide an alternative strategy. In the random storm method, the hindcast time series of environmental variables can be broken into independent storms by selecting an appropriate threshold value and any number of environmental variables can be added without additional difficulty.

3) Application of the proposed long term extreme analysis strategy in this work for response-based design analysis of floating structure: Response-based methods aim to design a structure to withstand combinations of critical *N*-year return period responses, rather than responses in a combination of *N*-year environmental conditions (Standing et al., 2002). The case study demonstrated that response-based analysis method could reduce maximum design excursions and line tensions by about 20% compared with the traditional deterministic

approach. This approach is capable of quantifying the probability of exceeding design loads and therefore risks. Having obtained the long term response statistics by this improved method, the response based design method will estimate the environmental design conditions that produce the response with a certain return period, typically 100 years, and evaluate the safety and load factors required to ensure some target level of reliability.

4) Predicting the fatigue life is another critical problem for design and analysis of mooring lines: To ensure the safety of the mooring system, it is necessary to evaluate the fatigue life of mooring lines. The fatigue life estimation will include the full range of load conditions expected in a structure's life which is an extremely time-consuming process. The hybrid time and frequency domain method can be used to perform the simulations and then the fatigue life can be calculated based on the assumption of Palmgren-Miner law with the T-N curve. In addition, the effect of drag coefficient on fatigue life prediction can be studied considering the variation of drag coefficient and the importance of drag coefficient selection.

5) Reliability analysis for moored FPSO system: The uncertainties from the environment loads and response model would have a great influence on the extreme response and fatigue life prediction. Reliability analysis could take these uncertain factors into account. Based on the estimated probabilistic distribution of extreme response and fatigue life, the limit state function can be constructed. The first order reliability method (FORM) could be employed for the reliability analysis. The effect of these uncertain factors on the reliability index can be conducted by sensitivity analysis. The asymptotic approximation method also can be applied to the reliability analysis.

References

Angus, J. E. 1994. The Probability Integral Transform and Related Results. *Siam Review*, 36(4), 652-654.

API RP 2SK. 2005. Design and Analysis of Stationkeeping Systems for Floating Structures. American Petroleum Institute.

Atalik, T. S. and Utku, S. 1976. Stochastic Linearization of Multi-Degree-Of-Freedom Non-Linear Systems. *Earthquake Engineering & Structural Dynamics*, 4(4), 411-420.

Baar, J. J. M. Heyl, C. N. and Rodenbusch, G. 2000. Extreme Responses of Turret Moored Tankers. *Offshore Technology Conference*, OTC 12147. Houston, Texas, USA.

Baarholm, G. S. and Moan, T. 2001. Application of Contour Line Method to Estimate Extreme Ship Hull Loads Considering Operational Restrictions. *Journal of Ship Research*, 45(3), 228-240.

Barltrop, N. D. P. and Adams, A. J. 1991. Dynamics of Fixed Marine Structures. London: Butterworth-Heinemann.

Barltrop, N. 1998. Floating Structures: A Guide for Design and Analysis. Houston: Oilfield Publications Limited.

Battjes, J. A. 1972. Long-Term Wave Height Distributions at Seven Stations Around the British Isles. *Deutsche Hydrographische Zeitschrift*, 25(7), 179-189.

Brown, D. T. and Mavrakos, S. 1999. Comparative Study On Mooring Line Dynamic Loading. *Marine Structures*, 12(3), 131-151.

BS EN ISO 19901-7:2005. Petroleum and Natural Gas Industries -Specific Requirements for Offshore Structures - Part 7: Stationkeeping Systems for Floating Offshore Structures and Mobile Offshore Units.

Chakrabarti, S. K. and Cotter, D. C. 1979. Motion Analysis of Articulated Tower. *Journal of the Waterway Port Coastal and Ocean Division*, 105(3), 281-292.

Chen, X. 2001. Dynamic Analysis of Mooring Lines by Using Three Different Methods Formulation. *Proceedings of the Eleventh International Offshore and Polar Engineering Conference*, Stavanger, Norway.

Connaire, A., Kavanagh, K., Ahilan, R. V. and Goodwin, P. 1999. Integrated Mooring & Riser Design: Analysis Methodology. *Offshore Technology Conference*, OTC 10810. Houston, Texas, USA.

Correa, F. N., Senra, S. F., Jacob, B. P., Masetti, I. Q. and Mourelle, M. M. 2002. Towards the Integration of Analysis and Design of Mooring Systems and Risers Part II- Studies on a DICAS System. *Proceedings of 21st International Conference on Offshore Mechanics and Arctic Engineering*, OMAE2002-28151. Oslo, Norway.

Devroye, L. 1986. Non-Uniform Random Variate Generation. New York: Springer-Verlag.

DNV-OS-E301. 2010. Position Mooring. DNV Offshore Standard.

DNV-RP-F205. 2010. Global Performance Analysis of Deepwater Floating Structures. DNV Recommended Practice.

Efron, B. and Tibshirani, R. J. 1993. An Introduction to the Bootstrap. London: Chapman & Hall.

Fan, T. Qiao D. and Yan J. 2017. An improved quasi-static model for mooring-induced damping estimation using in the truncation design of mooring system. *Ocean Engineering*, 136, 322-329.

Farnes, K. A. and Moan, T. 1993. Extreme Response of a Flexible Riser System Using a Complete Nonlinear Long-Term Approach. *Proceedings of the Third International Offshore and Polar Engineering Conference*, Singapore.

FPS2000. 1992. Mooring and Positioning. Marintek.

Garrett, D. L. 1982. Dynamic Analysis of Slender Rods. *Journal of Energy Resources Technology*, 104(12), 302-307.

Garrett, D. L. 2005. Coupled Analysis of Floating Production Systems. *Ocean Engineering*, 32(7), 802 – 816.

Garrett, D. L. Gordon, R. B. and Chappell, J. F. 2002. Mooring- and Riser-Induced Damping in Fatigue Seastates. *Proceedings of 21st International Conference on Offshore Mechanics and Arctic Engineering*, OMAE2002-28550. Oslo, Norway.

Ghadimi, R. 1988. A Simple and Efficient Algorithm for the Static and Dynamic Analysis of Flexible Marine Risers. *Computers and Structures*, 29(4), 541-555.

Grime, A. J. and Langley, R. S. 2003. On the Efficiency of Crossing Rate Prediction Methods Used to Determine Extreme Motions of Moored Offshore Structures.

Applied Ocean Research, 25(3), 127-135.

Hahn, G. D. 1991. A Modified Euler Method for Dynamic Analysis. *International Journal for Numerical Methods in Engineering*, 32, 943-955.

Hamilton, J. 1980. Three-Dimensional Fourier Analysis of Drag Force for Compliant Offshore Structures. *Applied Ocean Research*, 2(4), 147-153.

Haring, R. E. and Heideman, L. C. 1978. Gulf of Mexico Rare Wave Return Periods. *Offshore Technology Conference*, OTC 3230. Houston, Texas, USA.

Haver, S. Sagli, G. and Gran, T. M. 1998. Long Term Response Analysis of Fixed and Floating Structures. *Ocean Wave Kinematics, Dynamics and Loads on Structures Symposium*, Houston, USA.

Haver, S. and Nyhus, K. A. 1986. A Wave Climate Description for Long Term Response Calculations. *Proceedings of the Fifth International Offshore Mechanics and Arctic Engineering Symposium*, Tokyo, Japan.

He, W., Diez, M., Zou, Z., Campanac, E. and Stern, F. 2013. URANS Study of Delft Catamaran Total/Added Resistance, Motions and Slamming Loads in Head Sea Including Irregular Wave and Uncertainty Quantification for Variable Regular Wave and Geometry. *Ocean Engineering*, 74, 189-217.

HSE Report. 2003. Analysis of Accident Statistics for Floating Monohull and Fixed Installations. Health and Safety Executive.

Huang, S. 1994. Dynamic Analysis of Three-Dimensional Marine Cables. *Ocean Engineering*, 21(6), 587-605.

Huang, S. and Vassalos, D. 1993. A Numerical Method for Predicting Snap Loading of Marine Cables. *Applied Ocean Research*, 15, 235-242.

Huntington, D. E. and Lyrintzis, C. S. 1998. Improvements to and Limitations of Latin Hypercube Sampling. *Probabilistic Engineering Mechanics*, 13(4), 245-253.

Huse, E. 1986. Influence of Mooring Line Damping upon Rig Motions. *Offshore Technology Conference*, OTC 5204. Houston, Texas, USA.

Huse, E. 1991. New Developments in Prediction of Mooring System Damping. *Offshore Technology Conference*, OTC 6593. Houston, Texas, USA.

Huse, E. and Matsumoto, K. 1988. Practical Estimation of Mooring Line Damping. *Offshore Technology Conference*, OTC 5676. Houston, Texas, USA.

Huse, E. and Matsumoto, K. 1989. Mooring Line Damping Due to First- and Second-Order Vessel Motion. *Offshore Technology Conference*, OTC 6137. Houston, Texas, USA.

Hwang, Y. L. 1986. Nonlinear Dynamic Analysis of Mooring Lines. *Proceedings of the 5th International Offshore Mechanics and Arctic Engineering Symposium*, Tokyo, Japan.

Isaaks, E. H. and Srivastava, R. M. 1990. An Introduction to Applied Geostatistics. New York: Oxford University Press.

Jahns, H. O. and Wheeler, J. D. 1972. Long-Term Wave Probabilities Based On Hindcasting of Severe Storms. *Offshore Technology Conference*, OTC 1590. Houston, Texas, USA.

Kim, M. H., Koo, B. J., Mercier, R. M. and Ward, E. G. 2005. Vessel/Mooring/Riser Coupled Dynamic Analysis of a Turret-Moored FPSO Compared with OTRC Experiment. *Ocean Engineering*, 32(14-15), 1780-1802.

Krolikowski, L. P. and Gay, T. A. 1980. An Improved Linearization Technique for Frequency Domain Riser Analysis. *Offshore Technology Conference*, OTC 3777. Houston, Texas, USA.

Lang, D. W., Connolly, A., Lane, M. and Connaire, A. D. 2005. Advances in Frequency and Time Domain Coupled Analysis for Floating Production and Offloading Systems. *Proceedings of 24th International Conference on Offshore Mechanics and Arctic Engineering*, OMAE2005-67396. Halkidiki, Greece.

Langley, R. S. 1984. The Linearisation of Three Dimensional Drag Force in Random Seas with Current. *Applied Ocean Research*, 6(3), 126-131.

Larsen, C. M. and Olufsen, A. 1992. Extreme Response Estimation of Flexible Risers by Use of Long Term Statistics. *Proceedings of the Second International Offshore and Polar Engineering Conference*, San Francisco, California, USA.

Le Cunff, C., Ryu, S., Heurtier, J. and Duggal, A. S. 2008. Frequency-Domain Calculations of Moored Vessel Motion Including Low Frequency Effect. *Proceedings of 27th International Conference on Offshore Mechanics and Arctic Engineering*, OMAE2008-57632. Estoril, Portugal.

Leong, D., Low, Y. M. and Kim Y. 2018. Long-Term Extreme Response Prediction of Mooring Lines Using Subset Simulation. *Proceedings of 37th International Conference on Offshore Mechanics and Arctic Engineering*, OMAE2018-77064. Madrid, Spain.

Lim, D.H. and kim, Y.H. 2018. Design wave method for the extreme horizontal slow-drift motion of moored floating platforms. *Applied Ocean Research*, 71. 85-105.

Liu, Y. G. and Bergdahl, L. 1998. Improvement On Huse's Model for Estimating Mooring Cable Induced Damping. *Proceeding of 17th International Conference on Offshore Mechanics and Arctic Engineering*, OMAE98-0353. Lisbon, Portugal.

Liu, Y. and Bergdahl, L. 1999. On Combination Formulae for the Extremes of Wave-Frequency and Low-Frequency Responses. *Applied Ocean Research*, 21(1), 41-46.

Low, Y. M. and Langley, R. S. 2006. Time and Frequency Domain Coupled Analysis of Deepwater Floating Production Systems. *Applied Ocean Research*, 28(6), 371-385.

Luo, Y. and Baudic, S. 2003. Predicting FPSO Responses Using Model Tests and Numerical Analysis. *Proceedings of The Thirteenth International Offshore and Polar Engineering Conference*, Honolulu, Hawaii, USA.

Lyons, G. J. Brown, D. T. and Lin, H. M. 1997. Drag Coefficients for Mooring Line Hydrodynamic Damping. *Proceedings of the Seventh International Offshore and Polar Engineering Conference*, Honolulu, USA.

Ma, K., Duggal, A., Smedley, P., L'Hostis, D. and Shu, H. 2013. A Historical Review on Integrity Issues of Permanent Mooring Systems. *Offshore Technology Conference*, OTC 24025. Houston, Texas, USA.

Madsen, H. O. Krenk, S. and Lind, N. C. 1986. Methods of Structural Safety. New York: Dover Publications.

Matsumoto, K. 1991. The Influence of Mooring Line Damping on the Prediction of Low-Frequency Vessel Motions at Sea. *Offshore Technology Conference*, OTC 6660. Houston, Texas, USA.

Mavrakos, S. A., Papazoglou, V. J., Triantafyllou, M. S. and Hatjigeorgiou, J. 1996. Deep Water Mooring Dynamics. *Marine Structures*, 9(2), 181-209.

Molin, B. 1994. Second-Order Hydrodynamics Applied to Moored Structures - a State-Of-The-Art Survey. *Ship Technology Research*, 99(41), 59-84.

Naess, A. Gaidai, O. and Haver, S. 2007. Efficient Estimation of Extreme Response of Drag-Dominated Offshore Structures by Monte Carlo Simulation. *Ocean Engineering*, 34, 2188-2197.

Naess, A. Gaidai, O. and Karpa, O. 2013. Estimation of Extreme Values by the Average Conditional Exceedance Rate Method. *Journal of Probability and Statistics*, 2013, 1-15.

Naess, A. and Gaidai, O. 2008. A Monte Carlo Approach to Prediction of Extreme Response Statistics of Drag Dominated Offshore Structures. *Journal of Offshore Mechanics and Arctic Engineering*, 130(11), 1-6.

Naess, A. and Gaidai, O. 2008. Monte Carlo Methods for Estimating the Extreme Response of Dynamical Systems. *Journal of Engineering Mechanics*, 134(8), 628-636.

Naess, A. and Gaidai, O. 2009. Estimation of Extreme Values From Sampled Time Series. *Structural Safety*, 31(4), 325-334.

Naess, A. and Moan, T. 2012. Stochastic Dynamics of Marine Structures.: Cambridge University Press.

Nakajima, T. Motora, S. and Fujino, M. 1982. On the Dynamic Analysis of Multi-Component Mooring Lines. *Offshore Technology Conference*, OTC 4309. Houston, Texas, USA.

Newman, J. N. 1974. Second-Order, Slowly-Varying Forces On Vessels in Irregular Waves. *Marine Vehicles*, 182-186.

Noble Denton. 2006. Floating Production System: JIP FPS Mooring Integrity.

NORSOK N-003. 2007. Actions and Action Effects. Norwegian Petroleum Industry.

Barton, C. 2018. 2014 Worldwide Survey of Floating Production, Storage and Offloading (FPSO) Units. *Offshore*, 133 (8), MAP1.

OCIMF**.** 1994. Prediction of Wind and Current Loads On VLCCs. London: Witherby & Co.,Ltd.

Ormberg, H. Sødahl, N. and Steinkjer, O. 1998. Efficient Analysis of Mooring Systems using De-Coupled and Coupled Analysis. *Proceedings of 17th International Conference on Offshore Mechanics and Arctic Engineering*, OMAE98-0351. Lisbon, Portugal.

Ormberg, H. and Larsen, K. 1998. Coupled Analysis of Floater Motion and Mooring Dynamics for a Turret-Moored Ship. *Applied Ocean Research*, 20(1-2), 55-67.

Pinkster, J. A. 1980. Low Frequency Second Order Wave Exciting Forces On Floating Structures. PhD Thesis, TU Delft.

Ran, Z. Kim, M. H. and Zheng, W. 1999. Coupled Dynamic Analysis of a Moored Spar in Random Waves and Currents (Time-Domain Versus Frequency-Domain Analysis). *Journal of Offshore Mechanics and Arctic Engineering*, 121(8), 194-201.

Rodenbusch, G. Garrett, D. L. and Anderson, S. L. 1986. Statistical Linearization of Velocity-Squared Drag Forces. *Proceedings of the Fifth International Offshore Mechanics and Arctic Engineering (OMAE) Symposium*, Tokyo, Japan.

Rubinstein, R. Y. and Kroese, D. P. 2007. Simulation and the Monte Carlo Method. New York: Wiley-Interscience.

Simpson, T. W., Timothy, M. M., Korte, J. J. and Farrokh, M. 1998. Comparison of Response Surface and Kriging Models for Multidisciplinary Design Optimization. *Proceedings of the 7th AIAA/USAF/NASA/ISSMO Symposium on Multidisciplinary Analysis & Optimization*, AIAA-98-4755.

Song, X., Gu, H., Zhang, X. and Liu, J. 2008. Pattern Search Algorithms for Nonlinear Inversion of High-Frequency Rayleigh-wave Dispersion Curves. *Computers & Geosciences*, 34(6), 611-624.

Soong, T. T. 2004. Fundamentals of Probability and Statistics for Engineers. New York: John Wiley and Sons.

Spanos, P. D., Ghosh, R., Finn, L. D. and Halkyard, J. 2005. Coupled Analysis of a Spar Structure Monte Carlo and Statistical Linearization Solutions. *Journal of Offshore Mechanics and Arctic Engineering*, 127, 11-16.

Standing, R. G., Eichaker, R., Lawes, H. D. and Campbell, B. 2002. Benefits of Applying Response-Based Design Methods to Deepwater FPSOs. *Offshore Technology Conference*, OTC14232.

Tahar, A. and Kim, M. H. 2003. Hull/Mooring/Riser Coupled Dynamic Analysis and Sensitivity Study of a Tanker-Based FPSO. *Applied Ocean Research*, 25(6), 367-382.

Tromans, P. S. A. V. 1995. Response Based Design Conditions in the North Sea: Application of a New Method. *Offshore Technology Conlerence*, OTC 7683. Houston, Texas, USA.

Vázquez-hernández, A. O. Ellwanger, G. B. and Sagrilo, L. V. S. 2011. Long-Term Response Analysis of FPSO Mooring Systems. *Applied Ocean Research*, 33, 375-383.

Walton, T. S. and Polachek, H. 1960. Calculation of Transient Motion of Submerged

Cables. *Mathematics of Computation*, 14, 27-46.

Wang, G. G. and Shan, S. 2006. Review of Metamodeling Techniques in Support of Engineering Design Optimization. *Journal of Mechanical Design*, 129(4), 370-380.

Webster, W. C. 1995. Mooring-Induced Damping. *Ocean Engineering*, 22(6), 571-591.

Wichers, J. E. W. and Devlin, P. V. 2001. Effect of Coupling of Mooring Lines and Risers on the Design Values for a Turret Moored. *Proceedings of the Eleventh International Offshore and Polar Engineering Conference*, Stavanger, Norway.

Winterstein, S. R., Ude, T. C., Cornell, C. A., Bjerager, P. and Haver, S. 1993. Environmental Parameters for Extreme Response: Inverse FORM with Omission Factors. *Proceedings of the International Conference on Structural Safety and Reliability*, Innsbruck, Austria.

Wu, S. C. 1976. The Effects of Current on Dynamic Response of Offshore Platforms. *Offshore Technology Conference*, OTC 2540. Dallas, Texas, USA.

Xu, Z. 2014. Drag Coefficient and Damping of Moorings and their Effect On FPSO Motions. PhD Thesis, University of Strathclyde.

Xu, Z. and Huang, S. 2014. Numerical Investigation of Mooring Line Damping and the Drag Coefficients of Studless Chain Links. *Journal of Marine Science and Application*, 13(1), 76-84.

Yang, H. and Wang, A. 2012. Fatigue Reliability Based Design Optimization of Bending Stiffener. *Journal of Ship Research*, 56(2), 120 – 128.

Appendix A Static Analysis for Multi-component Mooring lines by Catenary Equation

The static analysis of single component mooring line can be done by catenary equation method. This method neglects the environmental force and elasticity of mooring line. It can be used for the quasi-static analysis, especially in shallow water. The detail derivation can be found in the literature (Barltrop, 1998). The catenary geometry in Cartesian coordinate can be expressed as follows.

$$z = \alpha\left[\cosh(\frac{x}{\alpha}) - 1\right] \tag{A.1}$$

where $\alpha = \frac{T_H}{w}$, T_H is the horizontal tension in mooring line. w is the submerged weight per unit length. The configuration also can be expressed by formula with length of mooring line.

$$z = \alpha\left[\sqrt{1+(\frac{l}{\alpha})^2} - 1\right] \tag{A.2}$$

The horizontal scope (length in plan view from fairlead to touchdown point)

$$\begin{aligned} x &= \alpha \sinh^{-1}(\frac{l}{\alpha}) \\ &= \alpha \ln\left[\sqrt{1+(\frac{l}{\alpha})^2} + \frac{l}{\alpha}\right] \end{aligned} \tag{A.3}$$

The multi-component mooring lines are often employed. The catenary equations for the multi-component mooring lines (chain-wire-chain) are derived as follows.

The typical configuration of multi-component mooring lines (chain-wire-chain) is shown in Figure A.1. The touch down point and two points connecting wire with the

chains are indicated by node1, node 2 and node 3, respectively. L_i (i=1,2,3) is the partially or fully suspended length of the *i*-th component. w_i (i=1,2,3) is the submerged weight per unit length of the *i*-th component, H is the water depth between fairlead and seabed. T is the tension at the fairlead, T_H and T_v is the horizontal and vertical component of tension. The line 2 and line 3 are extended to be tangent to the horizontal line. The extension lengths are $\tilde{L}_2$ and $\tilde{L}_3$. The local coordinates, o_2-x_2-z_2 and o_3-x_3-z_3 are established at the points of tangency, respectively. Then the parameters of line 2 and line 3 can be estimated by previous catenary equations.

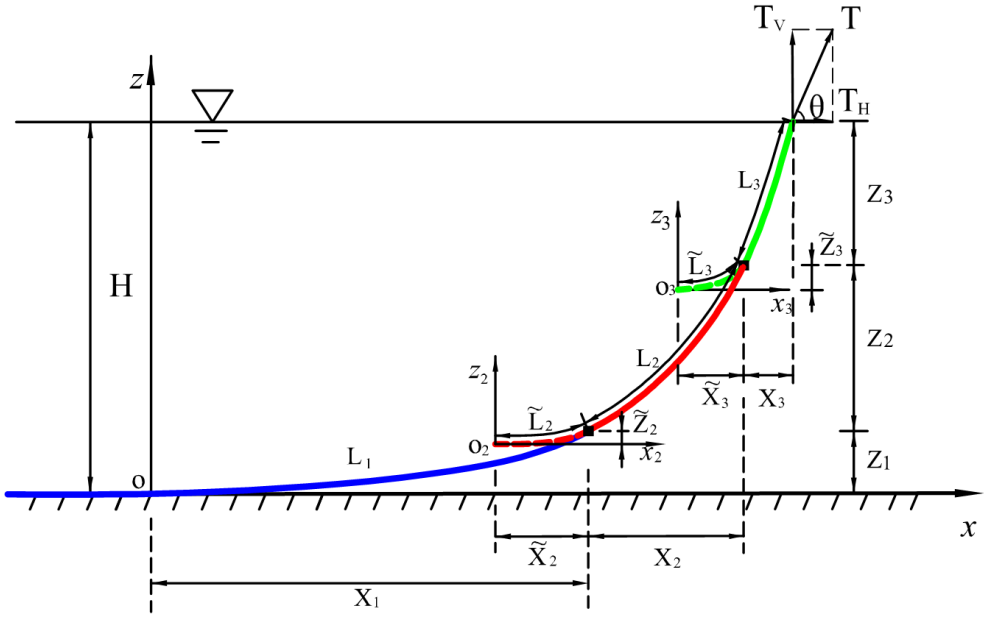

Figure A.1 Static analysis of multi-component mooring line

The vertical projection length of the *i*-th component, Z_i (i=1,2,3), can be calculated by the following equations.

$$Z_1 = \alpha_1 \left[\sqrt{1+(\frac{L_1}{\alpha_1})^2} - 1 \right] \tag{A.4}$$

$$Z_2 = \alpha_2 \left[\sqrt{1+(\frac{L_2+\tilde{L}_2}{\alpha_2})^2} - 1 \right] - \alpha_2 \left[\sqrt{1+(\frac{\tilde{L}_2}{\alpha_2})^2} - 1 \right] \tag{A.5}$$

$$Z_3 = \alpha_3\left[\sqrt{1+(\frac{L_3+\tilde{L}_3}{\alpha_3})^2}-1\right]-\alpha_3\left[\sqrt{1+(\frac{\tilde{L}_3}{\alpha_3})^2}-1\right] \tag{A.6}$$

where $\alpha_1 = \frac{T_H}{w_1}$; $\alpha_2 = \frac{T_H}{w_2}$; $\alpha_3 = \frac{T_H}{w_3}$.

At the node 2 and node 3,

$$T_{V2} = w_1 L_1 = w_2 \tilde{L}_2 \tag{A.7}$$

$$T_{V3} = w_1 L_1 + w_2 L_2 = w_3 \tilde{L}_3 \tag{A.8}$$

Then, the extended length can be estimated as follows.

$$\tilde{L}_2 = \frac{w_1 L_1}{w_2} \tag{A.9}$$

$$\tilde{L}_3 = \frac{w_1 L_1 + w_2 L_2}{w_3} \tag{A.10}$$

Submitting the Eq.(A.9)-Eq.(A.10) into the Eq.(A.4)-Eq.(A.6)

$$Z_1 = \alpha_1\left[\sqrt{1+(\frac{w_1 L_1}{T_H})^2}-1\right] \tag{A.11}$$

$$Z_2 = \alpha_2\left[\sqrt{1+(\frac{w_1 L_1 + w_2 L_2}{T_H})^2}-\sqrt{1+(\frac{w_1 L_1}{T_H})^2}\right] \tag{A.12}$$

$$Z_3 = \alpha_3\left[\sqrt{1+(\frac{w_1 L_1 + w_2 L_2 + w_3 L_3}{T_H})^2}-\sqrt{1+(\frac{w_1 L_1 + w_2 L_2}{T_H})^2}\right] \tag{A.13}$$

The vertical projection extended lengths are

$$\tilde{Z}_2 = \alpha_2\sqrt{1+(\frac{w_1 L_1}{T_H})^2} \tag{A.14}$$

$$\tilde{Z}_3 = \alpha_3\sqrt{1+(\frac{w_1 L_1 + w_2 L_2}{T_H})^2} \tag{A.15}$$

Similarly, we can obtain the horizontal projection extended length and the horizontal

projection length.

$$\tilde{X}_2 = \alpha_2 \ln\left[\sqrt{1+(\frac{w_1 L_1}{T_H})^2} + \frac{w_1 L_1}{T_H}\right] \tag{A.16}$$

$$\tilde{X}_3 = \alpha_3 \ln\left[\sqrt{1+(\frac{w_1 L_1 + w_2 L_2}{T_H})^2} + \frac{w_1 L_1 + w_2 L_2}{T_H}\right] \tag{A.17}$$

$$X_1 = \alpha_1 \ln\left[\sqrt{1+(\frac{w_1 L_1}{T_H})^2} + \frac{w_1 L_1}{T_H}\right] \tag{A.18}$$

$$X_2 = \alpha_2 \ln\left[\sqrt{1+(\frac{w_1 L_1 + w_2 L_2}{T_H})^2} + \frac{w_1 L_1 + w_2 L_2}{T_H}\right] - \tilde{X}_2 \tag{A.19}$$

$$X_3 = \alpha_3 \ln\left[\sqrt{1+(\frac{w_1 L_1 + w_2 L_2 + w_3 L_3}{T_H})^2} + \frac{w_1 L_1 + w_2 L_2 + w_3 L_3}{T_H}\right] - \tilde{X}_3 \tag{A.20}$$

The catenary geometry of the *i*-th component in the global coordinate can be expressed as follows.

$$\begin{cases} x(l) = \alpha_1 \ln\left[\sqrt{1+\left(\frac{l}{\alpha_1}\right)^2} + \frac{l}{\alpha_1}\right] \\ z(l) = \alpha_1\left[\sqrt{1+\left(\frac{l}{\alpha_1}\right)^2} - 1\right] \end{cases}; \ 0 < l \le L_1 \tag{A.21}$$

$$\begin{cases} x(l) = \alpha_2 \ln\left[\sqrt{1+\left(\frac{l}{\alpha_2}\right)^2} + \frac{l}{\alpha_2}\right] - \tilde{X}_2 + X_1 \\ z(l) = \alpha_2\left[\sqrt{1+\left(\frac{l}{\alpha_2}\right)^2} - 1\right] - \tilde{Z}_2 + Z_1 \end{cases} ; \ L_1 < l \le L_1 + L_2 \tag{A.22}$$

$$\begin{cases} x(l) = \alpha_3 \ln\left[\sqrt{1+\left(\dfrac{l}{\alpha_3}\right)^2} + \dfrac{l}{\alpha_3}\right] - \tilde{X}_3 + X_1 + X_2 \\ z(l) = \alpha_3\left[\sqrt{1+\left(\dfrac{l}{\alpha_3}\right)^2} - 1\right] - \tilde{Z}_3 + Z_1 + Z_2 \end{cases} ; L_1 + L_2 < l \le L_1 + L_2 + L_3 \tag{A.23}$$

And tension in the mooring lines is

$$\begin{cases} T_1(l) = \sqrt{(w_1 l)^2 + T_H^2}; & 0 < l \le L_1 \\ T_2(l) = \sqrt{(w_1 L_1 + w_2 l)^2 + T_H^2}; & L_1 < l \le L_1 + L_2 \\ T_3(l) = \sqrt{(w_1 L_1 + w_2 L_2 + w_3 l)^2 + T_H^2}; & L_1 + L_2 < l \le L_1 + L_2 + L_3 \end{cases} \tag{A.24}$$

The static analysis for multi-components mooring line can be performed by given different offsets and Figure A.2 presents the results according to the properties and length of lines in section 2.5.2. The results are also compared with the results from Orcaflex's as shown in Figure A.3. It can be seen that it can predict well the static response of multi-component mooring line.

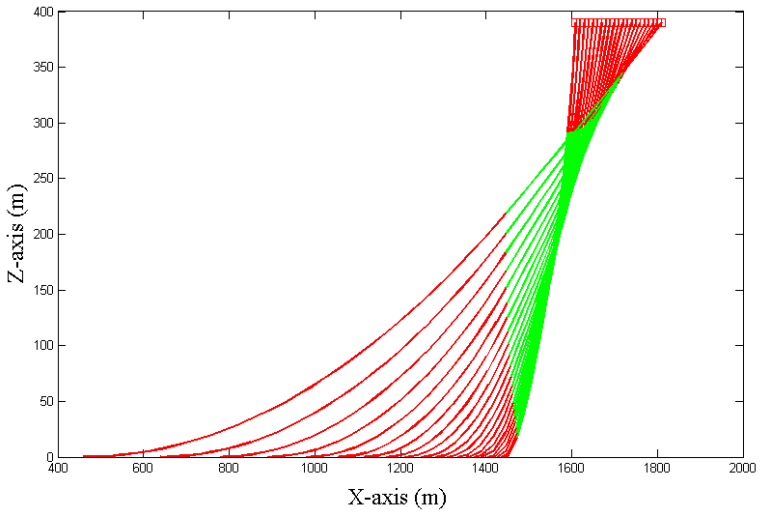

Figure A.2 Static analysis of multi-components mooring line

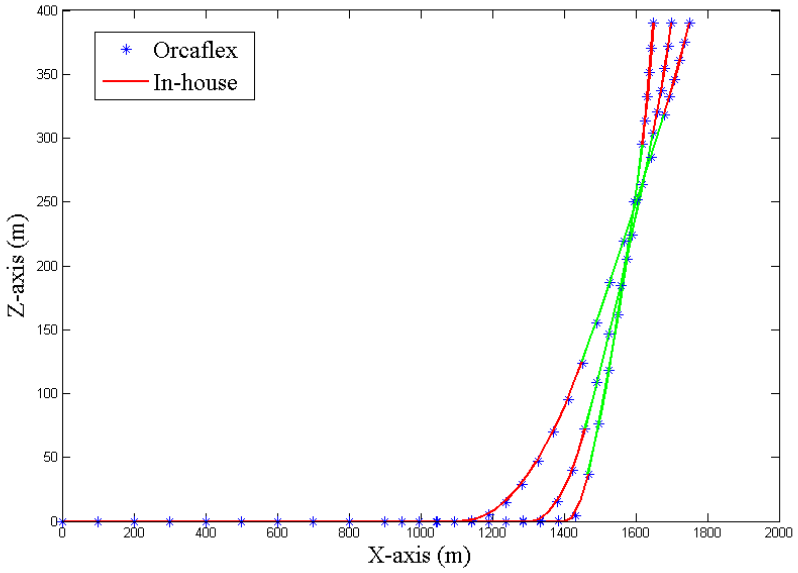

Figure A.3 Comparison of static analysis

Appendix B Transformation of Coordinates for Linearization

The velocity in the global coordinate are transformed into local coordinate and two un-correlated components can be found by principle component analysis. This method can simplify the evaluation of expected values.

The tangent to the lines in the global coordinate system, $\mathbf{e} = (e_x, e_y, e_z)$, is selected a base vector for local coordinate. Then a local orthonormal coordinate system including **e** can be determined. By defining a vector $\mathbf{a} = (e_z, -e_x, e_y)$ which is linearly independent of **e**. we can obtain another base vector normal to **e**:

$$\mathbf{f} = \frac{\mathbf{a} - (\mathbf{a} \cdot \mathbf{e})\mathbf{e}}{|\mathbf{a} - (\mathbf{a} \cdot \mathbf{e})\mathbf{e}|} \tag{B.1}$$

and the third base vector **g** is:

$$\mathbf{g} = \mathbf{e} \times \mathbf{f} \tag{B.2}$$

The orthogonal transformation

$$\mathbf{T} = \begin{bmatrix} f_x & f_y & f_z \\ g_x & g_y & g_z \\ e_x & e_y & e_z \end{bmatrix} \tag{B.3}$$

relates the element *f-g-e* coordinate system to the global *x-y-z* coordinate system. The covariance matrix in the element coordinate system is:

$$\mathbf{R}_{fge} = \mathbf{T}\mathbf{R}_{xyz}\mathbf{T}^T \tag{B.4}$$

Since only the relative velocity components normal to the line is counted in the drag force. The above covariance matrix can be reduced into 2x2 by ignoring the components in the direction of **e** and the covariance matrix

$$\mathbf{S} = \begin{bmatrix} R_{ff} & R_{fg} \\ R_{gf} & R_{gg} \end{bmatrix} \tag{B.5}$$

Next we can find the principal values and principal directions of the covariance matrix. The principal values are:

$$\sigma_{1,2}^2 = \frac{1}{2}(S_{11} + S_{22} \pm r) \tag{B.6}$$

where $r^2 = (S_{11} - S_{22})^2 + 4S_{12}^2$

Then choose an eigenvector which is also a unit vector such that:

$$\phi_1 = \frac{S_{12}}{\sqrt{(S_{11} - \sigma_1^2)^2 + S_{12}^2}} \tag{B.7}$$

$$\phi_2 = \frac{-(S_{11} - \sigma_1^2)}{\sqrt{(S_{11} - \sigma_1^2)^2 + S_{12}^2}} \tag{B.8}$$

The orthogonal transformation

$$\mathbf{V} = \begin{bmatrix} \phi_1 & \phi_2 & 0 \\ -\phi_2 & \phi_1 & 0 \\ 0 & 0 & 1 \end{bmatrix} \tag{B.9}$$

relates the *f-g-e* coordinate system to the principal directions of the relative velocity covariance matrix. The maximum velocity variance will be called the in-line direction, and the direction of minimum velocity variance will be called the transverse direction.

Thus the orthogonal transformation from the local principal coordinate system to the global coordinate system is:

$$\mathbf{P} = \mathbf{VT} \tag{B.10}$$

The relative velocity $\boldsymbol{V}^n$ in principal coordinate system is:

$$\boldsymbol{V}^n = \mathbf{P}\boldsymbol{V}_{xyz}^n \tag{B.11}$$

The current velocity in principal coordinate system is:

$$\boldsymbol{V}_c^n = \mathbf{P}\boldsymbol{V}_{c,xyz}^n \tag{B.12}$$

And the resulting mean force in local principal coordinate can be transformed back into global coordinate:

$$\overline{\mathbf{F}} = \left[\mathbf{VT}\right]^{-1}\mathbf{F}_m = \left[\mathbf{VT}\right]^T\mathbf{F}_m = \mathbf{P}^T\mathbf{F}_m \tag{B.13}$$

$$\begin{aligned}\mathbf{F}_D &= \mathbf{P}^T\mathbf{F}_{local} \\ &= \mathbf{P}^T\frac{1}{2}\rho C_D Dl\left(\mathbf{C}_e\boldsymbol{V}^n + \mathbf{F}_m\right) \\ &= \frac{1}{2}\rho C_D Dl\mathbf{P}^T\left(C_e\mathbf{PN}\boldsymbol{V} + \mathbf{F}_m\right)\end{aligned} \tag{B.14}$$

where

$$\boldsymbol{V}^{\boldsymbol{n}} = \begin{bmatrix} v_1 \\ v_2 \\ 0 \end{bmatrix} \quad \mathbf{F}_m = \begin{bmatrix} F_1^m \\ F_2^m \\ 0 \end{bmatrix}$$

Appendix C Fast integral method for Linearization

The linearized drag force needs to evaluate nested infinite integrals. Here introduce a method to transform it into a finite integral.

By making the following substitution:

$$\lambda = \frac{\sigma_2}{\sigma_1};\quad \alpha = \frac{V_{c1}}{\sigma_1};\quad \beta = \frac{V_{c2}}{\sigma_1};\quad \frac{\boldsymbol{V}+\boldsymbol{V_c}}{\sigma_1} = \begin{bmatrix} r\cos\theta & r\sin\theta \end{bmatrix} \tag{C.1}$$

The infinite integrals in Eq.(2.50) - Eq.(2.52) are transformed into the following finite integrals:

$$I_1 = \frac{1}{2\pi\lambda(1+\lambda^2)}\int_0^{2\pi}\int_0^{\infty} r^4 p(r,\theta)drd\theta \tag{C.2}$$

$$I_2 = \frac{1}{2\pi\lambda\alpha}\int_0^{2\pi}\int_0^{\infty} r^3\cos\theta p(r,\theta)drd\theta \tag{C.3}$$

$$I_3 = \frac{1}{2\pi\lambda\beta}\int_0^{2\pi}\int_0^{\infty} r^3\sin\theta p(r,\theta)drd\theta \tag{C.4}$$

where

$$p(r,\theta) = \exp\left\{-\frac{1}{2}\left[(r\cos\theta-\alpha)^2 + \frac{(r\sin\theta-\beta)^2}{\lambda^2}\right]\right\} \tag{C.5}$$

Following the manipulation, it can be shown that

$$I_2 = \frac{3}{\sqrt{\pi}\alpha}(\cos\delta Q_1 - \sin\delta Q_2) \tag{C.6}$$

$$I_3 = \frac{3\lambda}{\sqrt{\pi}\beta}(\sin\delta Q_1 + \cos\delta Q_2) \tag{C.7}$$

$$I_1 = \frac{\frac{3}{\sqrt{2\pi}}Q_0 - \alpha^2 I_2 - \beta^2 I_3}{1+\lambda^2} \tag{C.8}$$

where

$$Q_0 = \int_0^{\frac{\pi}{2}} \left[\chi^3(\delta+t) + \chi^3(\delta-t)\right] F(t) P_4(t) dt$$

$$Q_1 = \int_0^{\frac{\pi}{2}} \left[\chi(\delta+t) + \chi(\delta-t)\right] \cos(t) F(t) P_3(t) dt$$

$$Q_2 = \int_0^{\frac{\pi}{2}} \left[\chi(\delta+t) - \chi(\delta-t)\right] \sin(t) F(t) P_3(t) dt$$

And

$$F(t) = e^{-c^2\sin^2(t)}$$

$$P_4(t) = 1 + 4c^2\cos^2(t) + \frac{4}{3}c^4\cos^4(t)$$

$$P_3(t) = c\cos(t) + \frac{2}{3}c^3\cos^3(t)$$

And

$$\chi(t) = \sqrt{\cos^2(t) + \lambda^2\sin^2(t)}$$

$$\cos(\delta) = \frac{\alpha}{\sqrt{2}c}$$

$$\sin(\delta) = \frac{\beta}{\sqrt{2}c\lambda}$$

$$c = \sqrt{\frac{\alpha^2 + \beta^2/\lambda^2}{2}}$$

It should be noted that *t* appears only in trigonometric functions. In order to calculate the integrals in equations, a change of variable is made to improve the computational efficiency by eliminating the evaluation of trigonometric functions during the

numerical integration. By defined $x = \tan(\frac{t}{2})$, we have

$$dt = \frac{2}{1+x^2}dx = \gamma dx \tag{C.9}$$

$$\cos(t) = \frac{2}{1+x^2} - 1 = \gamma - 1 \tag{C.10}$$

$$\sin(t) = \frac{2x}{1+x^2} = \gamma x \tag{C.11}$$

$$\chi(t) = \sqrt{\cos^2(t) + \lambda^2 \sin^2(t)} = \sqrt{1 + (\lambda^2 - 1)\sin^2(t)} \tag{C.12}$$

$$\begin{aligned}\chi(\delta + t) &= \sqrt{1 + (\lambda^2 - 1)\sin^2(\delta + t)} = \sqrt{1 + (\lambda^2 - 1)(\sin\delta\cos t + \cos\delta\sin t)^2} \\ &= \sqrt{1 + (\lambda^2 - 1)[(\gamma - 1)\sin\delta + \gamma x\cos\delta]^2}\end{aligned} \tag{C.13}$$

$$\begin{aligned}\chi(\delta - t) &= \sqrt{1 + (\lambda^2 - 1)\sin^2(\delta - t)} = \sqrt{1 + (\lambda^2 - 1)(\sin\delta\cos t - \cos\delta\sin t)^2} \\ &= \sqrt{1 + (\lambda^2 - 1)[(\gamma - 1)\sin\delta - \gamma x\cos\delta]^2}\end{aligned} \tag{C.14}$$

After the change of the variable, the trapezoidal rule is used to evaluate these integrals numerically.

Appendix D Confidence Interval

A probabilistic model is represented by probability density distribution function which involves unknown parameter θ that can be estimated from independently observed data or samples. $\hat{\theta}$ is an estimate of parameter θ. The estimation criteria including unbiasedness, minimum variance and consistency are used to evaluate the quality of an estimate (Soong, 2004). The point estimation approach can estimate the unknown parameter based on the estimation criteria by method of moments or maximum likelihood estimation.

Another approach for the parameter estimation problem is interval estimation which is a procedure by which bounds on the parameter value are obtained. Interval estimation provides more information about a population characteristic than does a point estimate that not only gives information on the numerical value of the parameter but also provides the level of confidence one can place on the possible numerical value of the parameter.

Suppose that a random sample $X_1, X_2, ..., X_n$ is drawn from a probability distribution with unknown parameter θ which needs to be estimated. Further suppose that $\underline{\theta} = \underline{\theta}(X_1, X_2, ..., X_n)$ and $\overline{\theta} = \overline{\theta}(X_1, X_2, ..., X_n)$ are two statistics can be determined from the sample. The interval $(\underline{\theta}, \overline{\theta})$ denotes the $100(1-\alpha)\%$ confidence interval for θ if $\underline{\theta}$ and $\overline{\theta}$ can be selected such that

$$P\left\{\underline{\theta}(X_1, X_2, ..., X_n) < \theta < \overline{\theta}(X_1, X_2, ..., X_n)\right\} = 1-\alpha \qquad \text{(D.1)}$$

The $\underline{\theta}$ and $\overline{\theta}$ are the lower and upper confidence limits for θ. The level of

confidence of the confidence interval indicates the probability that the confidence range captures this true population parameter. In applied practice, confidence intervals are typically stated at the 90%, 95% confidence level.

If population X is normally distributed, i.e. $X \sim N(\mu, \sigma^2)$. For population standard deviation σ is known, the confidence interval estimation of population mean μ can be estimated as follows.

$$\mathrm{CI}^{\pm} = \bar{X} \pm z_{\alpha/2} \frac{\sigma}{\sqrt{n}} \tag{D.2}$$

where $z_{\alpha/2}$ is the corresponding quantile of the normal distribution for a probability of $\alpha/2$ in each tail as shown in Figure D.1. The quantile values corresponding to confidence interval are presented in Table D.1.

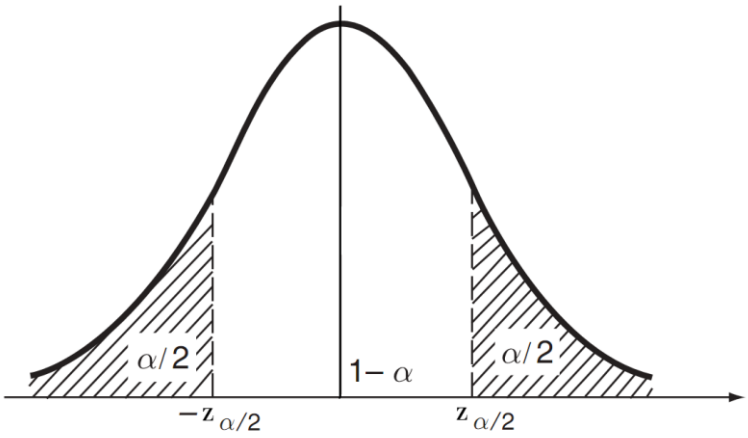

Figure D.1 100(1-α)% confidence limits for known standard deviation

Table D.1 Quantile value corresponding to confidence interval

Confidence interval	90%	95%	99%
$z_{\alpha/2}$	1.645	1.960	2.576

If the population standard deviation σ is unknown, we can substitute the sample standard deviation S which would introduce extra uncertainty, since S varies from sample to sample. The student's distribution is used instead of the normal distribution to estimate the confidence interval.

$$\mathrm{CI}^{\pm} = \bar{X} \pm t_{n-1,\alpha/2} \frac{S}{\sqrt{n}} \tag{D.3}$$

where $t_{n-1,\alpha/2}$ is the corresponding quantile of student's distribution with n-1 degrees of freedom for a probability of $\alpha / 2$ in each tail as shown in Figure D.2..

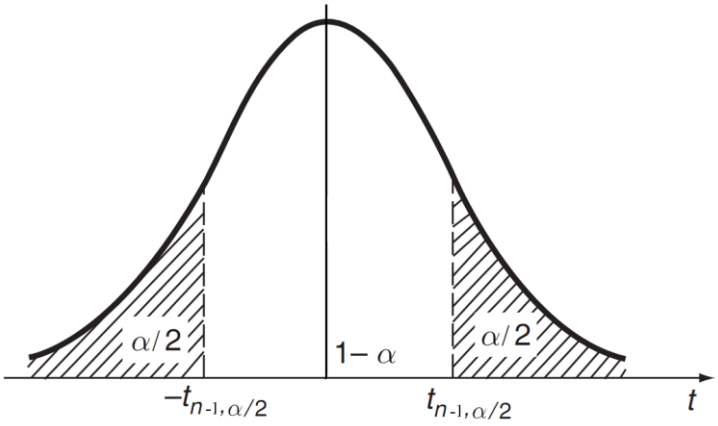

Figure D.2 100(1-α)% confidence limits for unknown standard deviation

Appendix E Bootstrap Method

The bootstrap method introduced by Efron (Efron and Tibshirani, 1993) is a statistical approach based on resampling from a distribution determined by the available sample of data. Assume that observations $x_1, x_2, ..., x_n$ as realizations of independent random variables with distribution function *F*. For the unknown *F*, empirical distribution function is used instead of the *F*, where a established for X on the basis of the observed data by allocating a probability of 1/n to each of the observed data points. That is the nonparametric approach for the bootstrap estimates.

The other approach is the parametric bootstrap for the known distribution function *F* with unknown parameter θ. The parameters are estimated from the observed data. The bootstrap method can be applied for the uncertainty qualification and confidence interval estimation. Assumed that the initial sample of n extreme values is drawn from a distribution i.e. Gumbel. The true parameter values of the Gumbel distribution are replaced by the estimated values obtained from the initial sample. A large number of independent bootstrap samples of size n can be generated from the distribution. For each sample, a new Gumbel distribution would be fitted and the corresponding statistical characteristic value such as median, most probable maximum (MPM) or 100(1-α)% fractile value can be identified. If the number of samples had been large enough, an accurate estimate of the confidence interval on the statistical characteristic value based on a sample of size n could be found. The mean and standard deviation of the statistical characteristic value can be calculated and then the coefficient of variance (COV) can be estimated.

Appendix F Laplace's Method

Laplace's method is a technique for evaluating an integral of the form as given in Eq.(F.1), where $f(x)$ is a twice-differentiable function and λ is a very large number, and the integration range can be infinite. This method is based on that the significant contributions to the integral mainly come from in a neighborhood of maximum point x^* of $f(x)$.

$$\int_a^b e^{\lambda f(x)} dx \tag{F.1}$$

Firstly, we take the Taylor series expansion of $f(x)$ around x^* up to quadratic order.

$$f(x) = f(x^*) + f'(x^*)(x - x^*) + \frac{1}{2} f''(x^*)(x - x^*)^2 + \cdots \tag{F.2}$$

x^* is the maximum point, which means it is a stationary point and concave down, i.e. $f'(x^*) = 0$ and $f''(x^*) < 0$. The Taylor series expansion of $f(x)$ becomes:

$$f(x) \approx f(x^*) - \frac{1}{2}\left| f''(x^*) \right| (x - x^*)^2 \tag{F.3}$$

Then substituting this approximation expansion of $f(x)$ into the integral, we can obtain that

$$\int_a^b e^{\lambda f(x)} dx \approx e^{\lambda f(x^*)} \int_a^b e^{-\frac{\lambda}{2}\left| f''(x^*) \right| (x - x^*)^2} dx \tag{F.4}$$

It can be seen that the integral becomes the form of Gaussian integral which can be evaluated. The larger the value of λ, the more closely the integral aligns with a Gaussian integral. The general Gaussian integral is given as follows.

$$\int_{-\infty}^{\infty} e^{-\frac{(x-\mu)^2}{2\sigma^2}} dx = \sqrt{2\pi}\sigma \tag{F.5}$$

Given that the exponential decays quite rapidly away from the stationary point x^*, particularly for large value of λ. The portions far away from the stationary point do not make significant contributions to the integral. Then the approximate prediction for the integral can be done by evaluating the Gaussian integral, shown as follows.

$$\int_a^b e^{\lambda f(x)} dx \approx e^{\lambda f(x^*)} \frac{\sqrt{2\pi}}{\sqrt{\lambda \left| f(x^*) \right|}} \tag{F.6}$$

The approximation is asymptotically correct as λ tends towards infinite. The larger the value of λ, the shaper the peak of the integrand at x^* and the more accurate the asymptotic approximation for the integral.

List of Publication

1. Aijun Wang, Shan Huang, Nigel Barltrop. Long Term Extreme Analysis of FPSO Mooring Systems Based on Kriging Metamodel. Proceedings of the 33rd International Conference on Ocean, Offshore and Arctic Engineering. OMAE2014-24609.
2. Aijun Wang, Shan Huang, Nigel Barltrop. Dynamic Analysis of Mooring Lines in Time and Frequency Domain. ICMT 2014 International Conference on Maritime Technology.
3. Aijun Wang, Shan Huang, Nigel Barltrop. Extreme Analysis of Mooring System Using Contour Line Method. ICMT 2014 International Conference on Maritime Technology.